AD631777

DEUTSCHE FORSCHUNGSANSTALT FÜR LUFT- UND RAUMFAHRT E.V.

INSTITUT FÜR FLUGMECHANIK

PROF. DR. H. BLENK

FINAL REPORT

PARACHUTE CANOPIES DURING INFLATION

H.-D. Melzig

P. K. Schmidt

BRAUNSCHWEIG

September 1965

AF EOAR

September 1965

FINAL REPORT
PARACHUTE CANOPIES DURING INFLATION

H.-D. MELZIG
P. K. SCHMIDT

DEUTSCHE FORSCHUNGSANSTALT FÜR LUFT- UND RAUMFAHRT
INSTITUT FÜR FLUGMECHANIK
BRAUNSCHWEIG, GERMANY

The research reported in this document has been sponsored by the AERONAUTICAL SYSTEMS DIVISION, AFSC through the European Office, Office of Aerospace Research, United States Air Force.

FOREWORD

This Technical Report was prepared by the Institut für Flugmechanik of the Deutsche Forschungsanstalt für Luft- und Raumfahrt e. V. (DFL) under USAF Contract Nr. AF 61(052)-681. The work was sponsored by the Air Force Flight Dynamics Laboratory, Research and Technology Division, AFSC, through the European Office, Office of Aerospace Research, USAF. The work was administered by the European Office, Office of Aerospace Research, USAF, in Brussels, Belgium, Major W. C. Whicher and Major W. T. Campbell, Contracting Officers, and was directed technically by the Recovery and Crew Station Branch, AF Flight Dynamics Laboratory, RTD, AFSC, Mr. R. J. Berndt, Project Engineer.

The research effort was initiated in April 1963 and completed in April 1965, and was conducted under Project Nr. 6065 "Performance and Design of Deployable Aerodynamic Decelerators", and Task Nr. 606503, "Parachute Aerodynamics and Structures."

The manuscript was released by the authors in September 1965 for publication.

ABSTRACT

An experimental investigation and correlative analysis were conducted to determine the pressure distribution over the surface of parachute canopies during the period of inflation for the infinite mass case and to correlate pressure coefficients with inflating canopy shapes. Parachute canopy models of Circular Flat, 10% Extended Skirt, Ringslot, and Ribbon designs were tested under infinite mass conditions in a 9 x 12 ft low speed wind tunnel. External and internal pressure values were measured at various locations over the surface of the model canopies throughout the period of inflation, and generalized canopy profile shapes were obtained by means of photographic analysis.

Pressure coefficients derived for the steady state (fully open canopy) are quite comparable to the results of previous measurements. Peak pressure values during the unsteady period of inflation were found to be up to 5 times as great as steady state values.

The relationships between the pressure distribution and time for each of the canopy models deployed at free-stream velocities between 70 and 160 ft/sec are presented in detail and correlated with changing canopy shape. A complete shape analysis is made and a mathematical model is proposed.

T A B L E   O F   C O N T E N T S

ILLUSTRATIONS

ILLUSTRATIONS (cont.)

ILLUSTRATIONS (cont.)

T A B L E S

1. INTRODUCTION

Minimum weight and packing volume are basic requirements for parachute canopies for any application. To meet these requirements, knowledge of the stress distribution in the canopy is a prerequisite for the parachute designer. This applies in particular to the period of transient force generation, the parachute filling or opening process. In order to accomplish a valid determination of the canopy stress distribution and since attempts to measure the actual stresses in parachute canopies during the transient state have not been successful, the pressure distribution over the surface of an inflating parachute canopy must be known to yield a basis for the calculation. In addition, the shape and shape changes which a parachute canopy undergoes during the period of inflation must be known so that the calculation procedure may be generalized.

For the steady state condition, that is for the fully inflated parachute canopy, the calculation of stresses in the canopy has been attempted by Jones [1] and by Topping et al [2] . Only recently, an approach was developed by Heinrich and Jamison [3] to predict the canopy stress distribution for the transient state. Although this calculation approach considers synthesized canopy profile shapes through which the canopy evolves during the period of inflation, pressure coefficients were based upon results obtained during steady state measurements on these synthesized canopy shapes.

A great difficulty for all steady state considerations is that maximum stresses occur during the rapidly occurring canopy shape changes of the filling process, and pressure and stress values can vastly exceed steady state values.

A number of attempts have been made in the past to measure the actual pressure versus time relationships during the process of inflation. These attempts, however, have been unsuccessful primarily due to the non-availability of a pressure sensing method or device which would yield accurate results under the accceleration levels encountered during canopy inflation.

By means of a specially developed pressure transducer it has now become possible to measure pressure values at various locations on the canopy. In addition, an analysis was made of the changing canopy shape and related to the cahanging pressure distribution. The experimental investigation and correlative analysis were conducted for the case of parachute opening under infinite mass conditions, the case where there is no or only a relatively small velocity decay during the period of canopy inflation. Although the results of this investigation do not apply to all cases of parachute application, they do represent a major step towards a better knowledge of the parachute opening dynamics.

2. TEST CONDITIONS

A. Parachute Canopy Models

The investigation was performed on parachute canopy models of 4 basic types or design:

1. Solid cloth, circular flat type
2. Solid cloth, 10% flat extended type
3. Ringslot type
4. Flat circular ribbon (FIST) type

The solid cloth, circular flat type canopy model was based upon the design of the personnel type (C-9) canopy, incorporated 28 gores, and had a nominal diameter (D_o) of 53.5 inches.

The design of the solid cloth, 10% flat extended skirt type canopy model was based upon that of the troop type (T-10) canopy. The model incorporated 30 gores and had a nominal diameter (D_o) of 62.0 inches.

The ringslot and flat circular ribbon (FIST) type canopy models were fabricated of 24 gores with a geometric porosity of 16% for the ringslot and 18% for the flat circular (FIST) types. The ringslot type canopy model was constructed of 5 cloth rings and 1 vertical tape in each gore, the FIST type canopy model was constructed with 27 horizontal ribbons and 4 vertical tapes in each gore. These models had a nominal diameter (D_o) of 53.5 inches.

The cloth used in the fabrication of the canopy models met the German Kennblatt 1004 (Perlon; nominal cloth permeability at 1/2 inch H_2O: 130 cfm/ft^2; weight: 1.45 oz/yd^2).

Drawings of the four models are included in Appendix I.

B. Test Facilities and Test Method

All experimental investigations were performed in the 9 x 12 ft low speed wind tunnel of the Deutsche Forschungsanstalt für Luft- und Raumfahrt e.V. (DFL) in Braunschweig.

A schematic presentation of the test arrangement is shown in Figure 1. The canopy models were mounted in the wind tunnel test section in a stretched-out position, but prevented from inflating by two leather clamps, one enclosing the skirt and the other enclosing the middle section of the canopy. The wind tunnel was then brought up to specific speeds (70, 100, 130 and 160 ft/sec) and the clamps were suddenly released by burning a thin wire and by the action of springs attached to the clamps. Upon release of the clamps, the canopy models were free to inflate.

The distribution of the local pressure (internal, external and differential) over the canopy model from skirt to vent was measured by strain gage type pressure transducers attached to the canopy surface at specific locations. The pressure transducers were developed ba the Deutsche Forschungsanstalt für Luft- und Raumfahrt. A view of the pressure transducer is shown in Figure 2. The physical specifications of the sensing element are: weight 0.2 oz, diameter 1.2 inches, thickness 0.35 inches, capacity $\pm$ 0.5 psi.

Each sensing element is temperature and acceleration compensated. Errors in per cent of output under applied pressures of 0.3 psi as a function of g-loadings applied statically in three mutually perpendicular planes are shown in Figure 3. The influence of accelerations up to 200 g's is below 3% of the full scale output of the transducer.

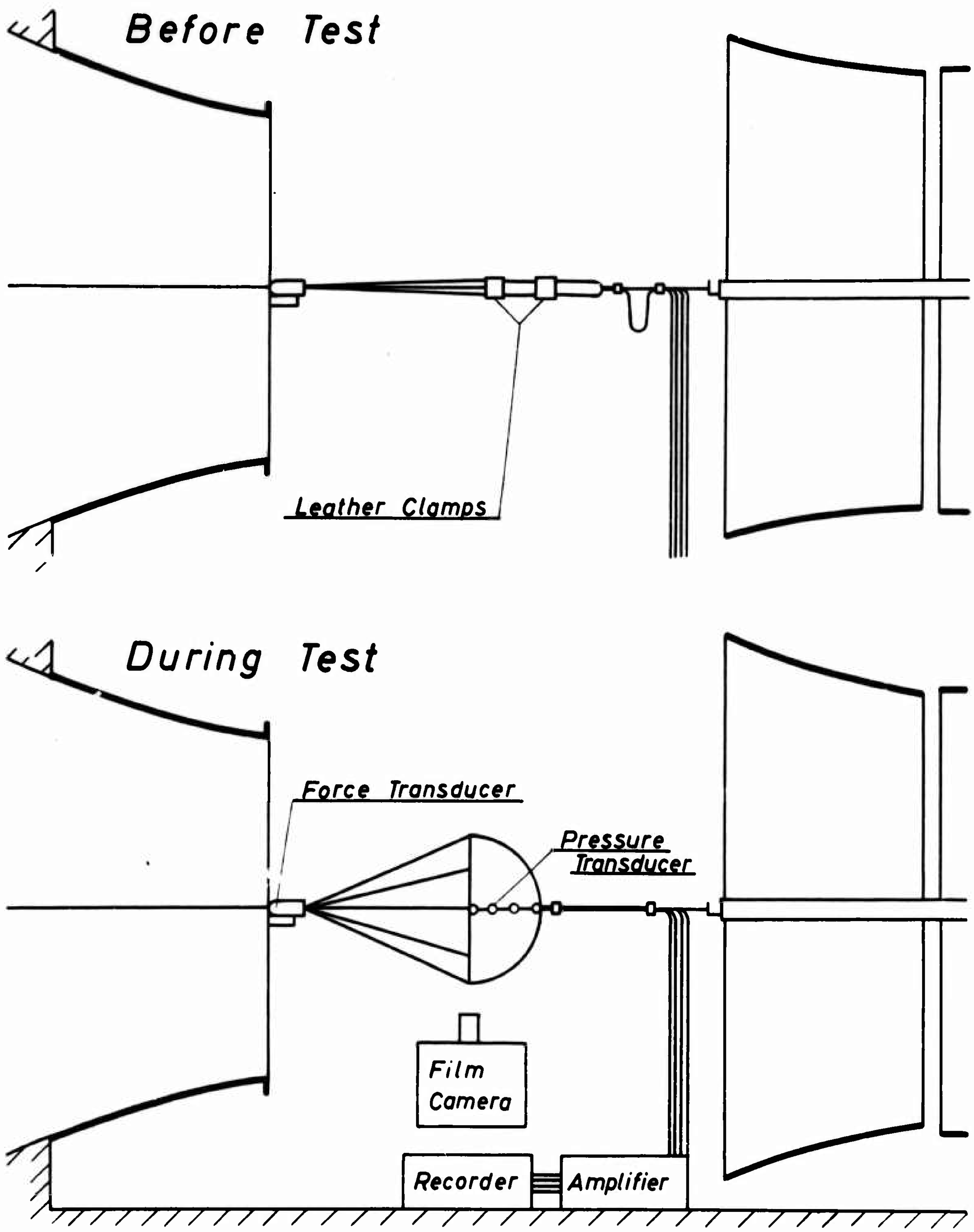

Figure 1 Test Arrangement in the Windtunnel

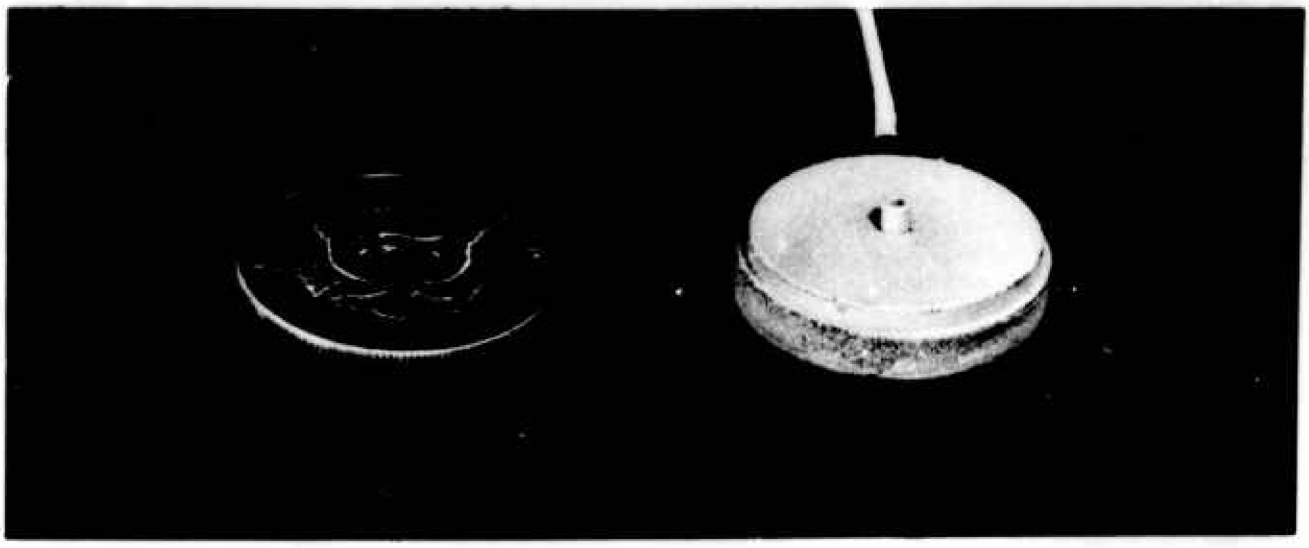

Figure 2 Pressure Transducer

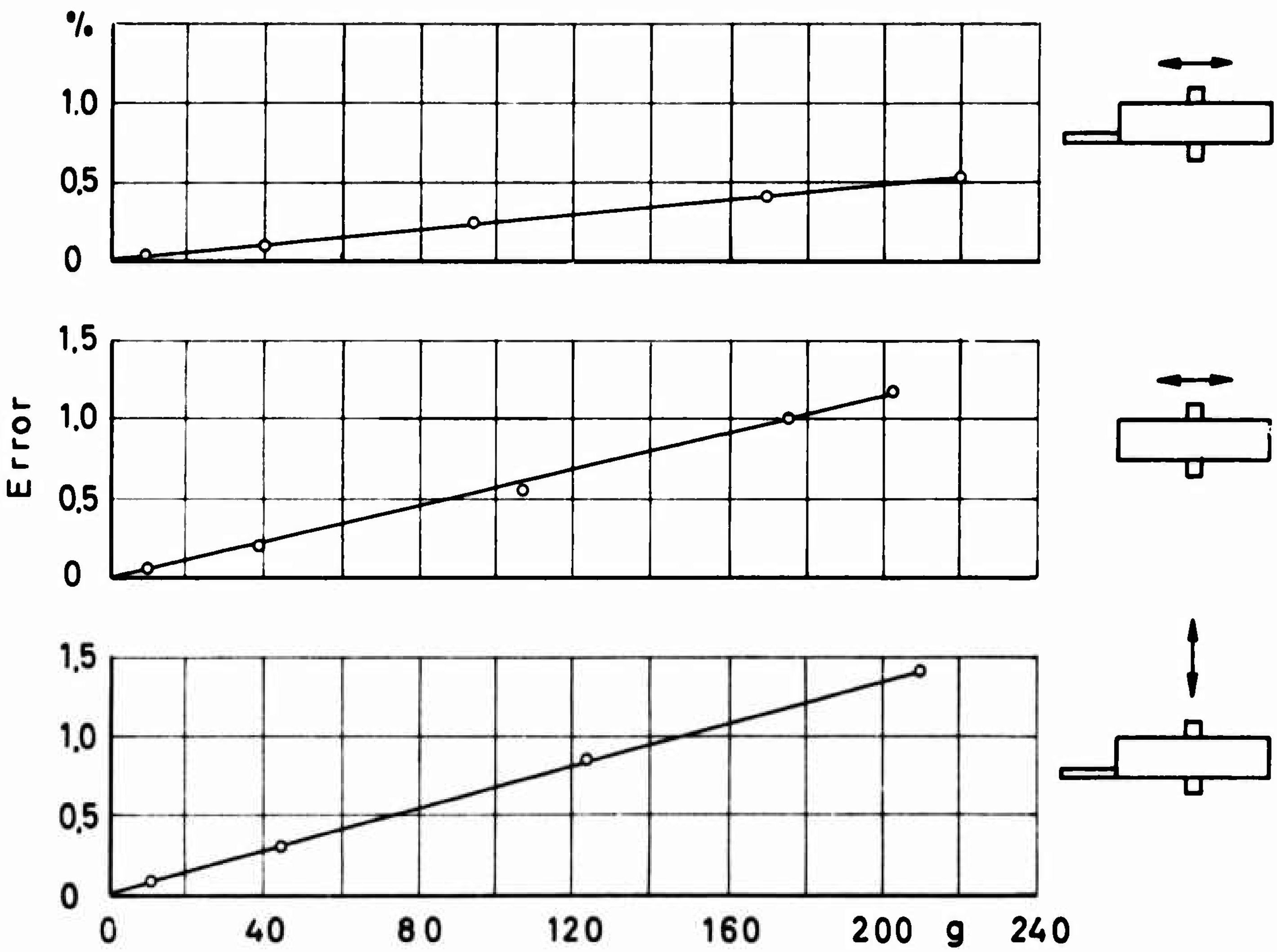

Figure 3 Error in % of 0.3 psi Output Versus g-Loading for the 3 Axes of Attack

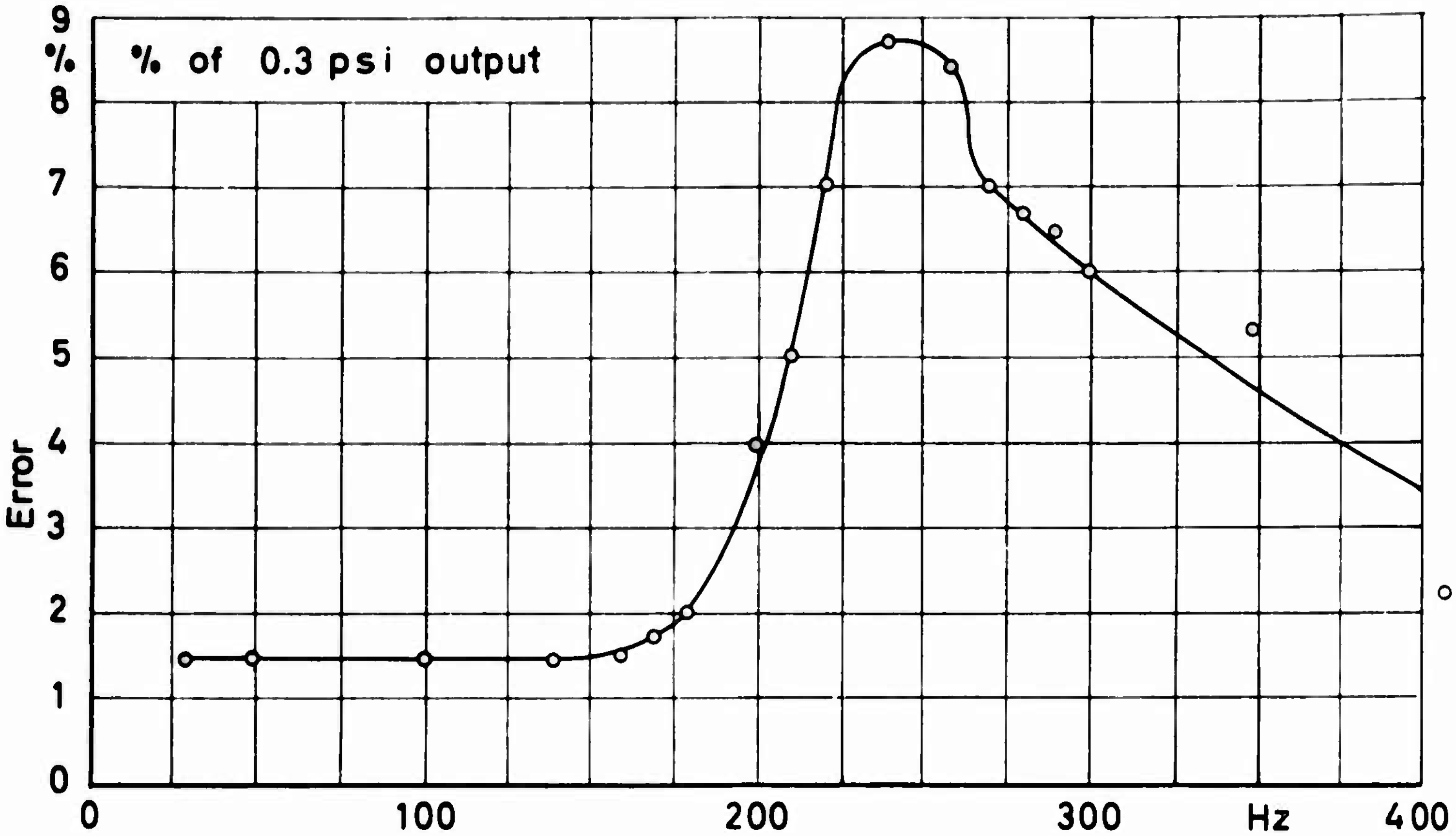

Figure 4 Frequency Response of Pressure Transducer

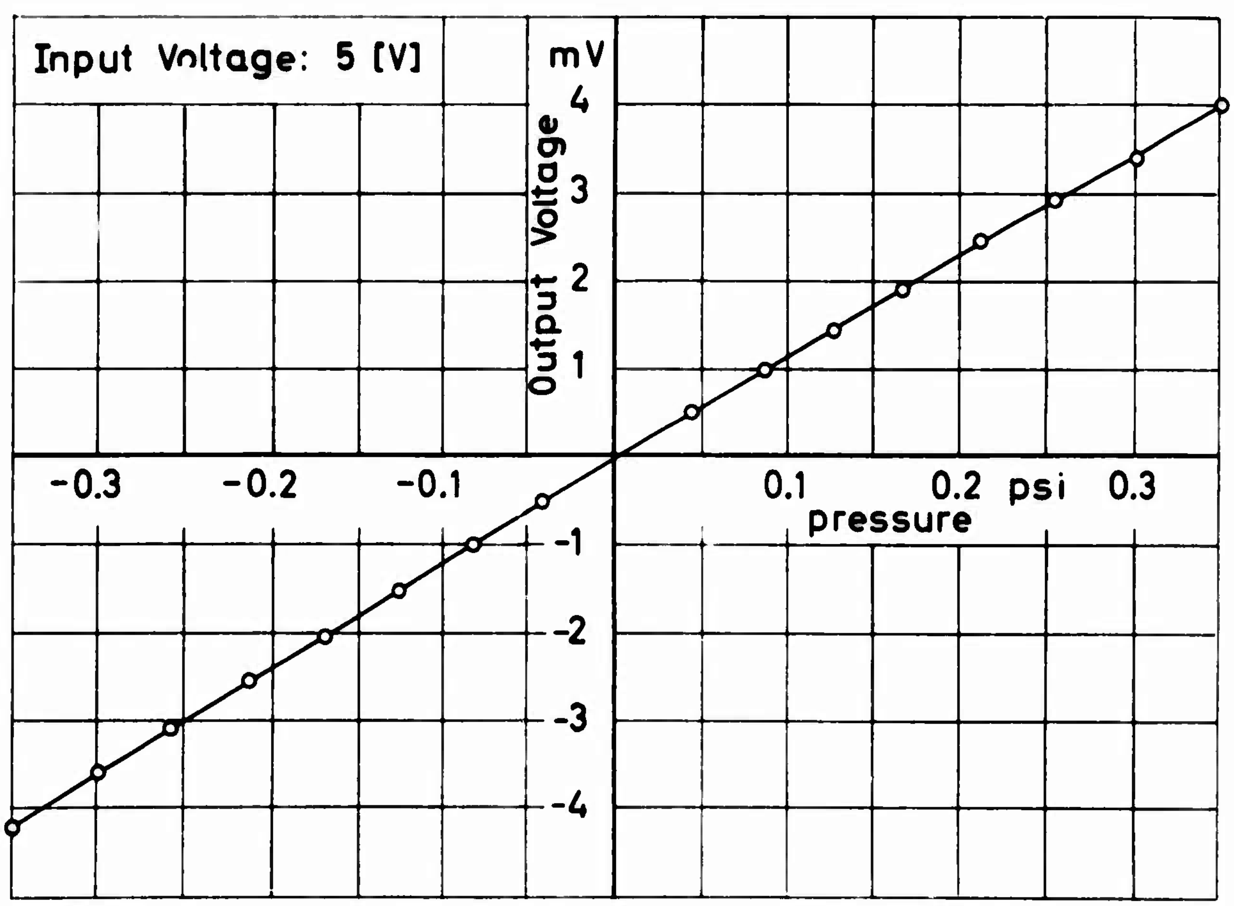

Figure 5 Linearity and Calibration of Pressure Transducer

Since accelerations experienced on the parachute canopy during inflation are not static but dynamic, that is portions of the cloth surface may move or oscillate with frequencies up to 100 cps, the frequency response of the transucer must be considered in order to determine the total introduced error under dynamic conditions. As indicated in Figure 4, the point of resonance of the transducer is approximately 250 cps with a maximum error of 9 % of the total output at an applied pressure of 0.3 psi. Up to an applied frequency of 170 cps, this error is only 1.5 %. Output voltage and linearity of the pressure transducer over a range of applied pressures are shown in Figure 5.

In addition to the pressure values, the forces generated by the parachute canopy were also recorded as measured by a strain gage type tensiometer. Hottinger carrier systems were used for the electronic measurements and the resulting signals recorded on a light-beam oscillograph Honeywell Visicorder.

C. Test Procedure

A total of four pressure transducers were located along the cord center lines of the canopies and distributed 90 degrees apart around the surface of the canopies because of weight influences. In addition, the location of the transducers was staggered in a manner shown in Figures 7 through 52 to obtain pressure measurements near the skirt, near the vent, and at two intermediate positions on the canopy. Additional measurements were made for comparative purposes with the transducers located along the gore center line (Figures 103 thru 105).

The complete filling process was photographed from one side by a high speed camera with 100 frames per second. From the photographic record, canopy profile shapes and projected canopy diameter values were obtained.

At the time of removal of the clamps setting the canopy free to inflate (time t = 0), a time base signal of 50 cps was initiated and recorded on both the oscillogram and the photographic film for synchronization purposes.

The internal, external, and differential pressure values were measured and recorded during different runs. For the measurements of the internal and external pressures, the barometric pressure was conducted by tubings to the outer and inner pressure taps of the transducer, respectively.

A total of four separate measurements were made for each condition in order to determine the repeatability of the measurements and obtain valid average data. Thus, four equal test runs for each of the four canopy types at four different speeds to obtain three different pressure (differential, internal, external) versus time relationships were performed for a total of 192 wind tunnel test runs.

In order to obtain background data on the acceleration distribution over the parachute canopies during the period of inflation, acceleration measurements were performed on each of the four canopy types for each of the four deployment speed conditions. For this purpose, miniature strain gage type accelerometers of approximately the same size and weight as those of the pressure transducers were located at the same points on the canopies where pressure measurements were taken. Maximum values were measured on the solid cloth flat circular type canopy models at a location near the canopy skirt which at the largest deployment speed (160 ft/sec) is accelerated at the beginning of inflation at approximately 50 g's and decelerated at the end of inflation at approximately 200 g's.

3. RESULTS AND ANALYSIS

The two major objectives of the program were:

1. To determine the characteristic relationships between the pressure and time for each of the four canopy types,
2. To correlate the pressure values and canopy shape at any point during canopy inflation.

In addition, a detailed analysis of the canopy shape development for the period of canopy inflation under infinite mass operating conditions was to be attempted.

A. Canopy Pressure Distribution

Reproductions of actual oscillograph records obtained from the tests are shown in Figure 6. These records represent the registration obtained on a flat circular ribbon type (FIST) canopy during four different test runs conducted at the same deployment condition of 130 ft/sec. Analyzing these registrations, two general statements may be made:

1. The reproducibility of the four measurements made at any one test condition was relatively good. This applies in particular to the solid cloth type canopies. Therefore, since no significant deviations occurred the results of only one measurement for each canopy type and deployment condition are included in this report.

2. As the original recordings illustrate, the pressures fluctuated during the steady state period (canopy fully inflated) due to flow conditions. During the unsteady period (canopy inflation), some fluctuations can occur due to the unsteady movement of the canopy material, in particular in the skirt area; however the mean values show increasing pressures with a more or less prominent peak. The determination of mean steady state values was sometimes difficult due to fluctuations in the pressure values and since actual steady state conditions were not reached immediately after canopy inflation, but several seconds later. To avoid cable breakage and other damages to the test set-up, especially at the high deployment velocity, the wind tunnel was shut down immediately after canopy filling was completed. To obtain more accurate steady state values, readings should be taken for at least five seconds during the steady state period. In general, however, the steady state values obtained are quite comparable to the results of former measurements [4] .

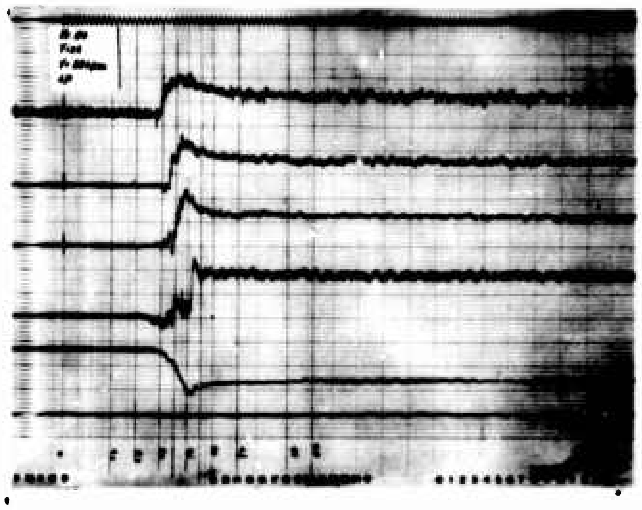

Run No.
80

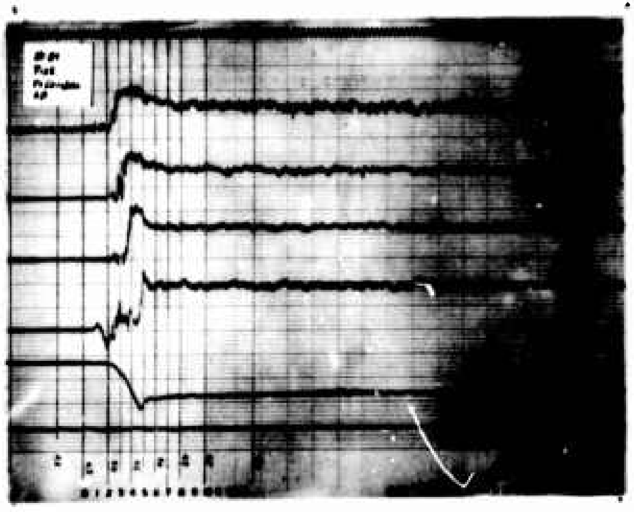

81

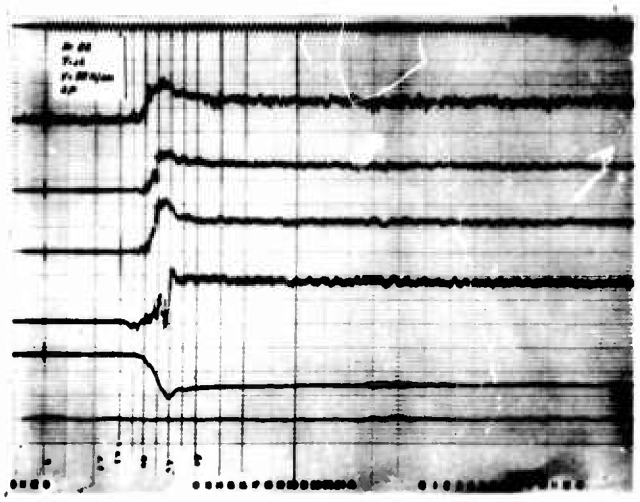

82

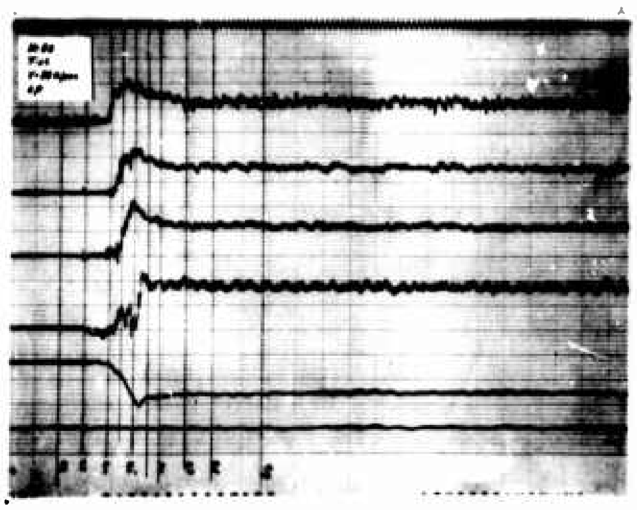

83

Figure 6

Reproducibility of experiments. Original registrations of 4 different runs under the same initial condition of v_o = 130 ft/sec for FIST.

The local pressures measured on the surface of the canopies were differential pressures, Δp, since atmosheric pressure was conducted by tubing to one of the ports of the pressure transducers. For open test section wind tunnels, the atmospheric pressure can be assumed to be equal to the static pressure of the airflow. The pressure values measured are expressed in coefficient form by relating these to the dynamic pressure of the airflow. Thus

$$c_p = \frac{\Delta p}{q} .$$

As mentioned above, the differential, internal, and external pressure distributions were measured. For each of the canopy types and test conditions, the differential, internal, and external pressure coefficients (c_{pd}, c_{pi}, and c_{pe}) for the four locations on the canopy were generalized (smoothed) and are plotted as a function of time in Figures 7 thru 52. In order to correlate pressure values to canopy shape, the instantaneous projected canopy diameter, D_p, was evaluated from the photographic recordings. Therefore, the relationship between projected canopy diameter ratio, D_p/D_o, as a function of time is shown also for each test run. A presentation of all three pressure coefficient (c_{pd}, c_{pi}, c_{pe}) versus time relationships for each test condition together with reproductions of the original oscillograph recordings is included in Appendix II.

In general, the pressure peak occurs first in the canopy vent area and travels very rapidly towards the skirt area. The pressure peaks occur slightly prior to the time at which the canopy reaches its fully inflated shape for the first time. For the solid cloth type canopy models, the pressure peaks from vent to skirt follow very rapidly one another, being separated in time only approximately 1/100 of a second. The last peak in the skirt area occurs at almost exactly the time at which the canopy is fully inflated. For the geometric porosity type canopies, the peak separation time is somewhat greater, for the FIST type canopy approximately 5/100 to 1/10 of a second, for the ringslot type canopy 1/10 of a second or more. The last peak in the area of the canopy skirt is again close to but before the fully inflated projected canopy diameter is reached for the first time.

Aside from the determination of pressure versus time relationships and pressure distributions, the determination of the magnitude of the pressure peaks is a significant result of this program. For comparative purposes, a pressure factor, F_p, can be defined which is the ratio between the maximum value of the pressure coefficient, c_{pmax}, and the value of the steady state pressure coefficient, c_{pst}, or

$$F_p = \frac{c_{pmax}}{c_{pst}}$$

A compilation of all maximum and steady state pressure coefficient values (c_{pmax} and c_{pst}) at the four locations on the four canopy types, the time increment between occurrence of pressure peaks in the areas of canopy vent and skirt, and the time at which the fully inflated projected canopy diameter, D_p, is reached for the first time is given in Table I for each of the four deployment speed conditions, v_o.

The steady state pressure coefficients, c_{pst}, in the area of the canopy skirt are approximately 1.0 for the internal and -0.7 for the external pressures, resulting in a differential pressure coefficient of 1.7. This is true for the extended skirt, FIST, and ringslot type canopies. These values are comparable to the results obtained by Heinrich [4] . For the circular flat type canopy steady state pressure coefficients of up to 1.5 for the internal, -1.0 for the external, and 2.5 for the differential pressures were obtained. These values are high and there is a wide variation of all values acquired on this canopy type. More tests appear to be necessary to verify the findings.

On the circular flat type canopy, peak differential pressures during inflation reached approximately three times the steady values at full canopy inflation. In one test, a pressure factor of 5.4 was even obtained at a location near the canopy skirt. At the higher deployment velocities of 130 and 160 ft/sec, the pressure factor decreased slightly due to the slightly lower peak pressure coefficient and the somewhat higher steady state pressure coefficient values.

For the extended skirt type canopy, differential pressure factors from 2.5 at a location near the canopy vent to 3.6 at a location near the canopy skirt were found. Again as for the circular flat type canopy, the pressure factors decreased with increasing deployment velocity. At a deployment velocity of 160 ft/sec, the pressure factors varied from a value of 2.1 to 2.8 from the location near the canopy vent to one near the skirt.

For the geometric porosity type canopies, the pressure factors are remarkably lower. The maximum pressure factor obtained on the flat circular ribbon (FIST) type canopy was 2.3, decreasing to 1.7 at the highest deployment velocity. For the ringslot type canopy, the maximum pressure factor was approximately 1.6, with no significant differences between the low and the high deployment velocities. For the geometric porosity type canopies, there was no significant difference in the magnitude of the pressure factor for locations near the canopy vent or the skirt.

Absolute filling times of each of the canopy types decrease with increasing deployment velocity as can be seen from the Figures and from the tabulated data in Table I. The filling times are shortest for the circular flat type canopy, become longer for the extended skirt and FIST ribbon type canopies, and are longest for the ringslot type canopy.

A correlation between pressure changes and changing canopy shape may be obtained from Figures 53 thru 60 in which the pressure coefficients (c_{pd}, c_{pi}, c_{pe}) are plotted as a function of the projected canopy diameter ratio, D_p/D_o. These diagrams clarify the pressure-shape relationship. For the circular flat type canopy, the curves for the four locations of the pressure sensing elements run very close together, thus indicating a very quick filling of the canopy. These relationships

Table 1 Peak and Steady State Values for c_p and D_p and corresponding times

Model	Pressure	Run No.	v_e ft/sec	c_p I (Vent) Max.	I (Vent) Steady	II Max.	II Steady	III Max.	III Steady	IV (Skirt) Max.	IV (Skirt) Steady	t at peaks I-IV 1/10 sec	t at Peak D_p 1/10 sec
Circular Flat	Differential	182	70	4,8	1,6	4,5	1,6	5,4	1,7	7,9	1,5	2,6-2,7	2,6
		183	100	4,2	1,6	4,6	1,8	4,3	1,8	6,6	2,5	2,1-2,2	2,2
		167	130	4,6	2,0	3,9	1,9	3,5	1,9	5,5	2,7	1,6	1,7
		191	160	2,9	2,1	3,0	1,9	3,4	1,7	4,8	2,4	1,4-1,5	1,4
	Internal	194	70	3,1	1,0	2,7	1,0	3,3	1,0	2,5	1,0	2,4	2,5
		200	100	3,6	1,4	4,0	1,6	3,4	1,5	2,8	1,4	1,9-2,0	2,0
		203	130	2,3	1,1	2,7	1,1	2,5	1,1	2,0	0,8	1,4	1,6
	External	211	70	-1,2	-0,4	-2,3	-0,6	-2,6	-0,5	-4,7	-1,2	2,3-2,9	3,0
		216	100	-1,2	-0,6	-2,0	-0,6	-2,3	-0,7	-2,7	-1,0	2,0-2,1	2,2
		218	130	-1,4	-0,5	-2,4	-0,5	-2,0	-0,8	-3,6	-0,8	1,5-1,6	1,7
Extended Skirt	Differential	139	70	2,7	1,1	4,1	1,4	4,8	1,4	5,8	1,6	3,0-3,5	3,5
		144	100	3,5	1,4	3,4	1,4	3,7	1,7	5,5	1,6	2,6-2,7	2,9
		148	130	3,5	1,5	3,5	1,5	3,2	1,6	3,7	1,5	2,3-2,4	2,5
		153	160	3,0	1,2	2,6	1,2	2,9	1,4	3,9	1,4	1,8-2,0	2,3
	Internal	157	70	3,2	0,8	3,1	0,8	2,3	0,9	2,5	0,9	3,5-3,6	3,5
		160	100	2,8	0,8	2,7	0,7	2,8	0,8	2,5	0,8	2,6-2,8	2,9
		163	130	3,0	1,5	3,0	1,5	2,7	1,5	2,7	1,5	2,7-2,8	2,8
		166	160	2,9	1,3	3,2	1,2	2,9	1,4	2,9	1,4	2,1	2,1
	External	221	70	-2,1	-1,1	-2,4	-1,4	-2,3	-0,9	-3,8	-1,5	3,4-3,8	3,7
		226	100	-1,1	-0,4	-1,3	-0,5	-2,4	-0,5	-3,0	-0,6	2,6-3,0	3,1
		231	130	-1,4	-0,5	-1,1	-0,3	-2,3	-0,5	-2,1	-0,5	1,0-2,2	2,2
		235	160	-0,9	-0,5	-1,8	-0,5	-1,5	-0,5	-2,2	-0,7	1,2-2,0	2,0
FIST	Differential	72	70	1,9	0,8	1,9	1,1	2,3	1,1	2,1	1,7	2,5-3,5	4,0
		76	100	1,7	0,9	2,1	1,0	2,5	1,2	2,4	1,8	1,7-2,5	3,0
		82	130	1,7	0,9	1,5	1,0	1,9	1,2	2,4	1,8	1,3-1,8	2,3
		86	160	1,5	0,9	1,9	1,2	2,2	1,3	2,1	1,7	1,3-1,8	2,1
	Internal	101	70	1,3	0,7	1,4	0,9	1,6	1,0	1,3	0,9	3,1-3,4	3,7
		97	100	1,3	0,8	1,5	0,9	1,5	1,0	1,4	0,9	2,5-2,9	3,2
		92	130	1,2	0,7	1,3	0,9	1,3	1,0	1,1	0,9	1,8-2,4	2,8
		88	160	1,2	0,8	1,5	1,0	1,4	1,0	1,0	0,8	1,1-1,7	2,2
	External	104	70	-0,7	-0,4	-1,3	0,7	-1,3	-0,4	-1,5	-0,7	2,8-3,6	3,6
		110	100	-1,5	-0,5	-1,7	-0,9	-0,7	-0,3	-0,8	-0,3	2,2-2,8	2,9
		117	130	-0,7	-0,3	-0,9	-0,4	-0,9	-0,4	-1,3	-0,8	1,0-1,8	2,0
		119	160	-0,7	-0,3	-0,8	-0,4	-1,1	-0,4	-1,3	-0,7	1,2-1,8	
Ringslot	Differential	7	70	1,3	0,9	1,7	1,1	1,9	1,4	2,0	1,6	1,8-3,4	4,2
		10	100	1,4	1,0	1,9	1,1	1,8	1,4	1,8	1,6	1,0-3,9	4,0
		14	130	1,2	0,9	2,0	1,2	1,6	1,3	1,4	1,3	1,4-2,5	3,0
		18	160	1,3	0,9	1,7	1,1	1,6	1,3	1,6	1,2	1,2-2,4	2,[illegible]
	Internal	22	70	1,0	0,6	1,4	0,9	1,2	1,0	1,0	0,9	2,3-3,3	3,9
		30	100	1,1	0,6	1,5	1,1	1,2	1,0	1,1	0,9	2,0-3,1	3,4
		51	130	1,1	0,6	1,4	1,0	1,0	0,9	0,8	0,7	1,5-2,8	2,5
		26	160	1,1	0,7	1,4	1,1	1,1	0,9	0,9	0,8	1,0-2,5	2,5
	External	34	70	-0,6	-0,4	-1,3	-0,3	-1,5	-0,4	-1,3	-0,4	2,0-4,0	4,0
		39	100	-0,7	-0,3	-0,9	-0,3	-0,8	-0,4	1,1	-0,4	2,0-3,4	4,0
		42	130	-0,8	-0,3	-1,2	-0,2	-0,8	-0,4	-0,9	-0,6	1,4-3,0	3,0
		47	160	-0,9	-0,4	-1,5	-0,3	-1,2	-0,5	-1,2	-0,7	1,1-2,3	3,0

show a slow increase in pressure at the beginning of inflation, with a rapid build-up in pressure immediately prior to achieving first full canopy inflation. A different characteristic is observed on the ringslot type canopy. The four curves representing the four pressure points from the canopy vent to the skirt are spread. Although the curves show a rapid increase in pressure at each location, they indicate that the canopy shape change does only slowly follow increasing pressures. The trends for the extended skirt and FIST ribbon type canopies are located between these two extreme trends.

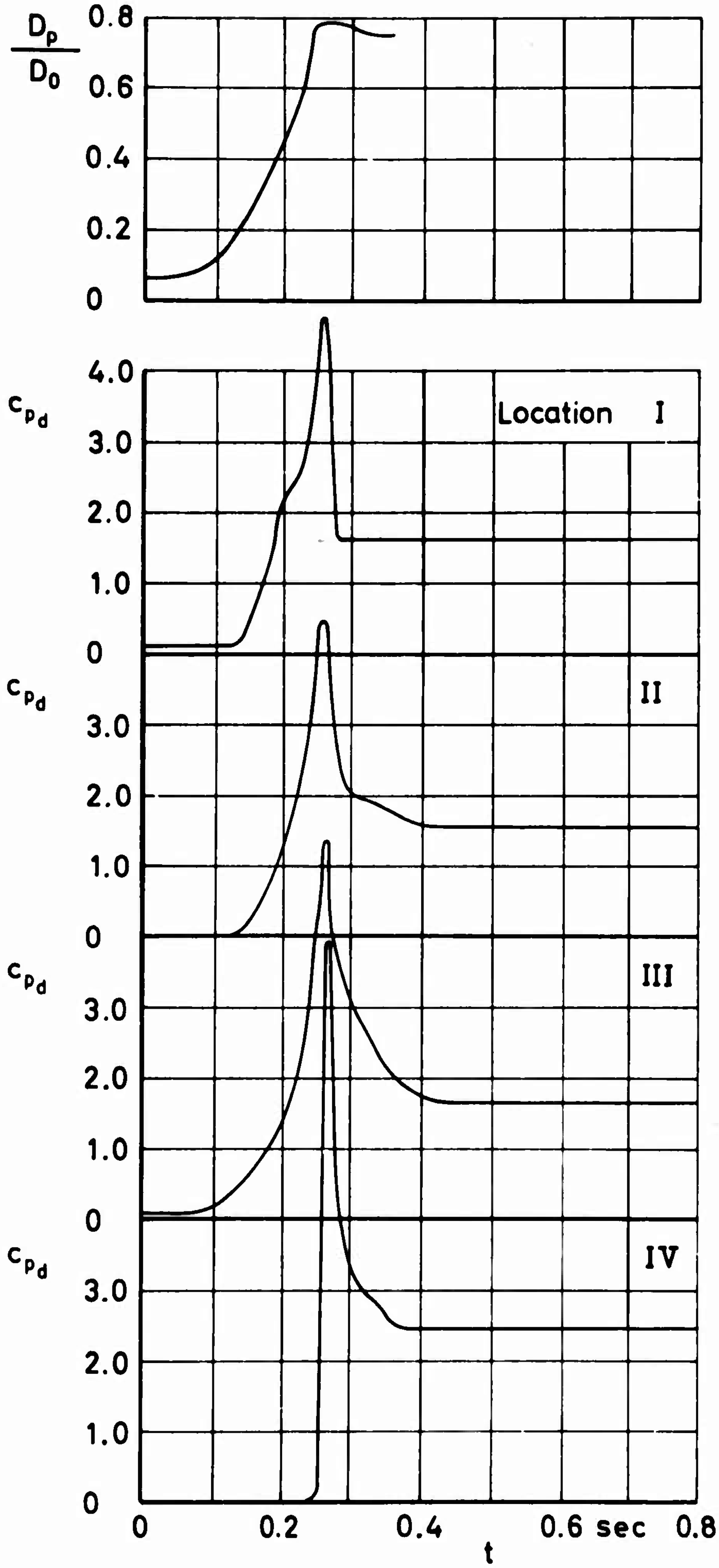

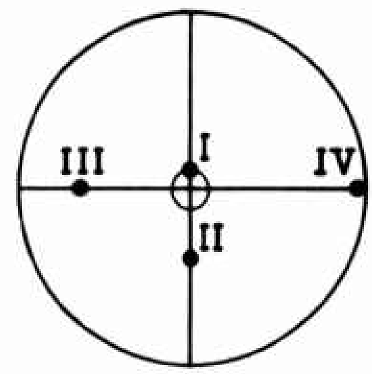

Location of pressure transducers on cord center line

Circular Flat

Figure 7 c_{p_d} and filling versus time

$v_0 = 70$ ft/sec

Run No. 182

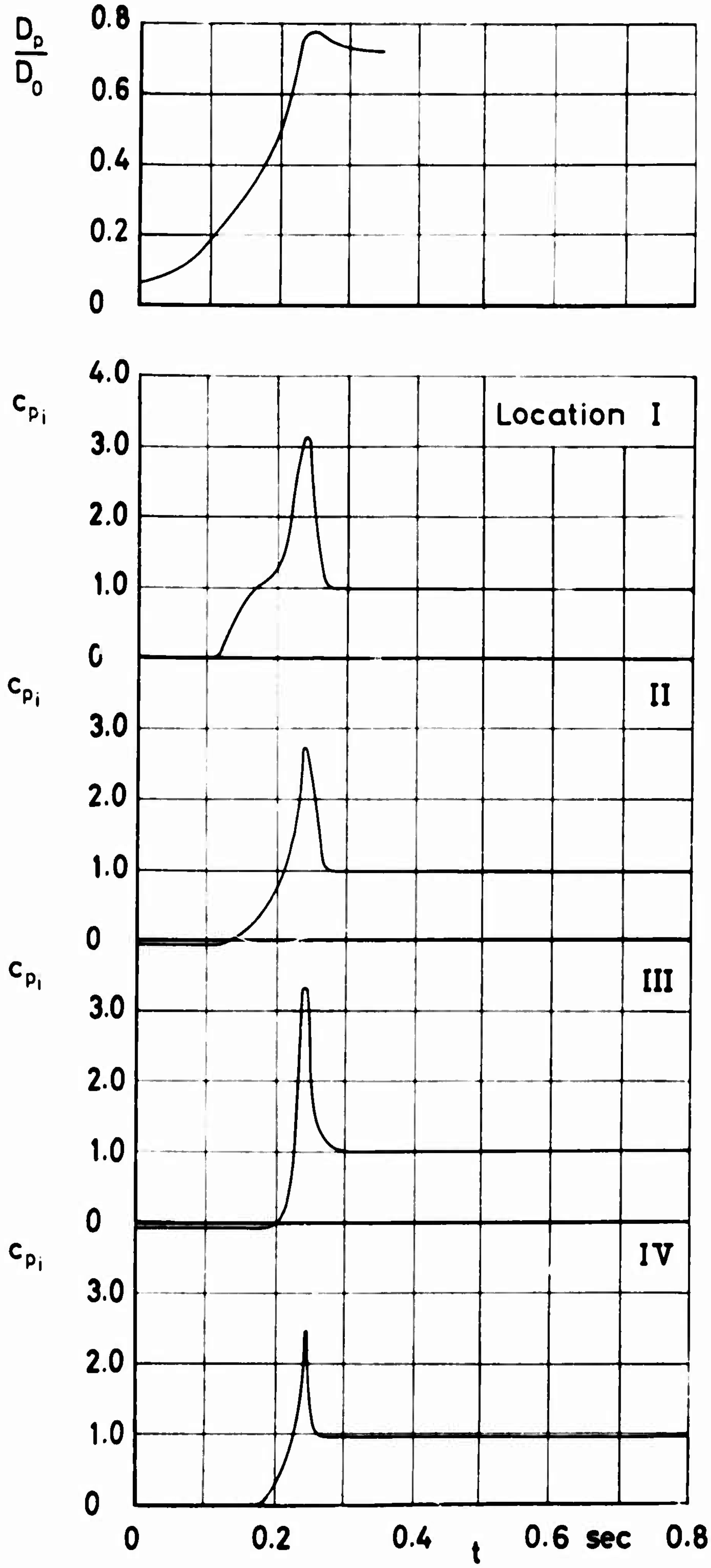

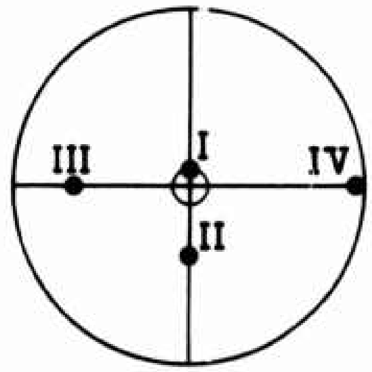

Location of pressure transducers on cord center line

Circular Flat

Figure 8 c_{p_i} and filling versus time

$v_0 = 70$ ft/sec

Run No. 194

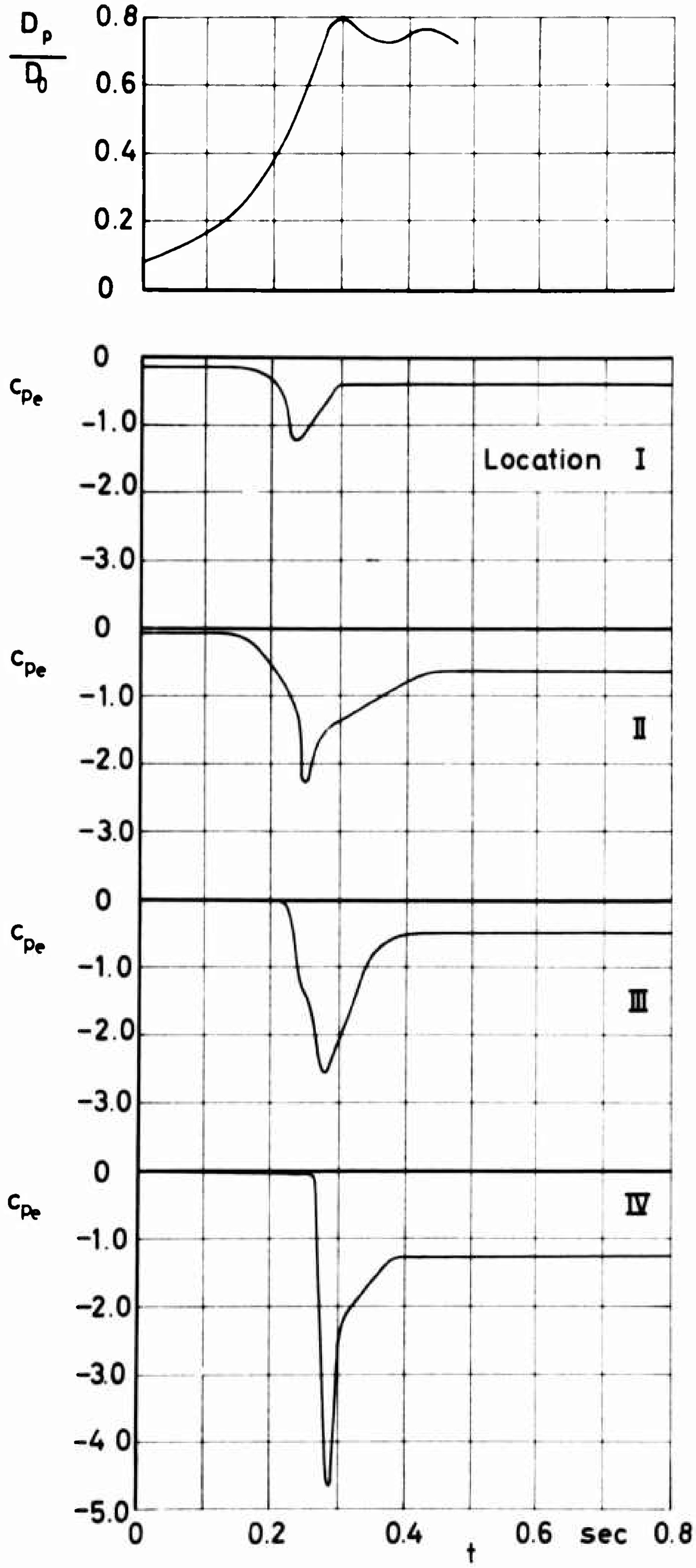

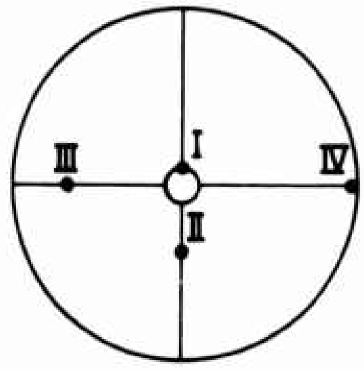

Location of pressure transducers on cord center line

Circular Flat

Figure 9 c_{p_e} and filling versus time

v_0 = 70 ft /sec

Run No. 211

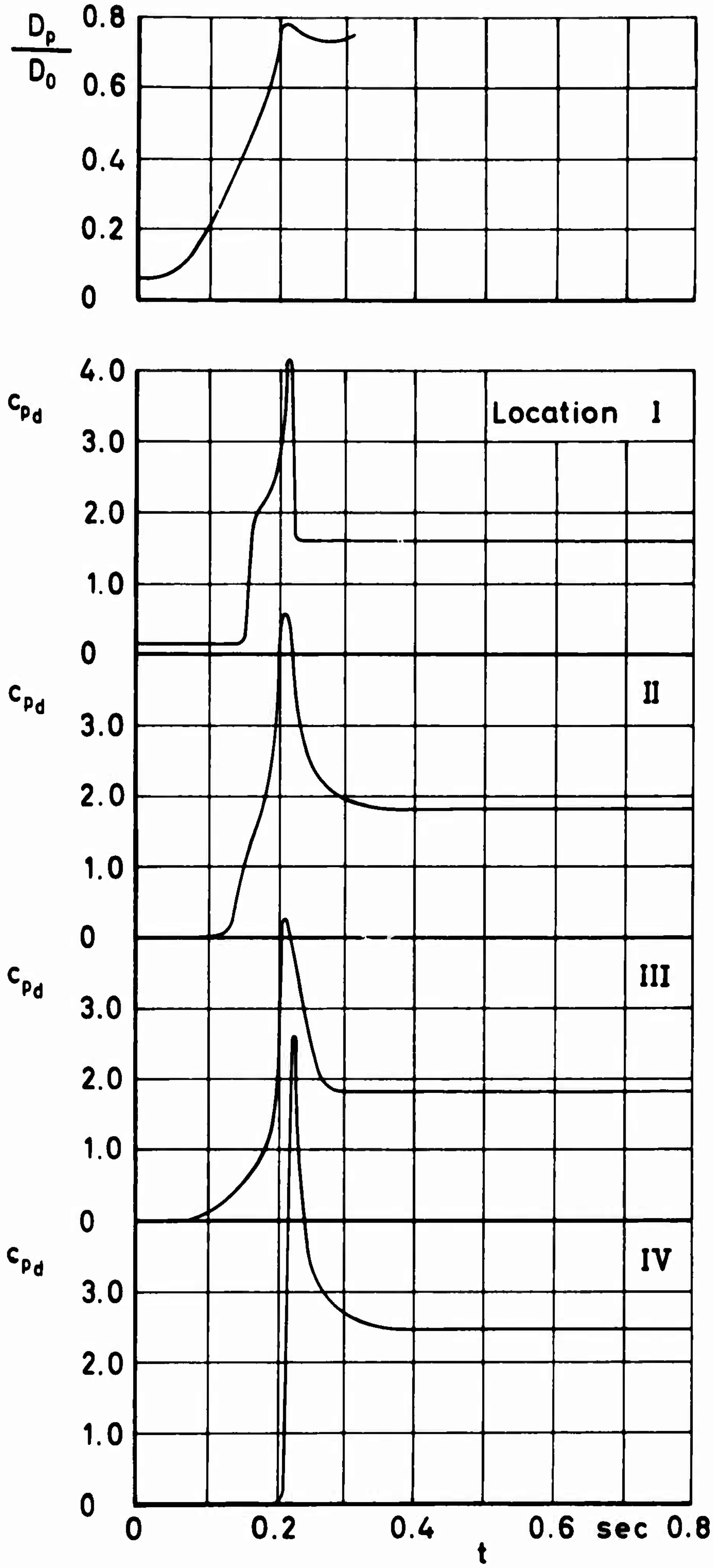

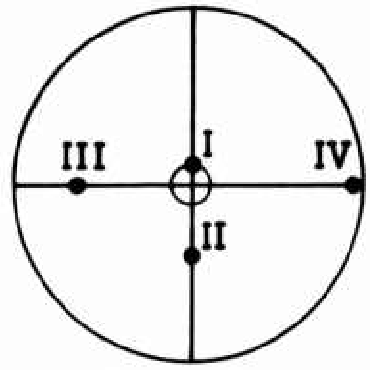

Location of pressure transducers on cord center line

Circular Flat

Figure 10 c_{p_d} and filling versus time

$v_0 = 100$ ft/sec

Run No. 183

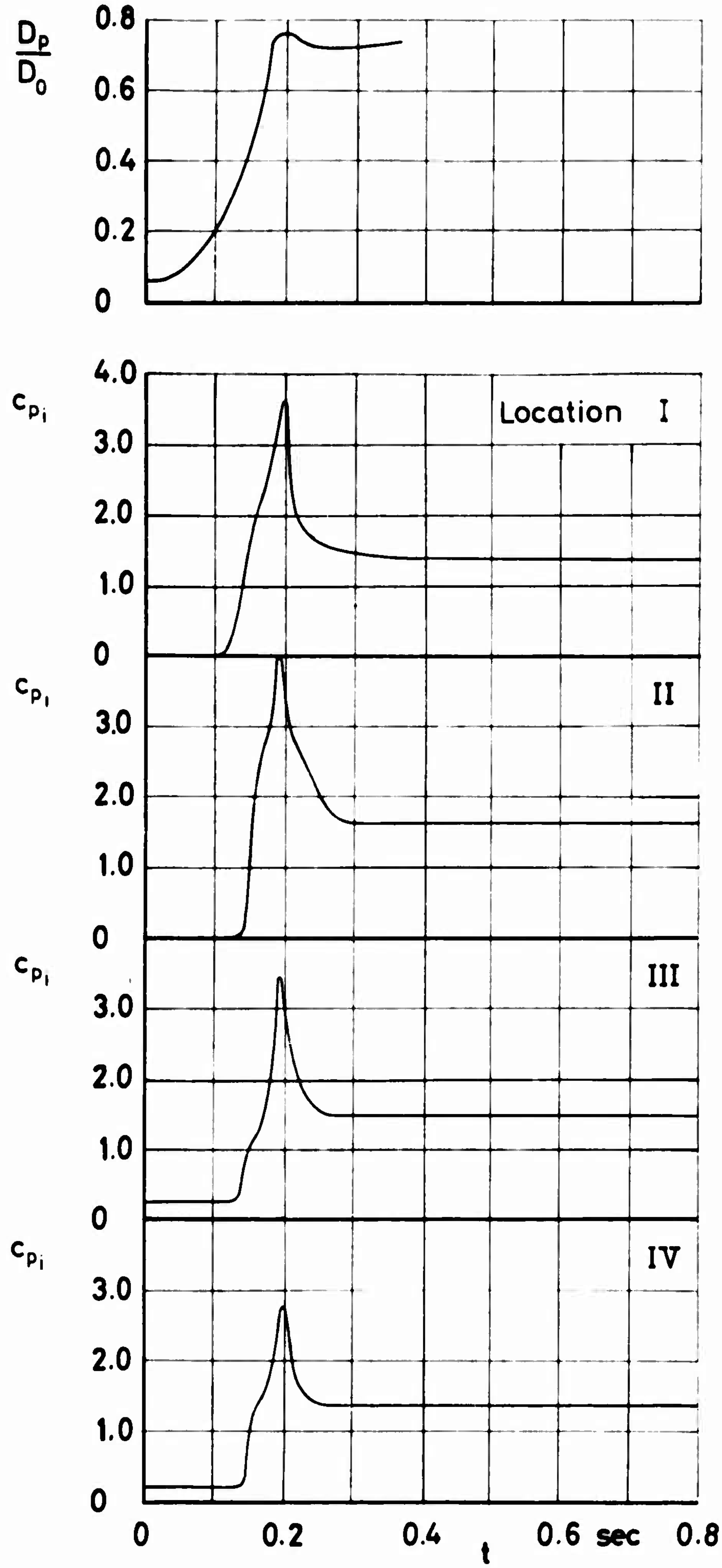

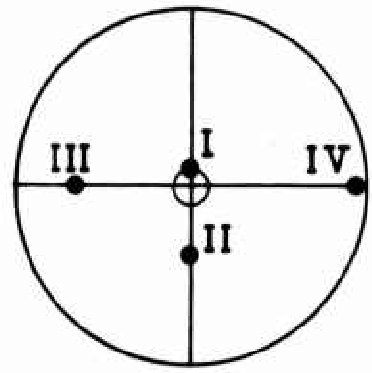

Location of pressure transducers on cord center line

Circular Flat

Figure 11 c_{p_i} and filling versus time
$v_0 = 100$ ft/sec
Run No. 200

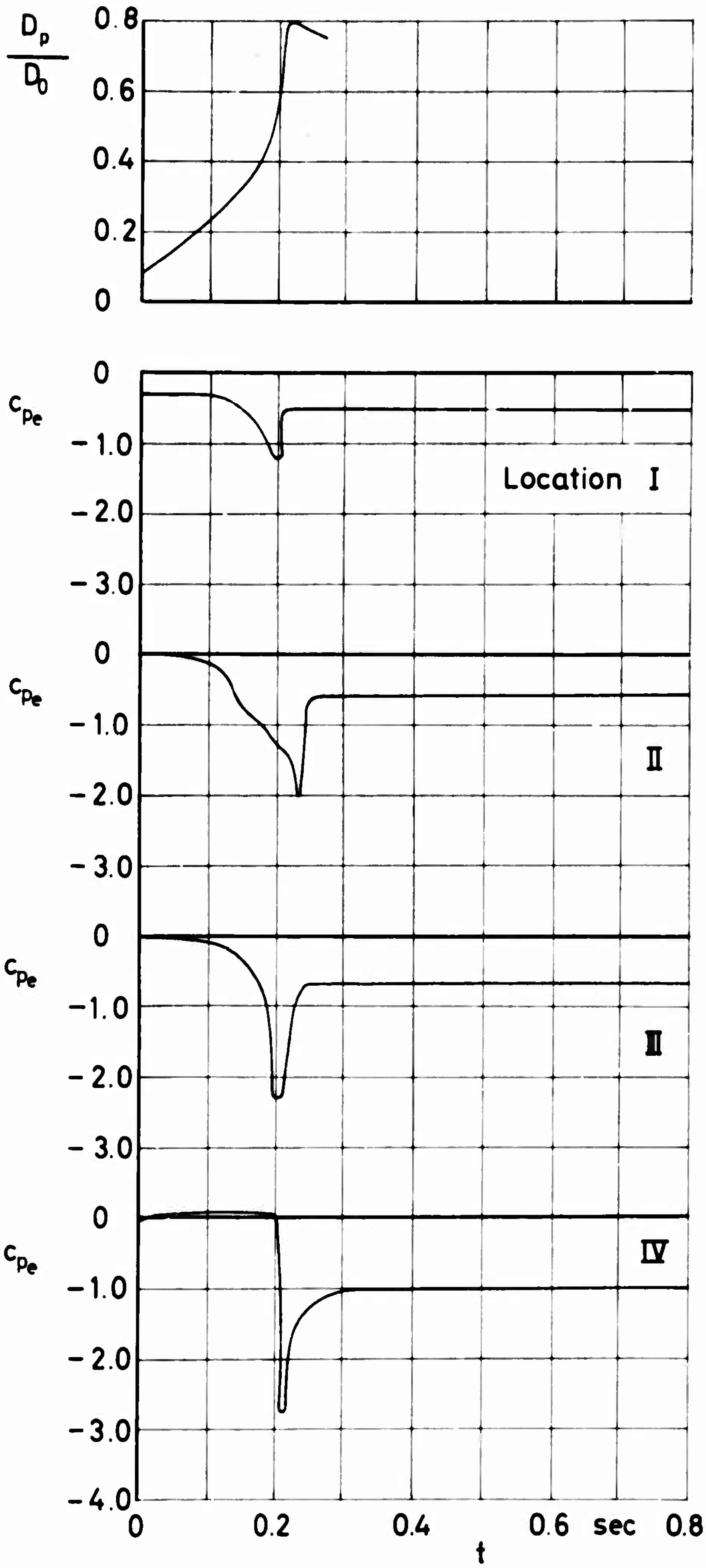

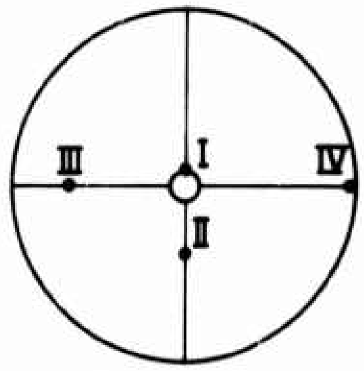

Location of pressure transducers on cord center line

Circular Flat

Figure 12 c_{p_e} and filling versus time

v_0 = 100 ft/sec
Run No. 216

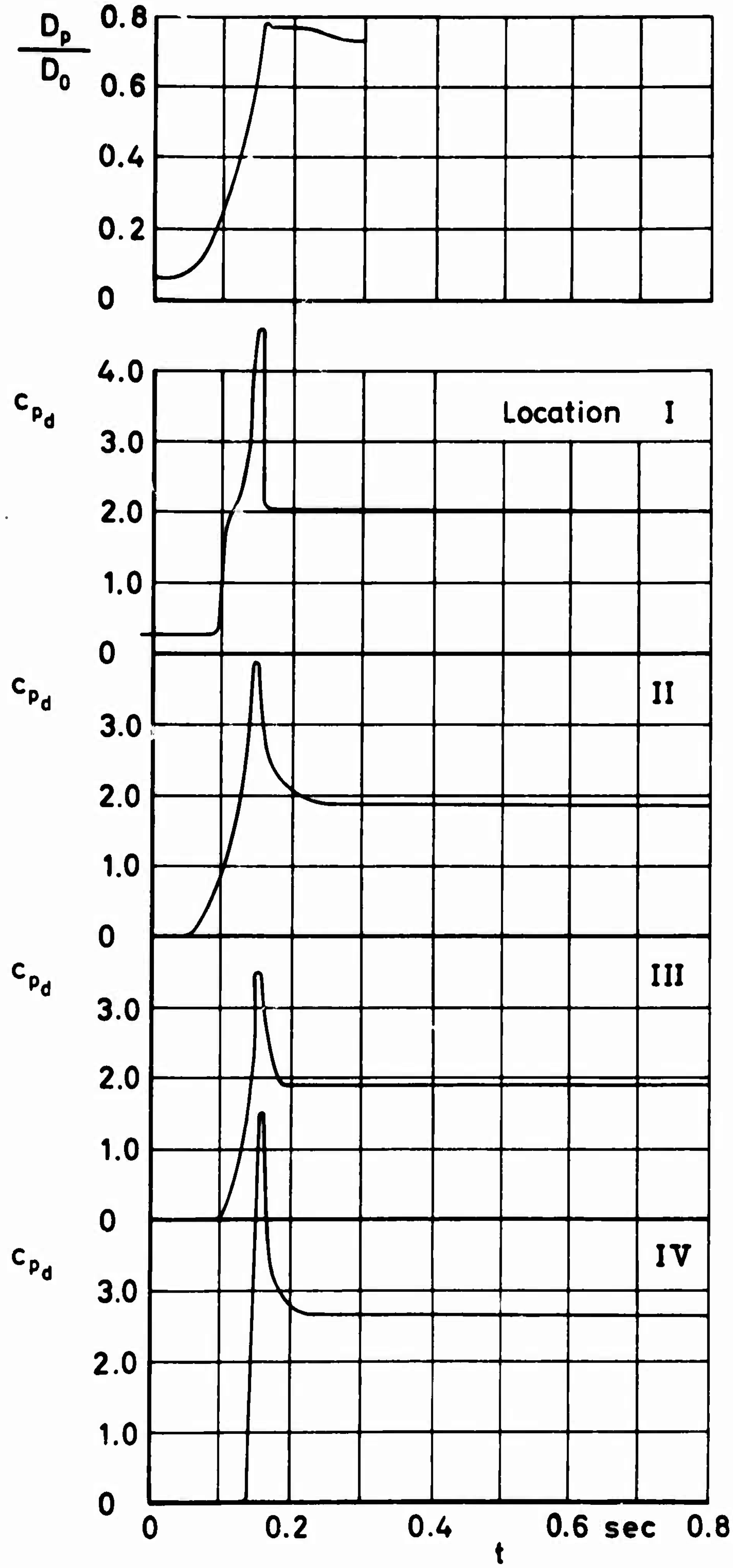

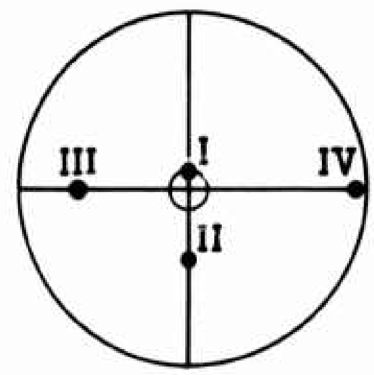

Location of pressure transducers on cord center line

Circular Flat

Figure 13 c_{p_d} and filling versus time

v_0 = 130 ft/sec

Run No. 167

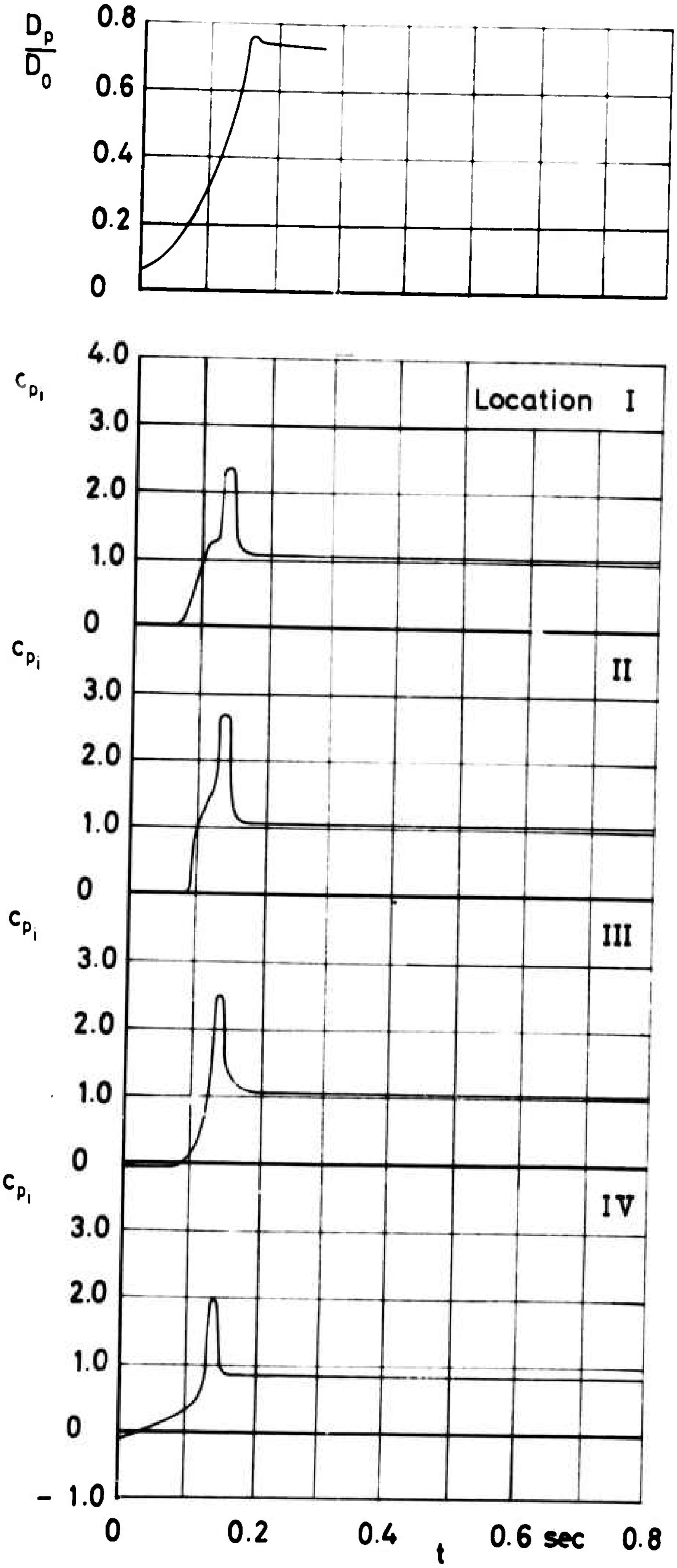

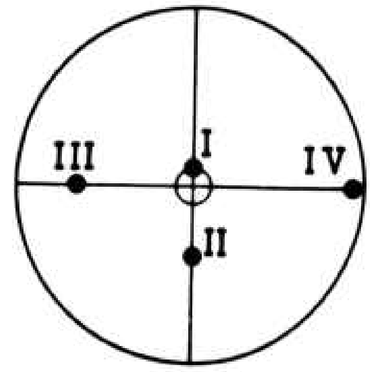

Location of pressure tranducers on cord center line

Circular Flat

Figure 14 c_{p_i} and filling versus time

v_0=130 ft/sec

Run No. 203

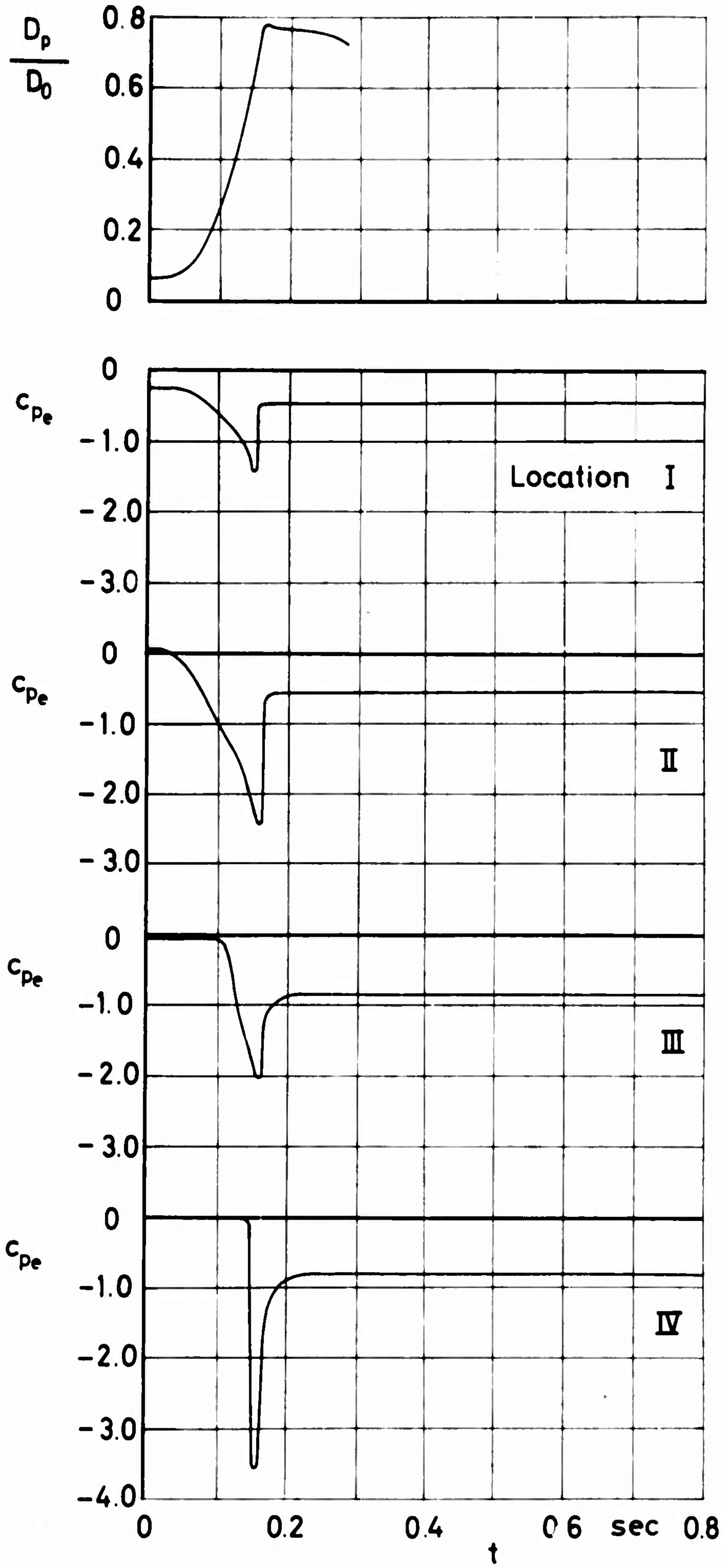

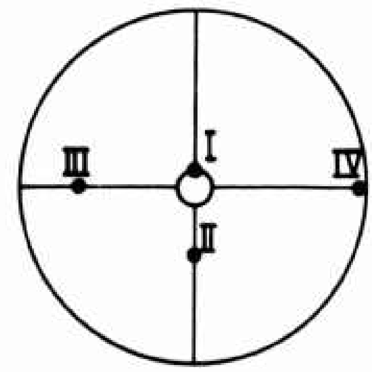

Location of pressure transducers on cord center line

Circular Flat

Figure 15 c_{p_e} and filling versus time

v_0 = 130 ft/sec
Run No. 218

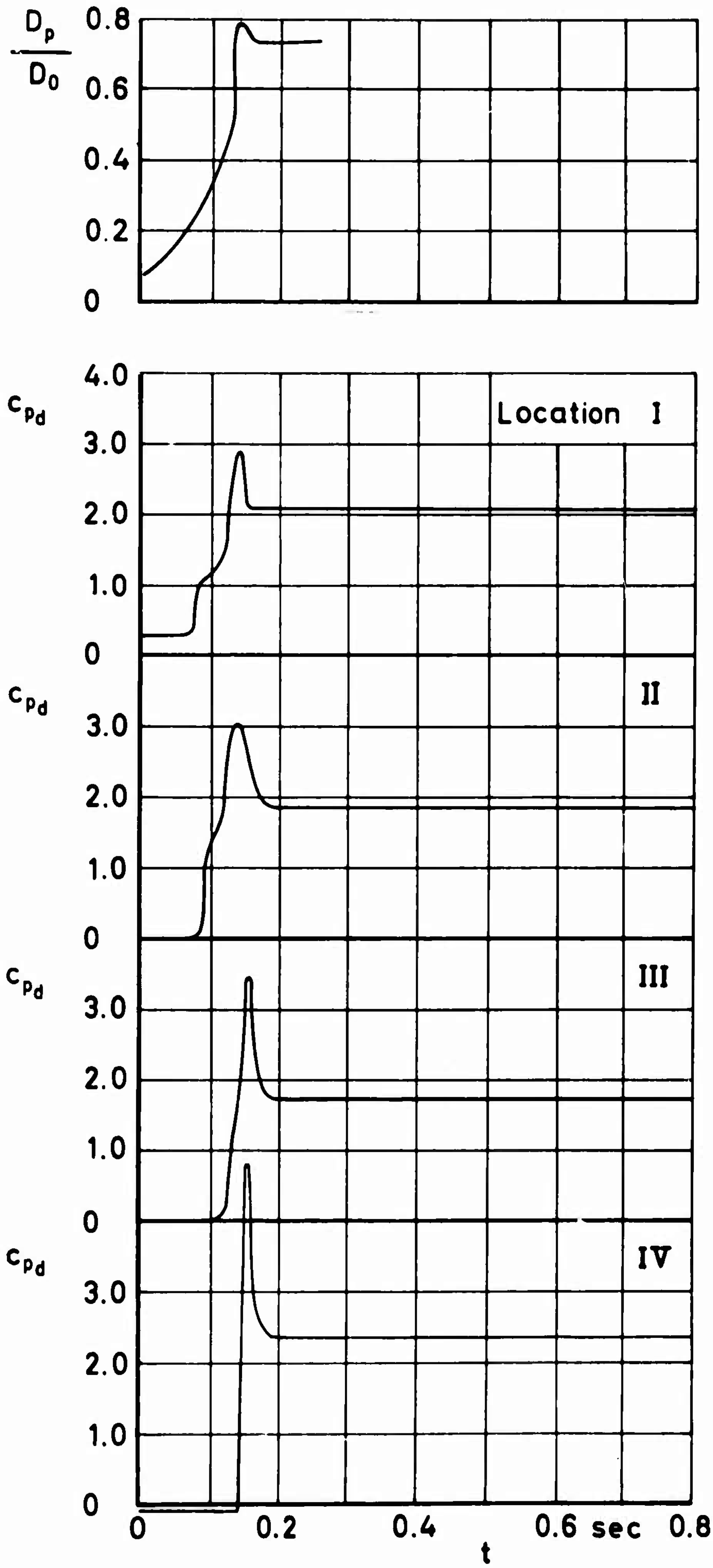

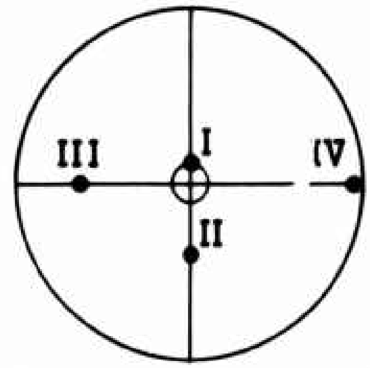

Location of pressure transducers on cord center line

Circular Flat

Figure 16 c_{p_d} and filling versus time

v_0 =160 ft/sec

Run No. 191

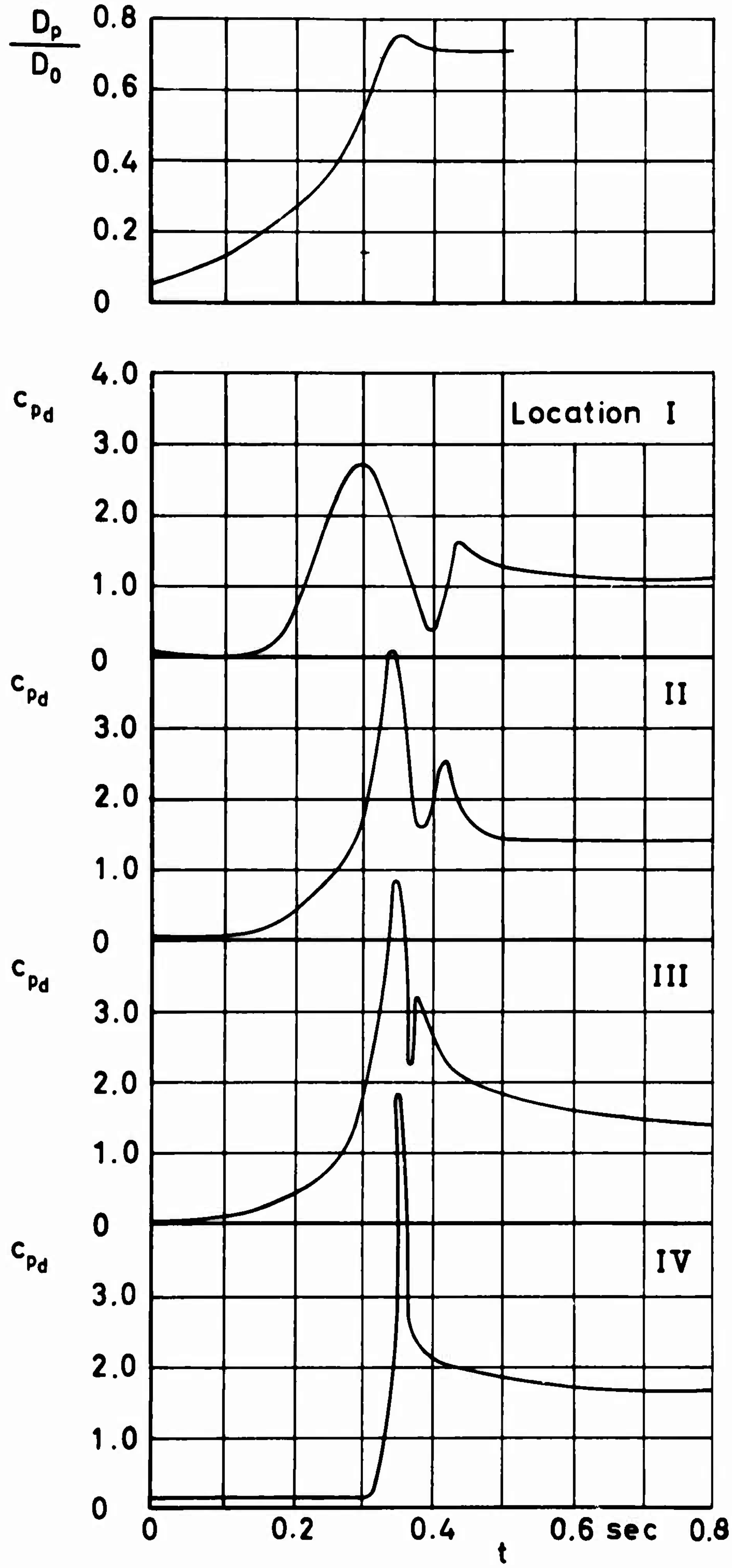

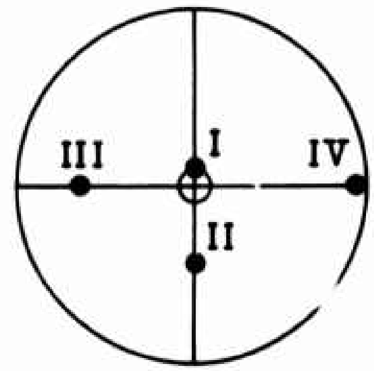

Location of pressure transducers on cord center line

Extended Skirt

Figure 17 c_{p_d} and filling versus time

$v_0 = 70\,ft/sec$

Run No. 139

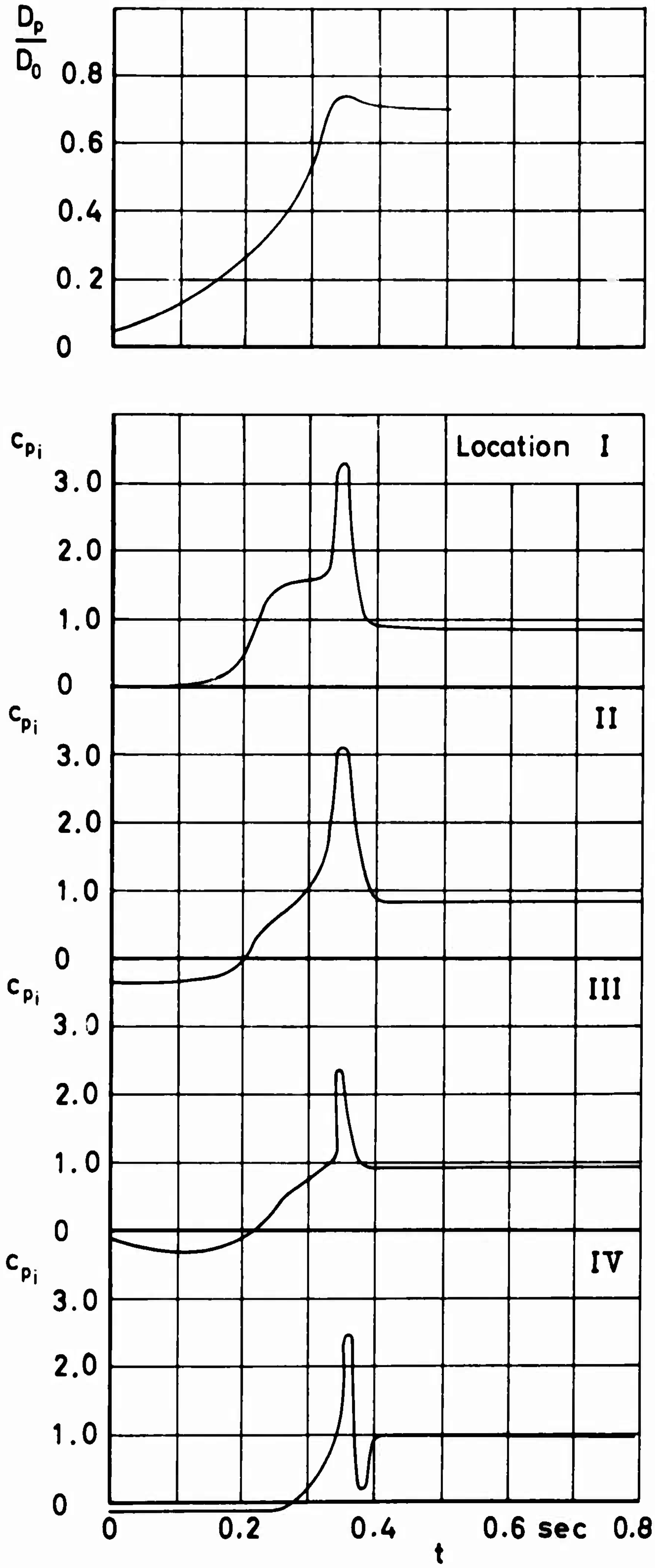

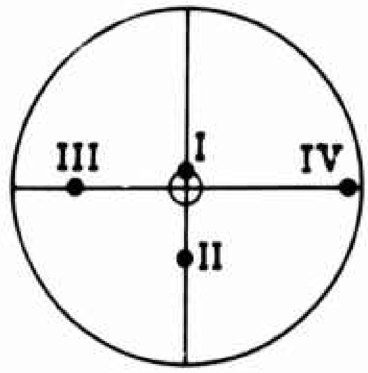

Location of pressure transducers on cord center line

Extended Skirt

Figure 18 c_{p_i} and filling versus time

$v_0 = 70$ ft/sec

Run No.157

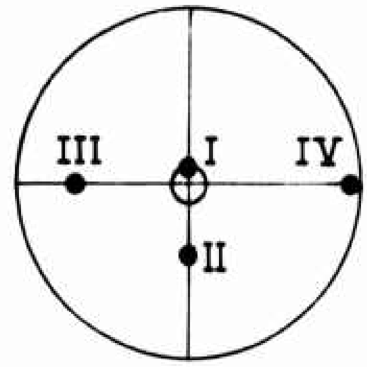

Location of pressure transducers on cord center line

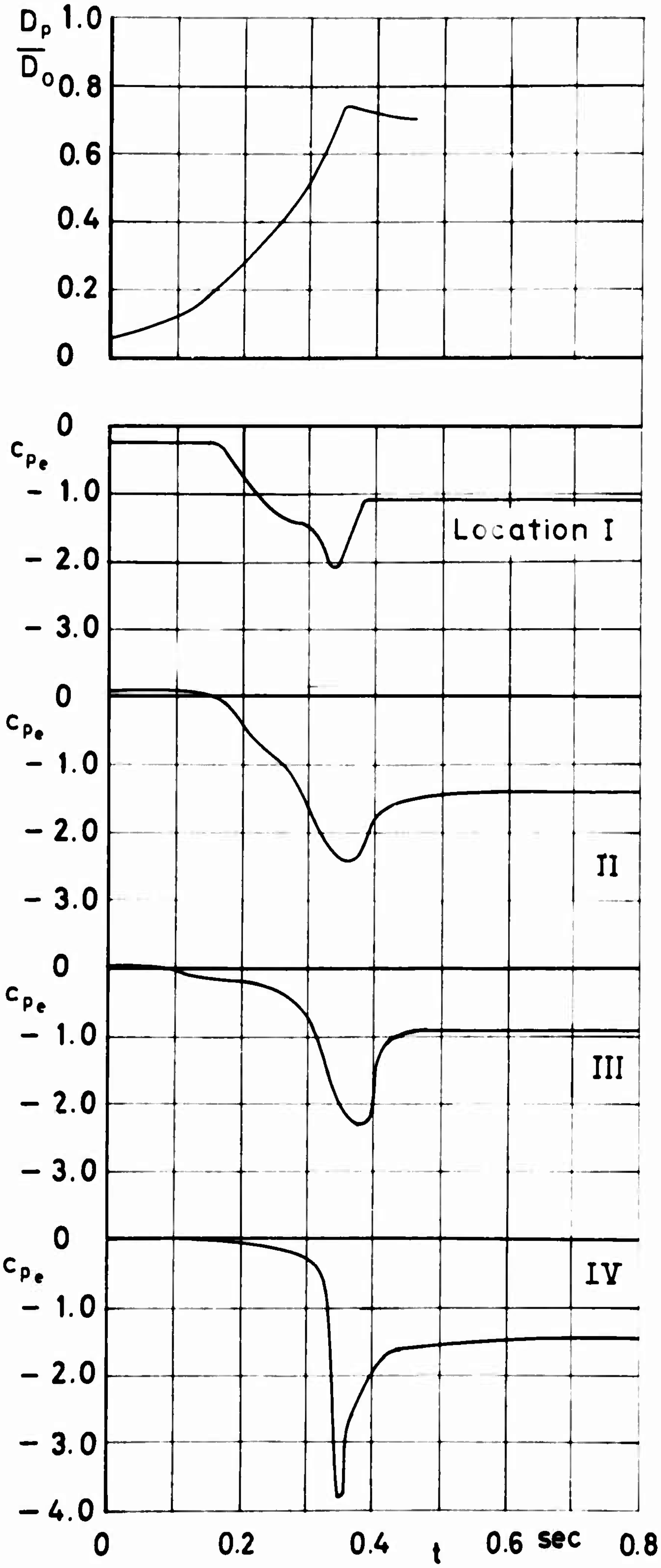

Extended Skirt

Figure 19 c_{p_e} and filling versus time
$v_0 = 70$ ft/sec
Run No 221

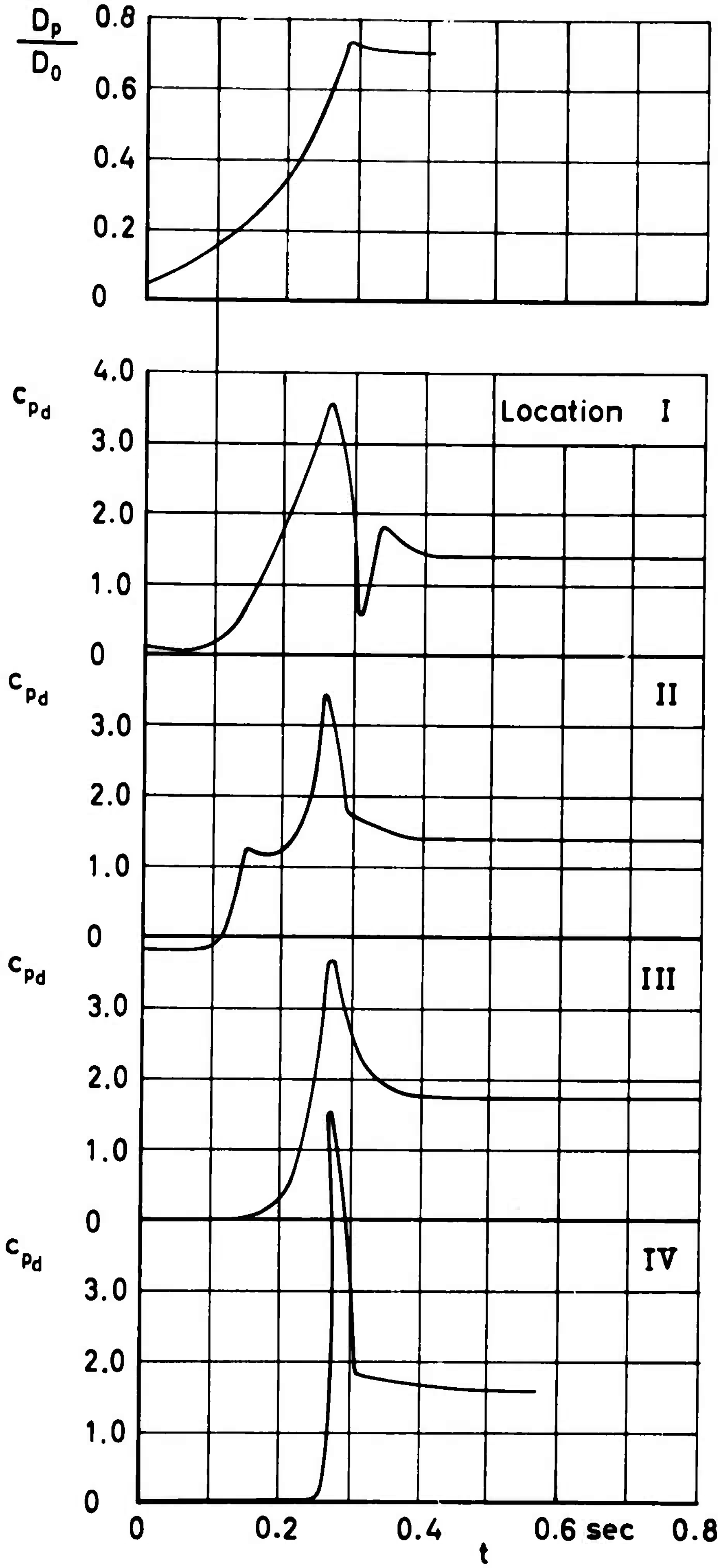

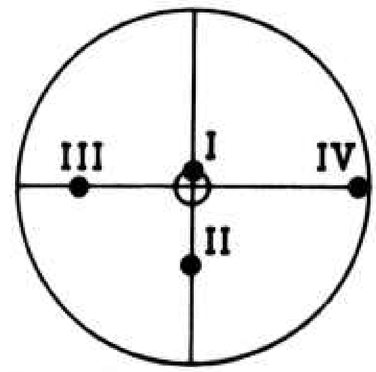

Location of pressure transducers on cord center line

Extended Skirt

Figure 20 c_{p_d} and filling versus time

$v_0 = 100$ ft/sec

Run No. 144

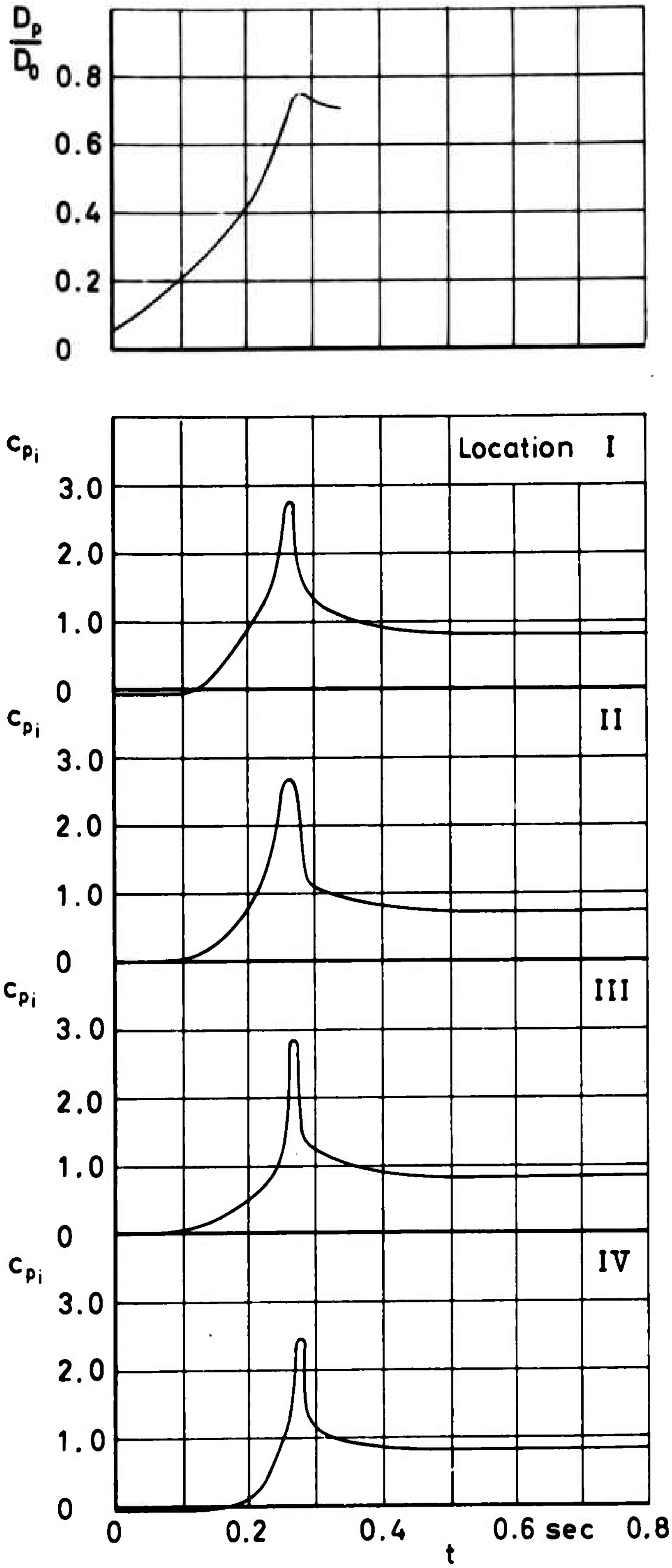

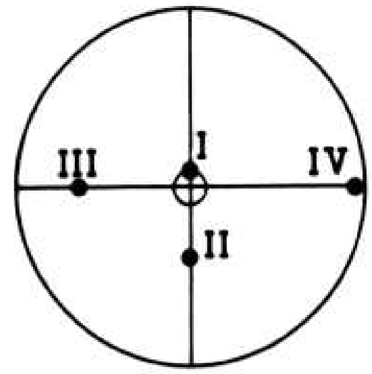

Location of pressure transducers on cord center line

Extended Skirt

Figure 21 c_{p_i} and filling versus time $v_0 = 100$ ft/sec Run No.160

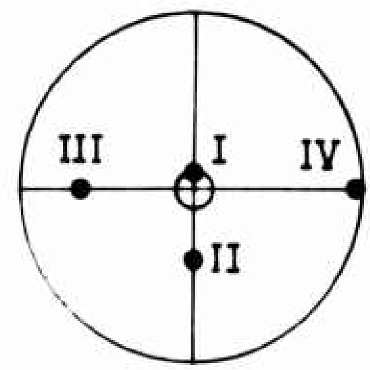

Location of pressure transducers on cord center line

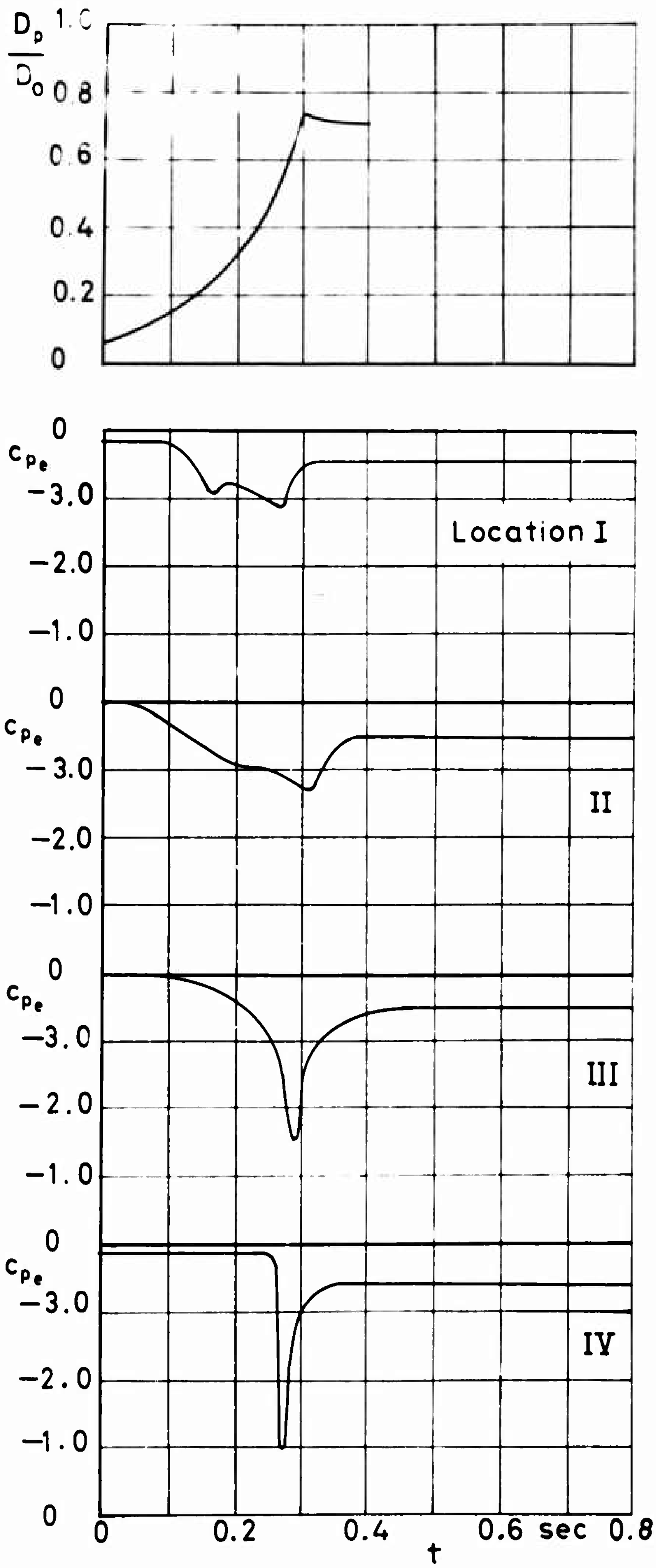

Extended Skirt

Figure 22 c_{p_e} and filling versus time $v_0 = 100$ ft/sec Run No 226

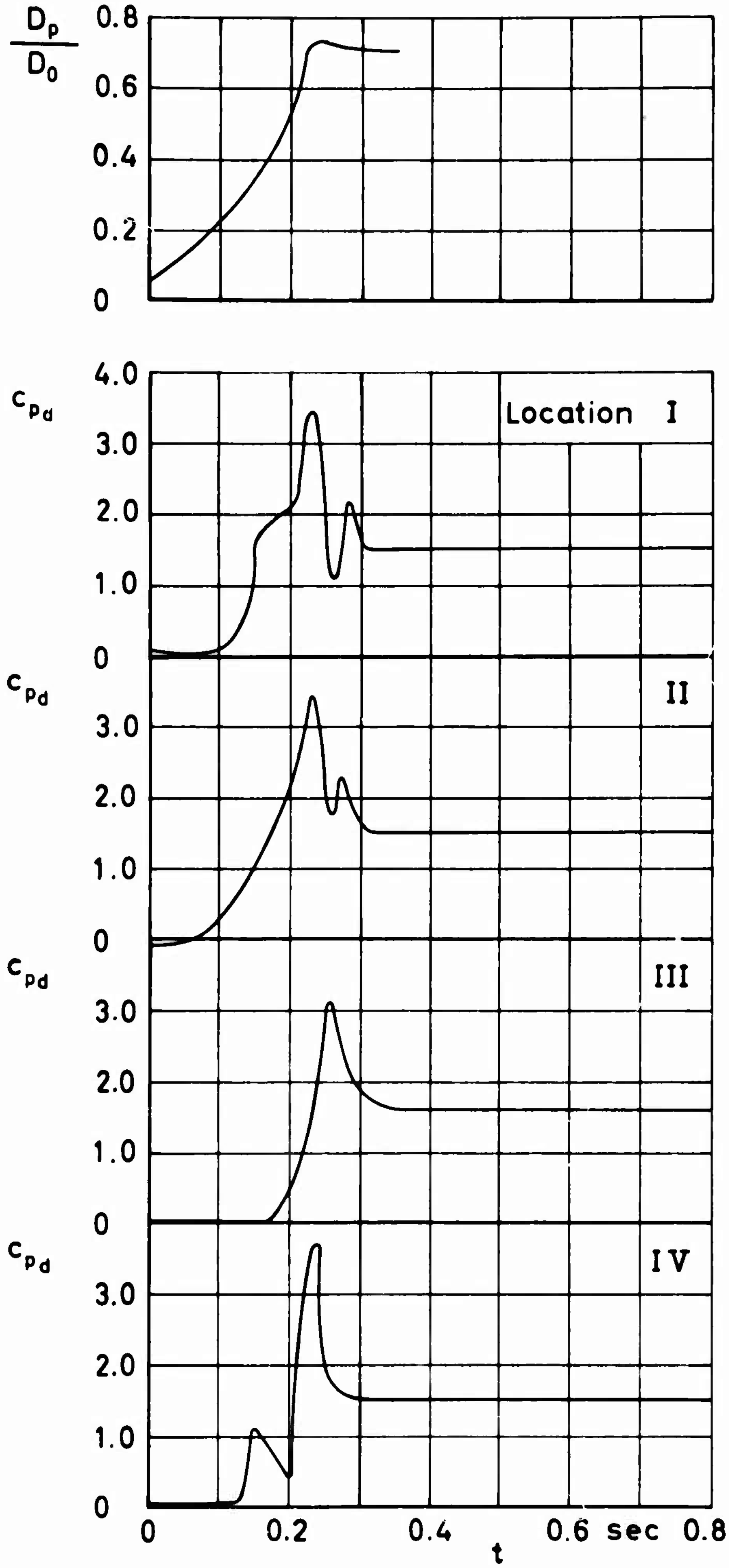

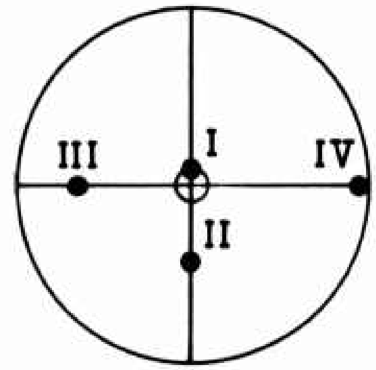

Location of pressure transducers on cord center line

Extended Skirt

Figure 23 c_{p_d} and filling versus time

v_0 = 130 ft/sec

Run No. 148

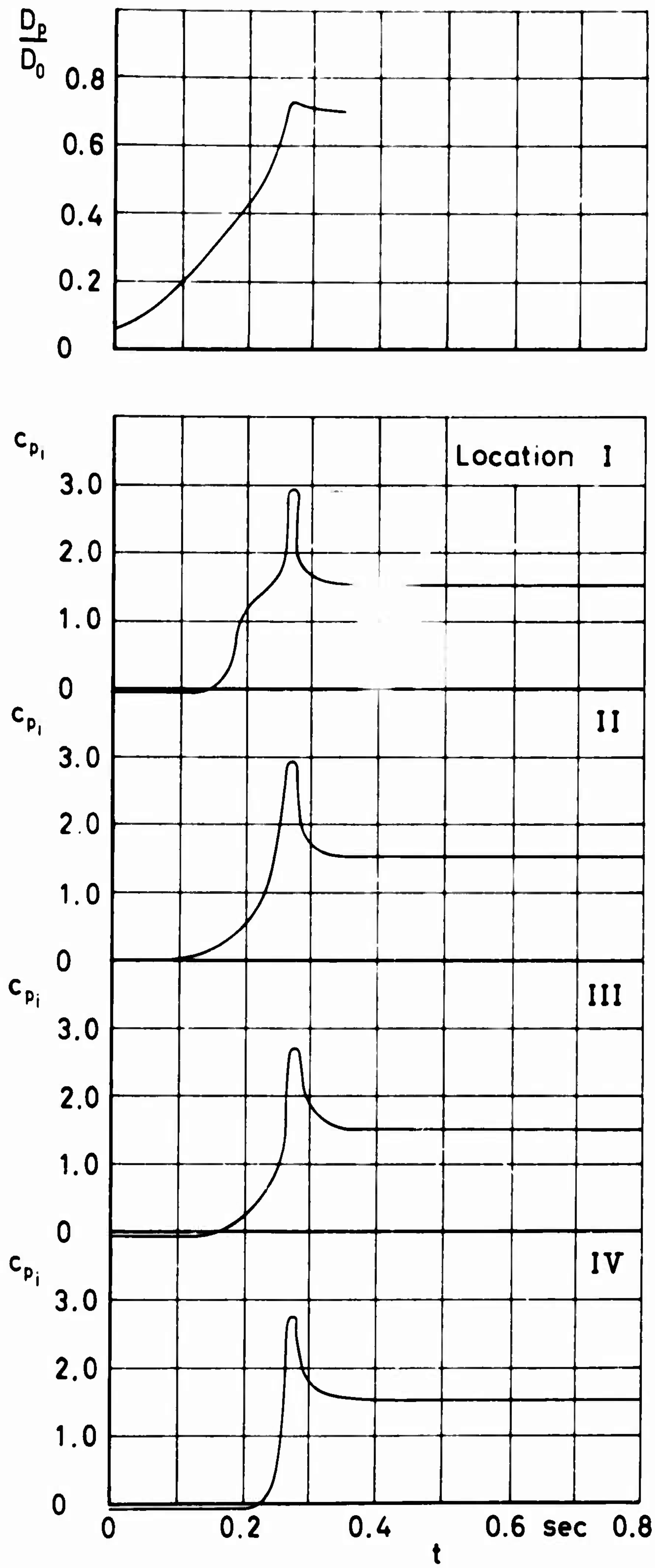

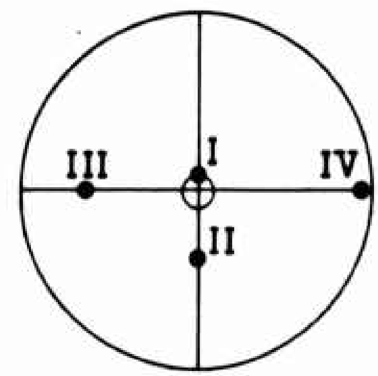

Location of pressure transducers on cord center line

Extended Skirt

Figure 24 c_{p_i} and filling versus time v_0=130 ft/sec Run No. 163

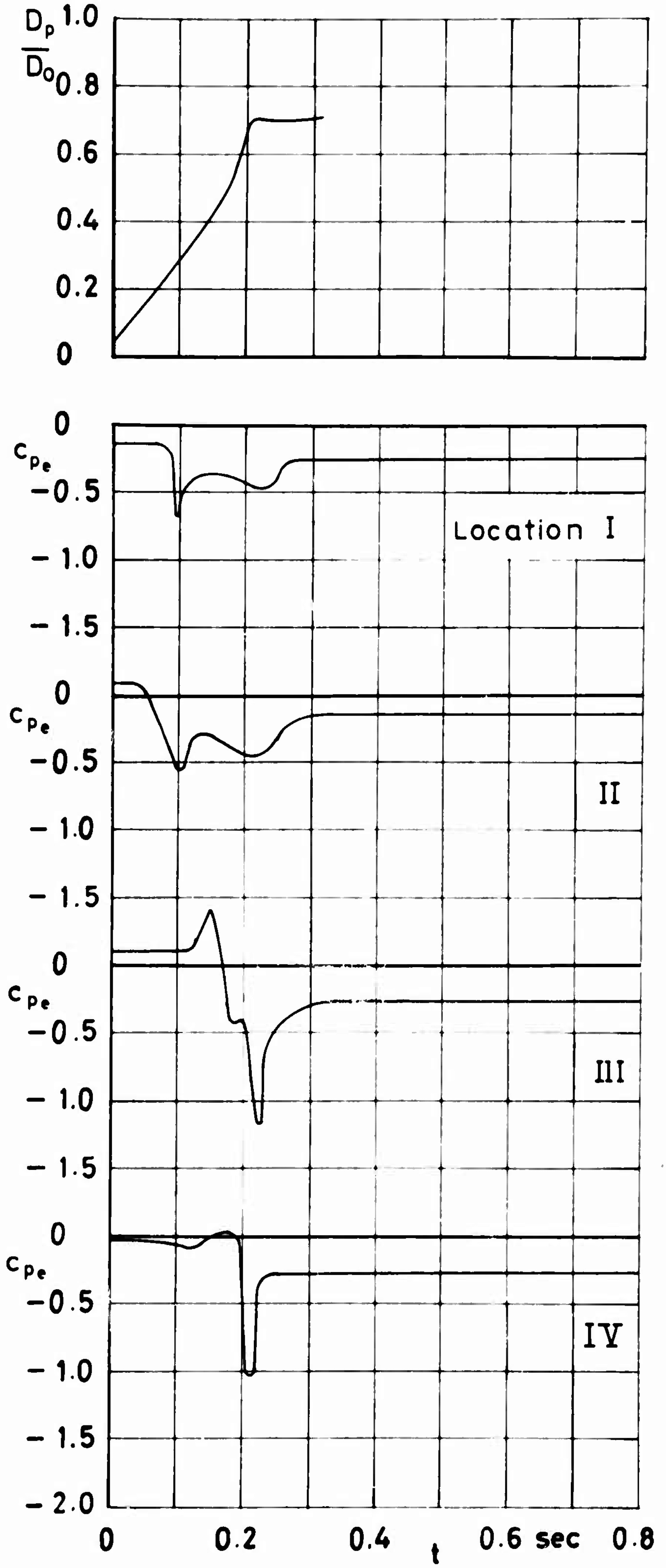

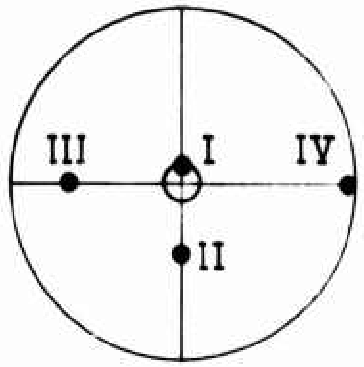

Location of pressure transducers on cord center line

Extended Skirt

Figure 25 c_{p_e} and filling versus time $v_0 = 130$ ft/sec Run No 231

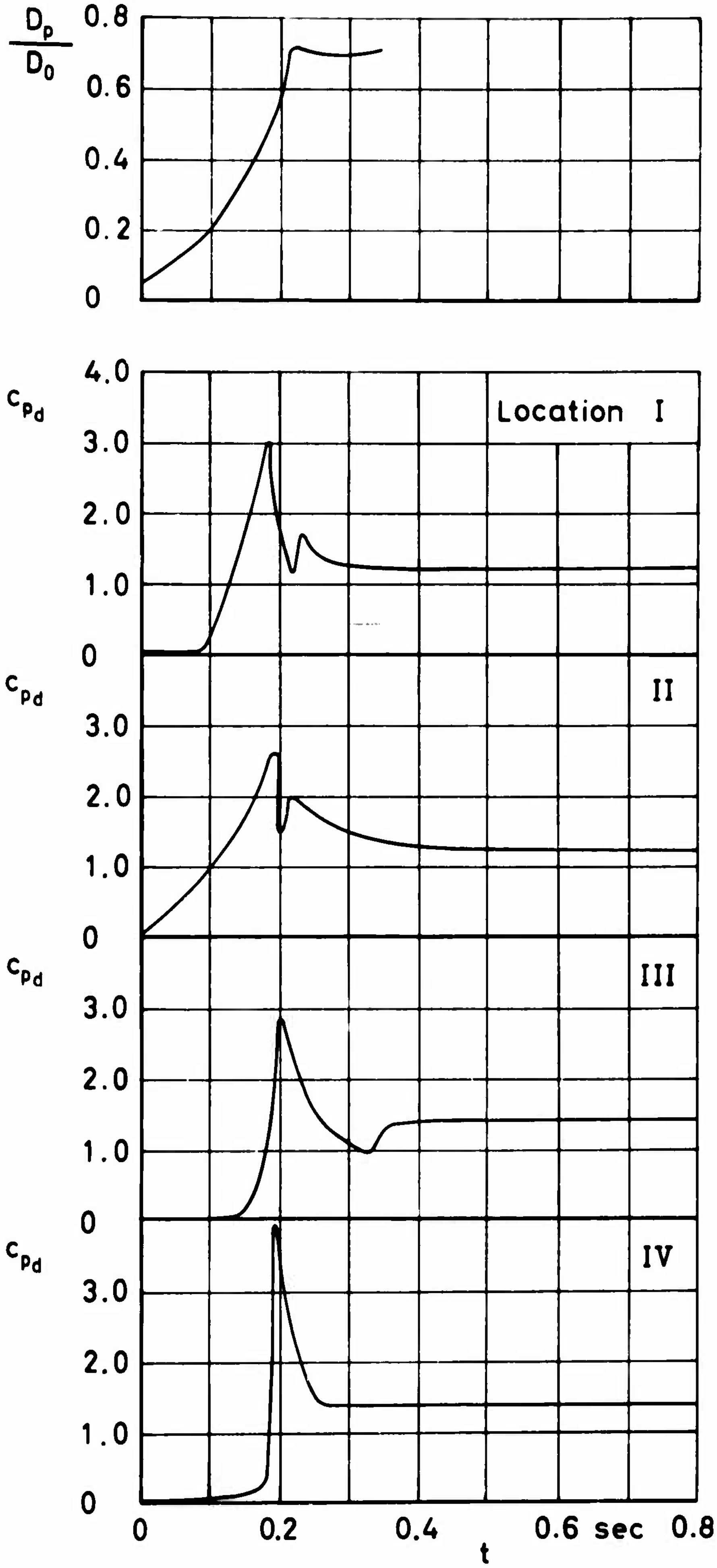

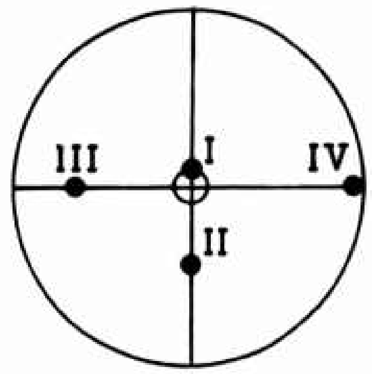

Location of pressure transducers on cord center line

Extended Skirt

Figure 26 c_{p_d} and filling versus time

$v_0 = 160$ ft/sec

Run No. 153

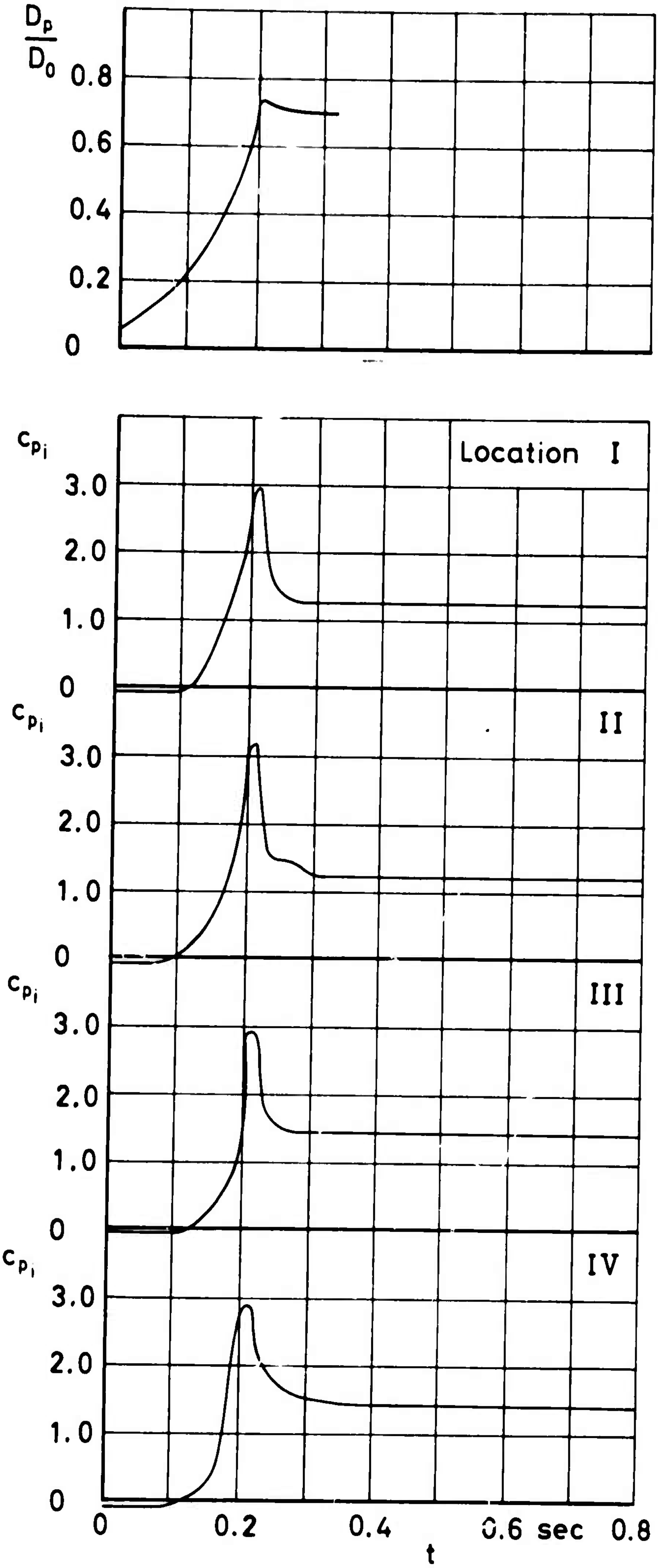

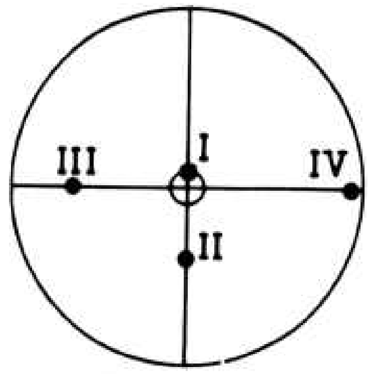

Location of pressure transducers on cord center line

Extended Skirt

Figure 27 c_{p_i} and filling versus time

$v_0 = 160$ ft/sec

R No. 166

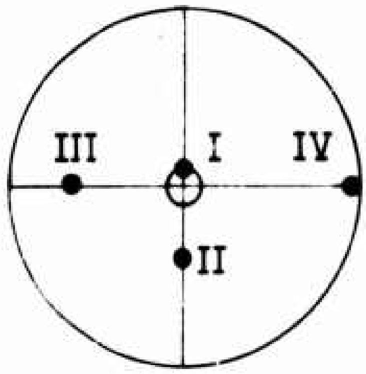

Location of pressure transducers on cord center line

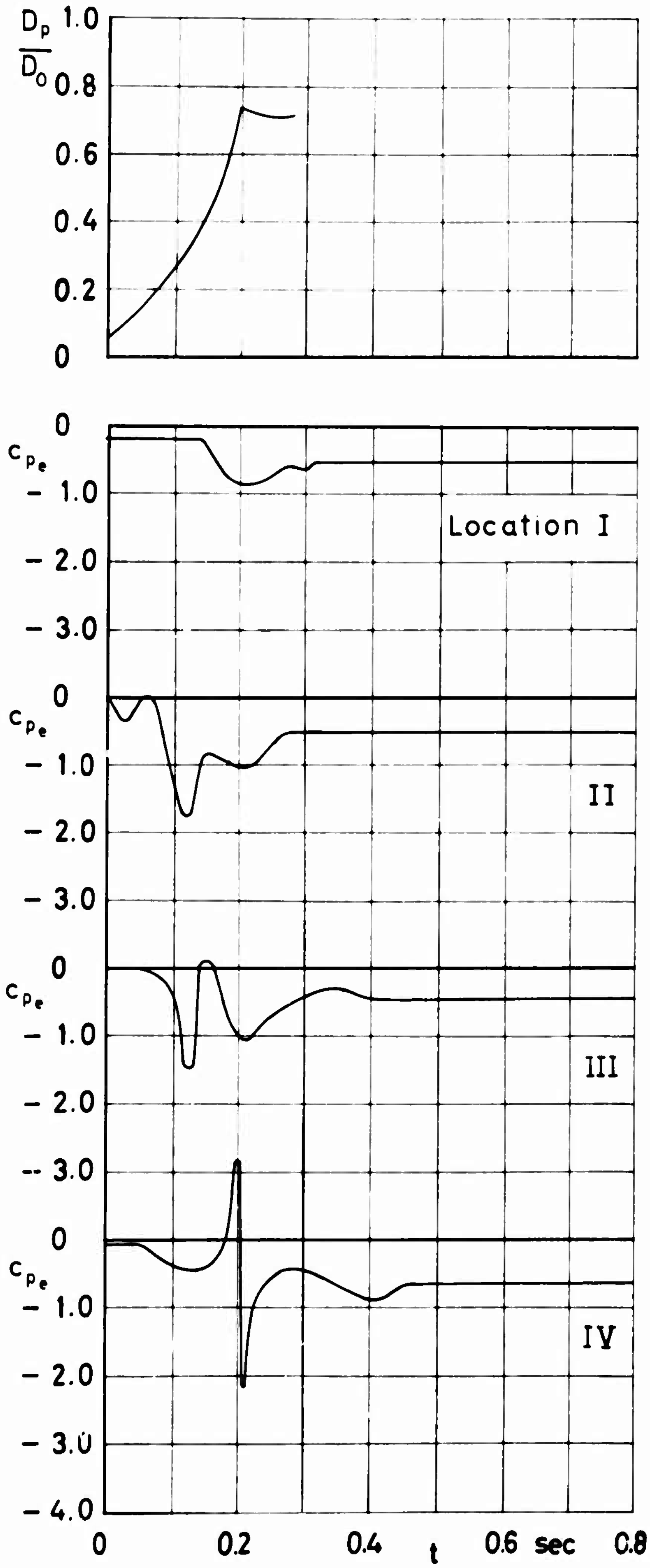

Extended Skirt

Figure 28 c_{p_e} and filling versus time $v_0 = 160$ ft/sec Run No 235

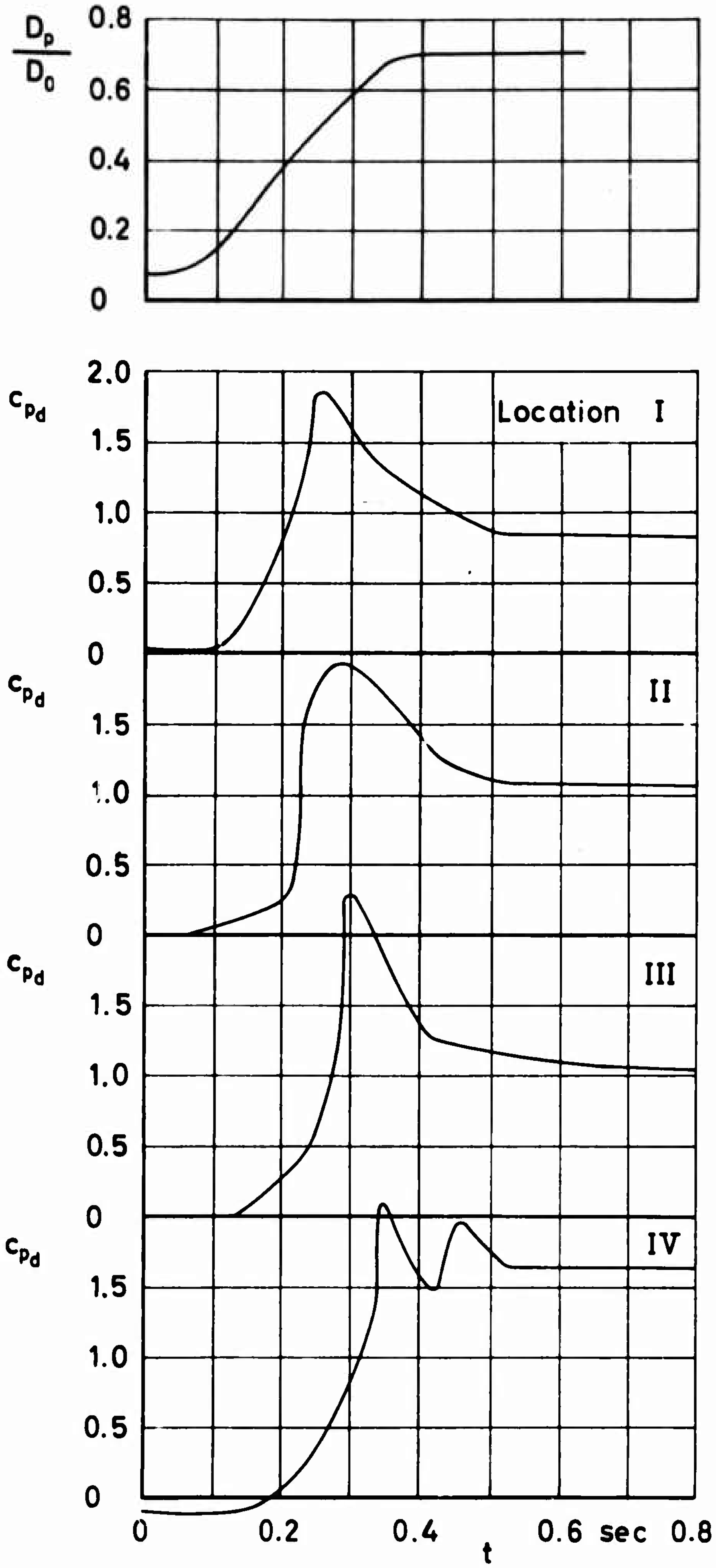

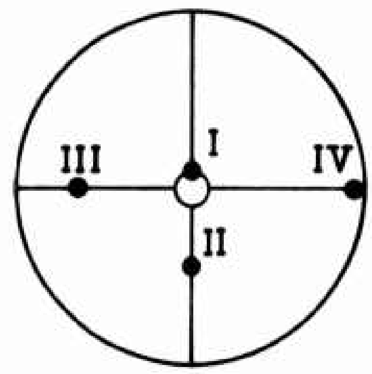

Location of pressure transducers on cord center line

FIST

Figure 29 c_{p_d} and filling versus time

v_0 = 70 ft/sec

Run No. 72

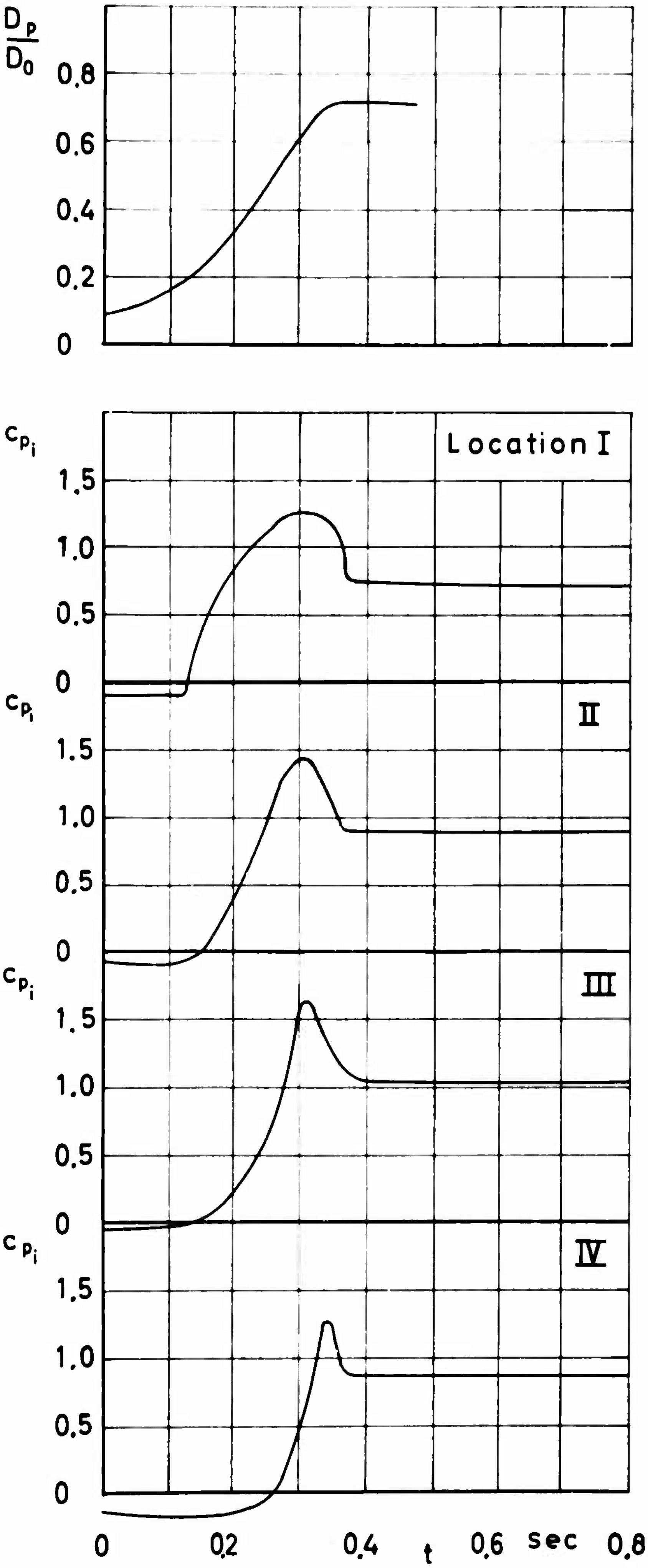

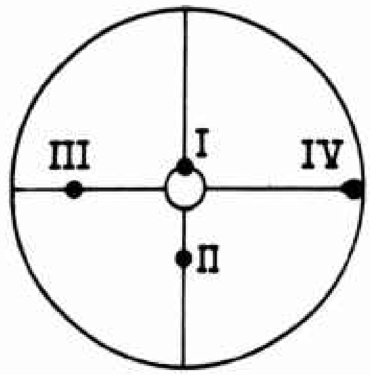

Location of pressure transducers on cord center line

FIST

Figure 30 c_{p_i} and filling versus time $v_0 = 70$ ft/sec Run No 101

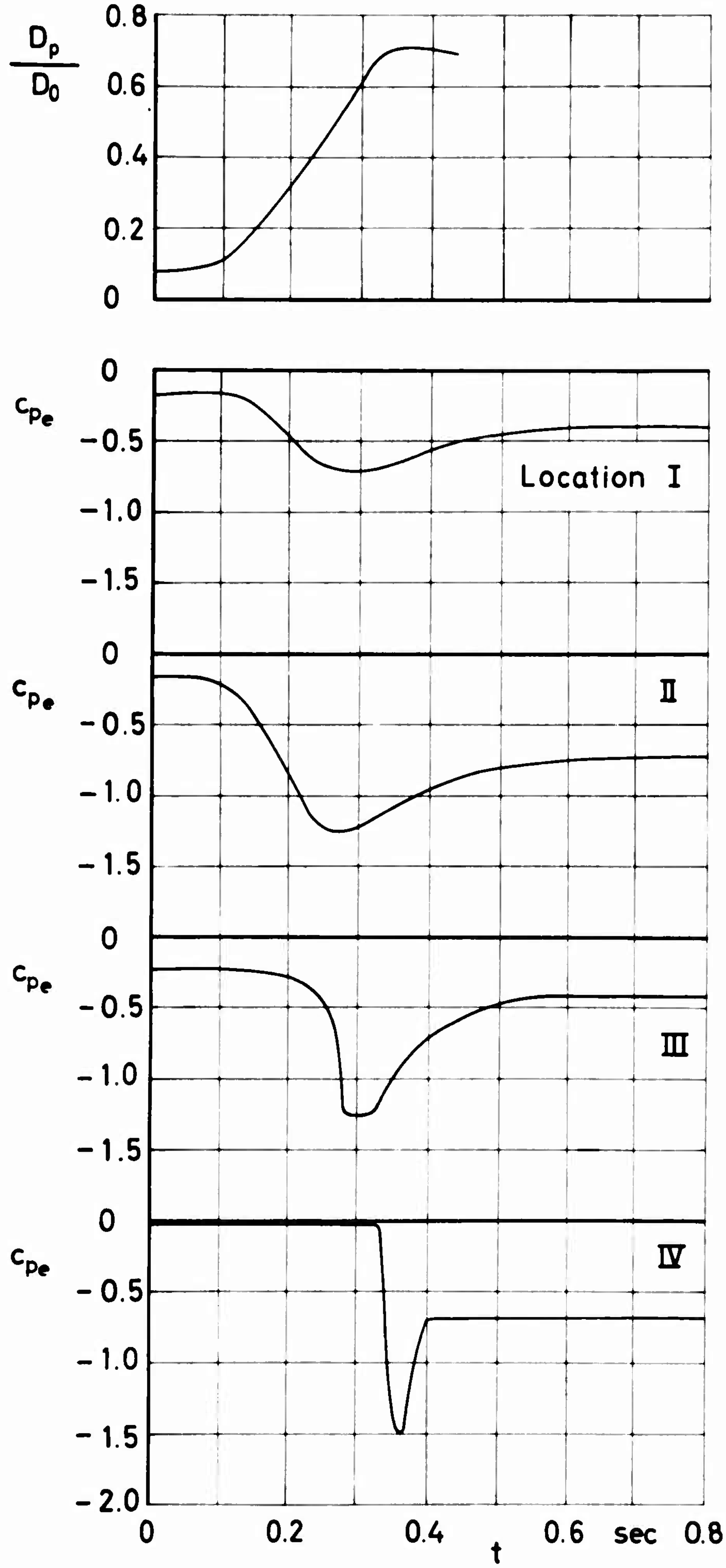

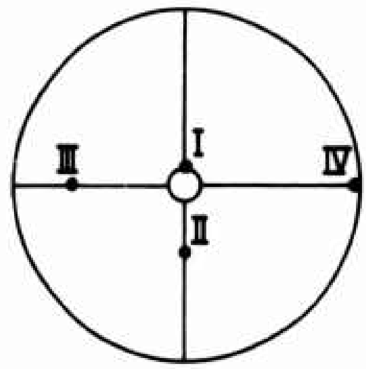

Location of pressure transducers on cord center line

FIST

Figure 31 c_{p_e} and filling versus time

v_0 = 70 ft / sec

Run No. 104

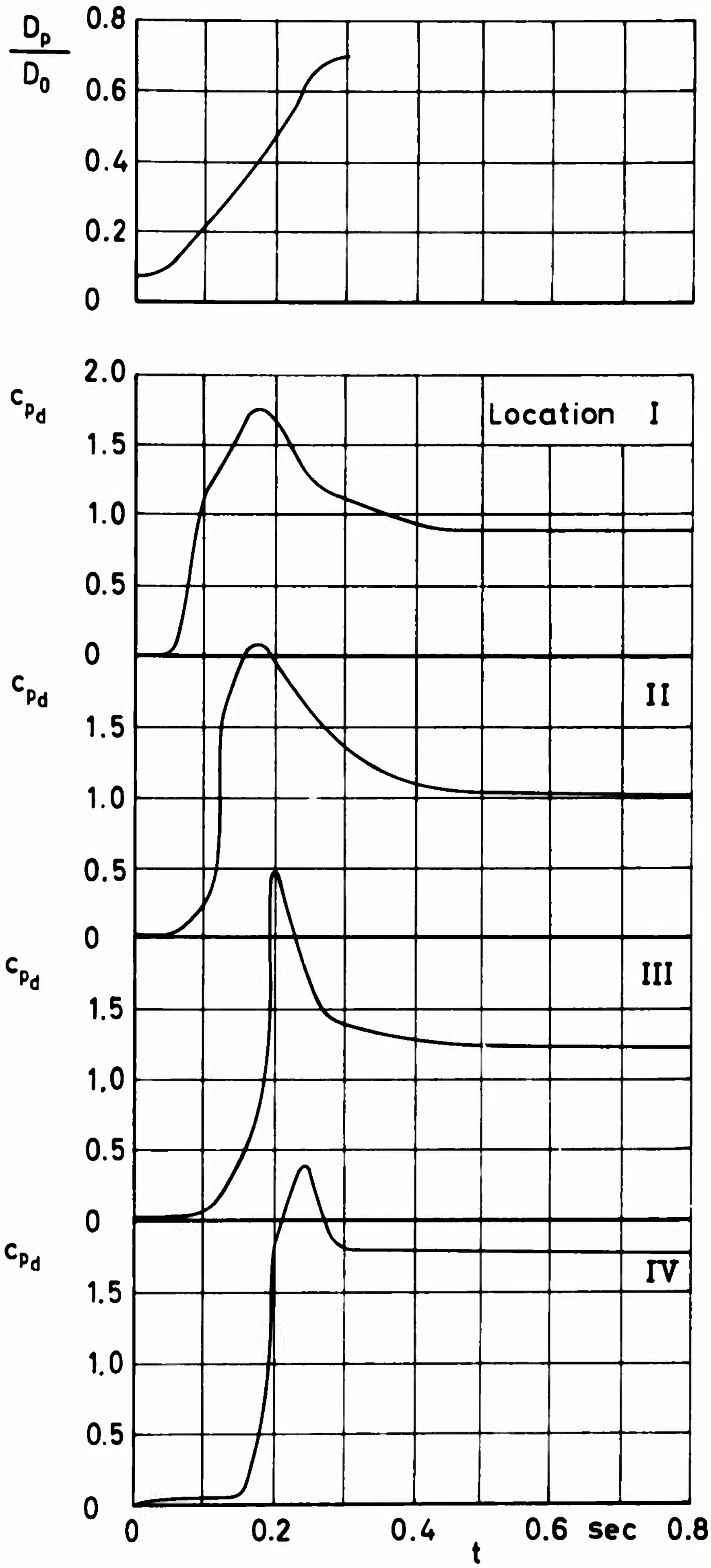

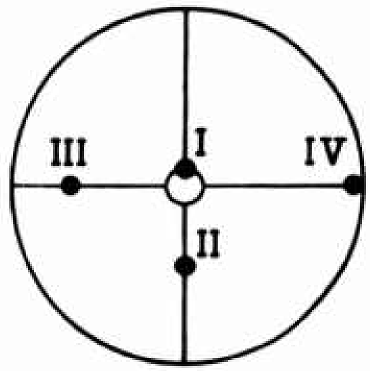

Location of pressure transducers on cord center line

FIST

Figure 32 c_{p_d} and filling versus time

$v_0 = 100$ ft/sec

Run No. 76

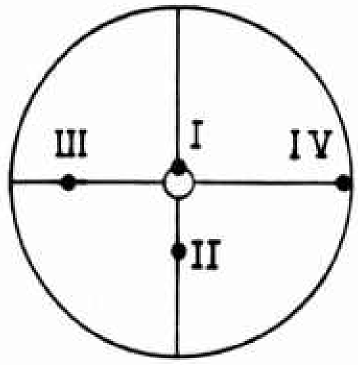

Location of pressure transducers on cord center line

FIST

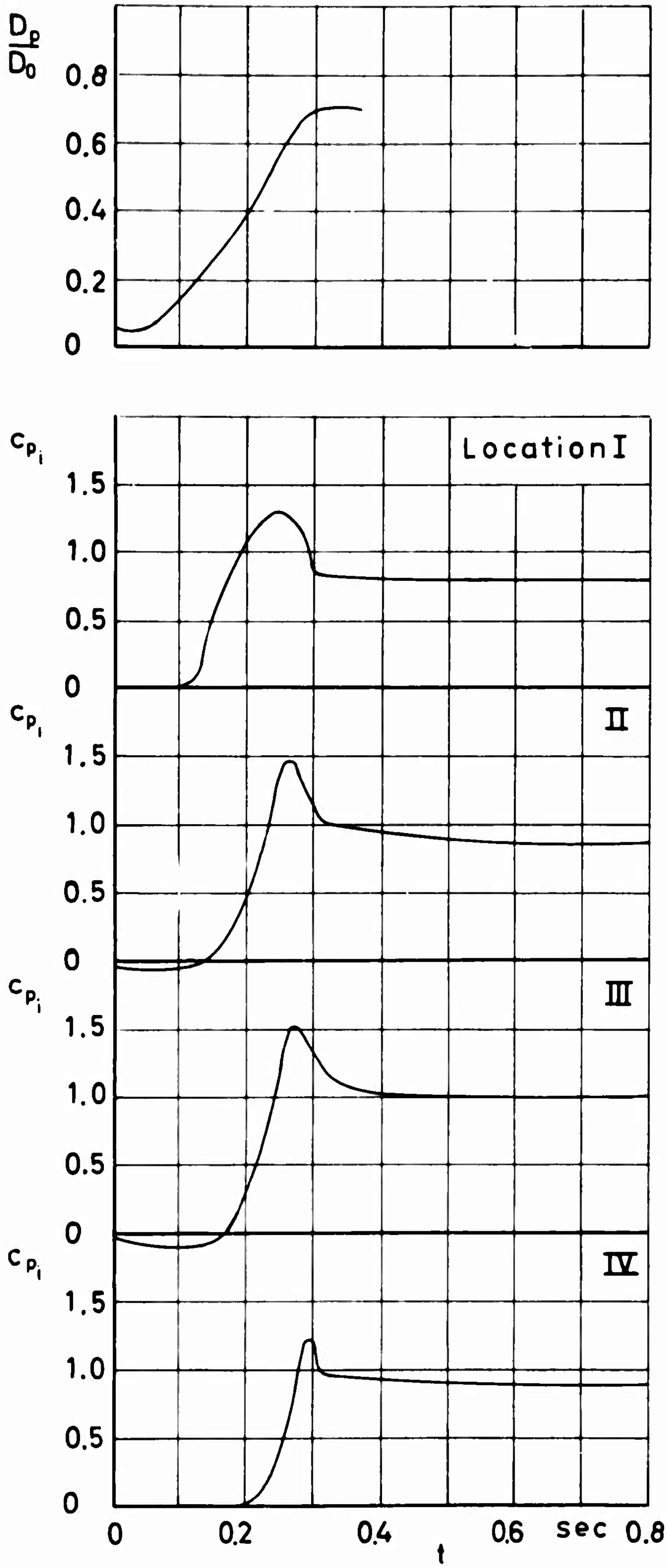

Figure 33 c_{p_i} and filling versus time $v_0 = 100$ ft/sec Run No 97

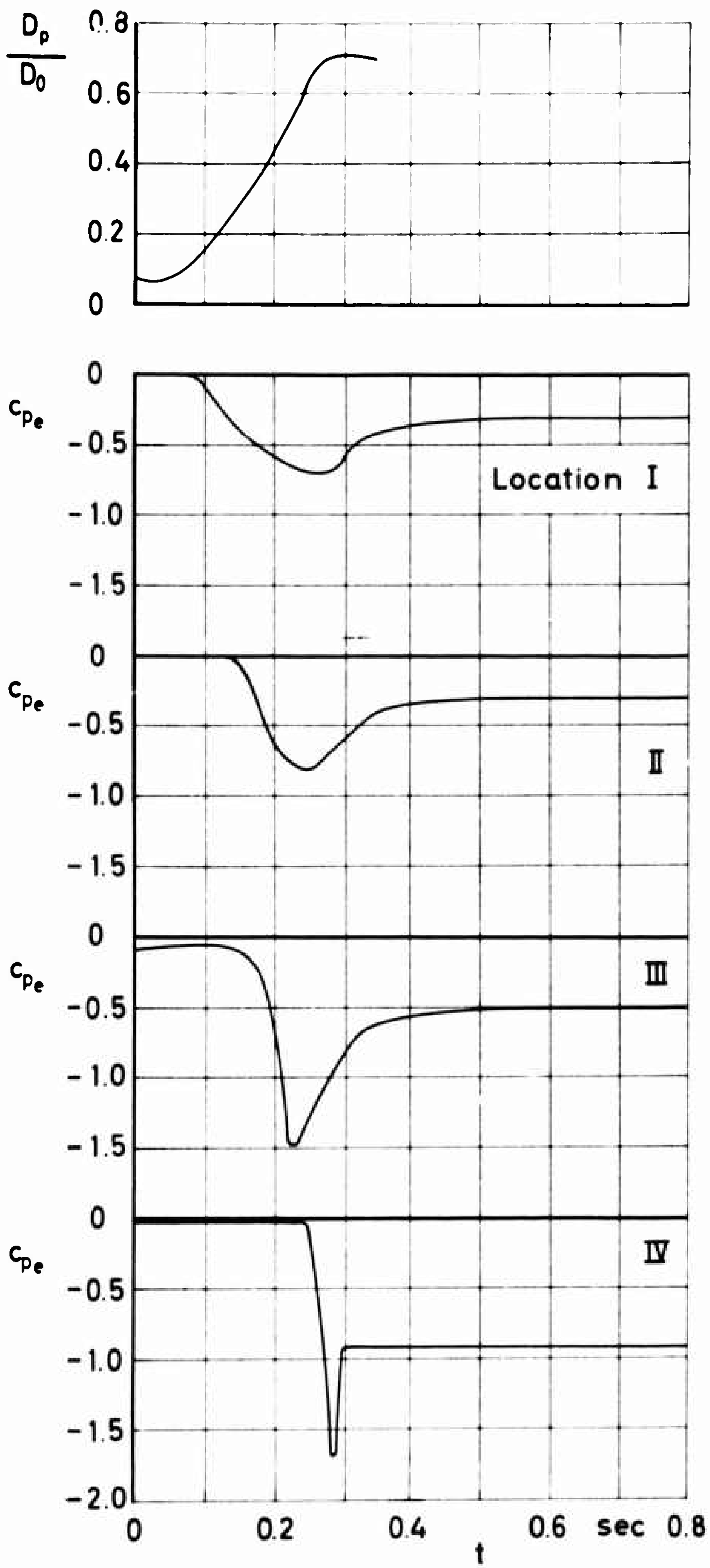

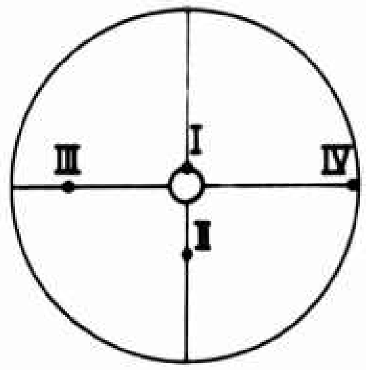

Location of pressure transducers on cord center line

FIST

Figure 34 c_{p_e} and filling versus time

v_0 = 100 ft / sec

Run No. 110

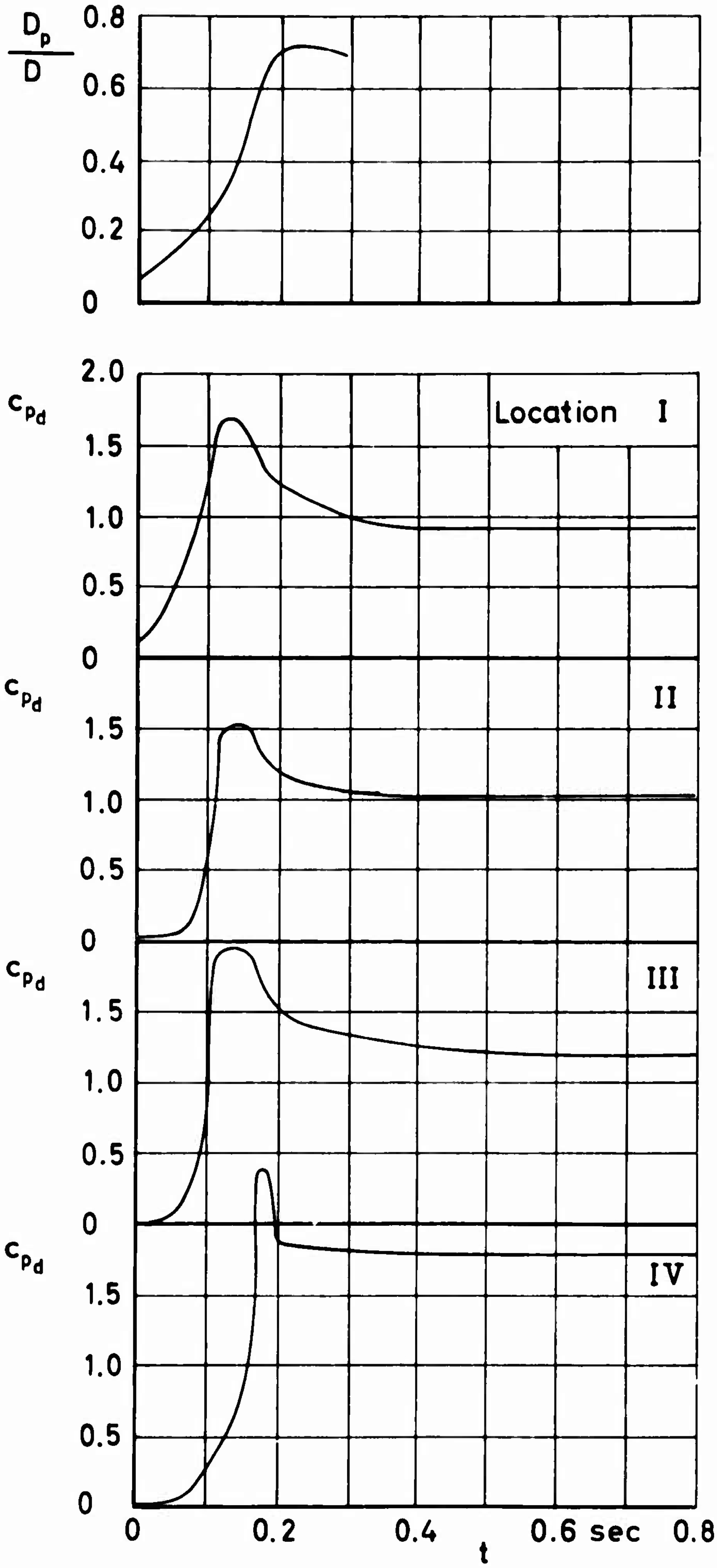

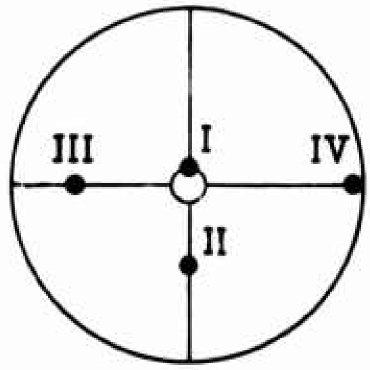

Location of pressure transducers on cord center line

FIST

Figure 35 c_{p_d} and filling versus time

v_0=130 ft/sec

Run No. 82

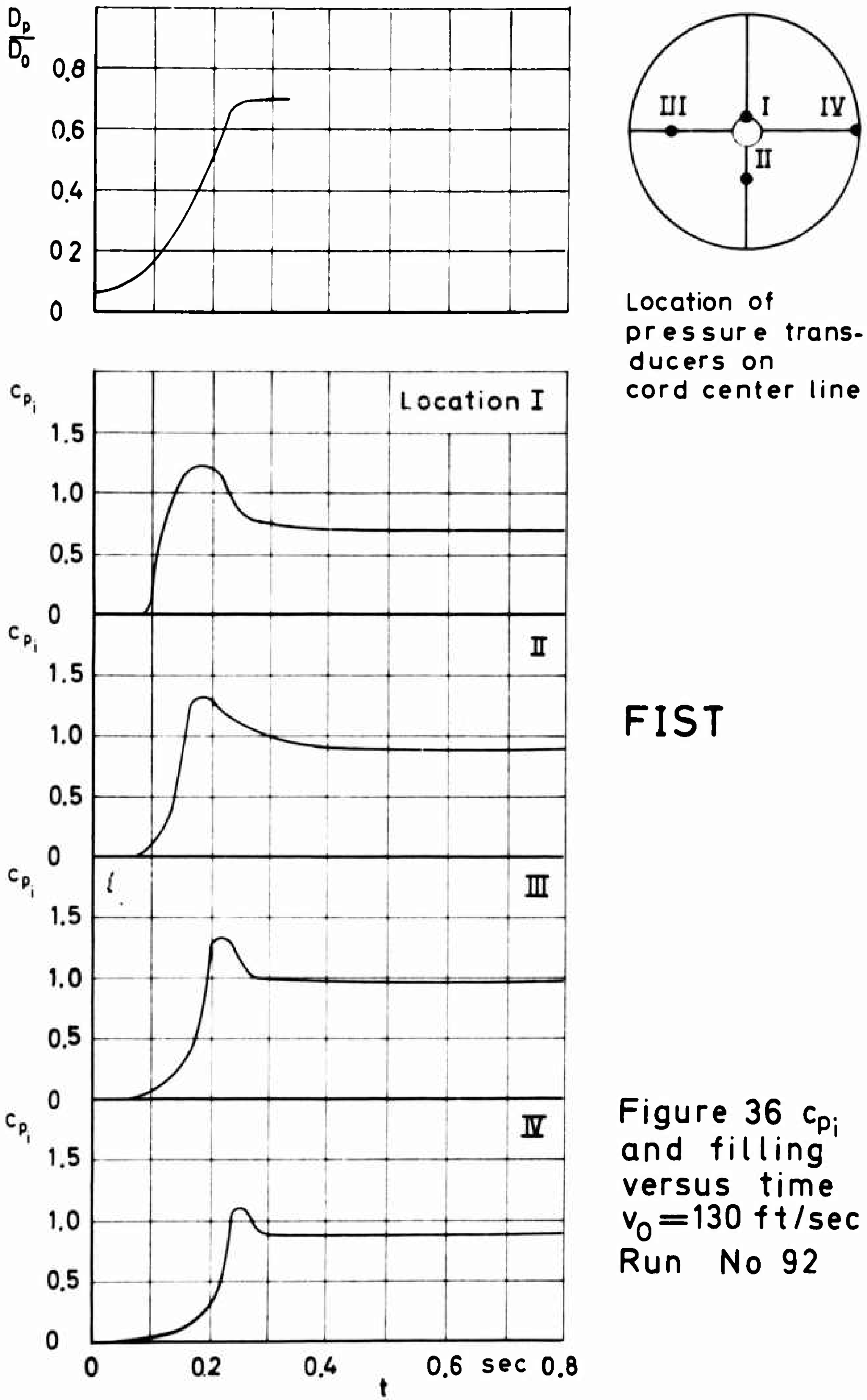

Location of pressure transducers on cord center line

FIST

Figure 36 c_{p_i} and filling versus time $v_0 = 130$ ft/sec Run No 92

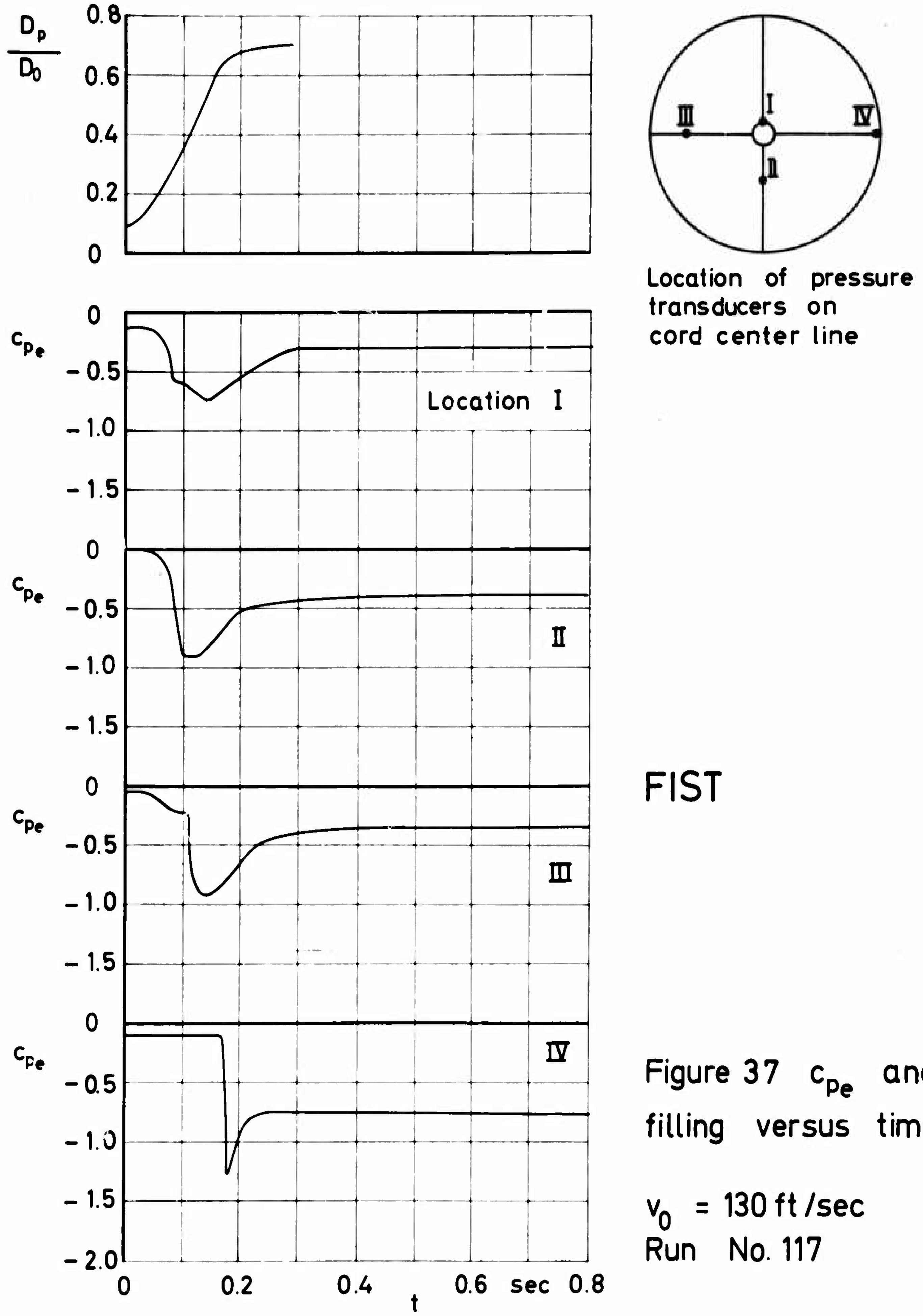

Location of pressure transducers on cord center line

FIST

Figure 37 c_{p_e} and filling versus time

v_0 = 130 ft/sec
Run No. 117

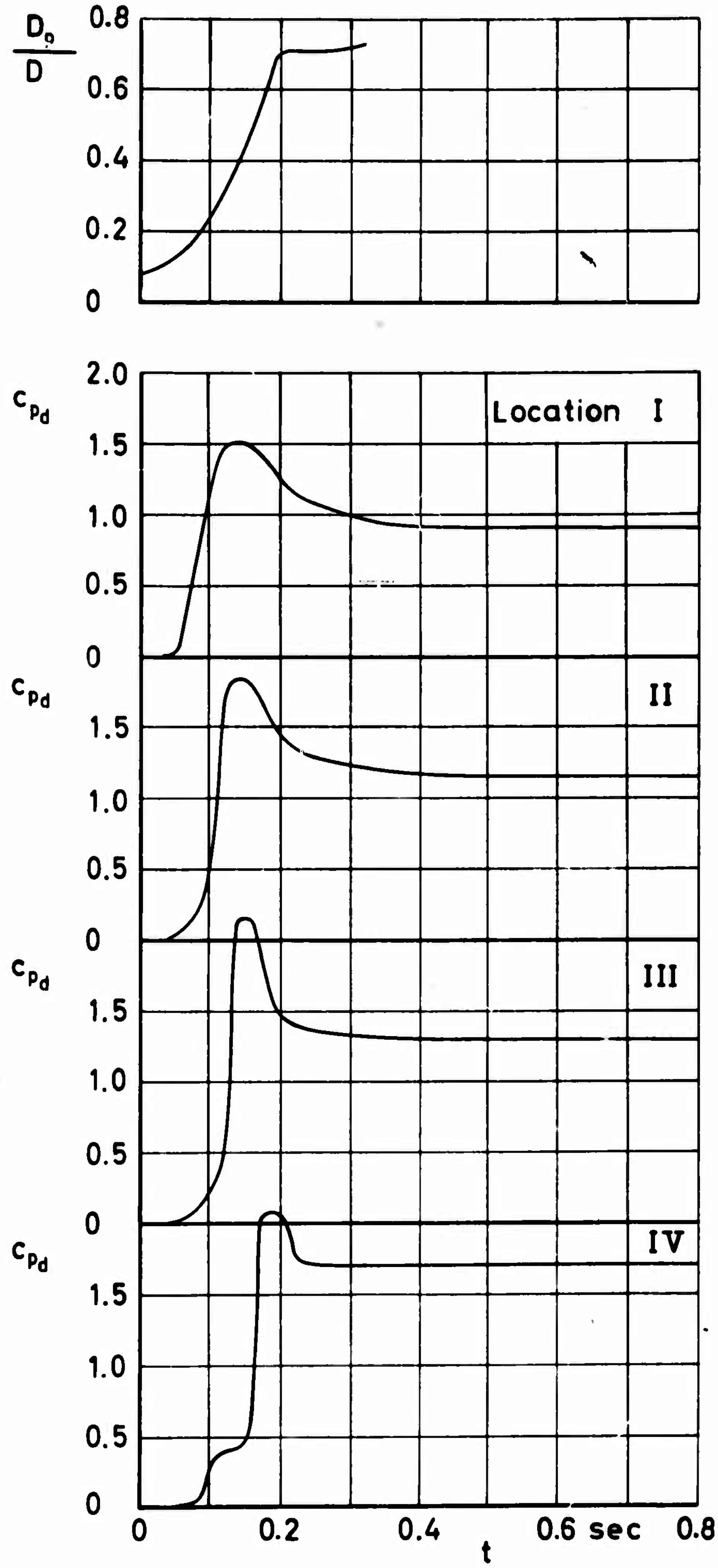

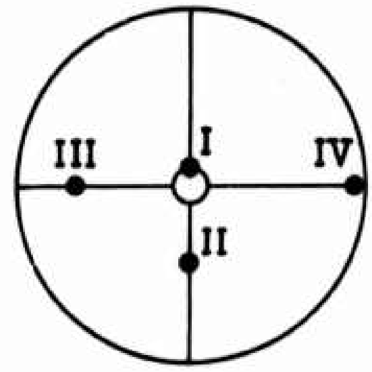

Location of pressure transducers on cord center line

FIST

Figure 38 c_{p_d} and filling versus time

v_0=160 ft/sec

Run No. 86

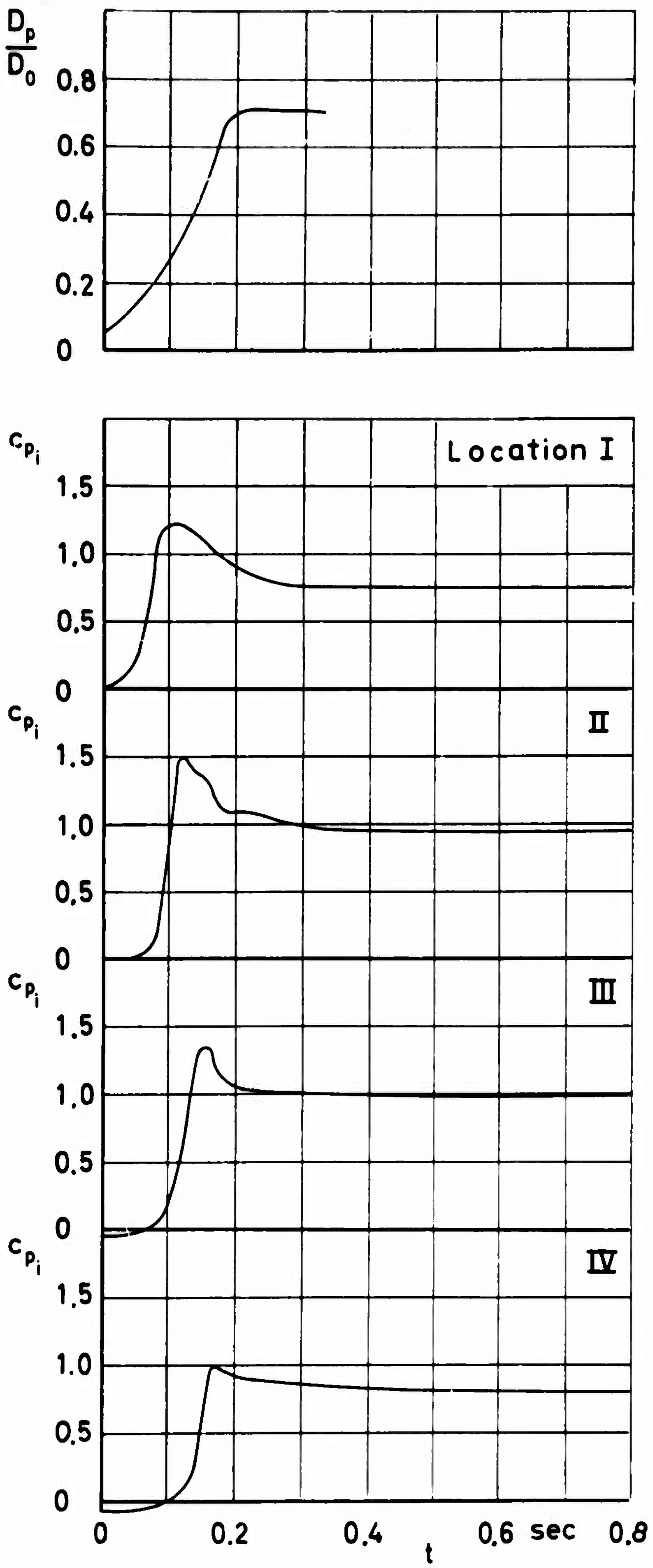

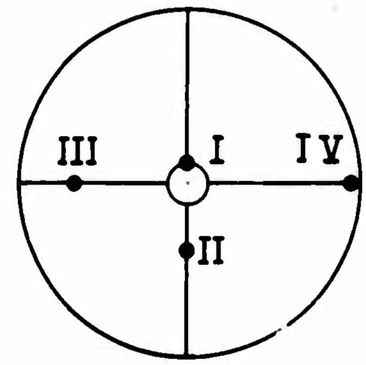

Location of pressure transducers on cord center line

FIST

Figure 39 c_{p_i} and filling versus time $v_0 = 160$ ft/sec Run No 88

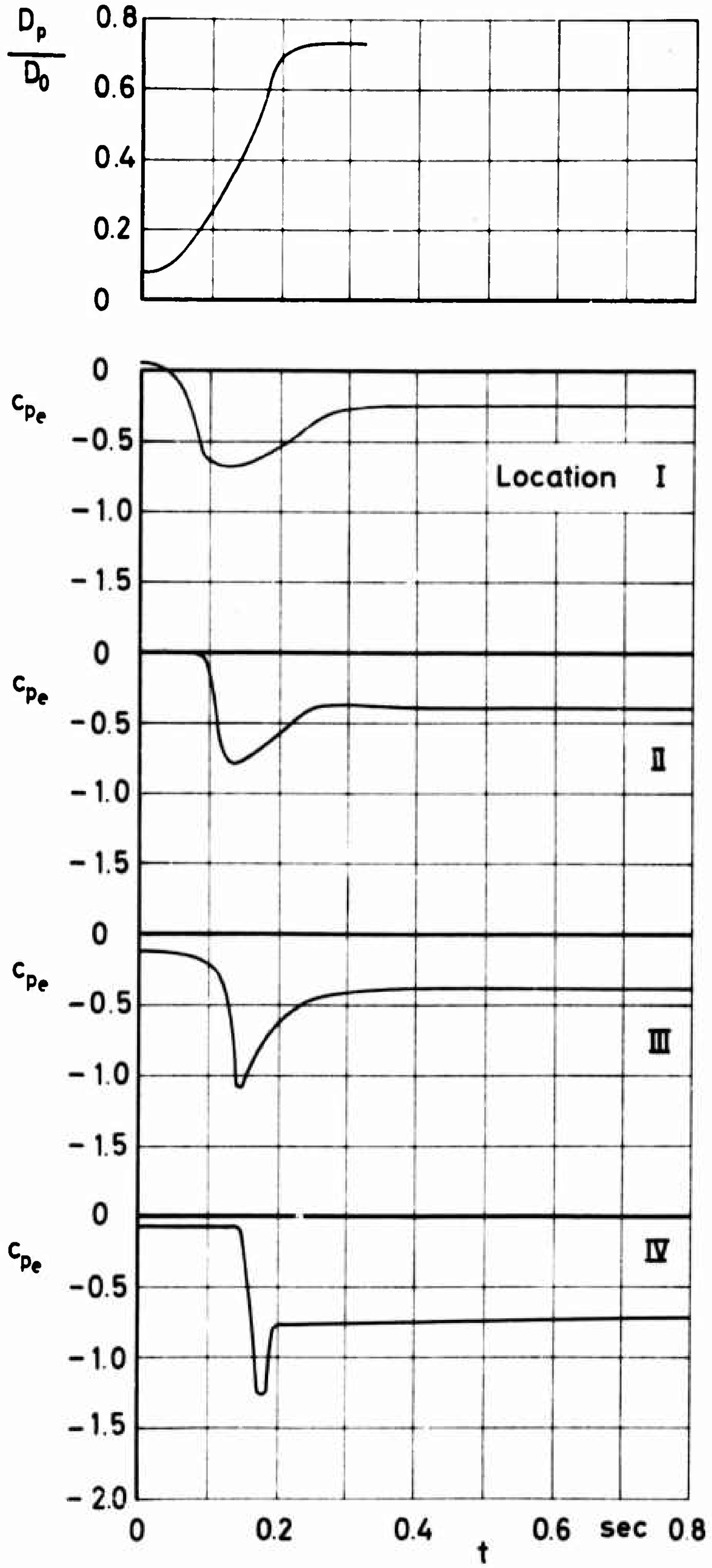

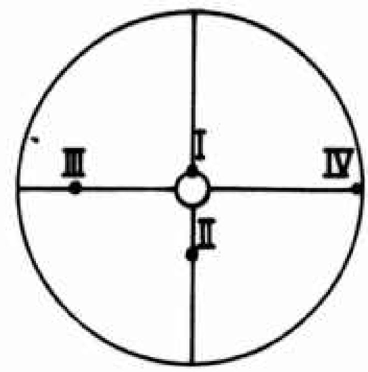

Location of pressure transducers on cord center line

FIST

Figure 40 c_{p_e} and filling versus time

v_0 = 160 ft / sec

Run No. 119

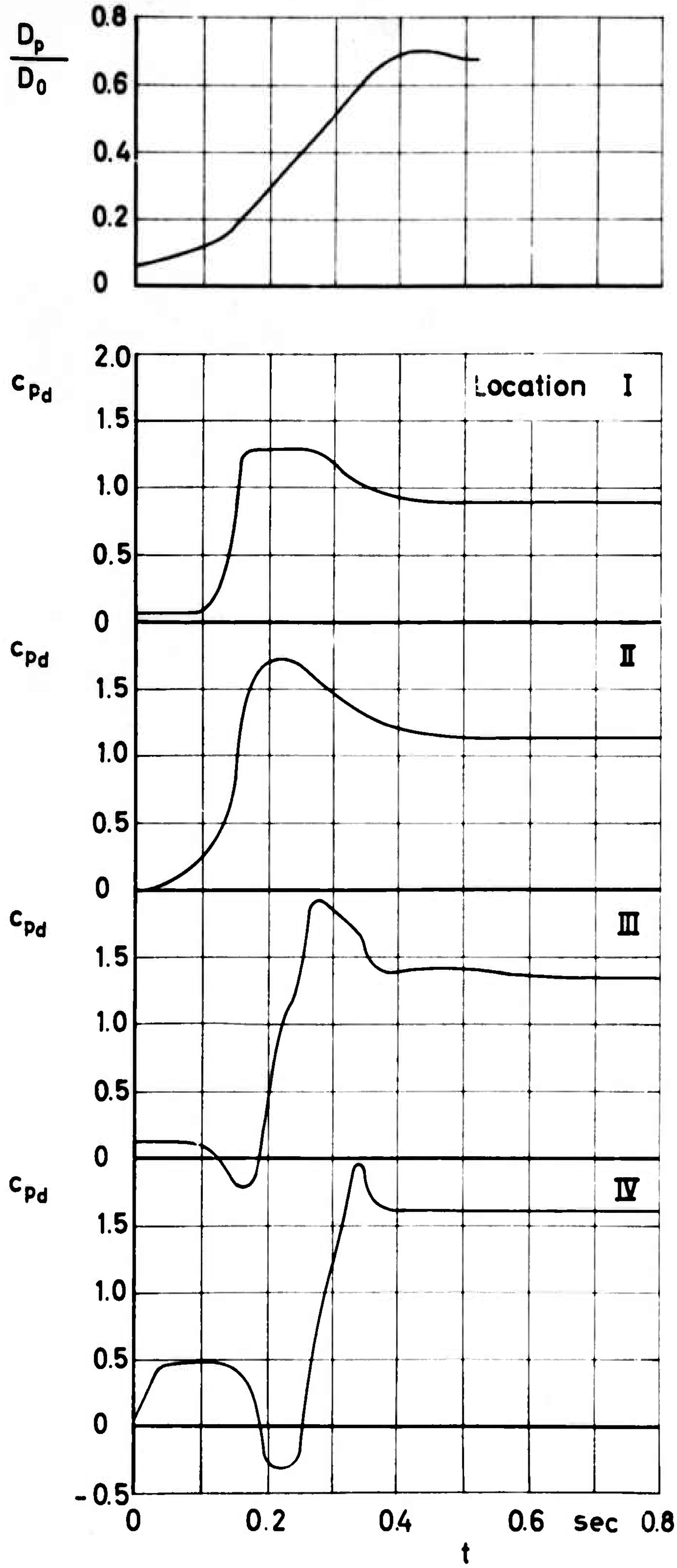

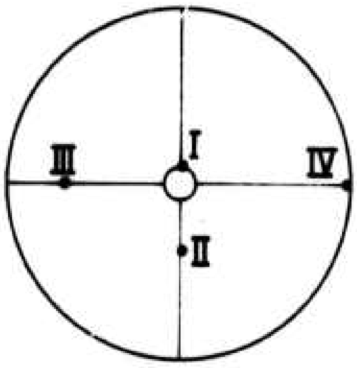

Location of pressure transducers on cord center line

Ringslot

Figure 41 c_{p_d} and filling versus time

v_0 = 70 ft / sec

Run No. 7

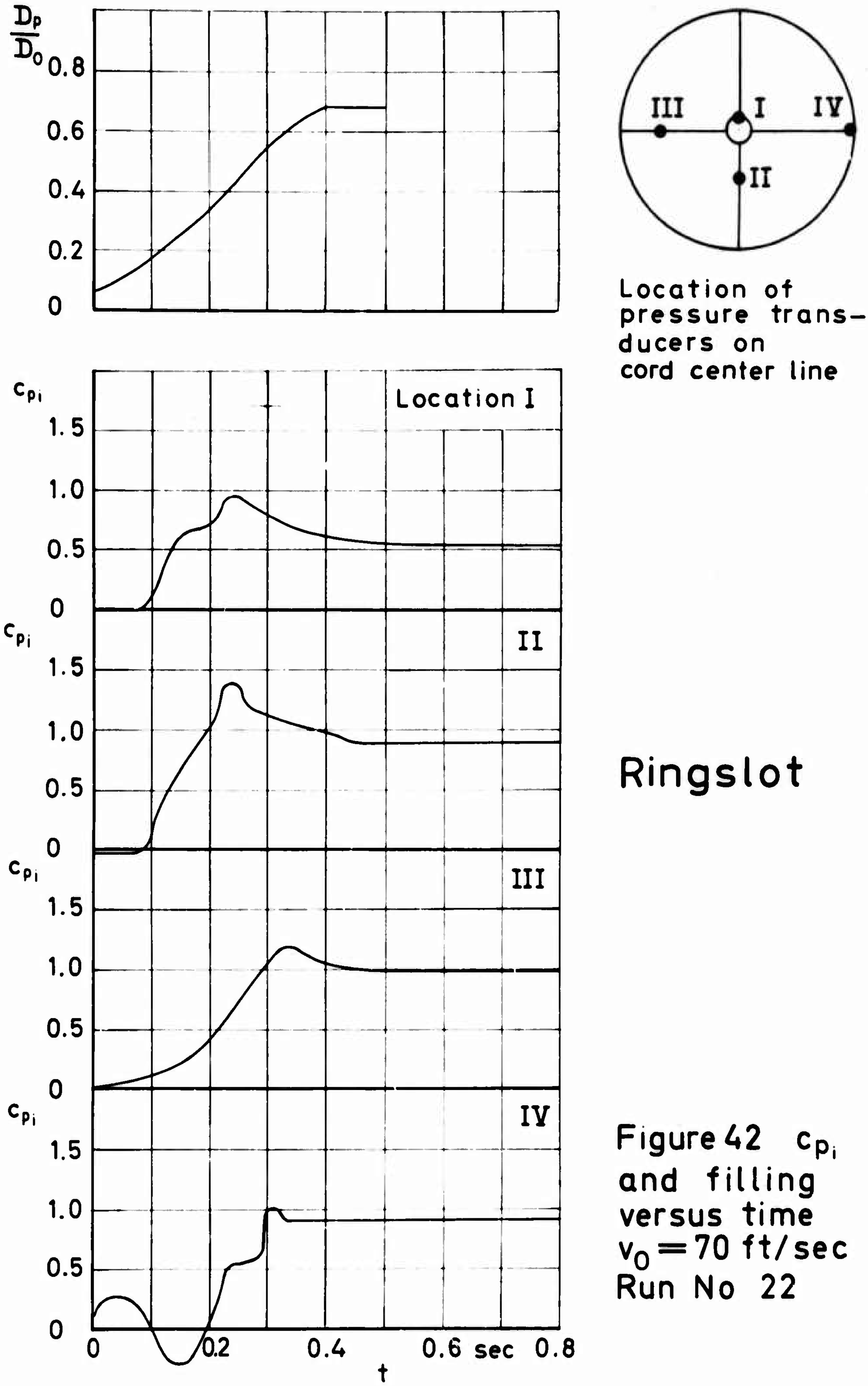

Location of pressure transducers on cord center line

Ringslot

Figure 42 c_{p_i} and filling versus time $v_0 = 70$ ft/sec Run No 22

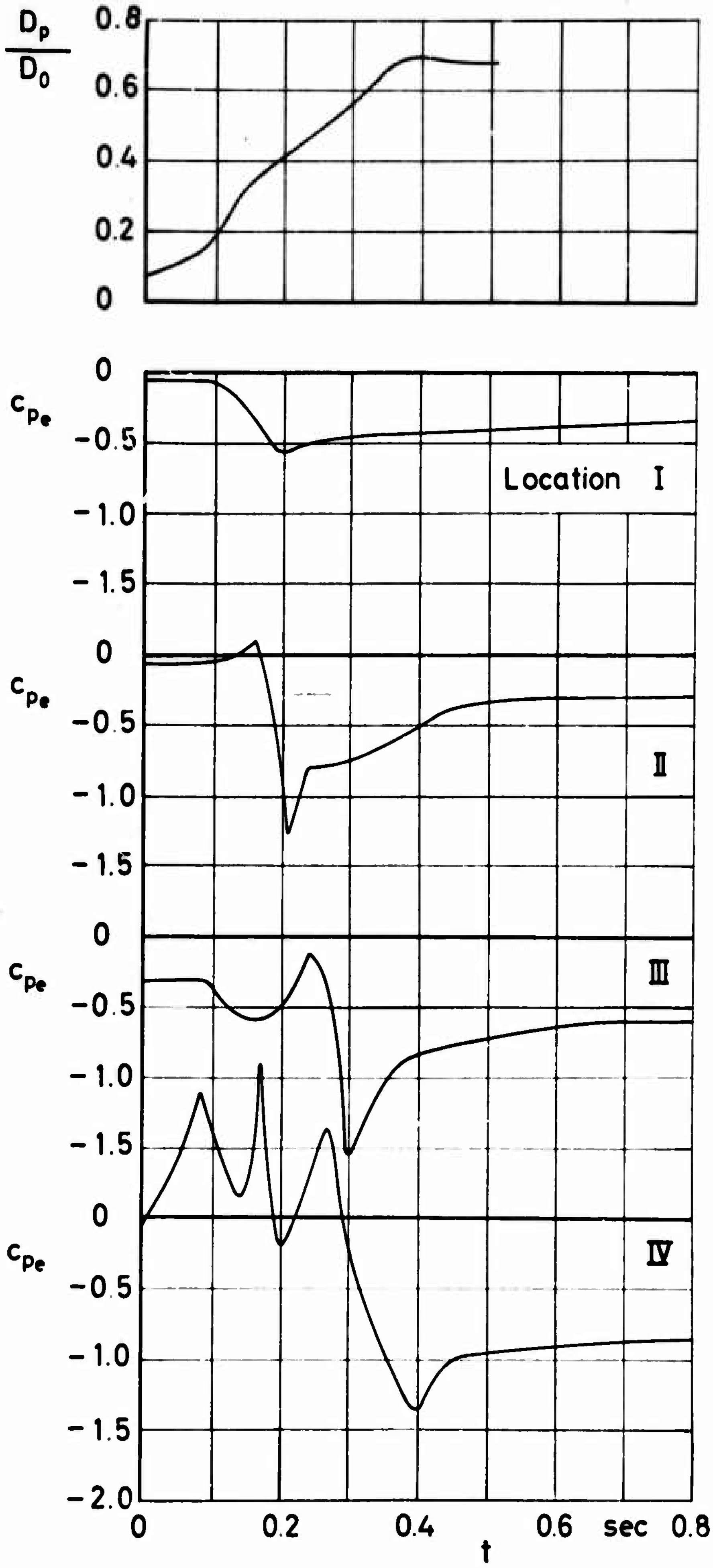

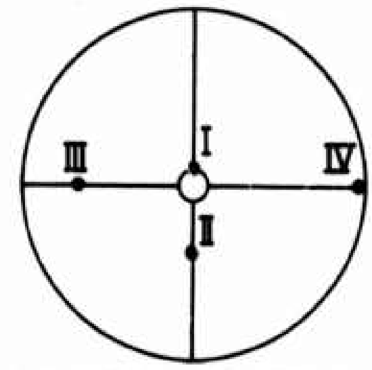

Location of pressure transducers on cord center line

Ringslot

Figure 43 c_{p_e} and filling versus time

v_0 = 70 ft/sec

Run No. 34

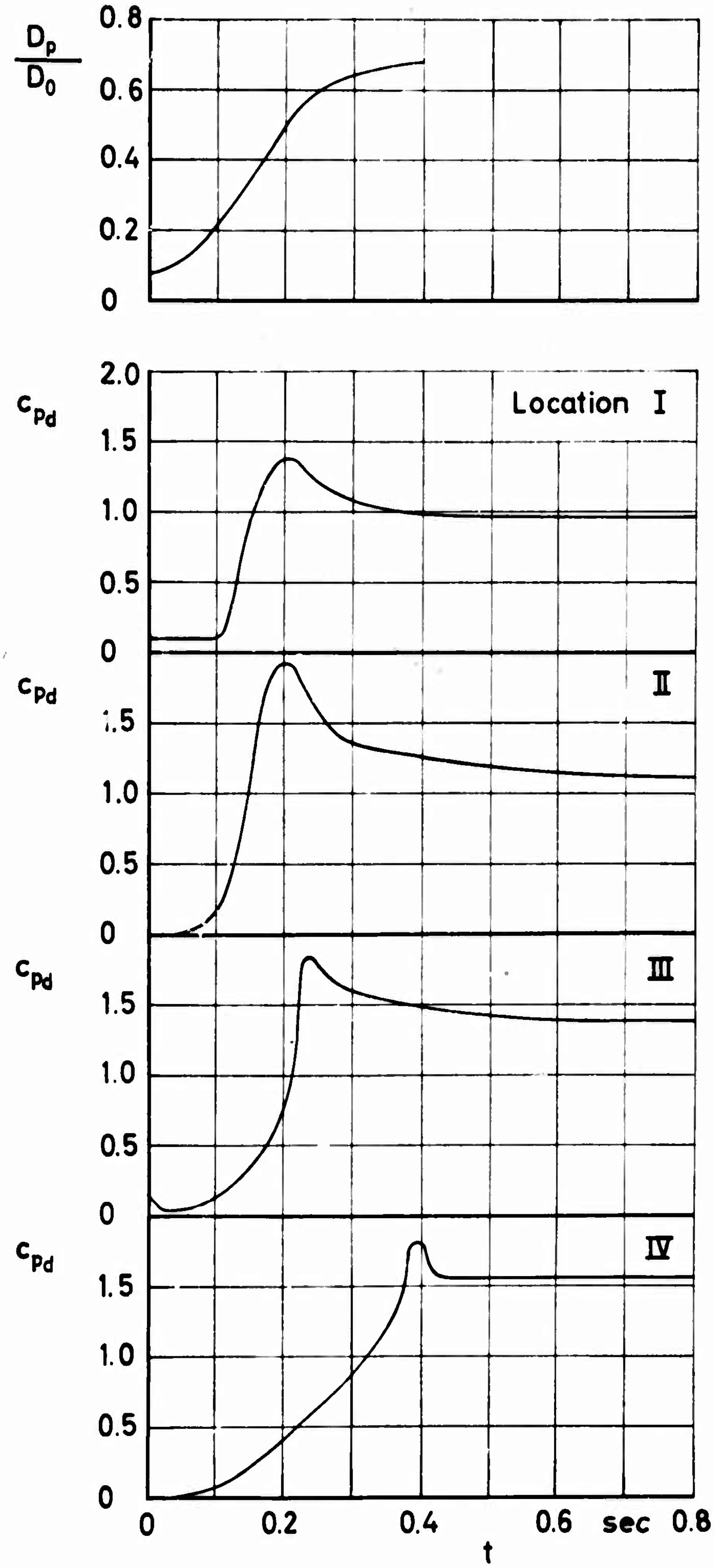

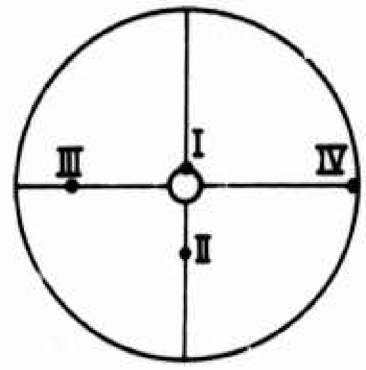

Location of pressure transducers on cord center line

Ringslot

Figure 44 c_{p_d} and filling versus time

v_0 = 100 ft /sec

Run No. 10

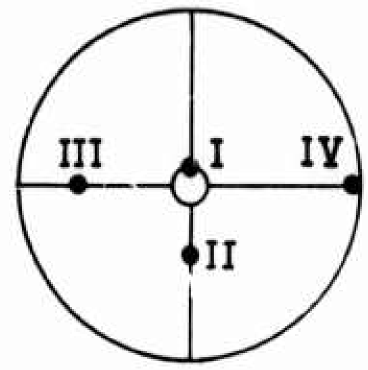

Location of pressure transducers on cord center line

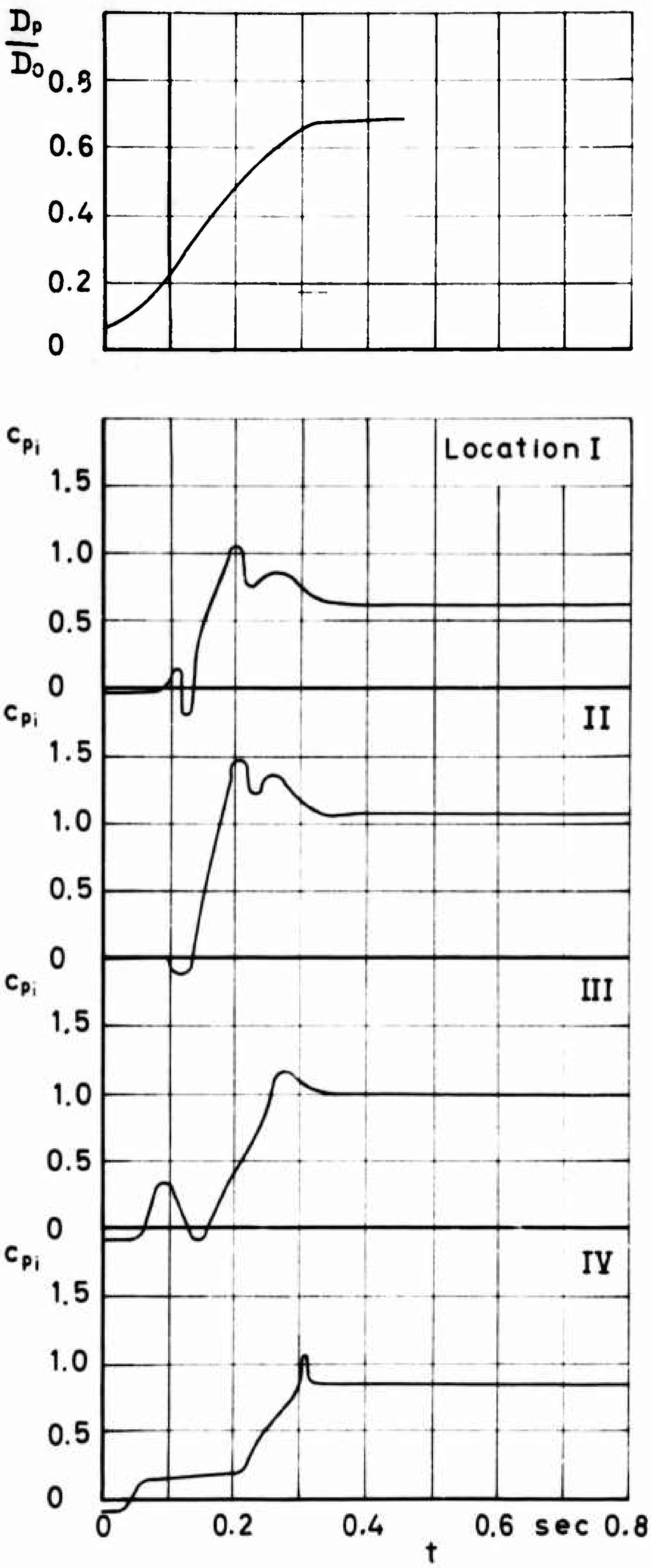

Ringslot

Figure 45 c_{p_i} and filling versus time $v_0 = 100$ ft/sec Run No 30

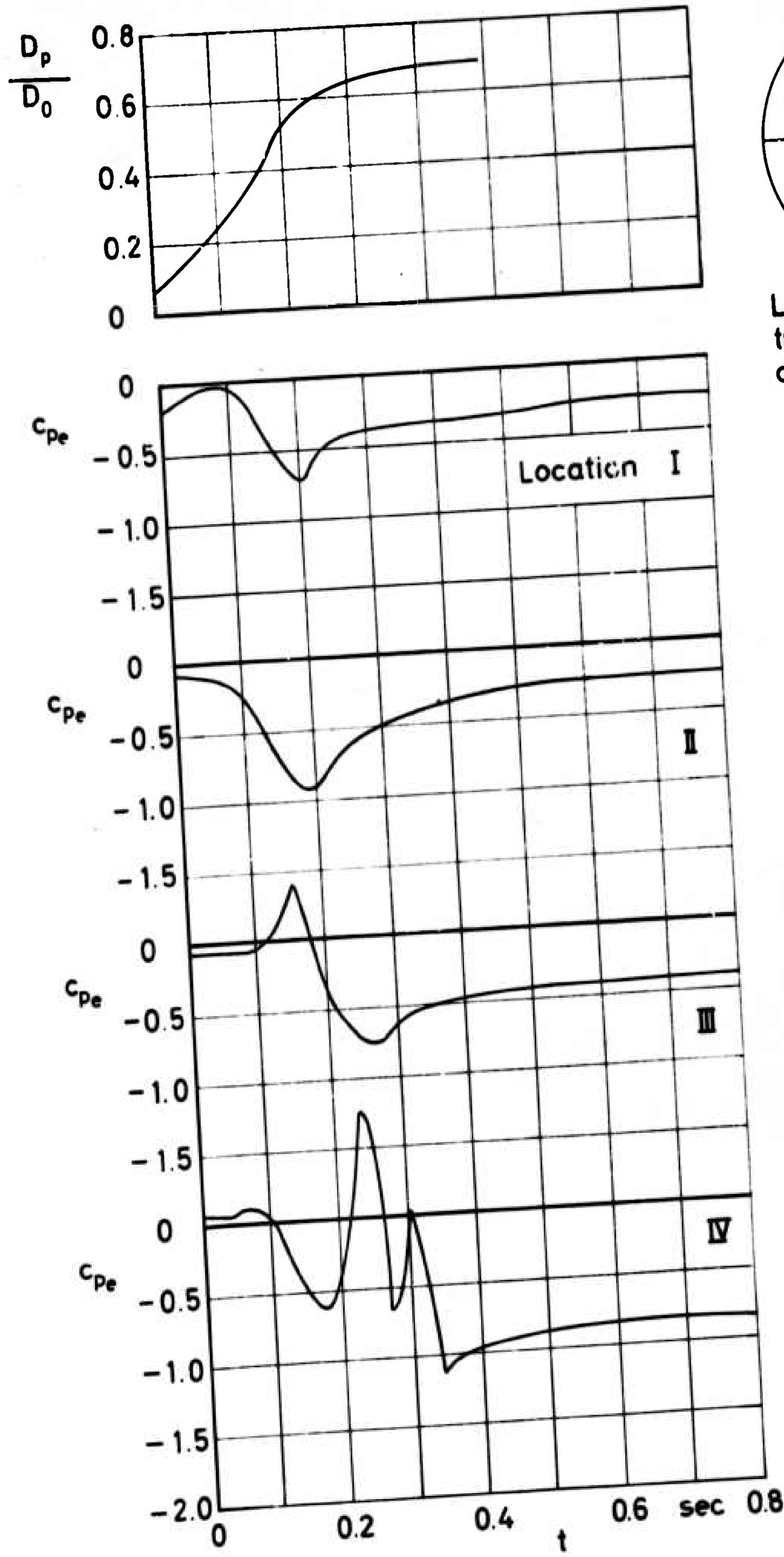

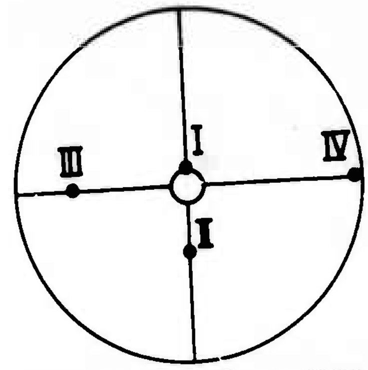

Location of pressure transducers on cord center line

Ringslot

Figure 46 c_{pe} and filling versus time

v_0 = 100 ft / sec

Run No. 39

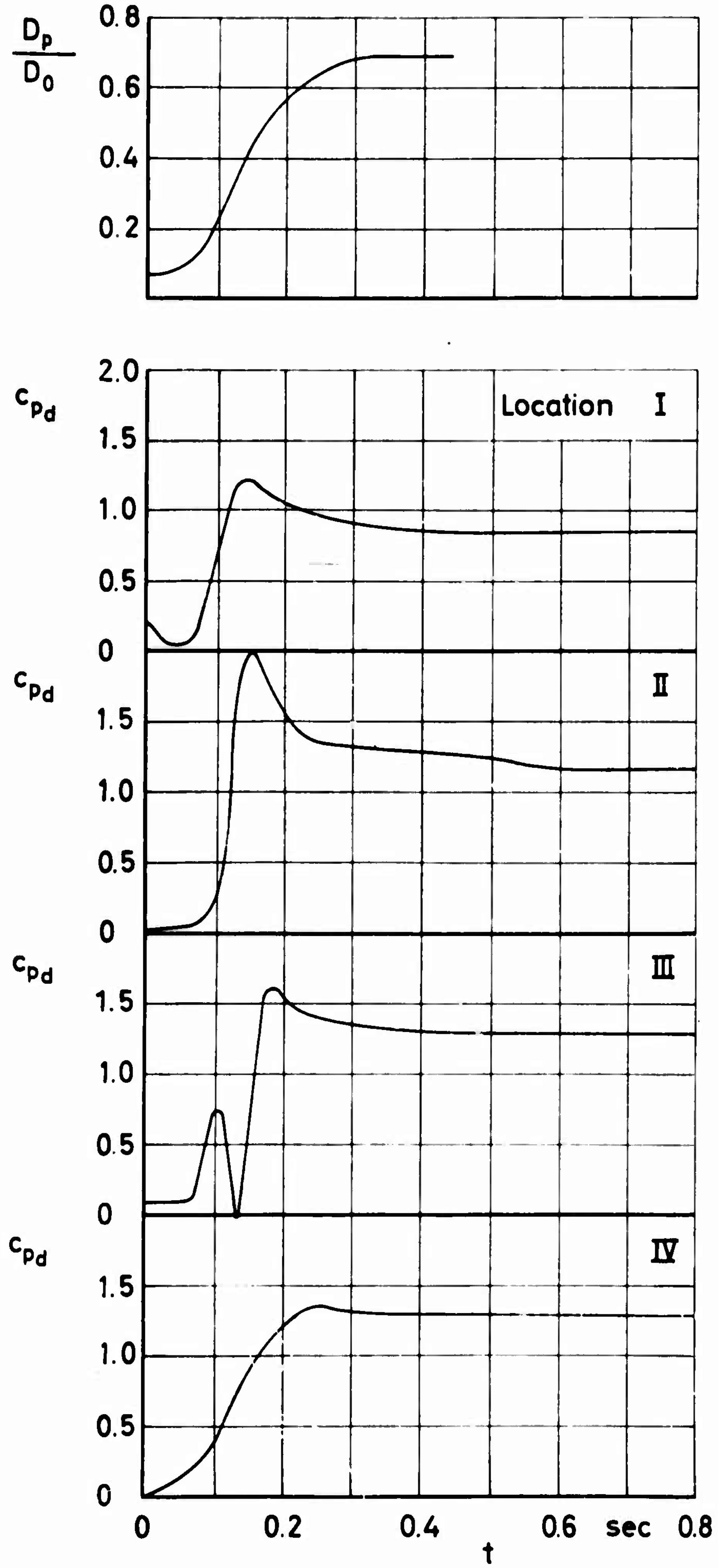

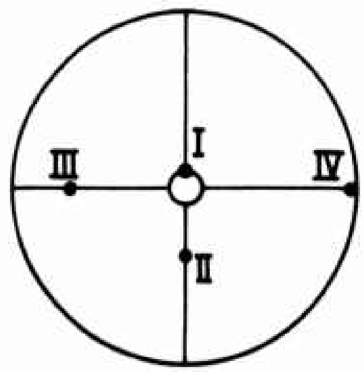

Location of pressure transducers on cord center line

Ringslot

Figure 47 c_{p_d} and filling versus time

v_0 = 130 ft/sec

Run No. 14

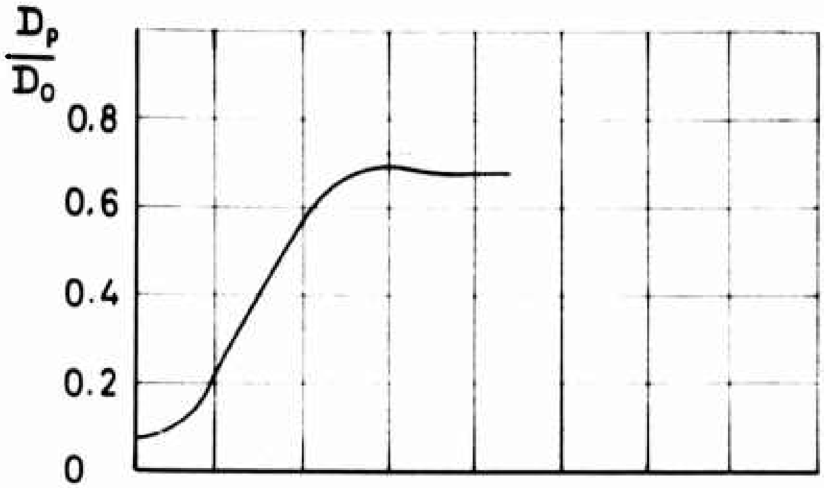

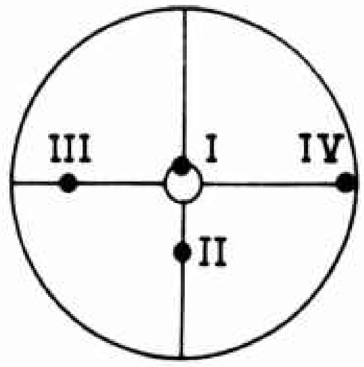

Location of pressure transducers on cord center line

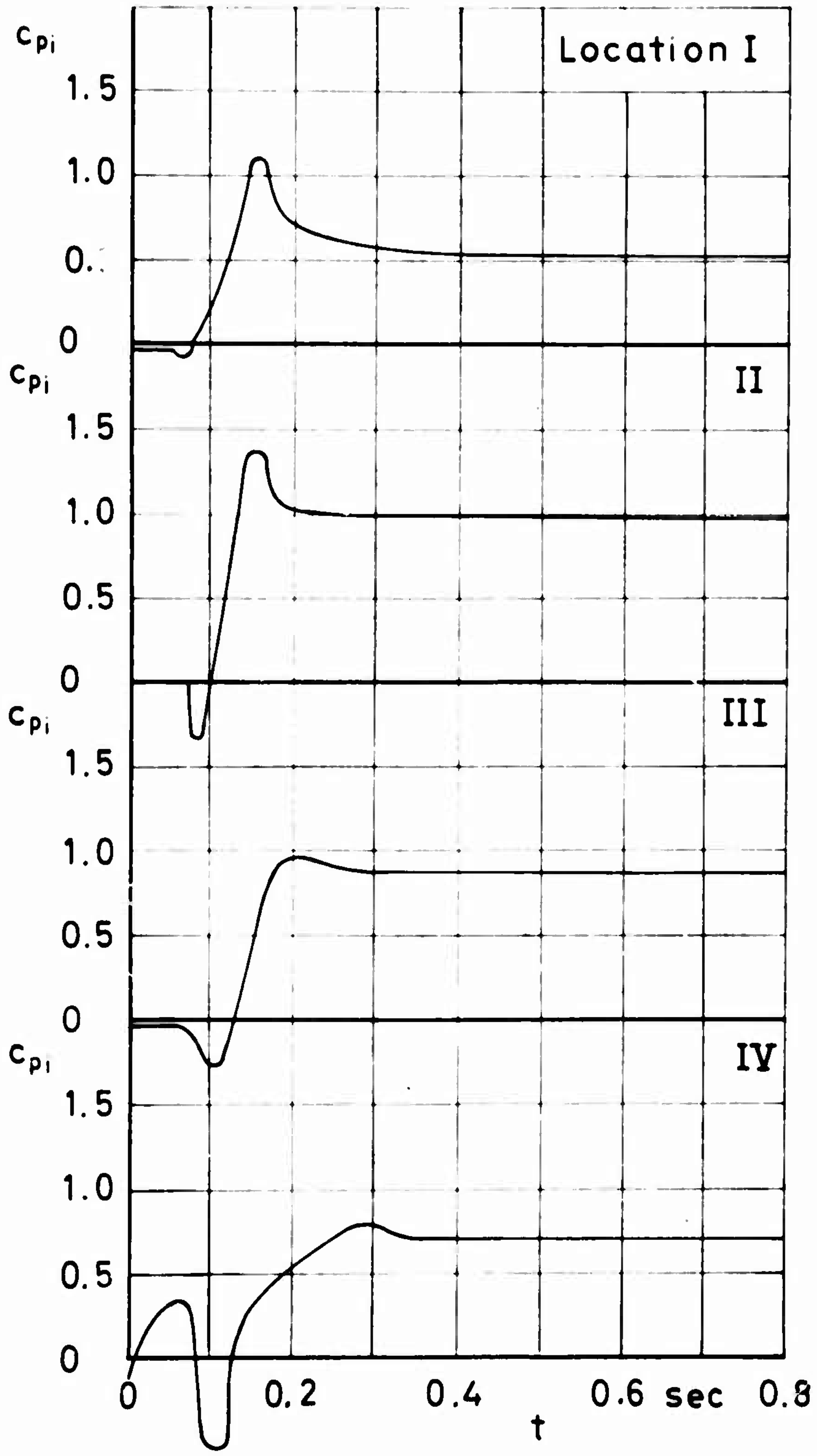

Ringslot

Figure 48 c_{p_i} and filling versus time v_0=130 ft/sec Run No 51

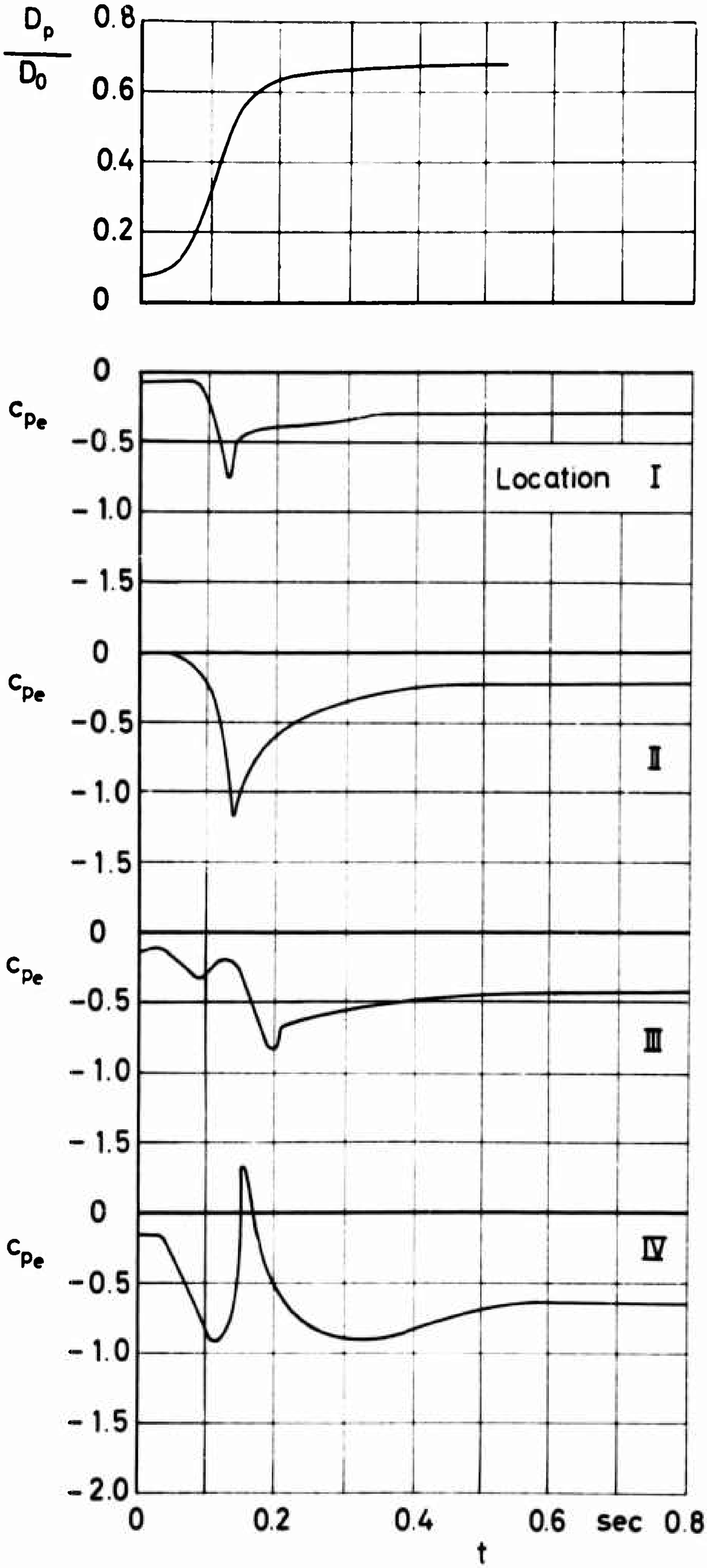

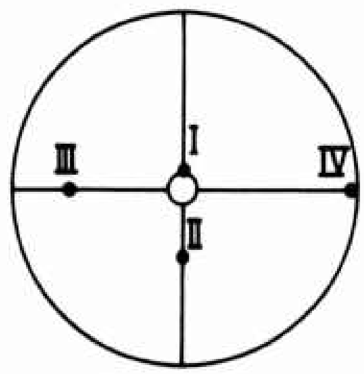

Location of pressure transducers on cord center line

Ringslot

Figure 49 c_{p_e} and filling versus time

v_0 = 130 ft/sec

Run No. 42

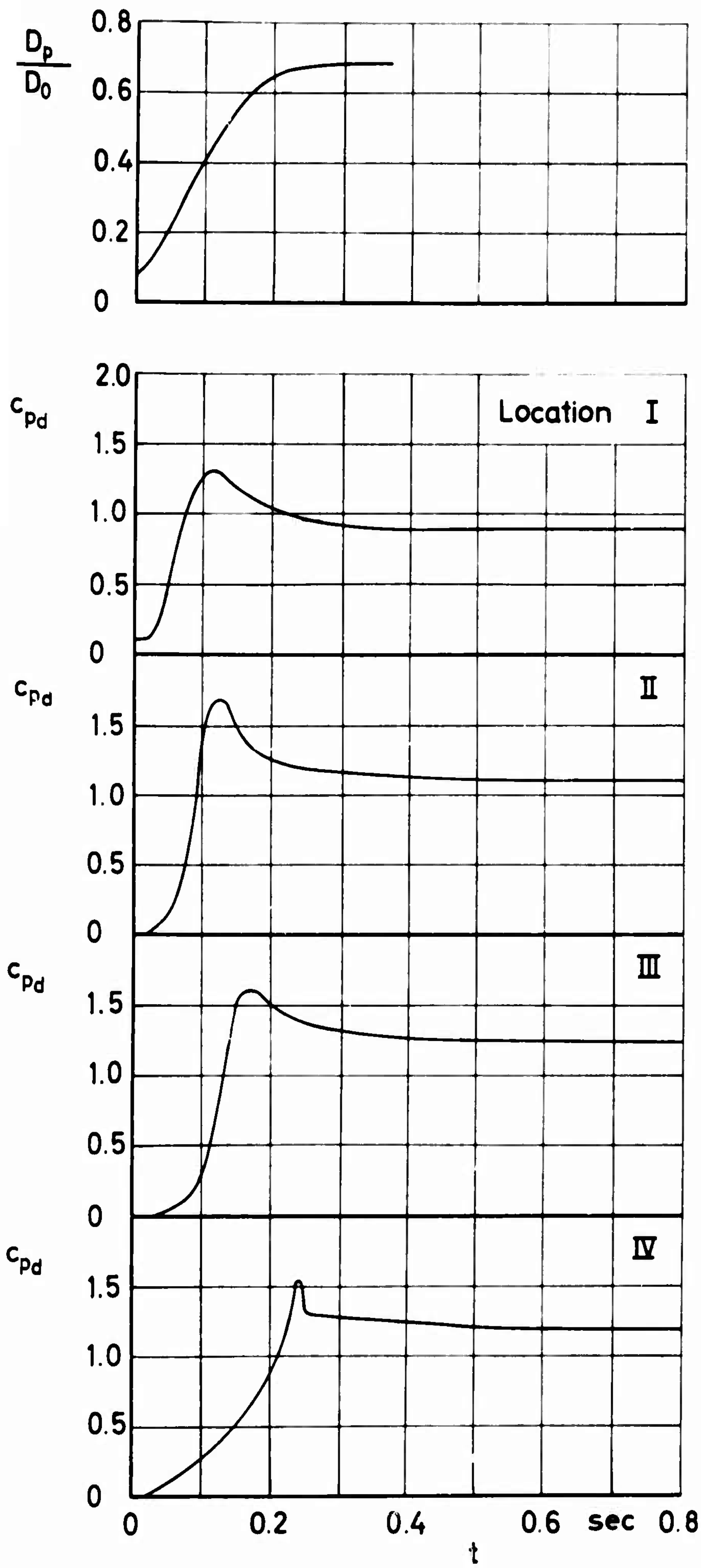

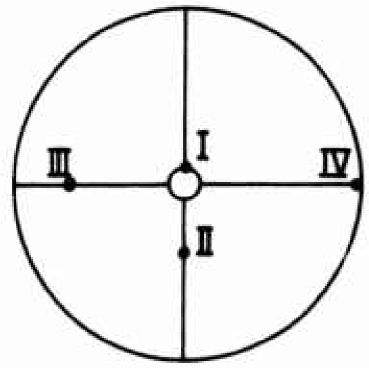

Location of pressure transducers on cord center line

Ringslot

Figure 50 c_{p_d} and filling versus time

v_0 = 160 ft/sec

Run No. 18

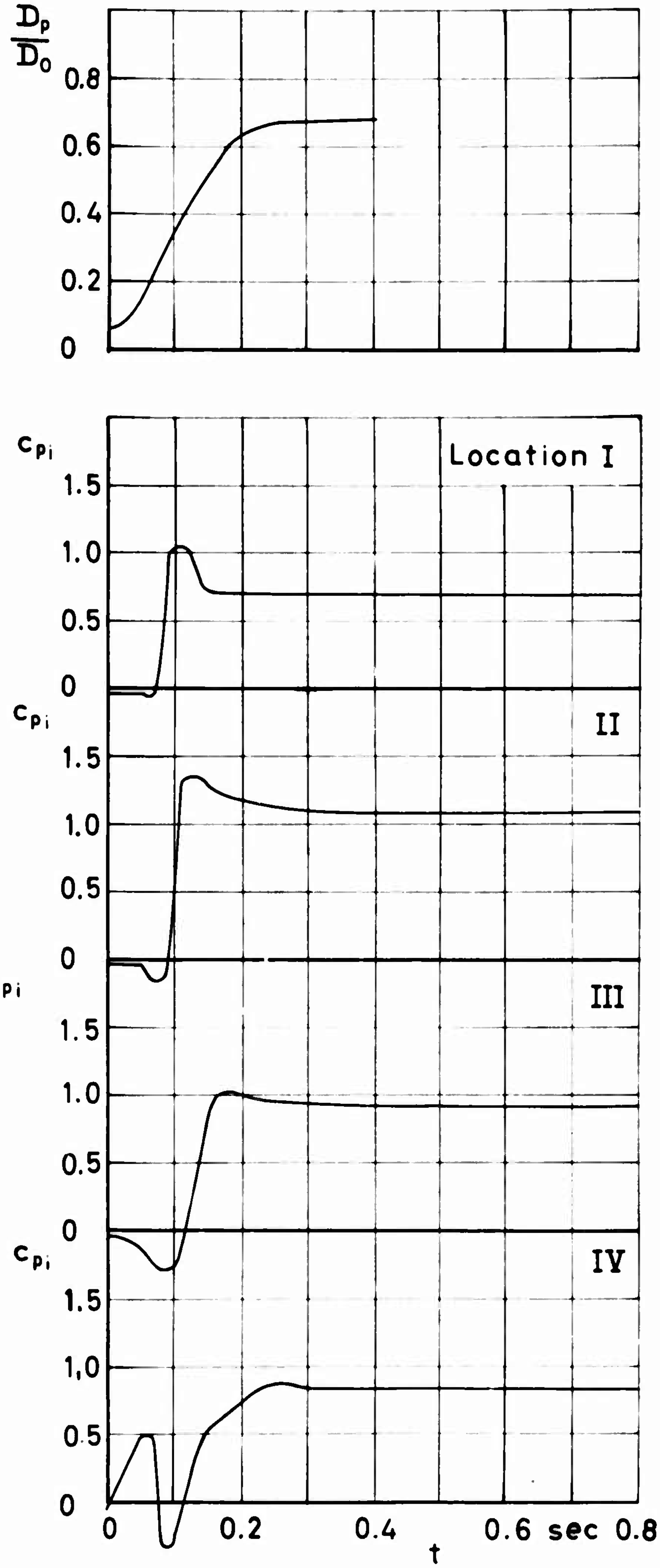

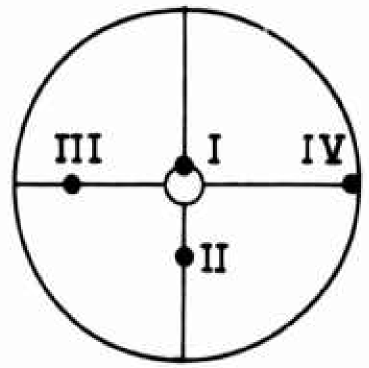

Location of pressure trans- ducers on cord center line

Ringslot

Figure 51 c_{p_i} and filling versus time
$v_0 = 160$ ft/sec
Run No 26

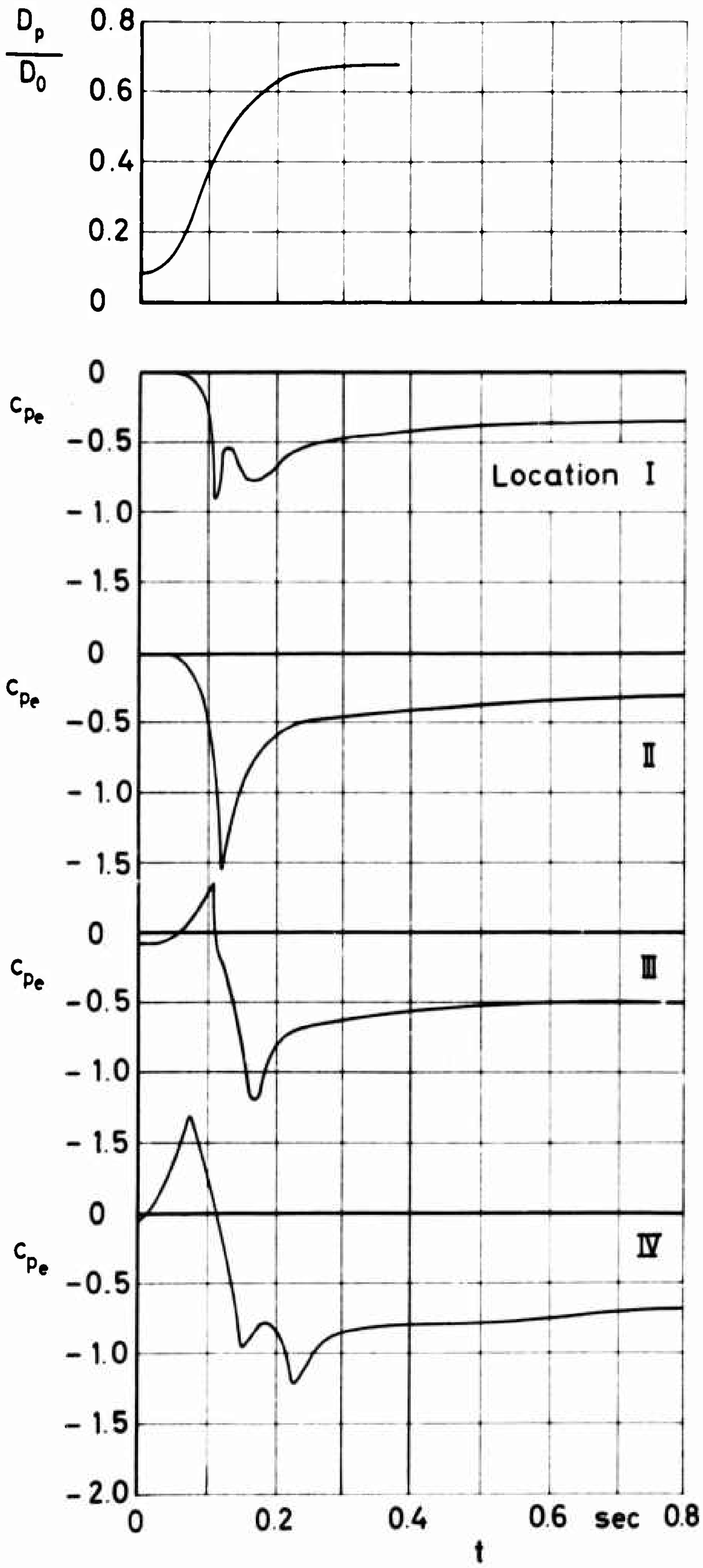

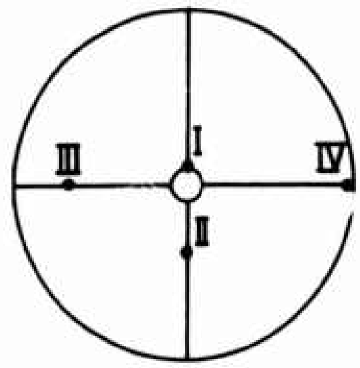

Location of pressure transducers on cord center line

Ringslot

Figure 52 c_{p_e} and filling versus time

v_0 = 160 ft/sec

Run No. 47

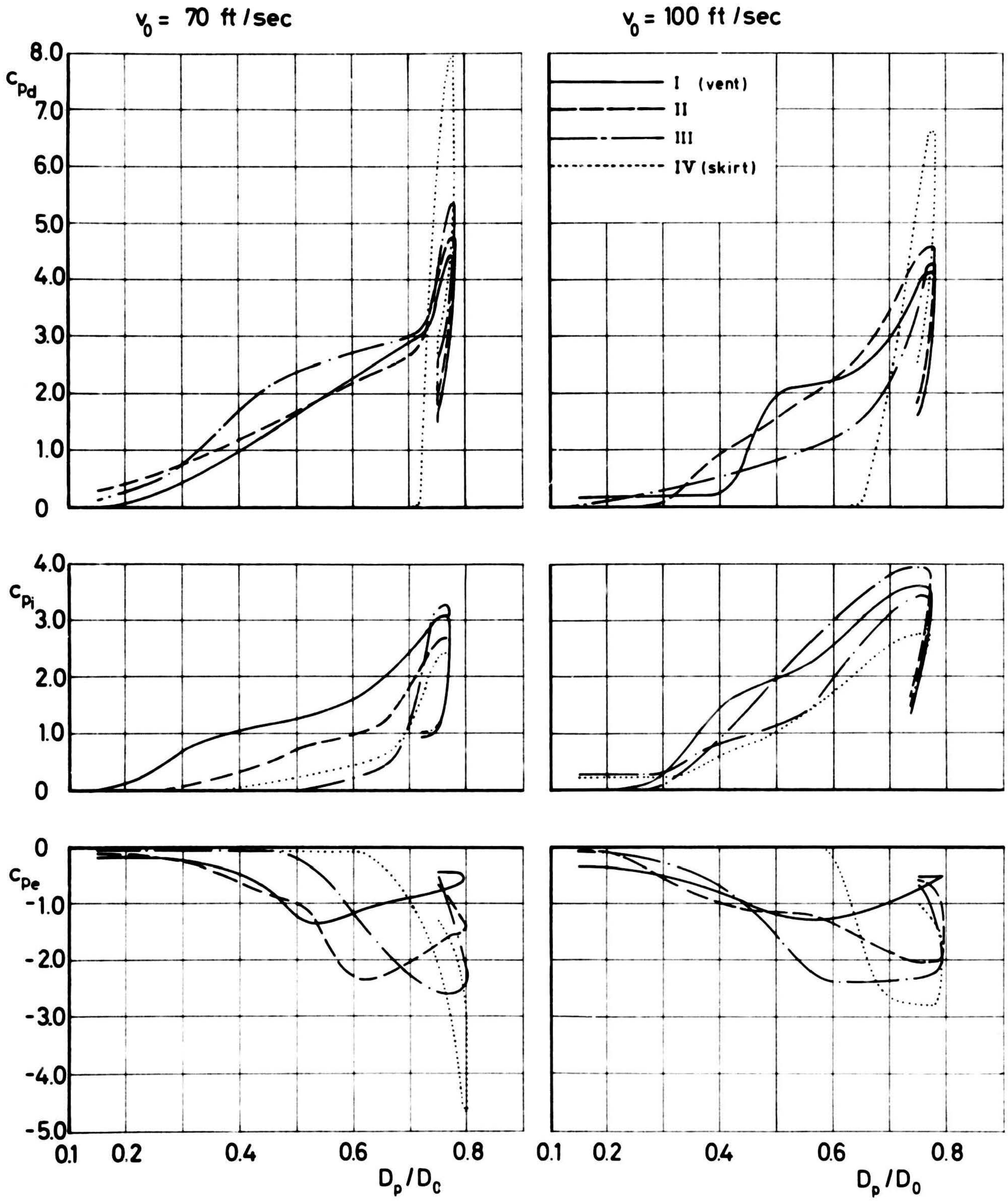

Figure 53 c_p versus D_p/D_0 for Circular Flat

Run No. 182; 194; 211; 183; 200; 216

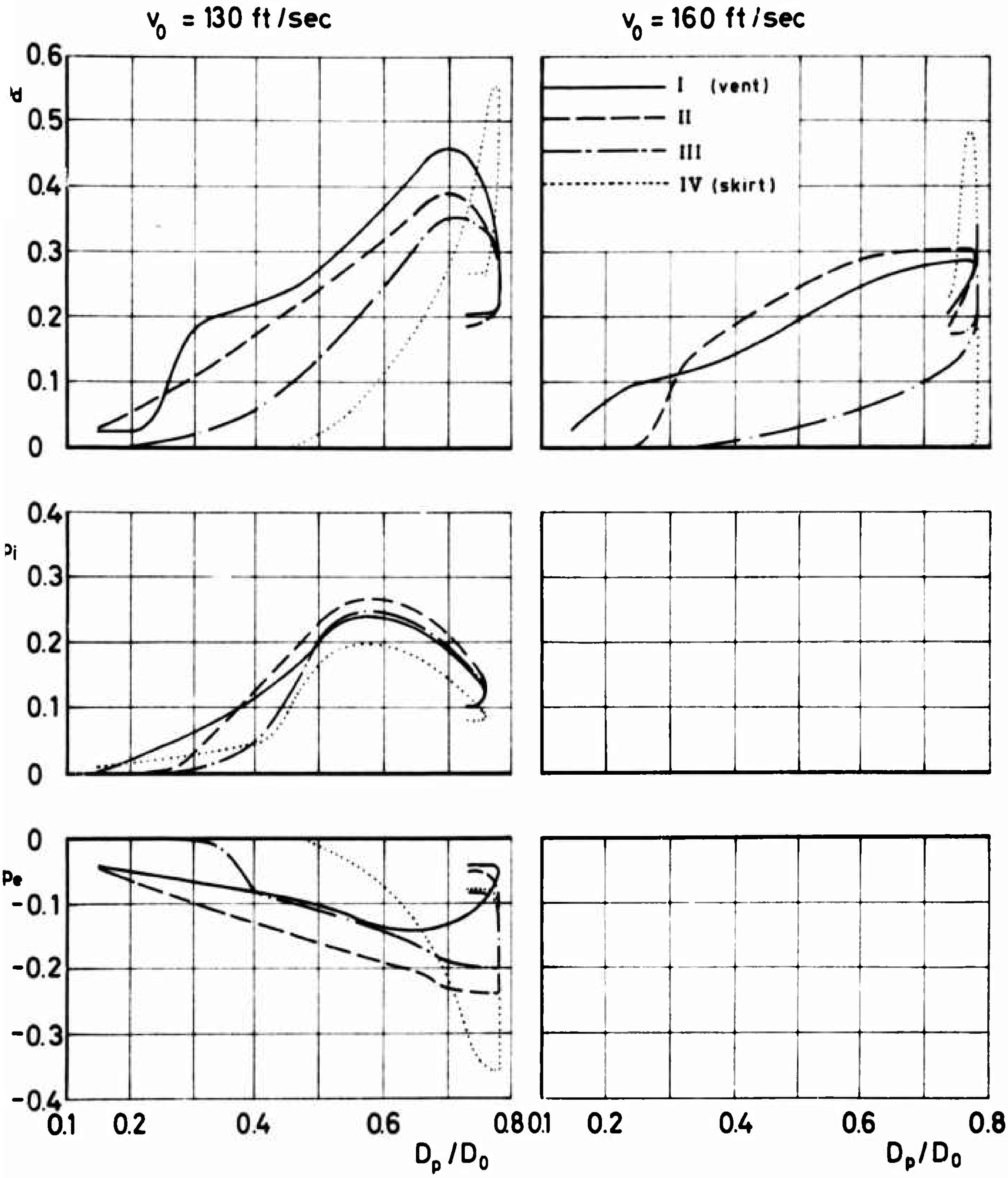

Figure 54 c_p versus D_p/D_0 for Circular Flat

Run No. 187; 203; 218; 191

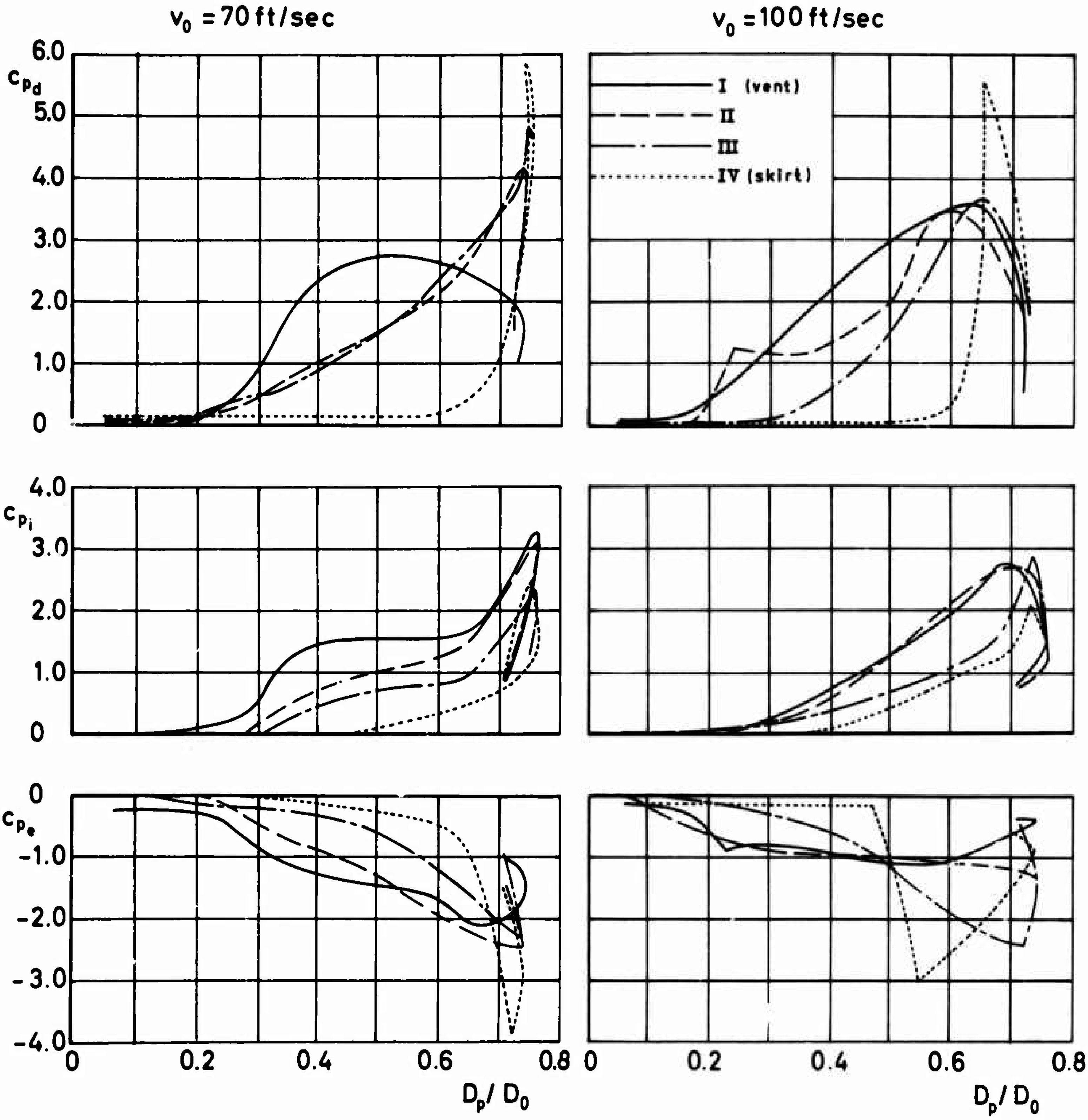

Figure 55 c_p versus D_p/D_0 for Extended Skirt

Run No. 139; 157; 221; 144; 160; 226

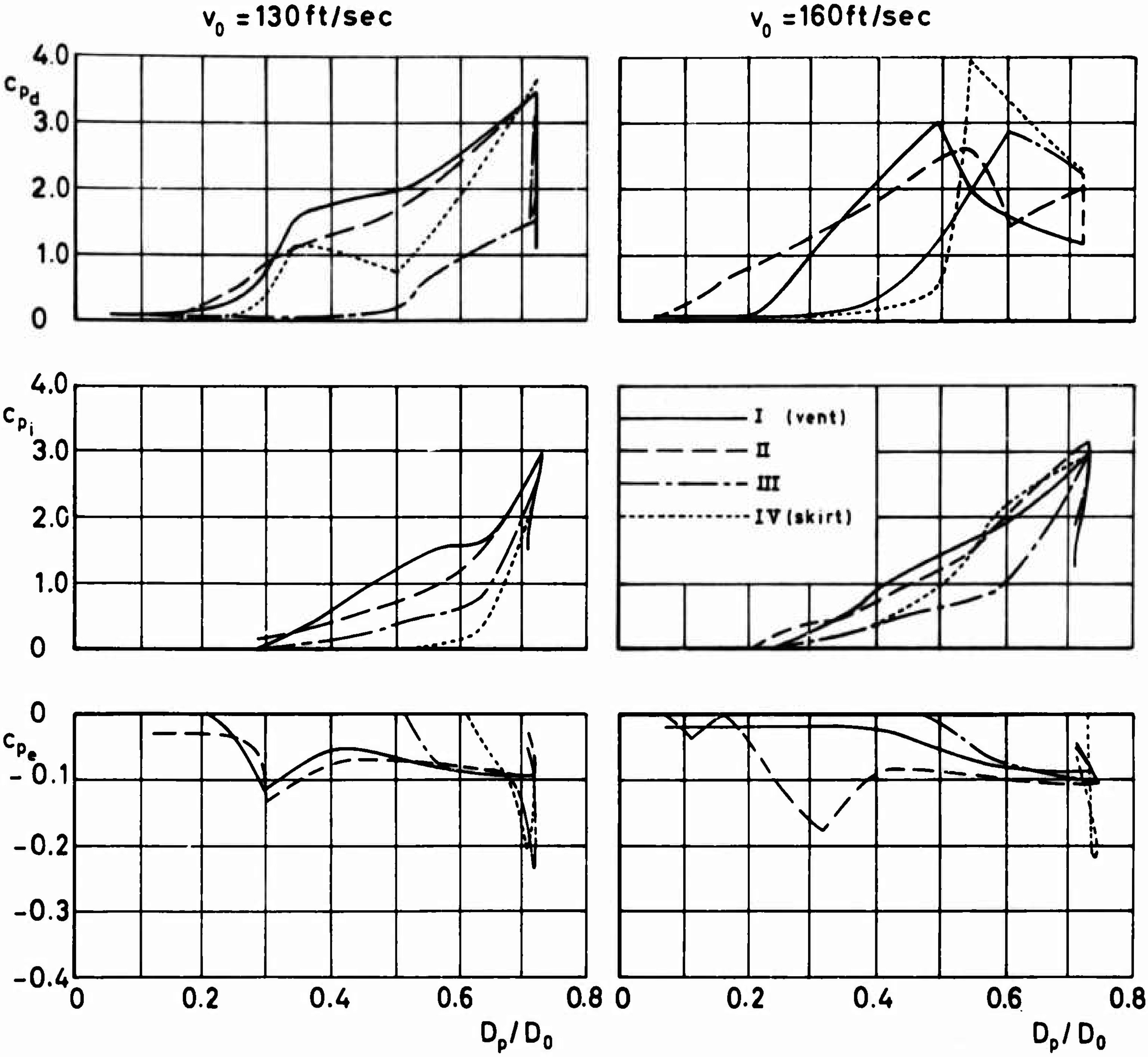

Figure 56 c_p versus D_p/D_0 for Extended Skirt

Run No. 148; 163; 231; 153; 166; 235

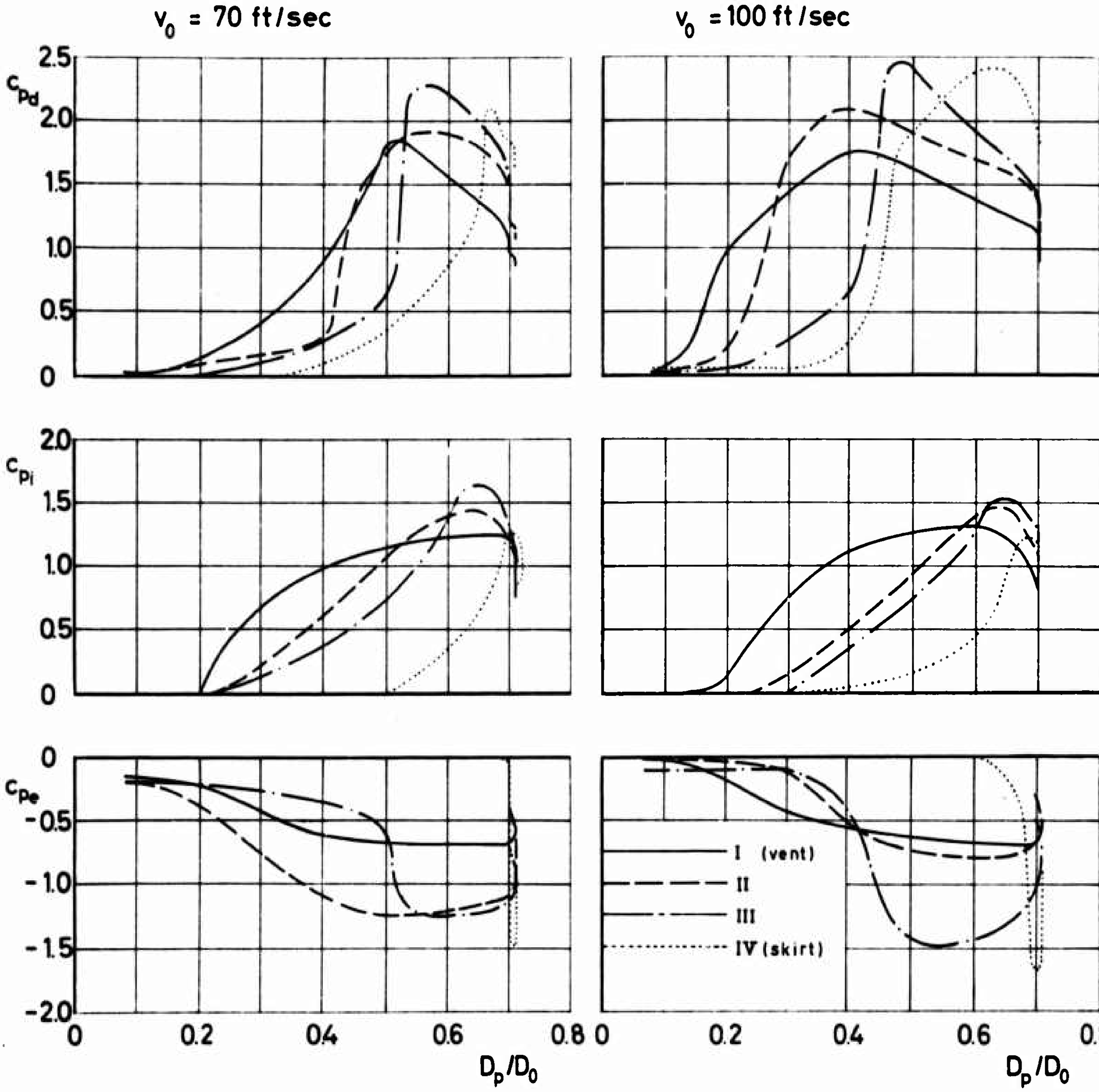

Figure 57 c_p versus D_p/D_0 for FIST

Run No. 72; 101; 104; 76; 97; 110

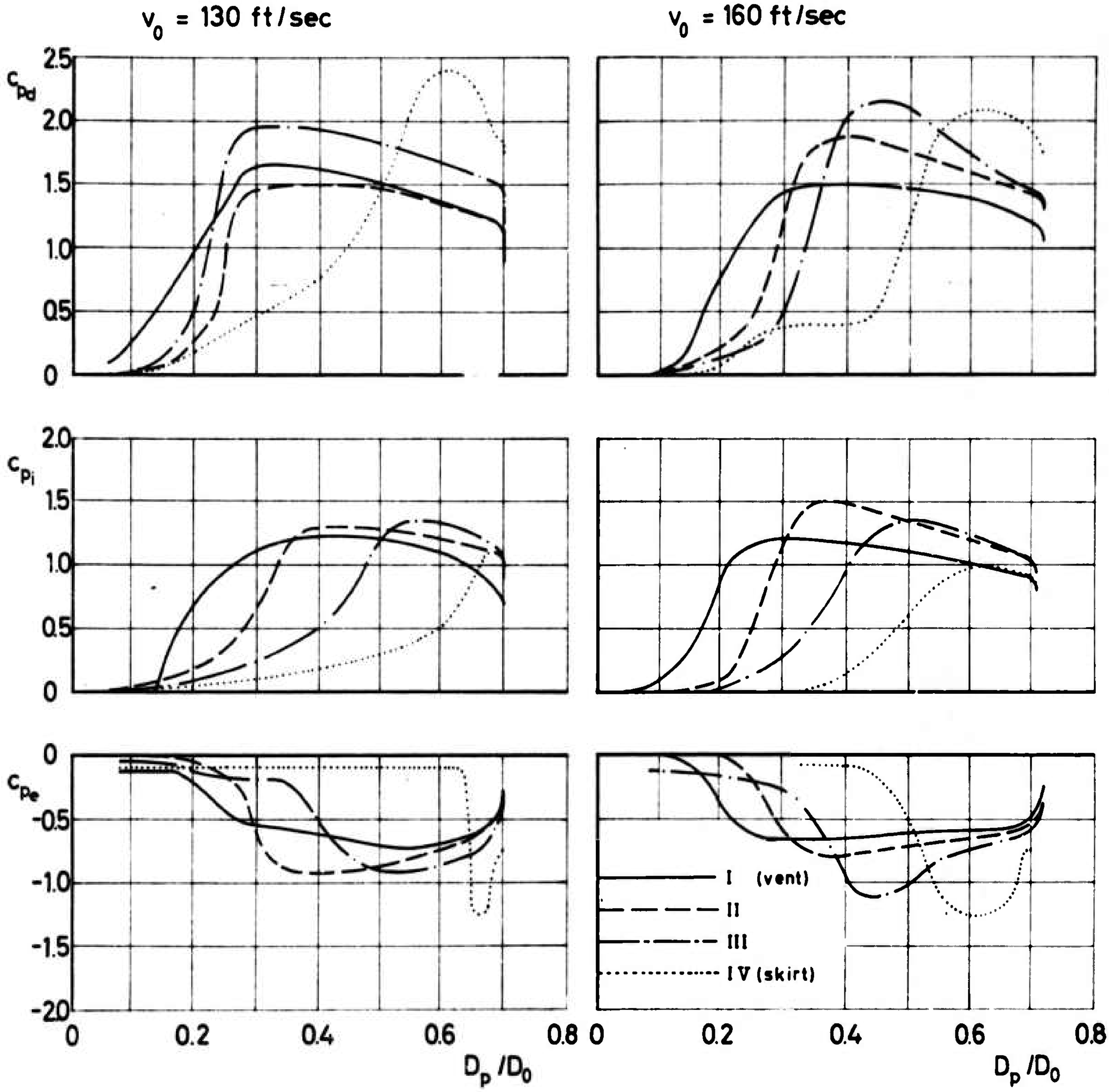

Figure 58 c_p versus D_p/D_0 for FIST

Run No. 82; 92; 117; 86; 88; 119

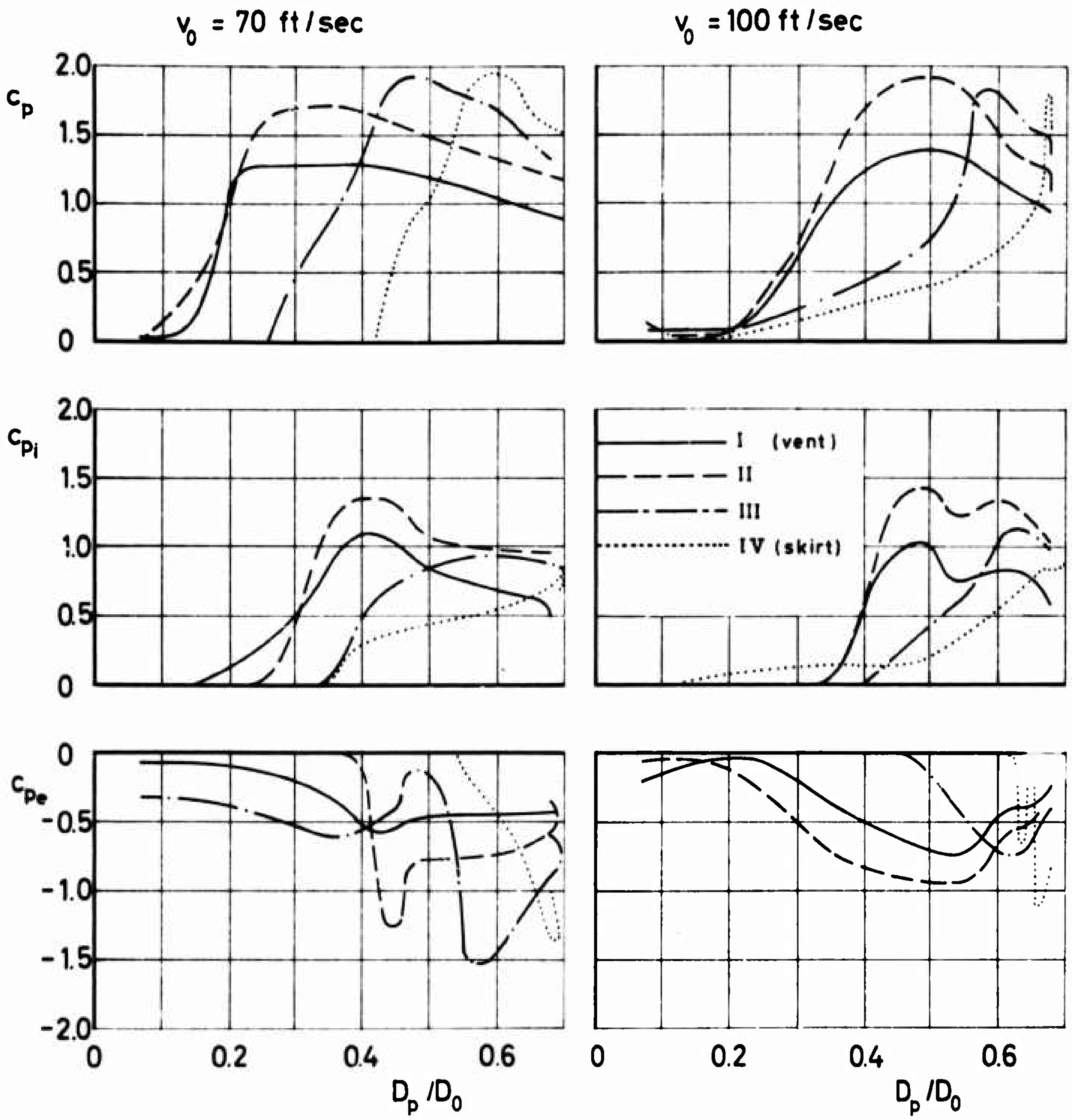

Figure 59 c_p versus D_p/D_0 for Ringslot

Run No. 7; 22; 24; 10; 30; 39

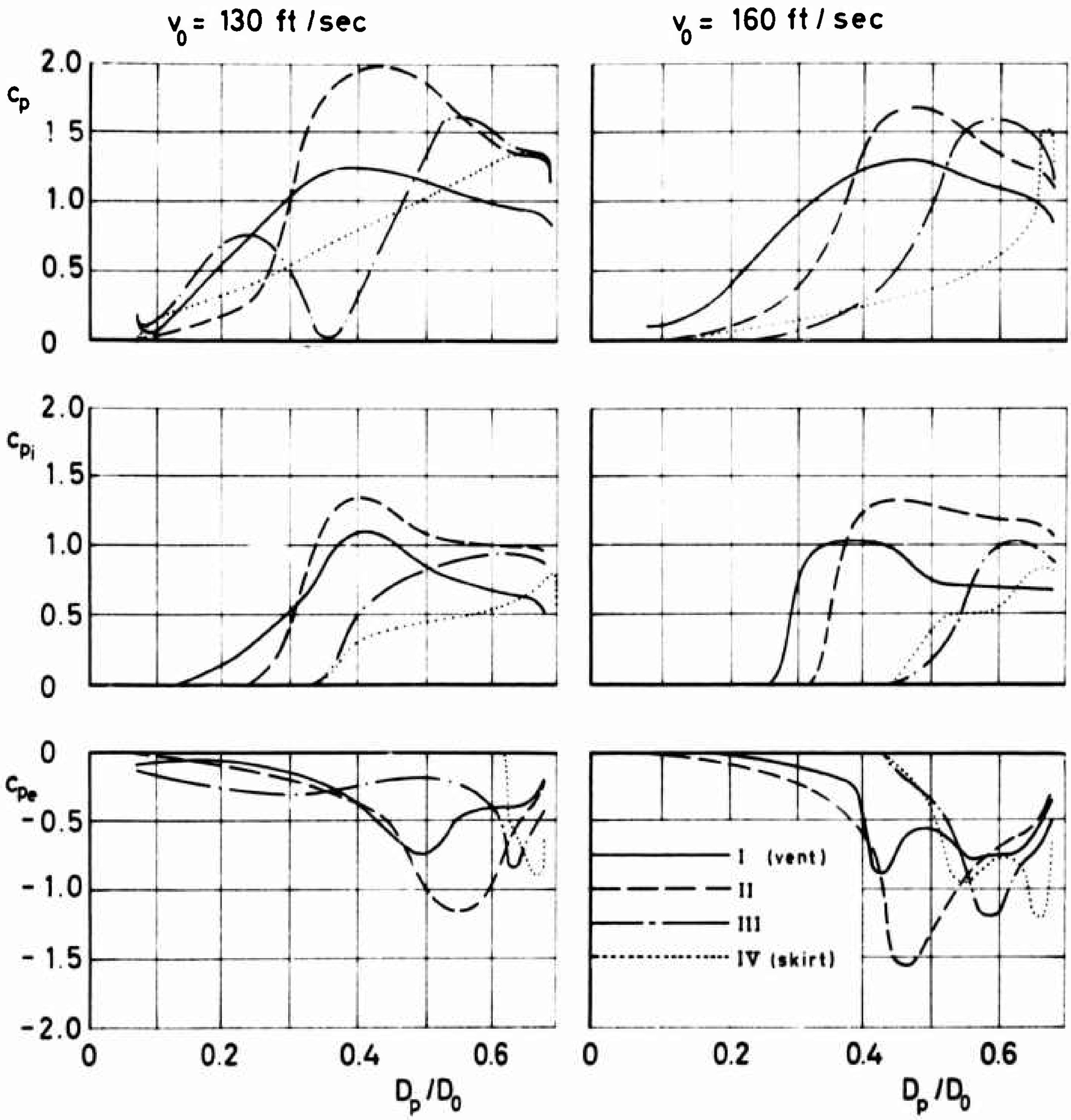

Figure 60 c_p versus D_p/D_0 for Ringslot

Run No. 14; 51; 42; 18; 26; 47

B. Canopy Shape Analysis

The objective of a "Shape Analysis" for the filling period of the parachute canopy was the mathematical description of the canopy shape as a function of time. Since the canopy is approximately rotational symmetric, it is sufficient to consider the profile views of the canopy.

To obtain representative profile views, specific frames of motion pictures taken from the side were analyzed. The profile views thus obtained yield a somewhat irregular and unsymmetric shape, as illustrated in Figures 61 and 62 by the solid lines which show an example for the circular flat type canopy. These shapes, however, can be graphically made symmetric, as is shown by the broken lines. The resulting shape shall be called the Symmetrized Photographic Shape.

This shape can be idealized in the following manner and then be described by means of specific parameters. This shape shall be called the Idealized Photographic Shape. The entire process of canopy filling may be divided into two phases. During Phase I, the canopy fills from the skirt towards the vent. The canopy shapes during this part of the filling period can then be described as consisting of four bodies of revolution depicted by the profile views in Figure 63:

1. A conical frustrum with lower base 2r, upper base 2a, and height ϱ ,

2. An added half-ellipsoid with major semi-axis a and minor semi-axis b,

3. An added cylinder,

4. And an added hemisphere. The height of the cylinder and added hemisphere along the axis of revolution is ϱ_*, and the diameter of the cylinder is $2r_*$.

At the time where

$$\rho_* = r_* - b\,(1 - \sqrt{1_* - r_*^2/a^2})$$

the cylinder disappears, and only the hemisphere remains added to the half-ellipsoid, meeting it with a secant equal to 2R. As defined by ρ_* and r_*, the radius of the hemisphere is then

$$r_\sim = (\sigma^2 + r_*^2)/2\sigma\,,$$

where

$$\sigma = \rho_* + b\,(1 - \sqrt{1 - r_*^2/a^2})$$

Phase II of the filling process begins at that point of time at which the canopy shape has assumed the shape of a conical frustrum to which is added a half-ellipsoid. From this point on the canopy fills from the vent towards the skirt. For the description of the canopy shape during this portion of the filling period, only four parameters are required: the lower base 2r, the upper base 2a, the height ρ of the conical frustrum, and the minor half-axis of the ellipsoid, b. During Phase II the canopy fills completely and opens with resulting rapid changes of 2r and 2a. Phase III may be defined as the steady state period in which the canopy shape no longer changes significantly and the values of each of the four parameters only fluctuate about their steady mean values.

An approximated description of the Idealized Photographic Shape as a function of time is possible by plotting the parameters of the shape versus time. For comparative purposes, the parameters are made dimensionless by dividing by the nominal canopy diameter, D_o. In addition, the time parameter is made dimensionless by dividing the time by a fictitious filling time t_*. This fictitious filling time is the time from burning the wire which held the leather clamps around the stretched-out canopy to the point where the steady state mean values of the parameters were reached for the first time.

The parameters of the idealized canopy shape are now made a function of t/t_*. With this, the Idealized Photographic Shape can be constructed for any value of t/t_* for any specific deployment condition and correlated with the pressure distribution for the same time t/t_*. Figures 64 thru 79 are plottings of the parameters of the Idealized Photographic Shape obtained by this method for the four types of parachute canopies. A qualitatively similar behavior can be seen for all four types of canopies.

The parameters $2a/D_o$, $2r/D_o$, b/D_o and ρ/D_o increase in value during Phase I, indicating a filling of the canopy from the skirt towards the vent with simultaneous enlargement of the shape. During Phase II the values of the parameters $2a/D_o$, $2r/D_o$ and b/D_o are increasing further until they reach the final steady state value at $t/t_* = 1$.

On the other hand, the value of the parameter ρ/D_o decreases after reaching a maximum value. By plotting all parameters for one type of canopy for the four different deployment speeds on one graph, all points for one parameter lie relatively close together as may be seen from Figures 80 thru 83. Therefore, it may be concluded that for the infinite mass case the development of the canopy shape is primarily dependent upon the dimensionless time ratio t/t_*. This agrees with findings by Berndt [5] which indicated that for the finite mass case the growth in projected canopy area as a function of the time ratio t/t_* follows an identical relationship for a given canopy type regardless of speed and altitude of deployment.

The spread of the measured points in Figures 80 thru 83 is probably due to the inexact reproducibility of the filling process of a parachute canopy.

Table 2 Approximations to the 4th power for phase II

$$f = a_o + a_1(t/t_e) + a_2(t/t_e)^2 + a_3(t/t_e)^3 + a_4(t/t_e)^4$$

		f	a_o	a_1	a_2	a_3	a_4
Circular Flat	v_o = 70 [ft/sec]	$2a/D_o$	-46.34	+217.05	-379.25	+294.50	-85.02
	t_e = 0.25 [sec]	$2r/D_o$	-120.12	+594.60	-1092.50	+884.51	-265.51
	0.72 = t/t_e = 1.00	b/D_o	-65.69	+309.04	-543.50	-423.51	-123.36
	Run No. 182	e/D_o	+61.72	-288.99	+508.67	-396.75	+115.42
	v_o = 100 [ft/sec]	$2a/D_o$	+56.84	-284.83	+531.73	-456.45	+133.42
	t_e = 0,20 [sec]	$2r/D_o$	+80.29	-395.86	+729.51	-594.03	+180.81
	0.70 = t/t_e = 100	b/D_o	+18.21	-85.69	+149.49	-113.91	+32.11
	Run No. 183	e/D_o	-49.59	-243.51	-441.61	+352.68	-104.92
	v_o = 130 [ft/sec]	$2a/D_o$	+3.64	-19.17	+38.77	-33.71	+11.[illegible]
	t_e = 0,16 [sec]	$2r/D_o$	-19.38	+98.14	-181.39	+146.26	-42.86
	0.69 = t/t_e = 1.00	b/D_o	-3.79	+18.01	-32.11	+26.15	-8.04
	Run No. 187	e/D_o	-4.21	+23.98	-46.29	+38.66	-12.06
	v_o = 160 [ft/sec]	$2a/D_o$	-18.14	+83.92	-141.37	+103.65	-27.35
	t_e = 0.14 [sec]	$2r/D_o$	+34.57	-169.80	+314.18	-258.92	+80.76
	0.64 = t/t_e = 1.00	b/D_o	-7.64	+40.04	-78.03	+67.47	-21.64
	Run No. 191	e/D_o	+10.54	-52.78	+101.90	-86.96	+27.38
Extended Skirt	v_o = 70 [ft/sec]	$2a/D_o$	-10.68	-60.42	-122.67	+108.67	-34.90
	t_e = 0.34 [sec]	$2r/D_o$	+5.32	-27.46	+55.40	-49.94	+17.54
	0.56 = t/t_e = 1.00	b/D_o	-1.64	+11.36	-26.42	+26.24	-9.30
	Run No. 139	e/D_o	+5.13	-27.86	+59.61	-55.24	+18.45
	v_o = 100 [ft/sec]	$2a/D_o$	-3.11	+19.36	-42.07	+40.62	-13.95
	t_e = 0.29 [sec]	$2r/D_o$	-6.81	+43.21	-97.39	+94.51	-32.68
	0.48 = t/t_e = 1.00	b/D_o	-1.62	+13.42	-35.38	+38.80	-14.98
	Run No. 144	e/D_o	-2.21	+10.11	-11.71	+2.50	+1.42
	v_o = 130 [ft/sec]	$2a/D_o$	-0.60	+3.52	-5.21	+3.59	-0.47
	t_e = 0.23 [sec]	$2r/D_o$	-4.41	+26.56	-55.11	+48.89	-15.09
	0.48 = t/t_e = 1.00	b/D_o	-1.91	+12.11	-27.47	+27.51	-9.97
	Run No. 148	e/D_o	-1.96	+10.79	-17.13	+10.70	-2.30
	v_o = 160 [ft/sec]	$2a/D_o$	+9.58	-56.65	+124.29	-117.15	+40.71
	t_e = 0.21 [sec]	$2r/D_o$	+17.57	-98.64	+206.45	-188.95	+64.38
	0.52 = t/t_e = 1.00	b/D_o	-3.68	+21.96	-48.47	+47.55	-17.10
	Run No. 153	e/D_o	-0.80	+6.02	-9.51	+5.05	-0.62
FIST	v_o = 70 [ft/sec]	$2a/D_o$	-7.06	+38.82	-75.99	+65.86	-20.94
	t_e = 0.36 [sec]	$2r/D_o$	+0,54	+0,55	-5.54	+9.56	-4.41
	0.50 = t/t_e = 1.00	b/D_o	-2.14	+11.51	-21.78	+18.10	-5.52
	Run No. 72	e/D_o	+3.28	-17.98	+38.22	-34.87	+11.43
	v_o = 100 [ft/sec]	$2a/D_o$	-4.62	+25.04	-47.79	+40.91	-12.88
	t_e = 0.26 [sec]	$2r/D_o$	-0.65	+6.27	-16.31	+18.36	-6.99
	0.50 = t/t_e = 1.00	b/D_o	-2.36	+12.42	-23.36	+19.53	-6.05
	Run No. 76	e/D_o	-0.10	+1.75	-2.40	+0.62	+0.22
	v_o = 130 [ft/sec]	$2a/D_o$	-3.27	+21.60	-50.76	+53.34	-20.23
	t_e = 0.22 [sec]	$2r/D_o$	-4.03	+29.37	-73.50	+79.11	-30.24
	0.50 = t/t_e = 1.00	b/D_o	-6.07	+36.20	-78.25	+73.67	-25.39
	Run No. 82	e/D_o	+8.78	-49.33	+105.94	-99.65	+34.34
	v_o = 160 [ft/sec]	$2a/D_o$	+1.39	-4.90	+6.50	-2.05	-0.25
	t_e = 0.20 [sec]	$2r/D_o$	-13.49	+74.86	-150.53	+132.34	-42.48
	0.55 = t/t_e = 1.00	b/D_o	-0.59	+5.05	-12.81	+13.71	-5.16
	Run No. 86	e/D_o	-1.25	+6.54	-8.99	+3.91	-0.11
Ringslot	v_c = 70 [ft/sec]	$2a/D_o$	-0.64	+4.37	-8.92	+9.91	-4.04
	t_e = 0.42 [sec]	$2r/D_o$	+1.52	-7.46	+14.40	-9.83	+2.07
	0,52 = t/t_e = 1.00	b/D_o	-4.46	+24.39	-48.46	+42.38	-13.67
	Run No. 7	e/D_o	+0.98	-4.56	+11.04	-12.06	+4.67
	v_o = 100 [ft/sec]	$2a/D_o$	+2.12	-12.85	+30.23	-27.97	+9.09
	t_e = 0.32 [sec]	$2r/D_o$	+3.54	-21.22	+48.54	-45.56	+15.35
	0.40 = t/t_e = 1.00	b/D_o	-1.08	+8.24	-21.52	+24.37	-9.86
	Run No. 10	e/D_o	-1.67	+10.74	-20.55	+15.37	-3.77
	v_o = 130 [ft/sec]	$2a/D_o$	+3.23	-19.94	+47.81	-46.59	+16.13
	t_e = 0.29 [sec]	$2r/D_o$	+2.49	-15.06	+36.53	-35.82	+12[illegible]3
	0.41 = t/t_e = 1.00	b/D_o	+8.34	-49.90	+109.95	-104.07	+35.83
	Run No. 14	e/D_o	-5.28	+34.77	-78.96	+75.98	-26.41
	v_o = 160 [ft/sec]	$2a/D_o$	+0.38	-2.70	+11.63	-14.75	+6.06
	t_e = 0.25 [sec]	$2r/D_o$	+1.08	-6.64	+18.59	-19.11	+6.75
	0.28 = t/t_e = 1.00	b/D_o	+0.15	-0.67	+2.57	-3.27	+1.33
	Run No. 18	e/D_o	+0.16	+1.29	-4.78	+5.65	-2.20

The parameters of the Idealized Photographic Shape can also be mathematically expressed as a function of t/t_* forming a polynomial in t/t_*. The coefficients of this polynomial are obtained by the method of least squares.

A regression to the fourth power was made for Phase II of the filling process for all four types of parachute canopies and for the four deployment velocities. Table II shows the results for each parameter in the form

$$f = a_0 + a_1 \, t/t_* + a_2 \, (t/t_*)^2 + a_3 \, (t/t_*)^3 + a_4 \, (t/t_*)^4$$

The shape can be described approximately by the parameters of the Idealized Photographic Shape stated in graphic form or in terms of a polynomial.

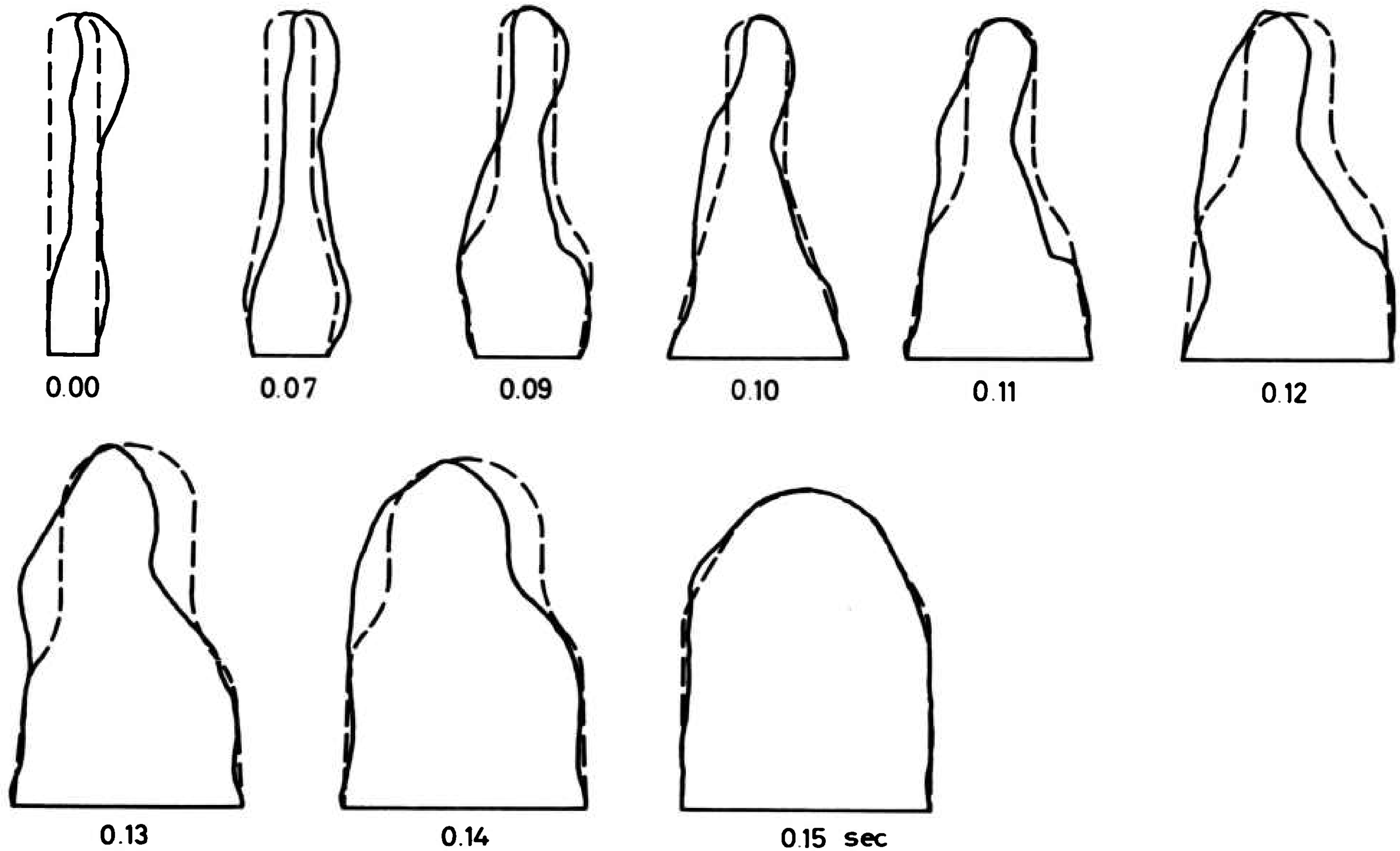

Figure 61 Photographic Shape (– – – –symmetrized) Phase I for Circular Flat, v_0 = 70 ft/sec, Run No. 194

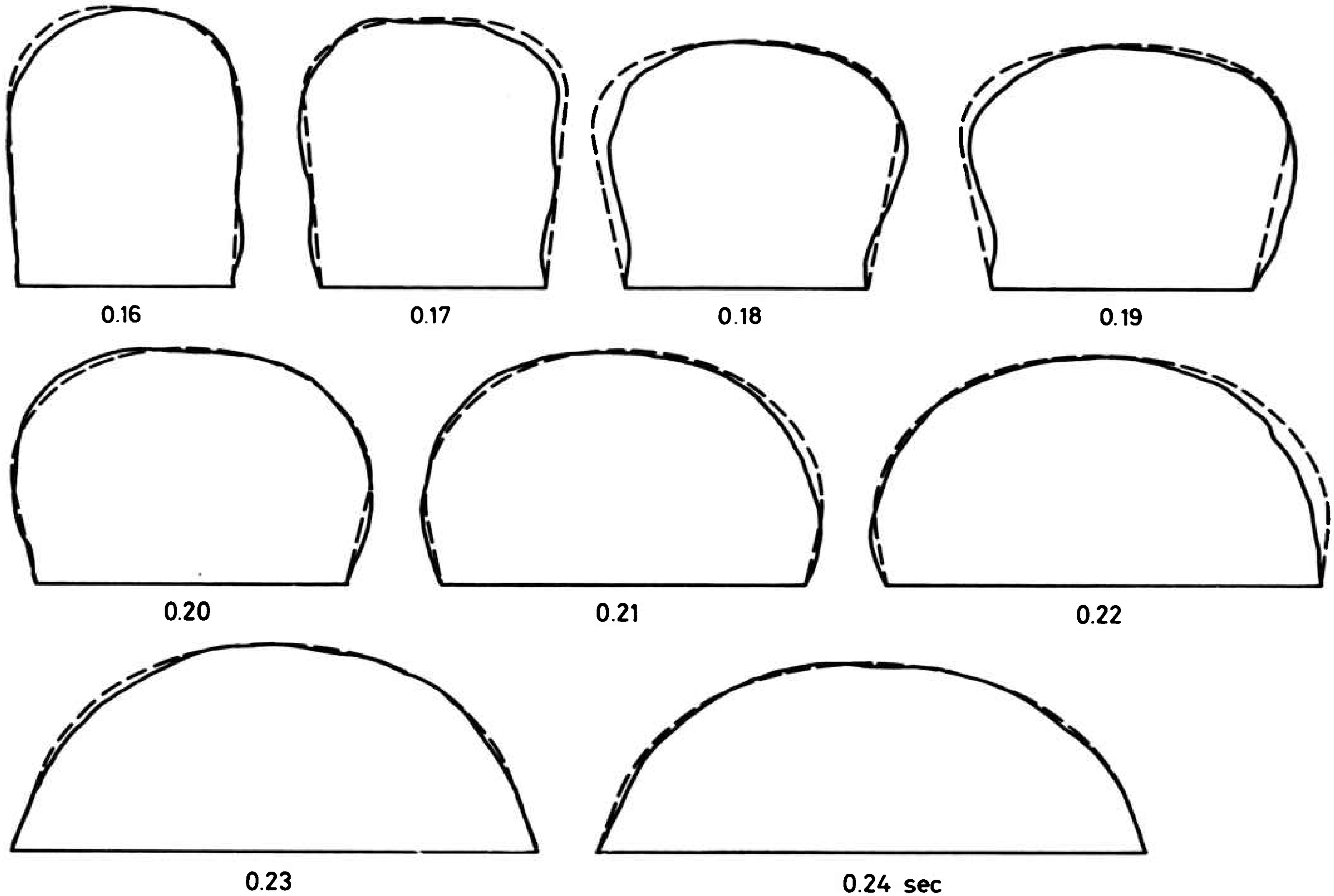

Figure 62 Photographic Shape (————symmetrized) Phase II for Circular Flat, $v_0 = 70$ ft/sec, Run No. 194

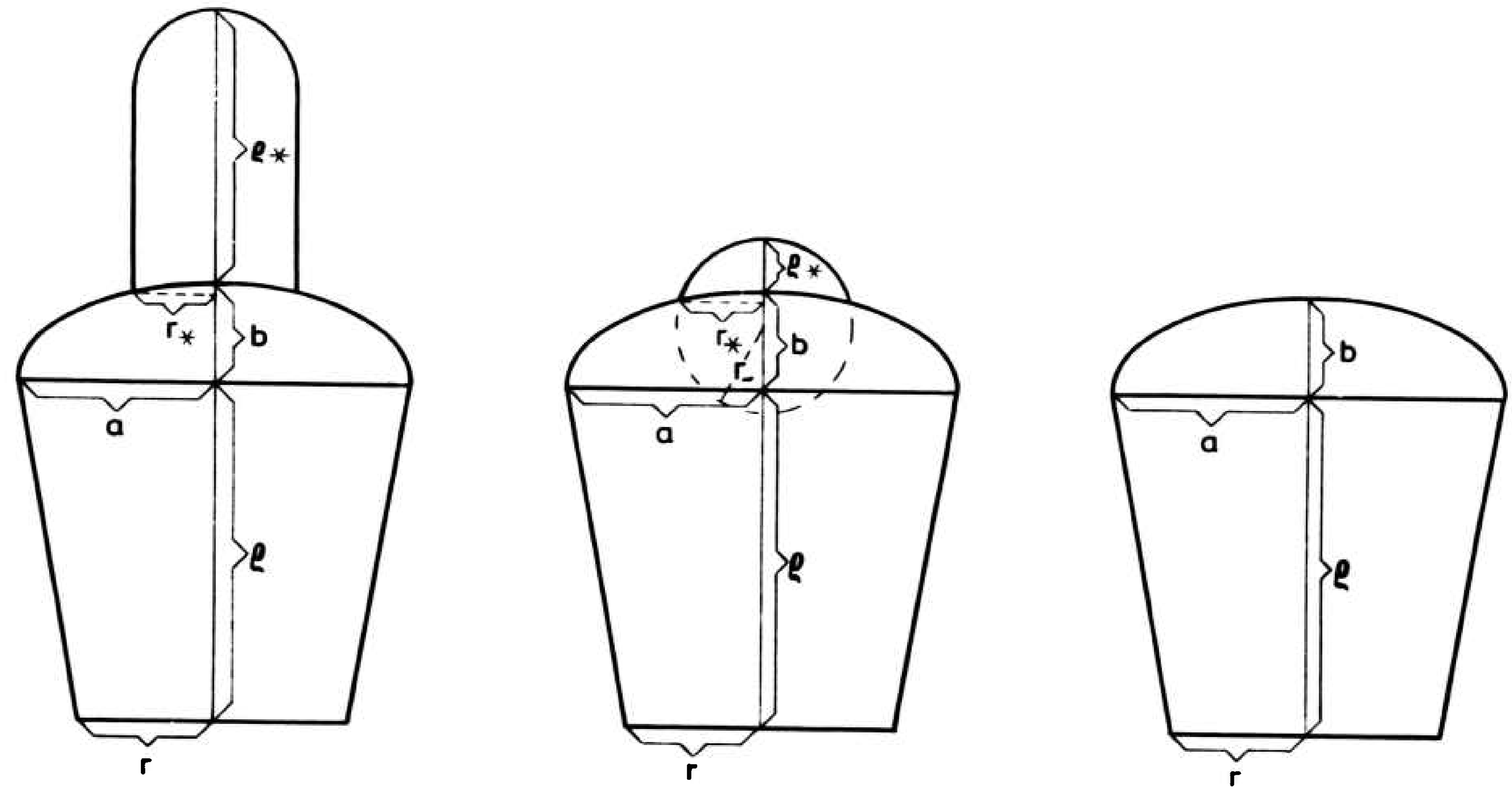

Phase I | Phase I | Phase II

$\ell_* > r_* - b\left(1-\sqrt{1-\frac{r_*^2}{a^2}}\right)$ | $\ell_* \leq r_* - b\left(1-\sqrt{1-\frac{r_*^2}{a^2}}\right)$

Figure 63 Idealized Photographic Shape Symbols

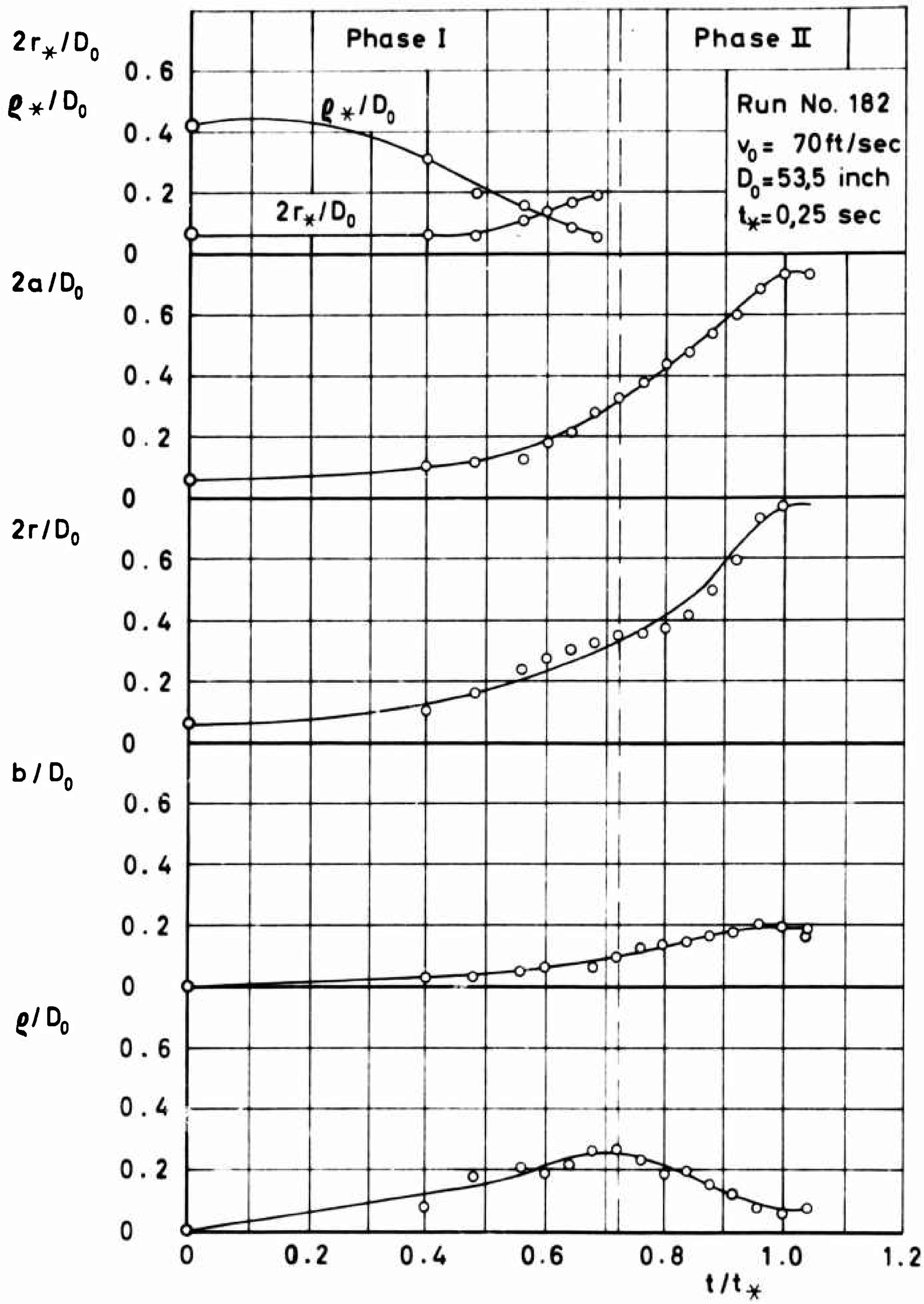

Figure 64 Parameters of Idealized Photographic Shape Versus Time for Circular Flat

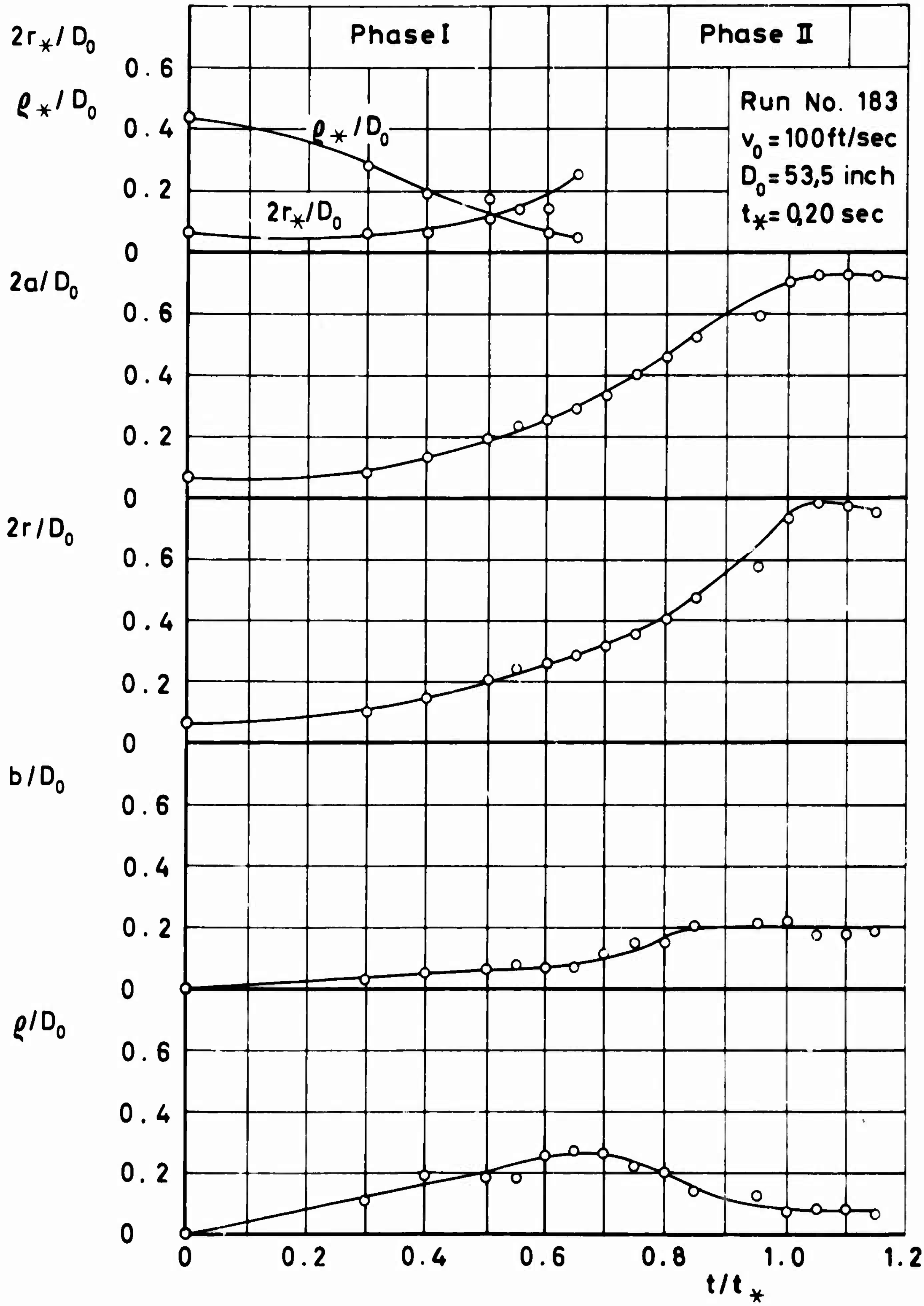

Figure 65 Parameters of Idealized Photographic Shape Versus Time for Circular Flat

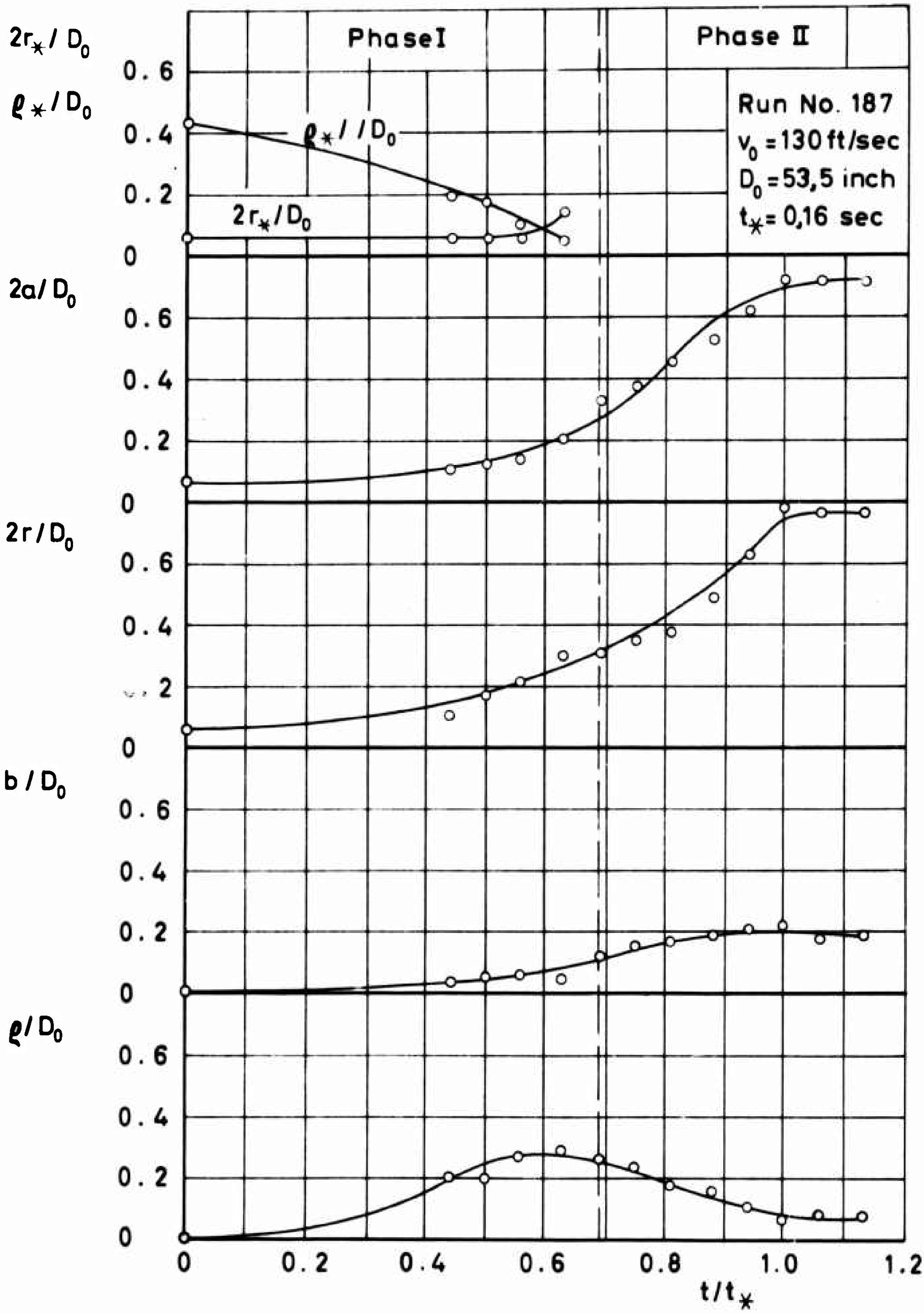

Figure 66 Parameters of Idealized Photographic Shape Versus Time for Cir⌐ ılar Flat

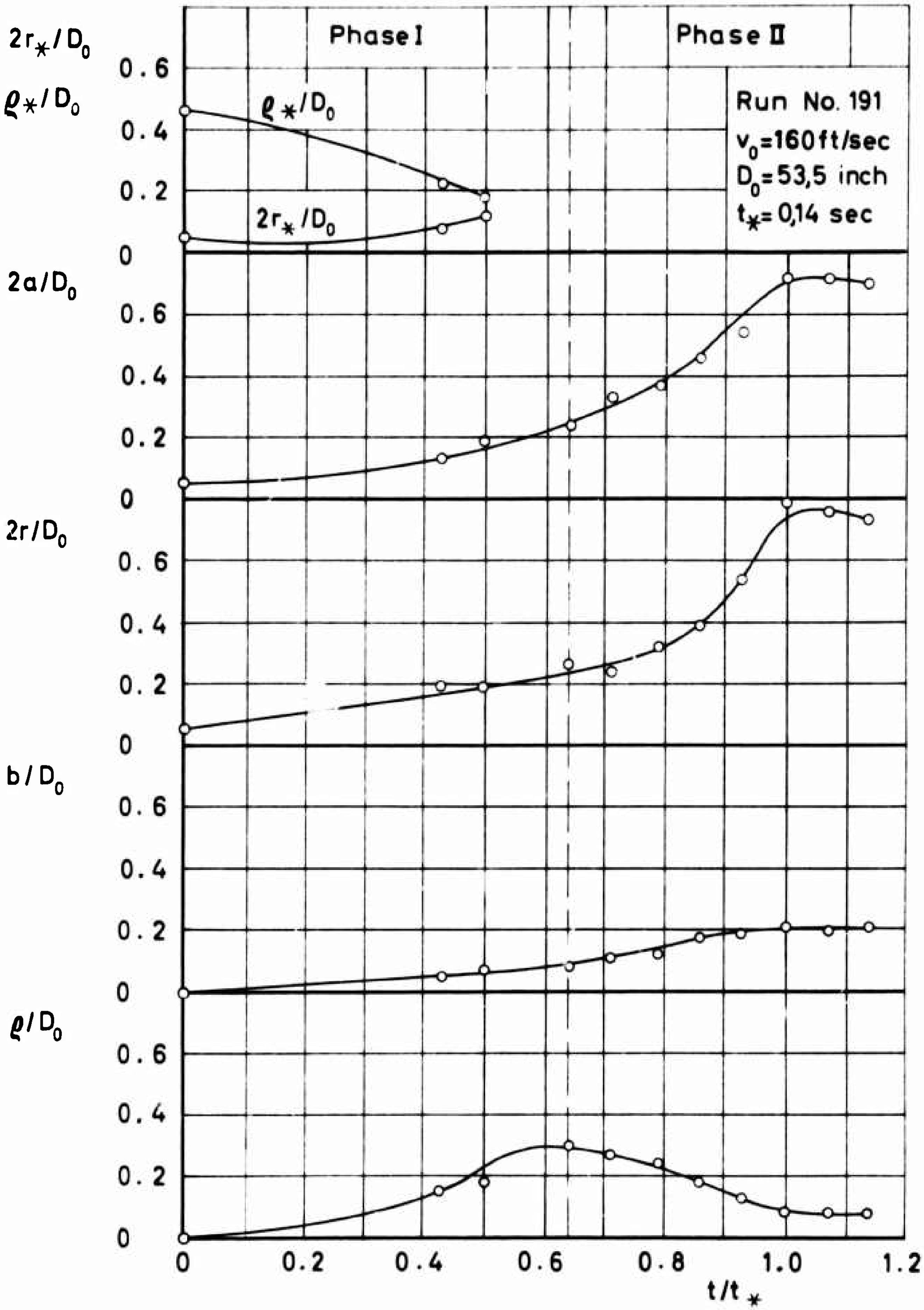

Figure 67 Parameters of Idealized Photographic Shape Versus Time for Circular Flat

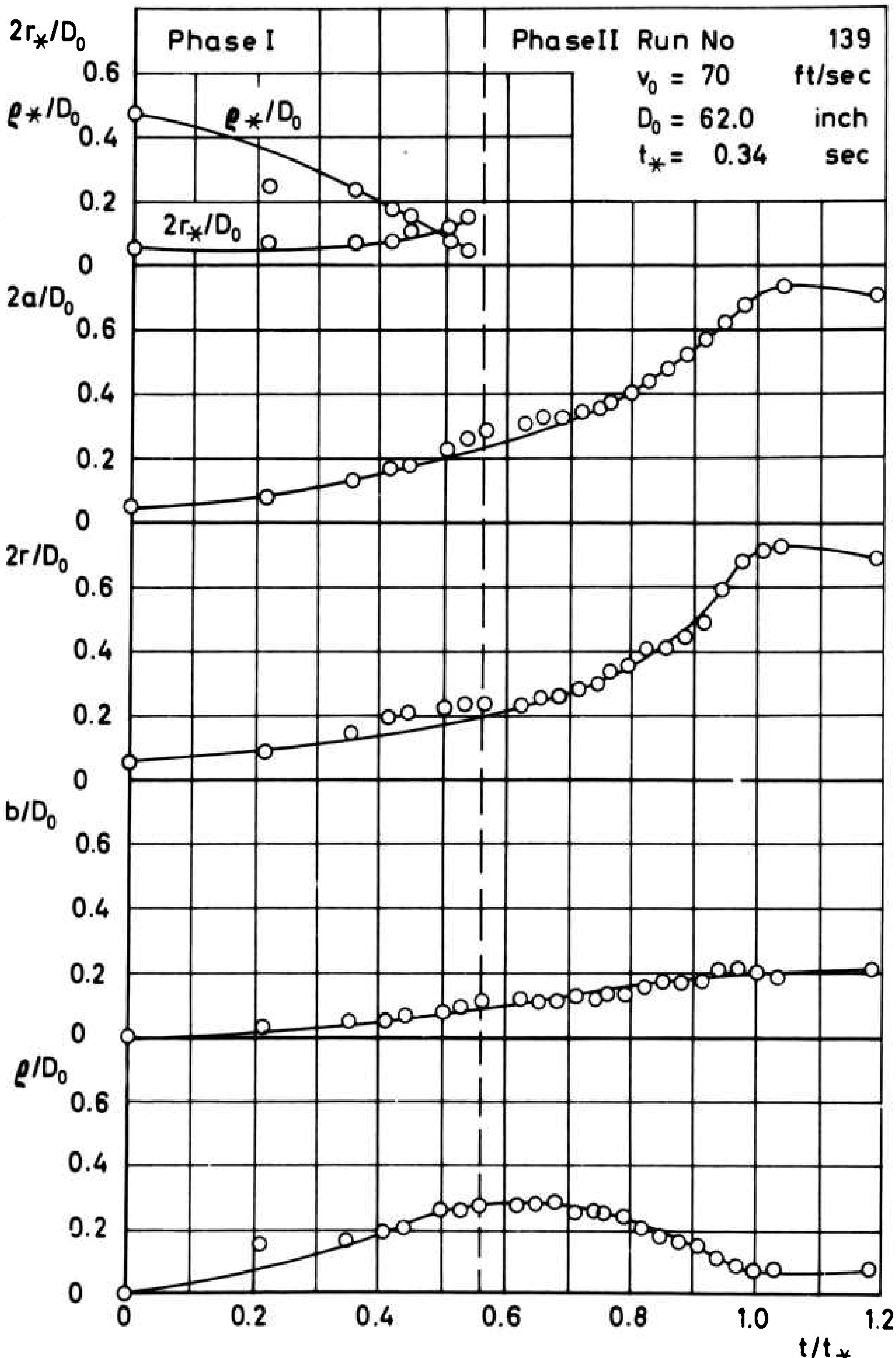

Figure 68 Parameters of Idealized Photographic Shape Versus Time for Extended Skirt

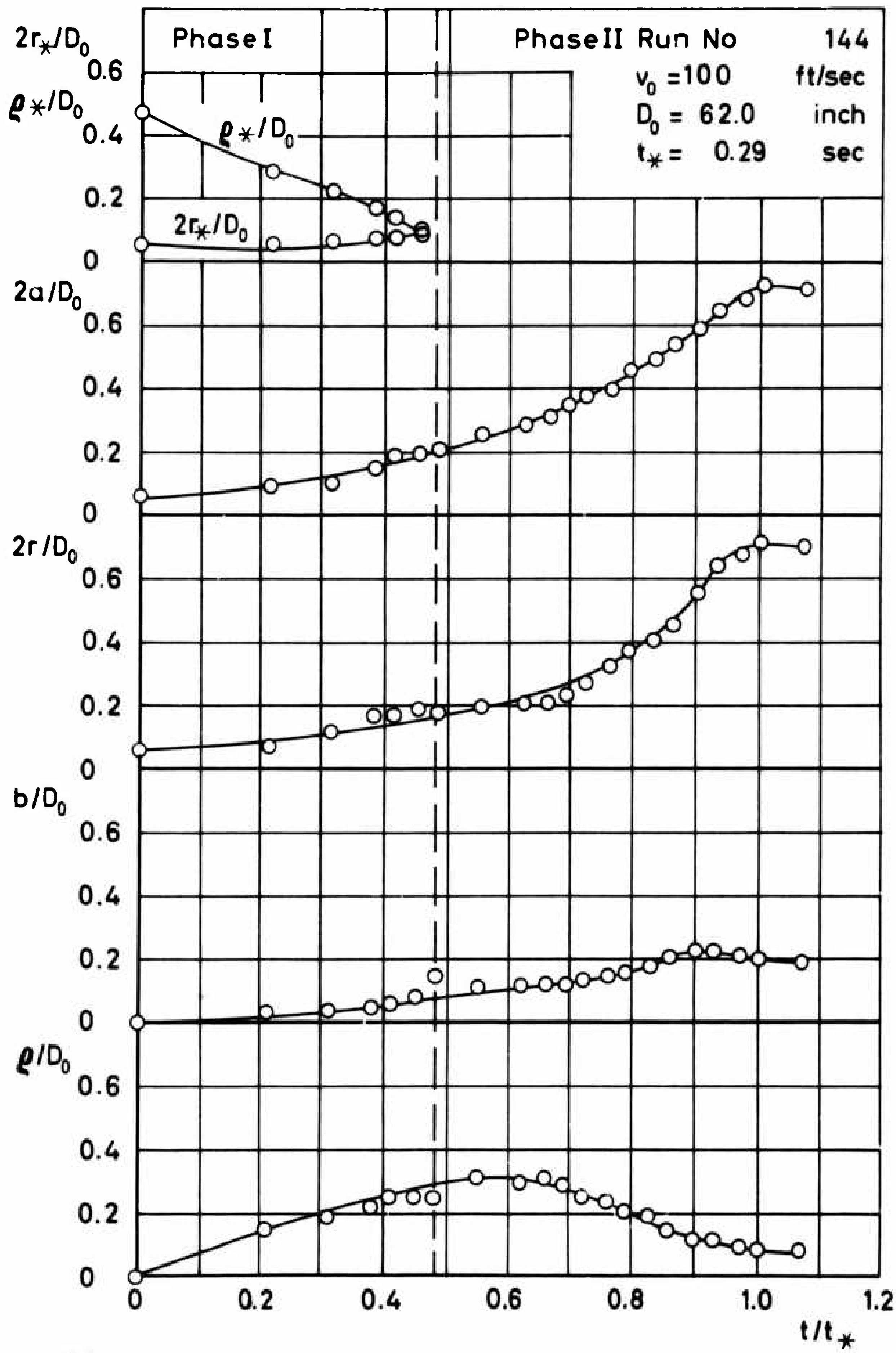

Figure 69 Parameters of Idealized Photographic Shape Versus Time for Extended Skirt

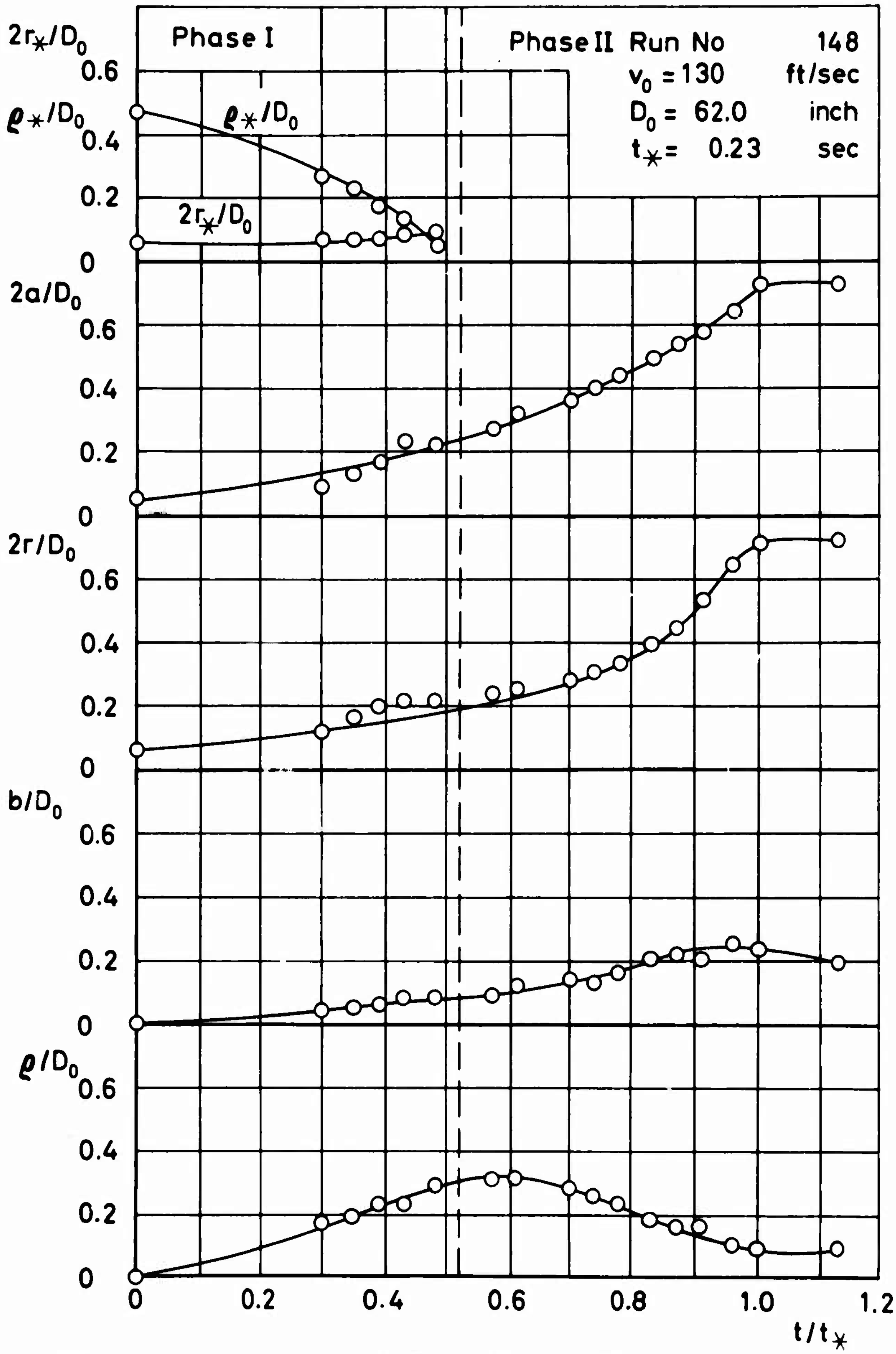

Figure 70 Parameters of Idealized Photographic Shape Versus Time for Extended Skirt

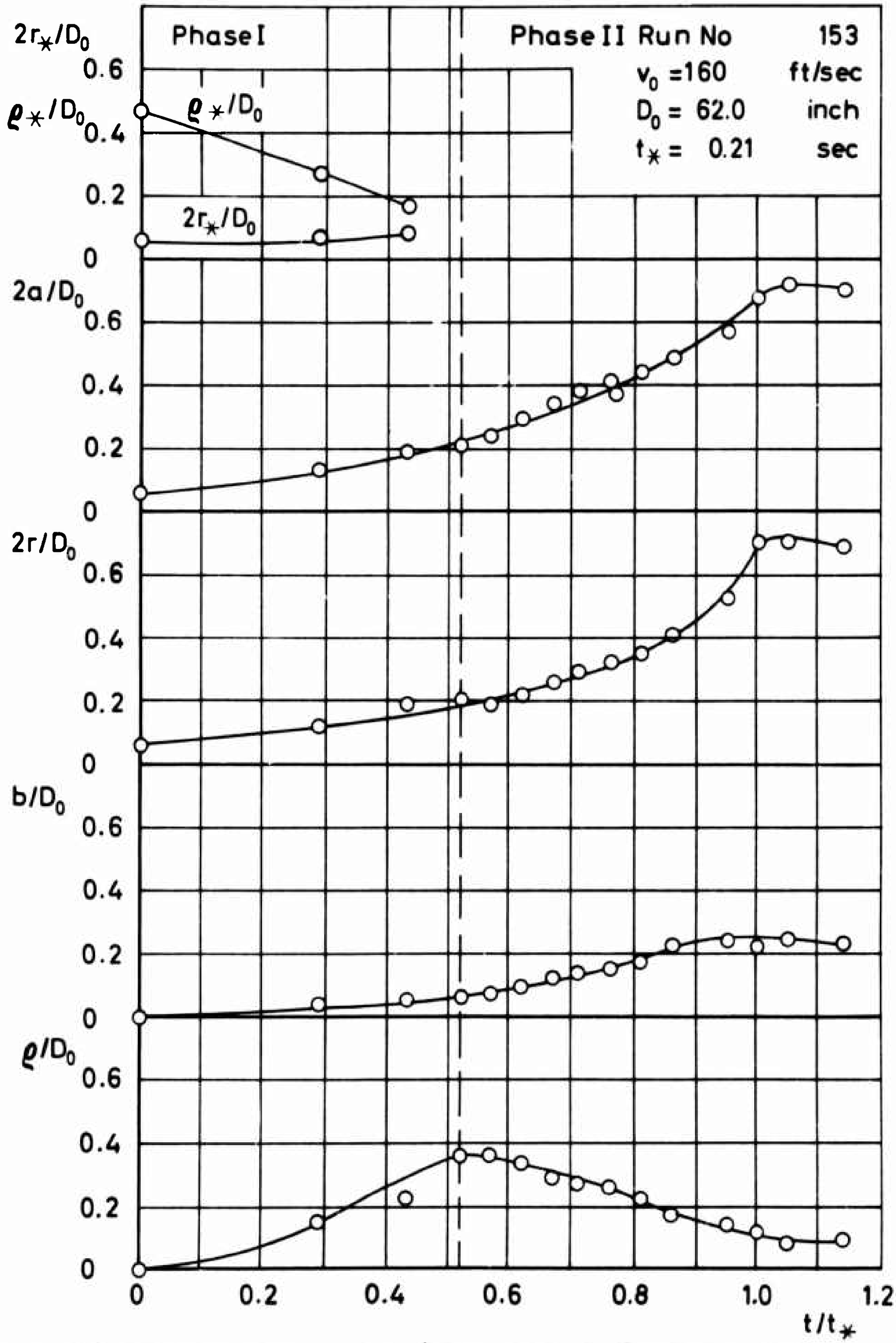

Figure 71 Parameters of Idealized Photographic Shape Versus Time for Extended Skirt

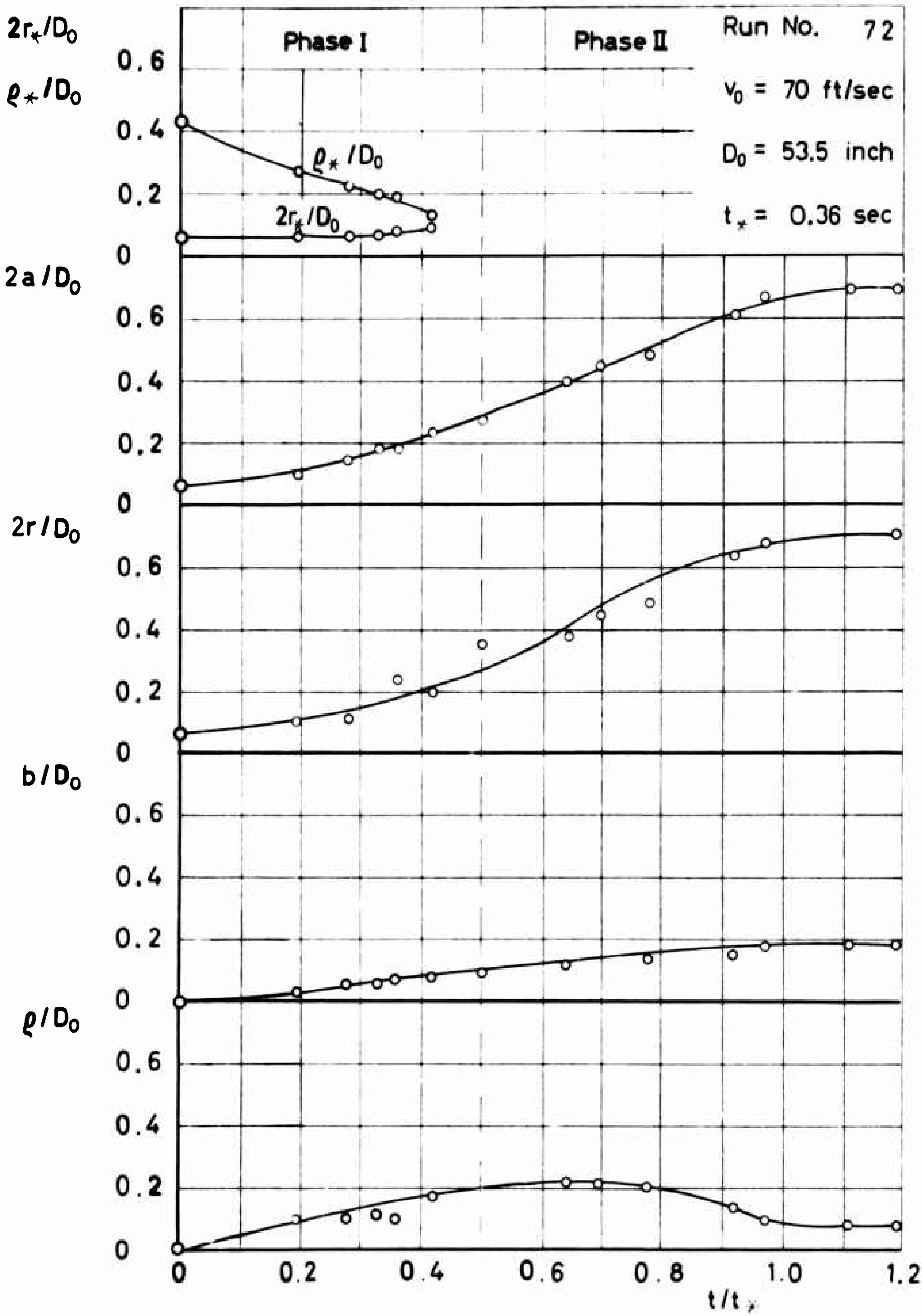

Figure 72 Parameters of Idealized Photographic Shape Versus Time for FIST

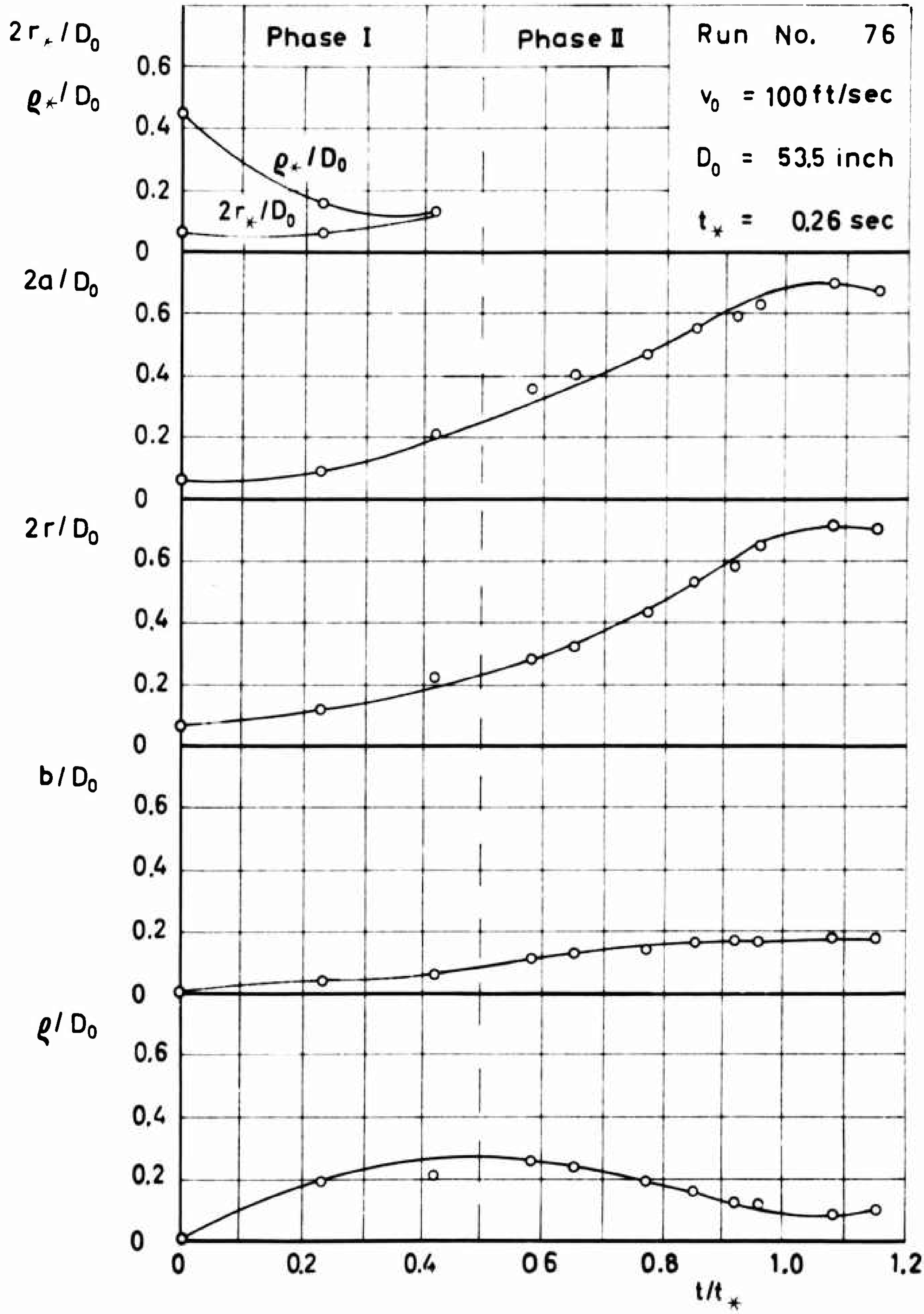

Figure 73 Parameters of Idealized Photographic Shape Versus Time for FIST

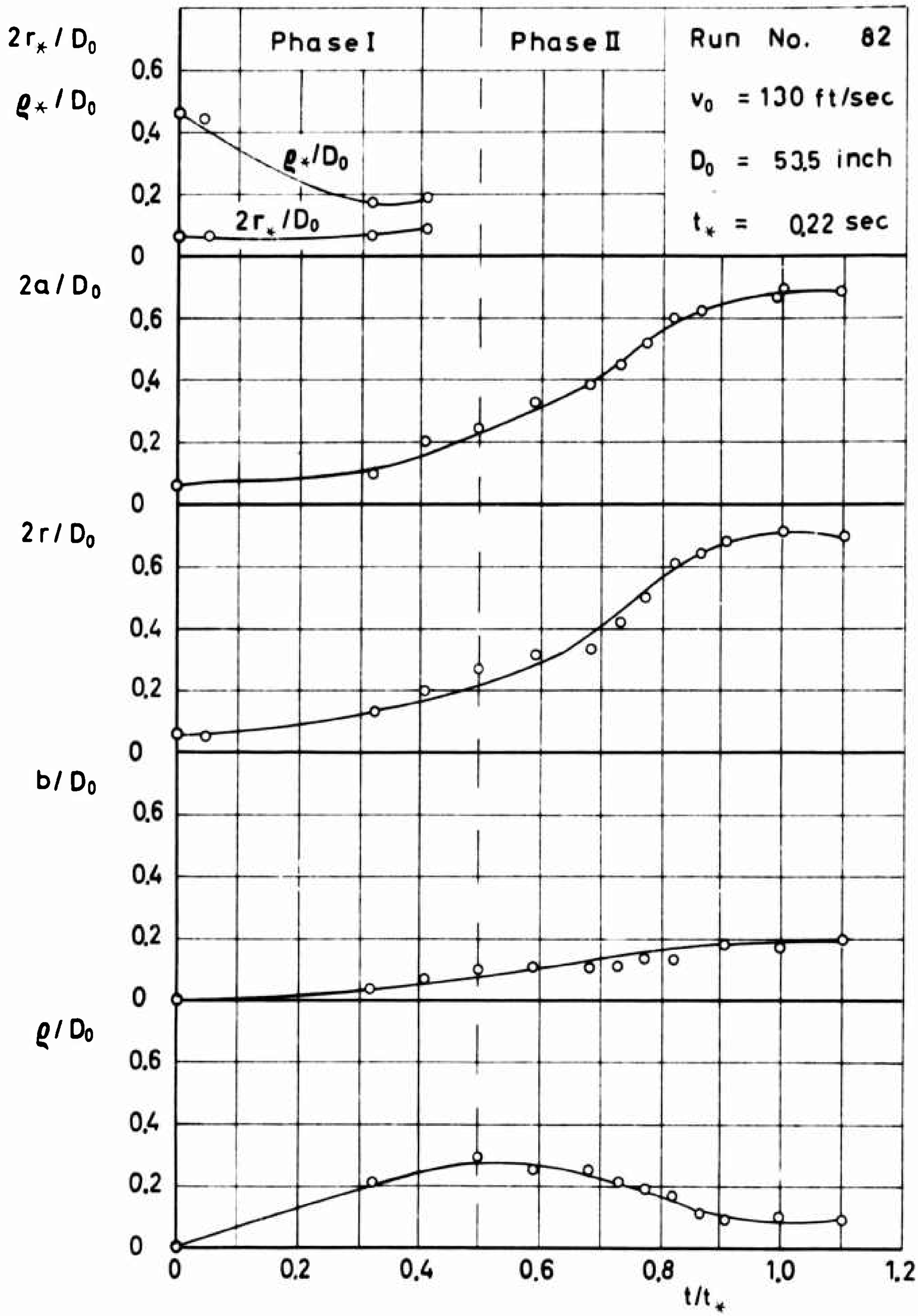

Figure 74 Parameters of Idealized Photographic Shape Versus Time for FIST

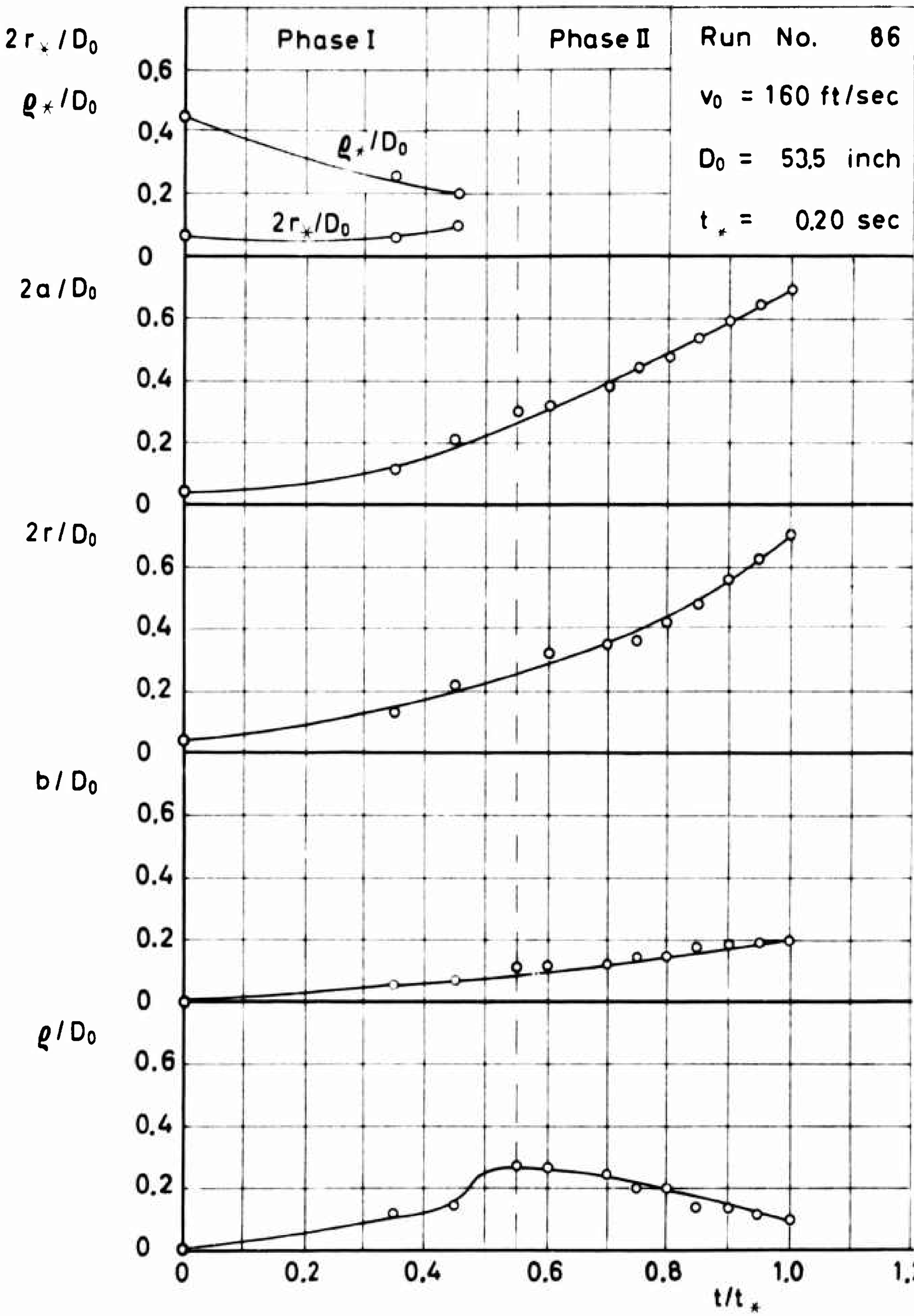

Figure 75 Parameters of Idealized Photographic Shape Versus Time for FIST

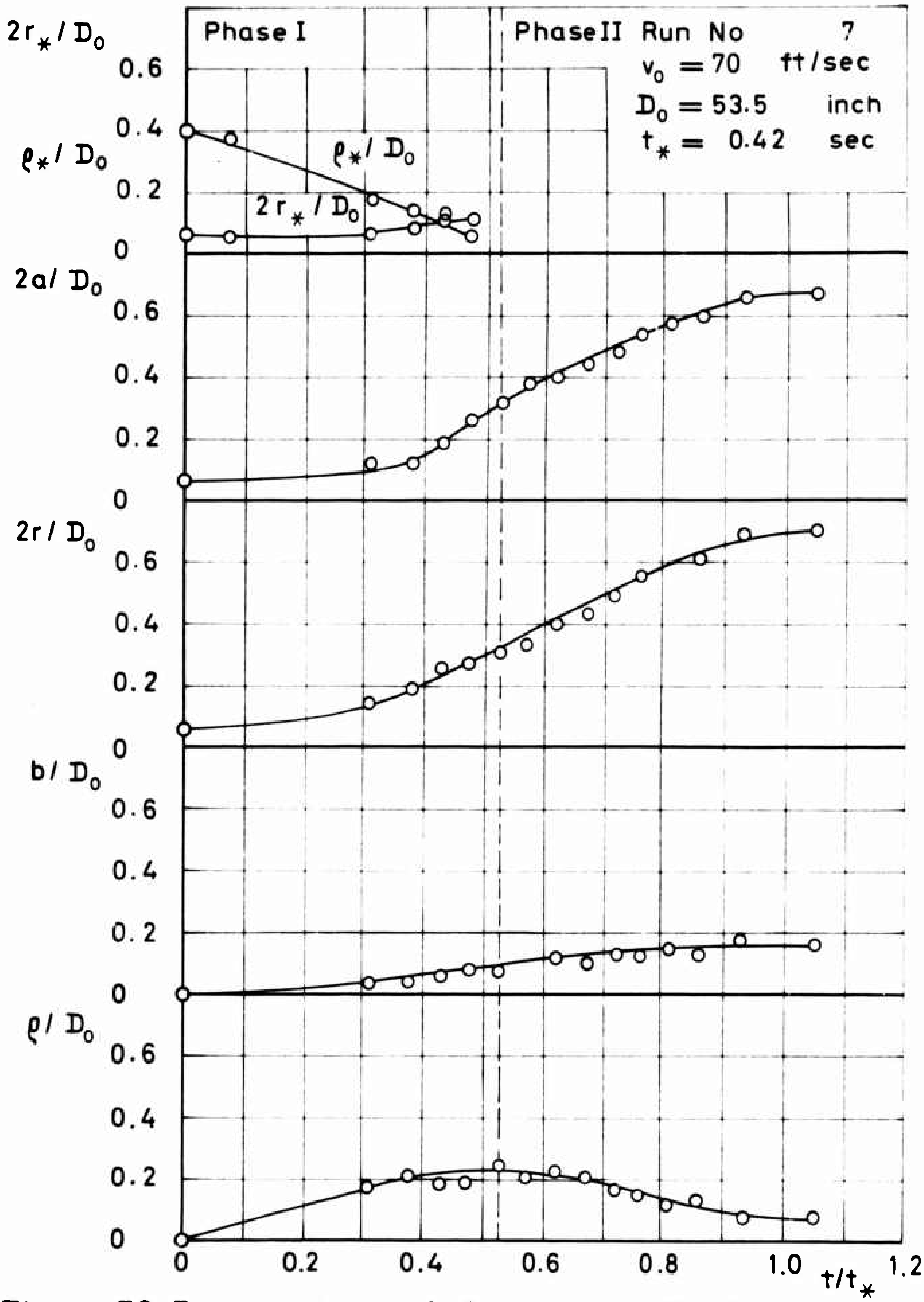

Figure 76 Parameters of Idealized Photographic Shape Versus Time for Ringslot

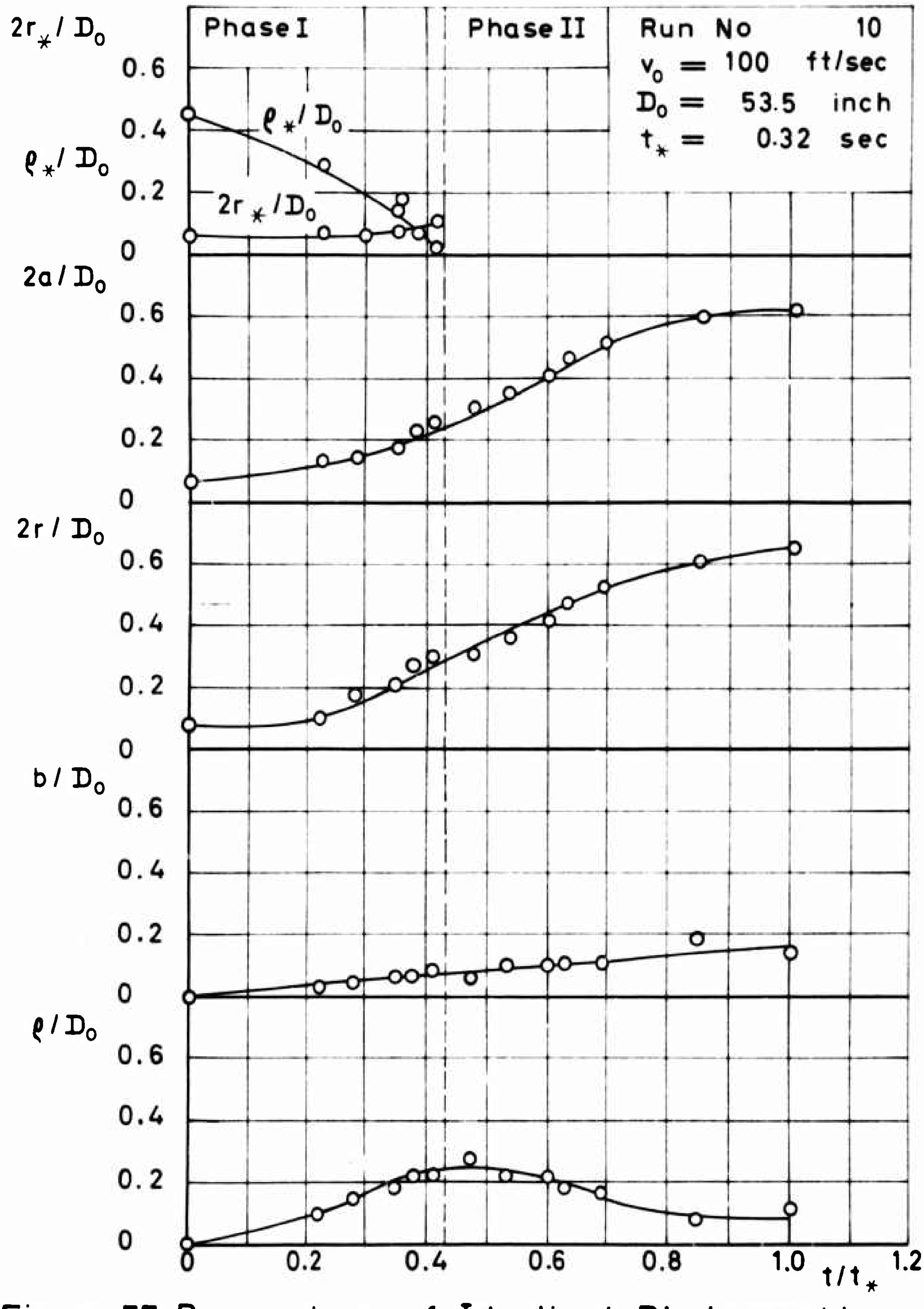

Figure 77 Parameters of Idealized Photographic Shape Versus Time for Ringslot

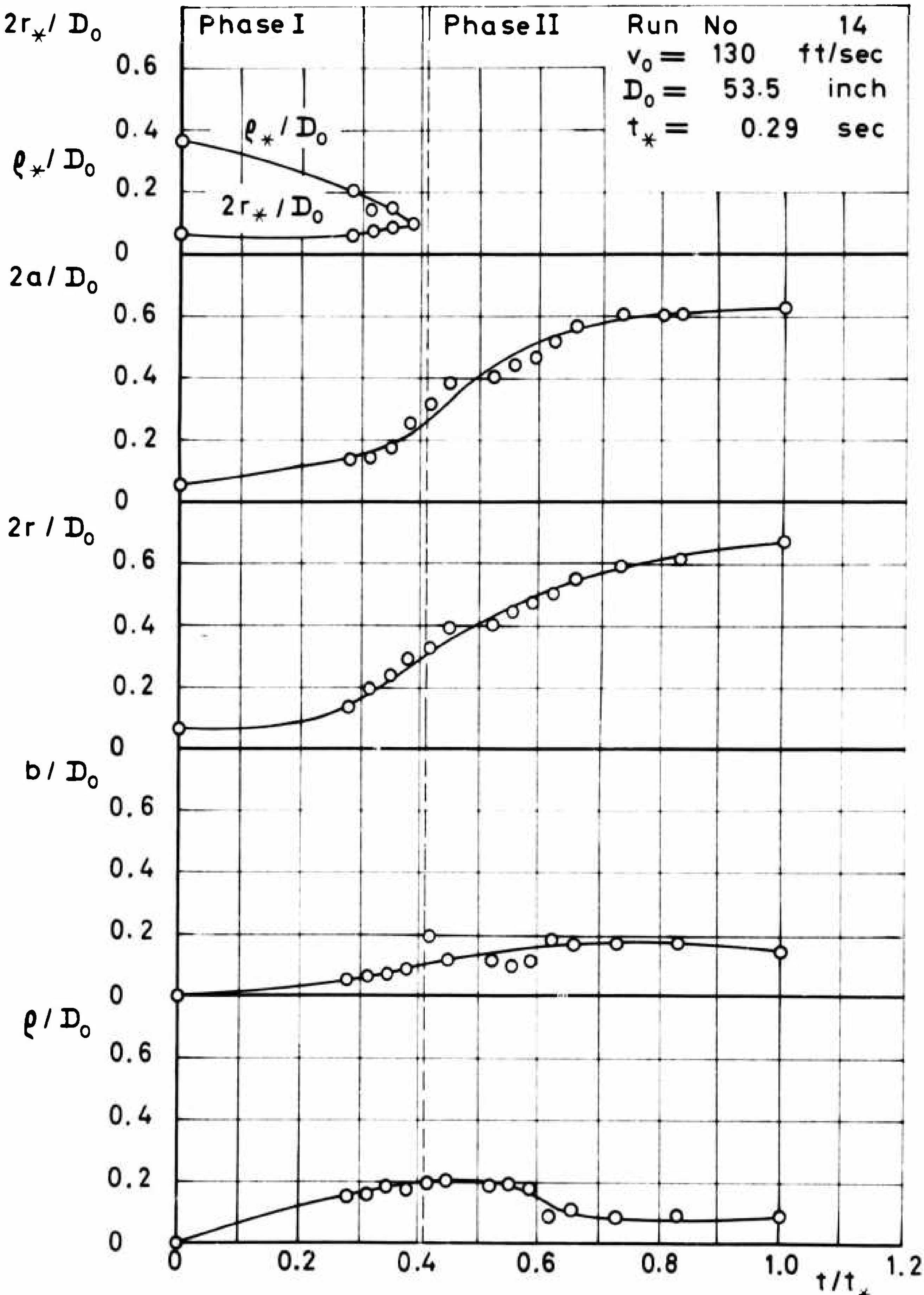

Figure 78 Parameters of Idealized Photographic Shape Versus Time for Ringslot

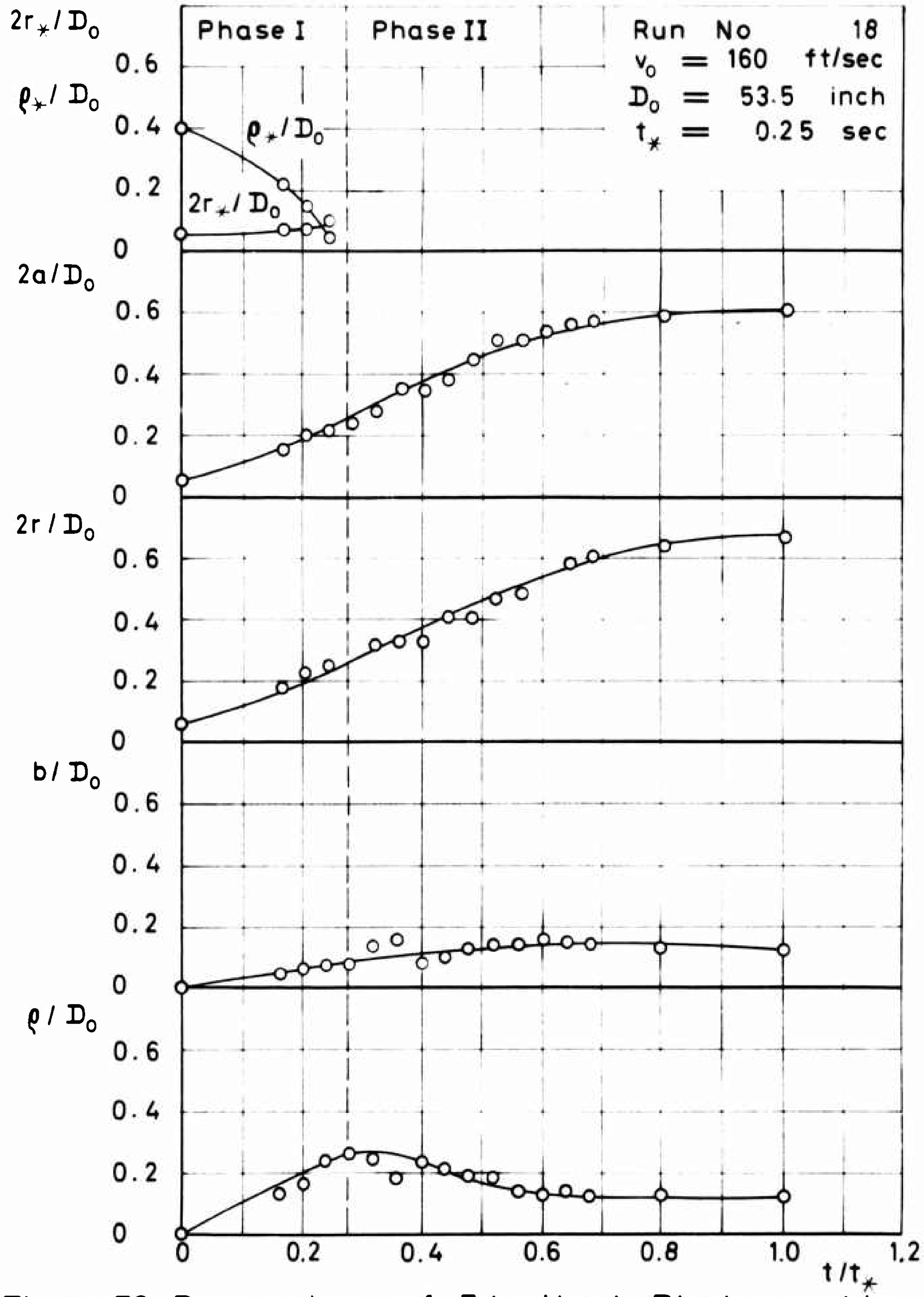

Figure 79 Parameters of Idealized Photographic Shape Versus Time for Ringslot

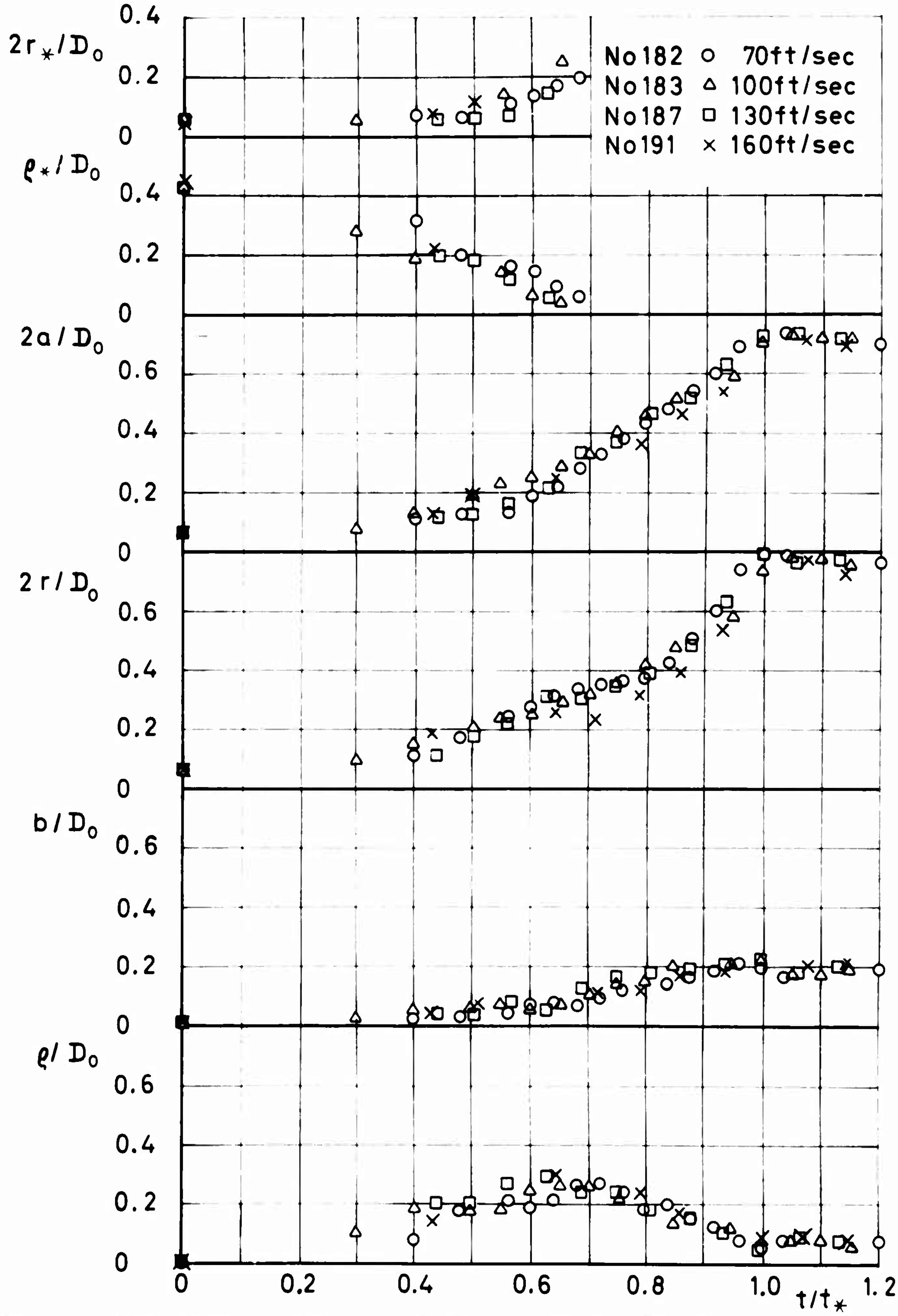

Figure 80 Parameters of Idealized Photographic Shape Versus Time for Circular Flat

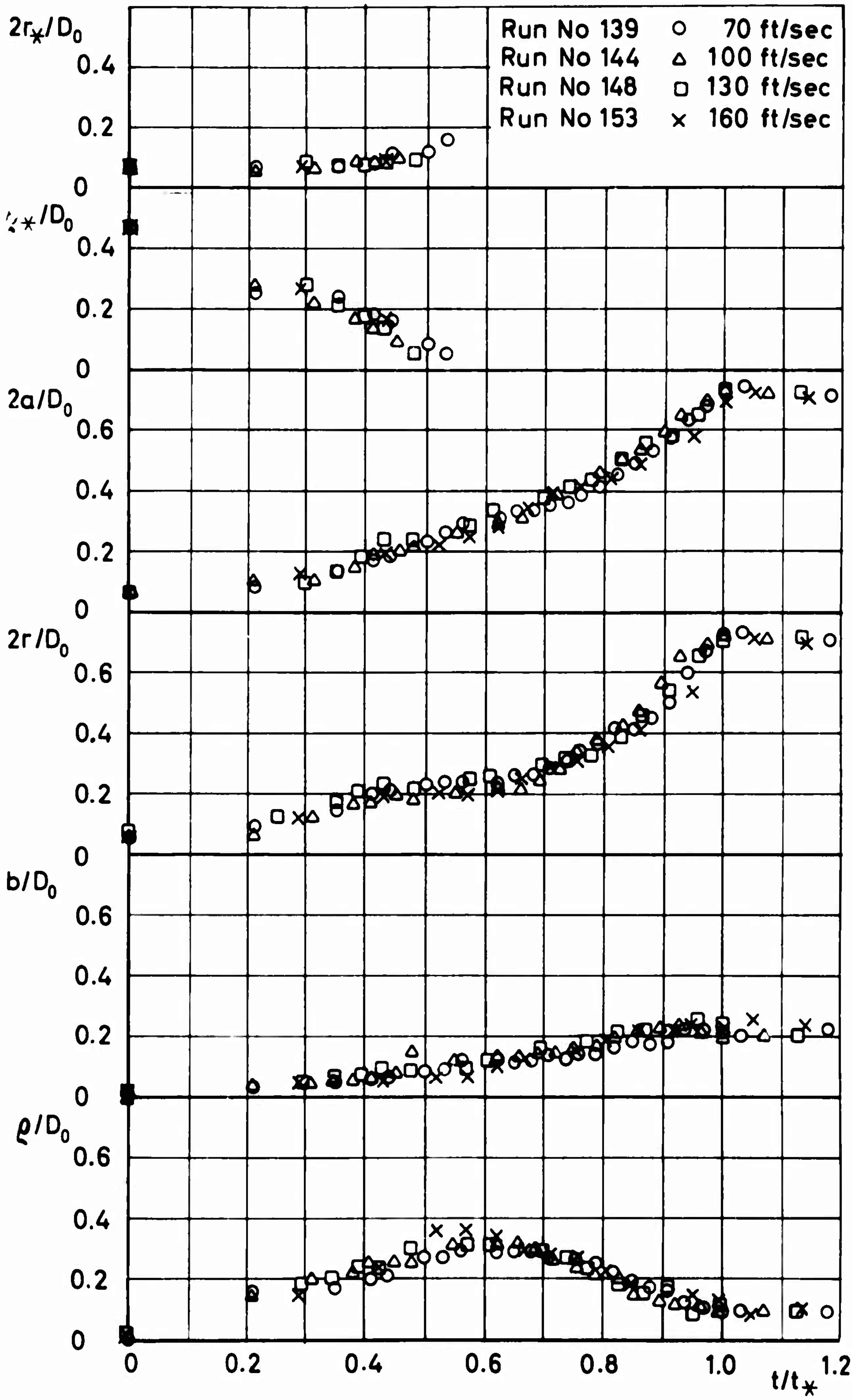

Figure 81 Parameters of Idealized Photographic Shape Versus Time for Extended Skirt

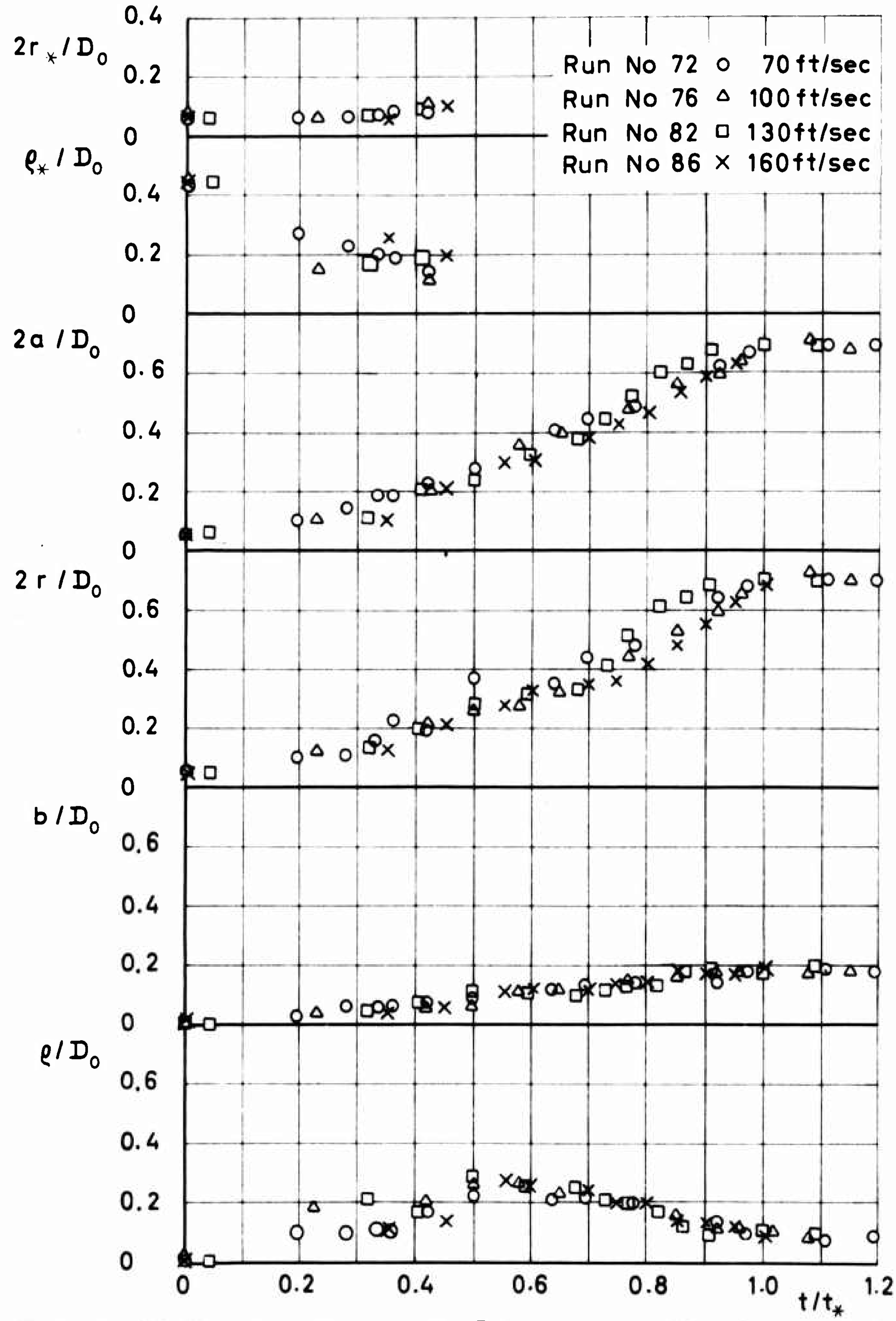

Figure 82 Parameters of Idealized Photographic Shape Versus Time for FIST

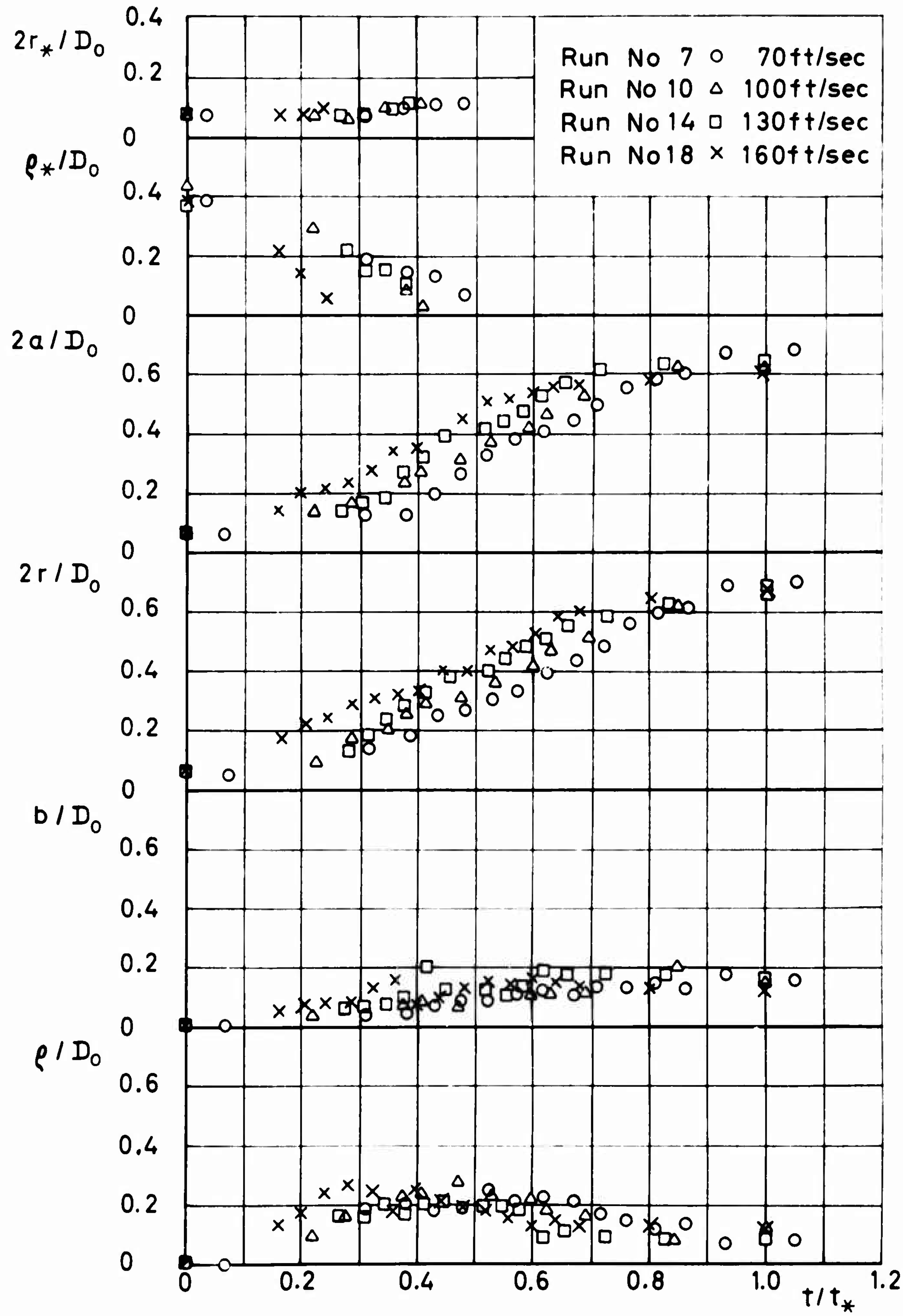

Figure 83 Parameters of Idealized Photographic Shape Versus Time for Ringslot

4. SUMMARY AND RECOMMENDATIONS

The change of the pressure distribution over the surface of four different types of parachute canopies during the period of inflation was experimentally determined for the infinite mass operating condition during low speed wind tunnel tests. The changing canopy shape during inflation was also determined and correlated to the changing pressures.

The results are presented in detail and provide for the first time a good knowledge of this vital relationship. In order to develop an analytical relationship between the changing pressure and the changing canopy shape, many more experimental tests will be required. These are necessary to eliminate abnormal variations in test conditions and canopy deployment.

In order to substantiate the findings obtained on canopy models, additional measurements of the dynamic pressure distribution should be performed on full scale canopies during free-flight tests.

For the finite mass operating case, quite different results and relationships may be expected. The two different operating modes should therefore be separated during further investigations.

5. REFERENCES

[1] Jones, R. A., On the Aerodynamic Characteristics of Parachutes. British ARC Report R & M No 862, June 1923.

[2] Topping, A. D. et al., A Study of Canopy Shapes and Stresses for Parachutes in Steady Descent. WADC-TR-55-294, Oct. 1955.

[3] Heinrich, H. G., Jamison L. R., Parachute Stress Analysis During Inflation and at Steady State. AIAA Entry Technology Conference, Williamsburg, Oct. 1964.

[4] Performance of and Design Criteria for Deployable Aerodynamic Decelerators. ASD-TR-61-579, Dec. 1963.

[5] Berndt, R. J., Experimental Determination of Parameters for the Calculation of Parachute Filling Times. German WGL-Jahrbuch 1964.

[6] Melzig, H. D., The Change of Pressure Distribution on Parachute Canopies During Inflation. Final Phase Aerodynamic Deceleration Course, University of Minnesota, July 1965.

APPENDIX I

PARACHUTE CANOPY MODELS

Detail drawings of the four canopy models used during the experimental test program are shown in Figures 84 thru 87.

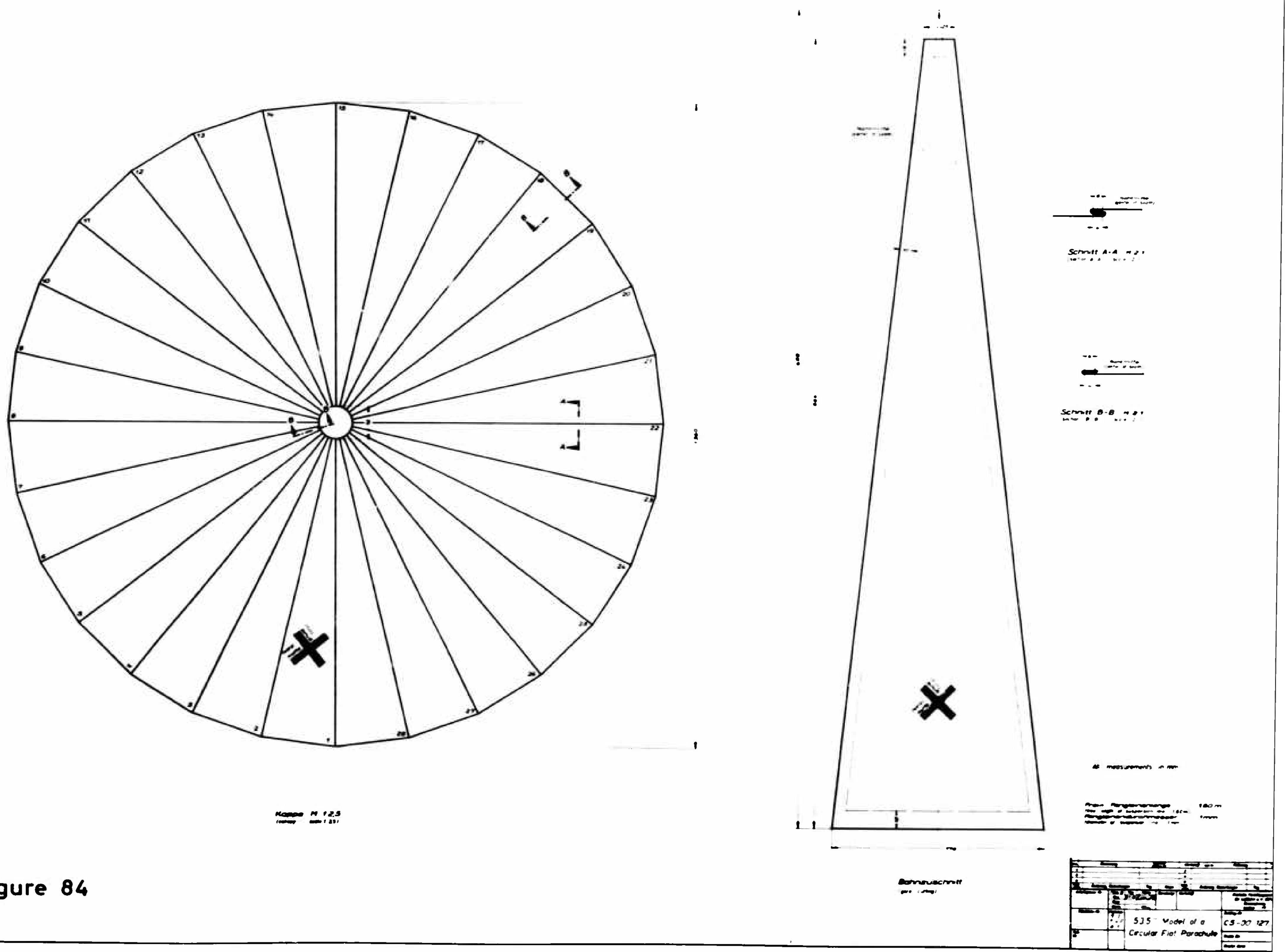
Schnitt A-A M 2:1
Schnitt B-B M 2:1
Kappe M 1:2,5
Bahnzuschnitt
All measurements in mm
535 Model of a Circular Flat Parachute
CS-30 127

Figure 84

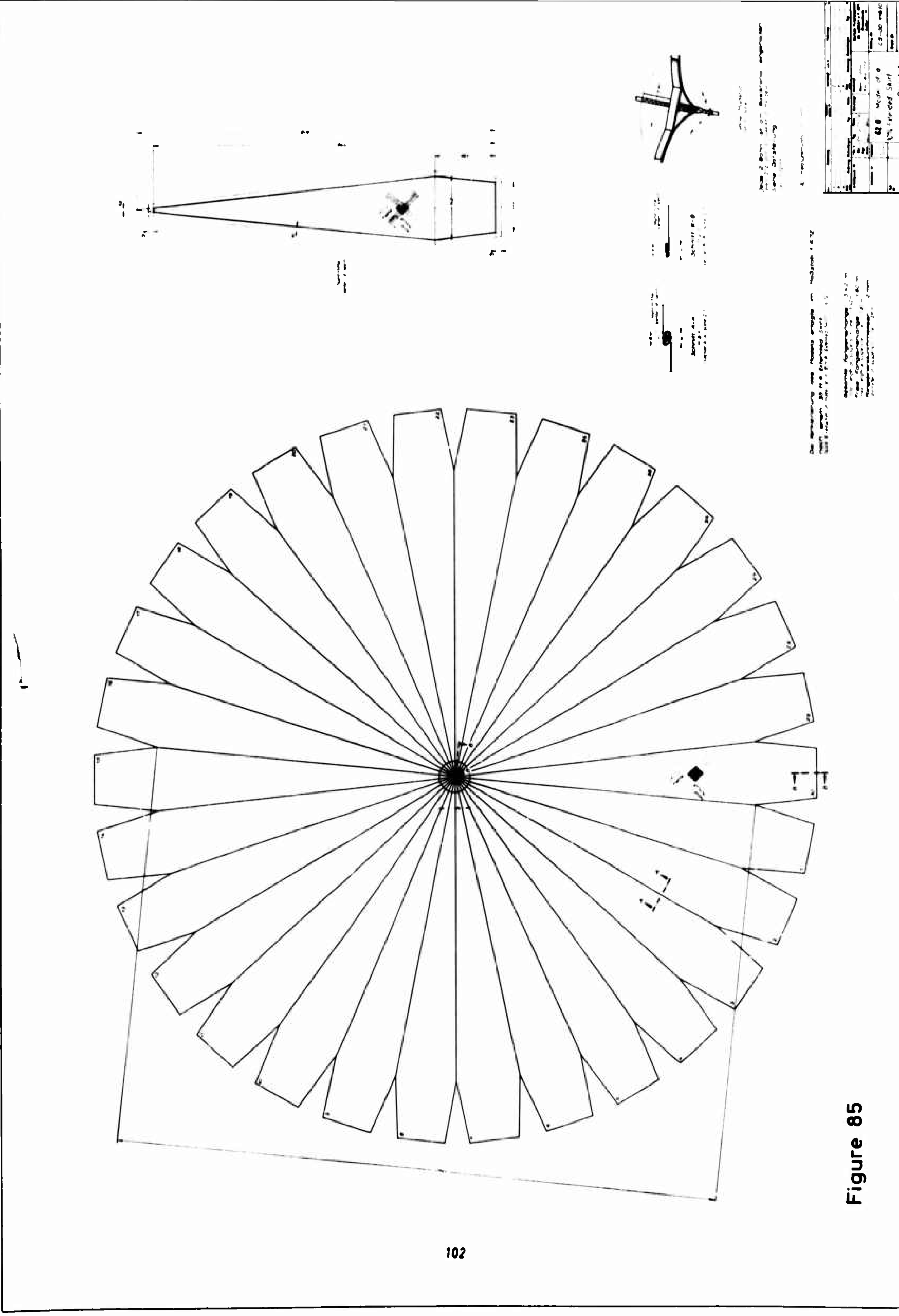

Figure 85

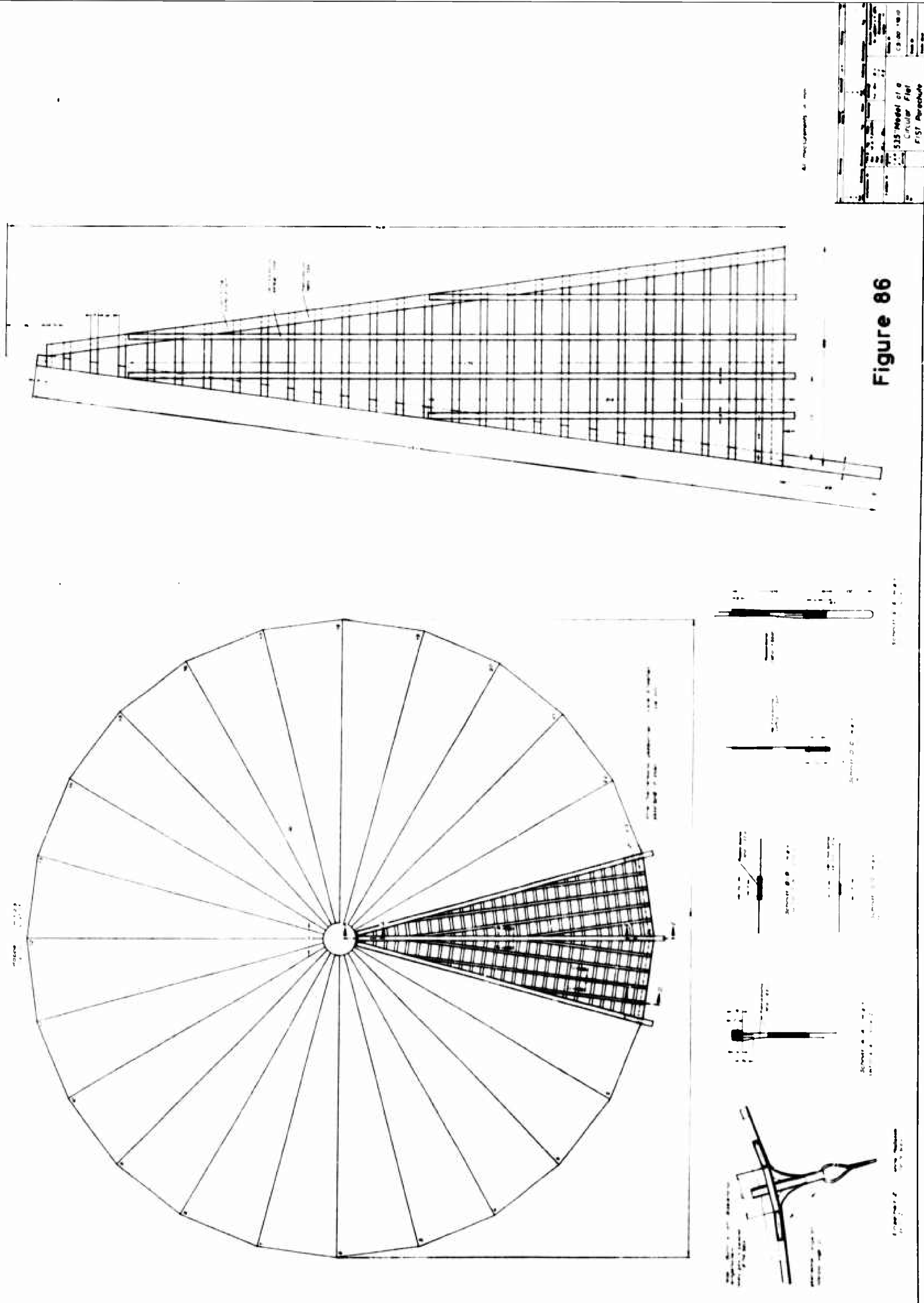

Figure 86

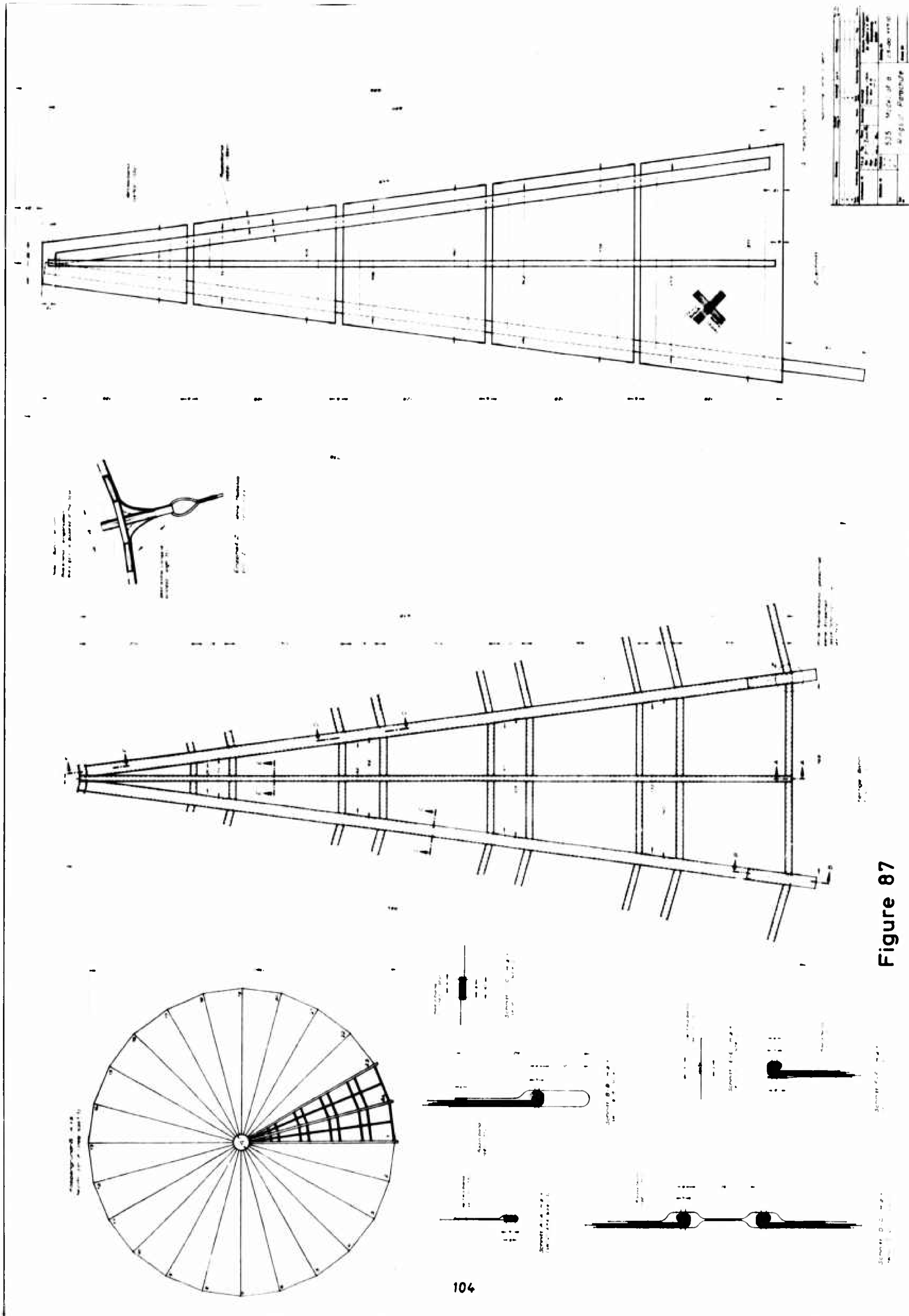

Figure 87

APPENDIX II

COMPARATIVE PRESSURE COEFFICIENT VERSUS TIME RELATIONSHIPS

A complete picture of the pressure versus time relationships for each canopy type and deployment velocity is presented in Figures 88 thru 102 in which the differential, internal and external pressure coefficients are plotted versus a common time base. Since the plottings are based upon smoothed data, reproduction of the original oscillograph traces are presented also to show the fluctuations in pressures actually encountered.

As may be seen on the original traces, a recording of the force generated by the canopy model during inflation was made during each run. Although a numerical evaluation of the force traces was not performed, they are presented here for correlative purposes.

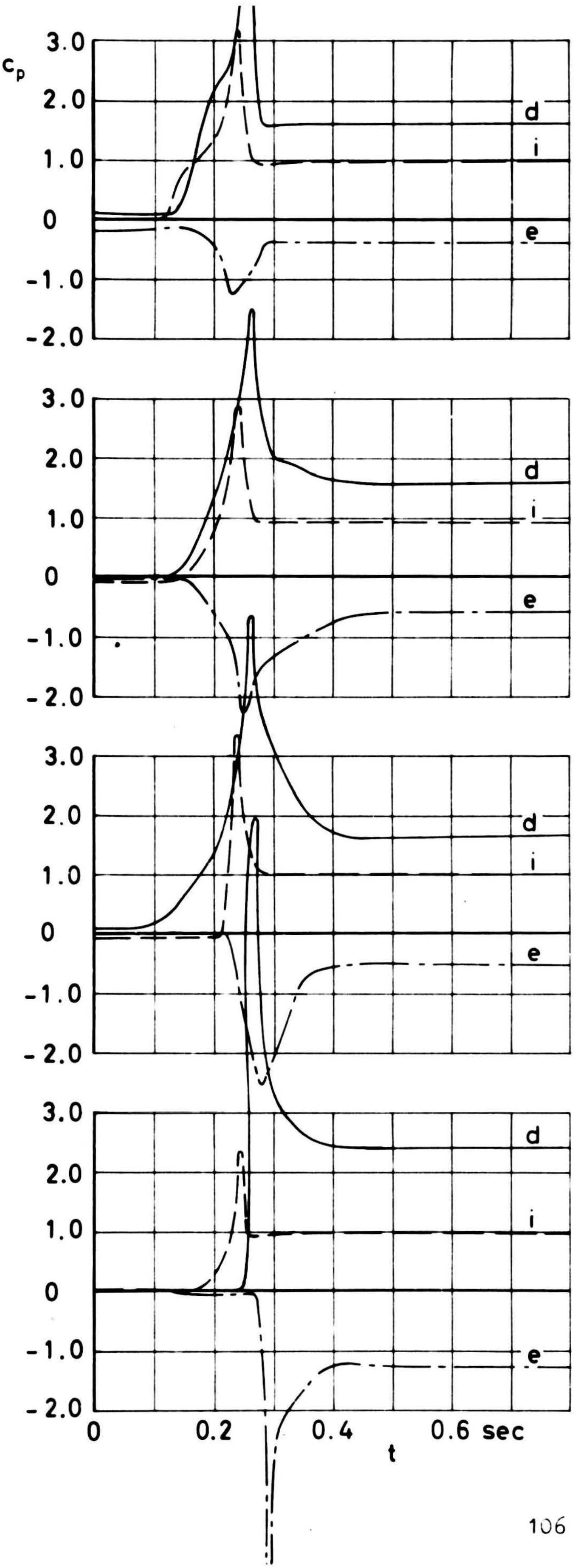

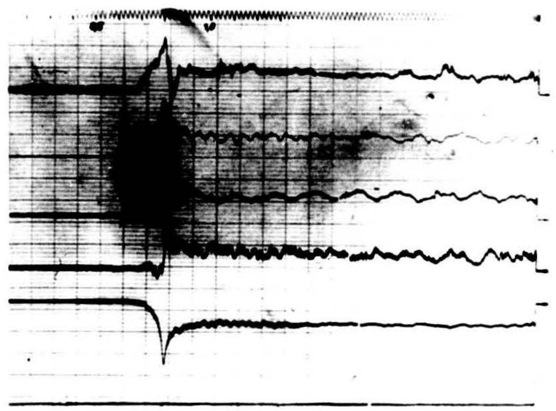

No.182 p_d differential pressure

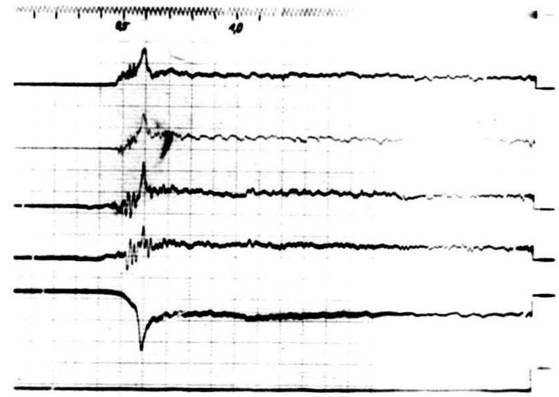

No.194 p_i internal pressure

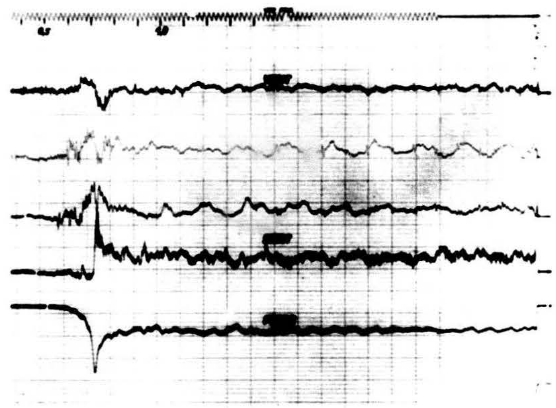

No. 211 p_e external pressure

Figure 88 c_p versus time for differential, internal and external pressure

$v_0 = 70$ ft/sec

Type: Circular Flat

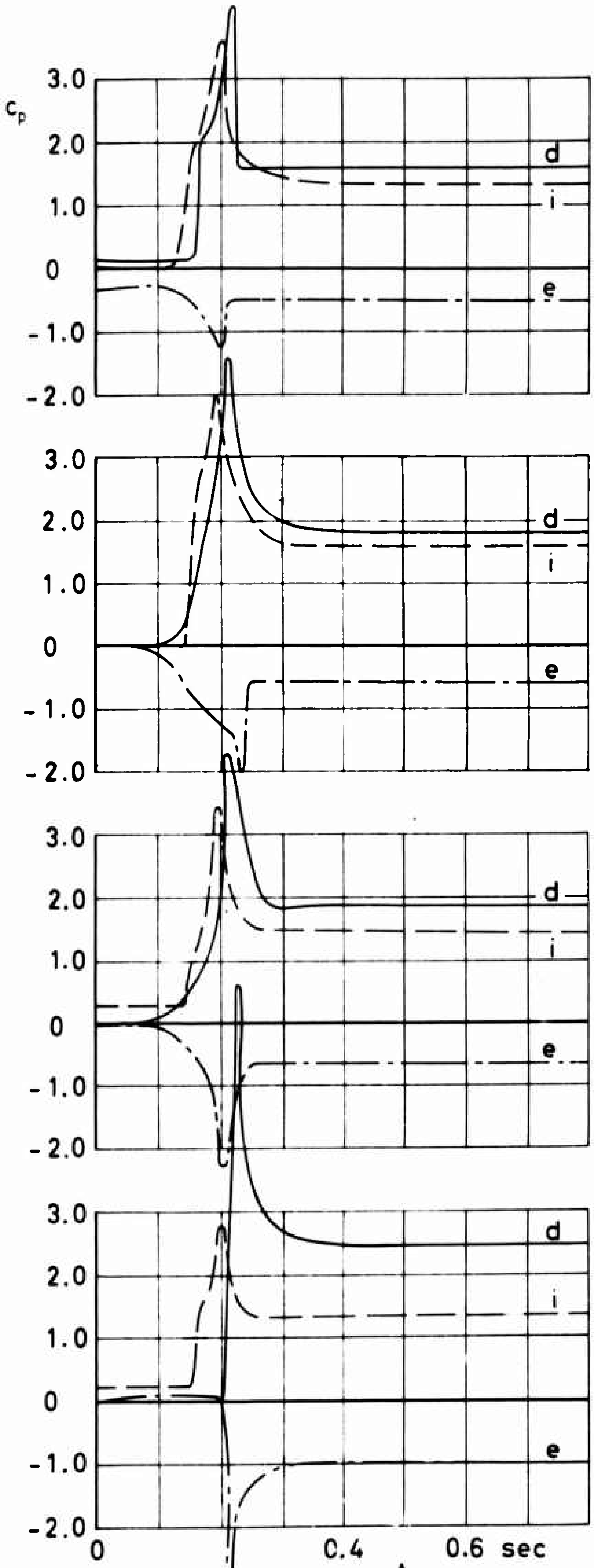

No. 183 p_d

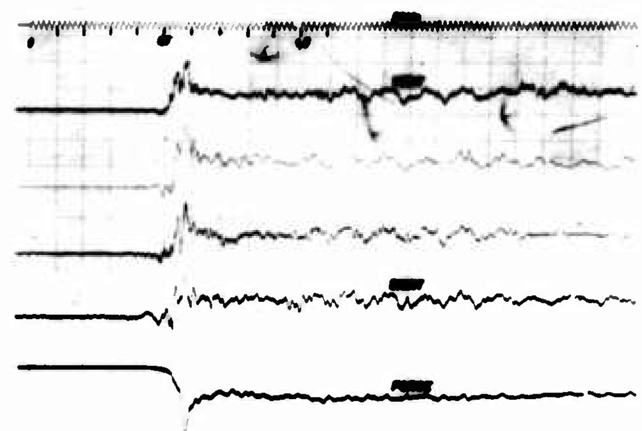

No. 200 p_i

No. 216 p_e

Figure 89 c_p versus time for differential, internal and external pressure

v_0 =100 ft/sec

Type: Circular Flat

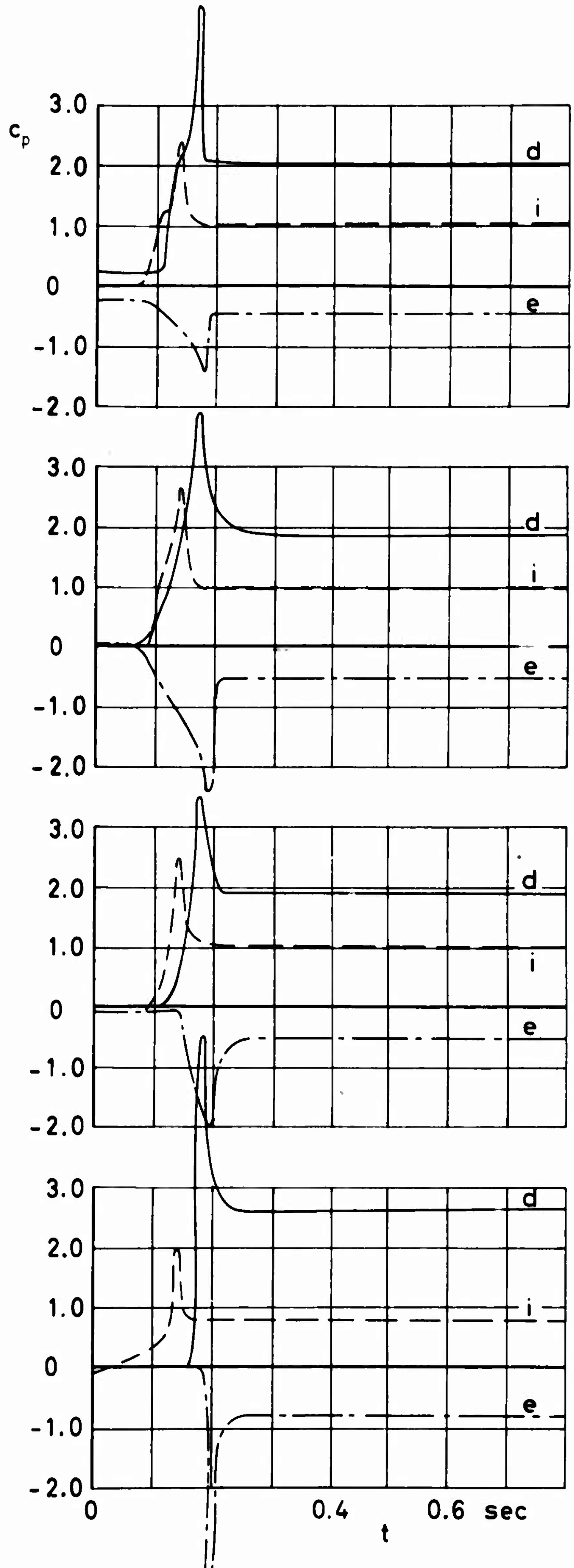

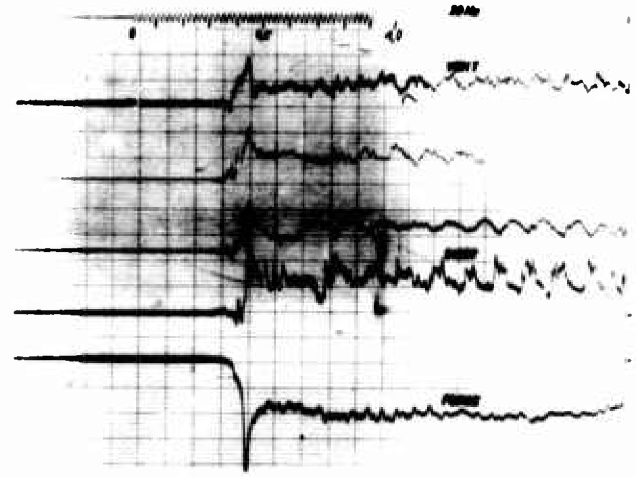

No.187 p_d

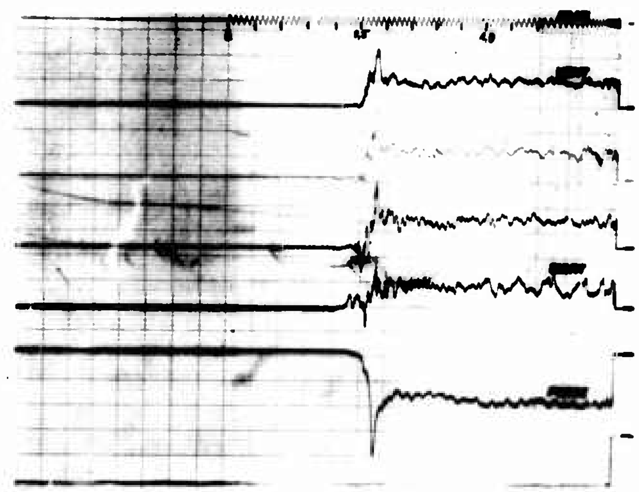

No.203 p_i

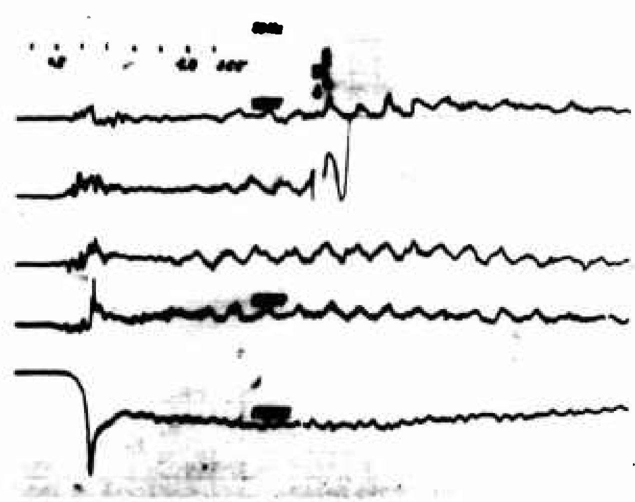

No.218 p_e

Figure 90 c_p versus time for differential, internal and external pressure

$v_0 = 130$ ft/sec

Type: Circular Flat

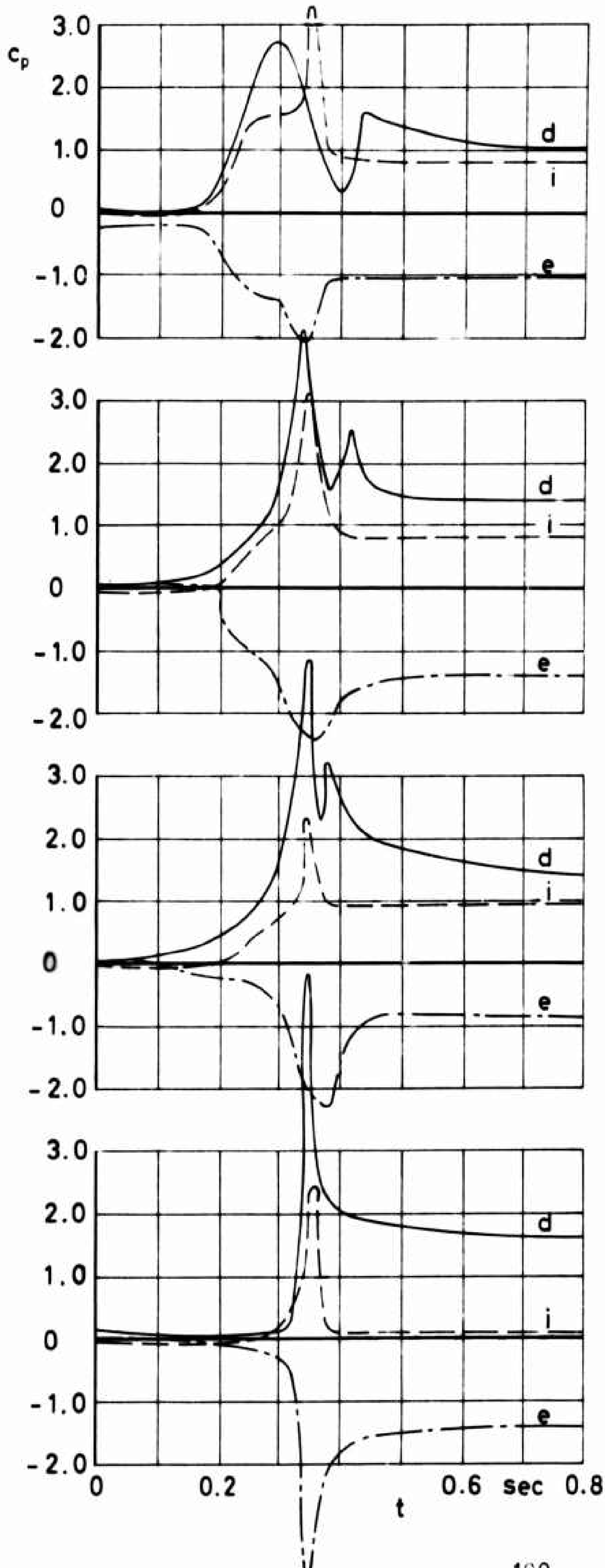

No.139 p_d differential pressure

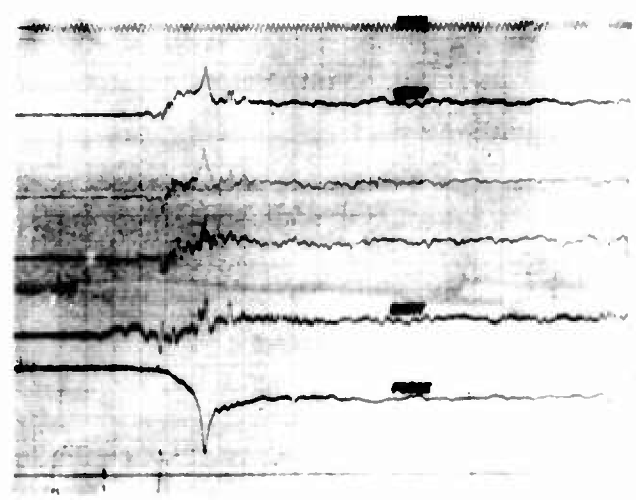

No.157 p_i internal pressure

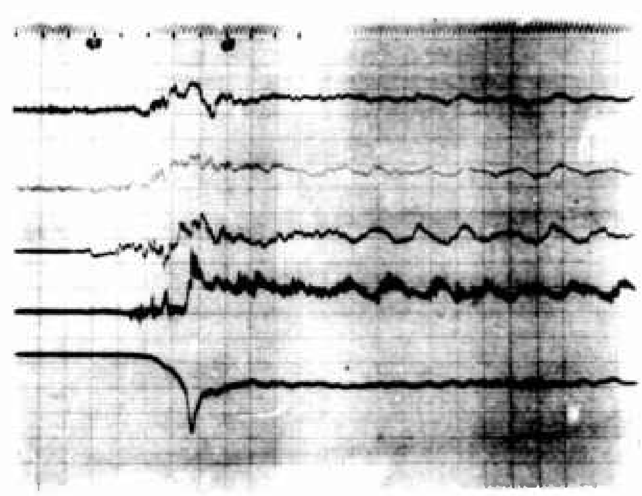

No.221 p_e external pressure

Figure 91 c_p versus time for differential, internal and external pressure

$v_0 = 70$ ft/sec

Type: Extended Skirt

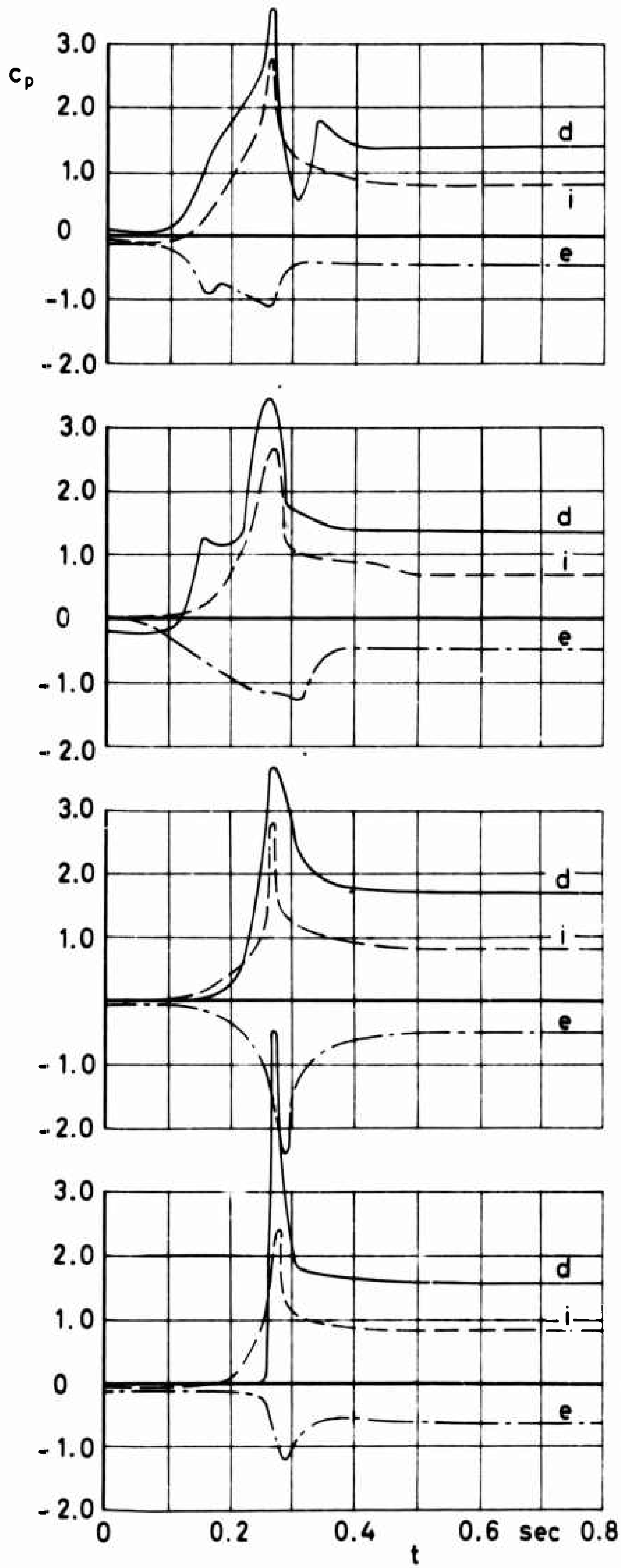

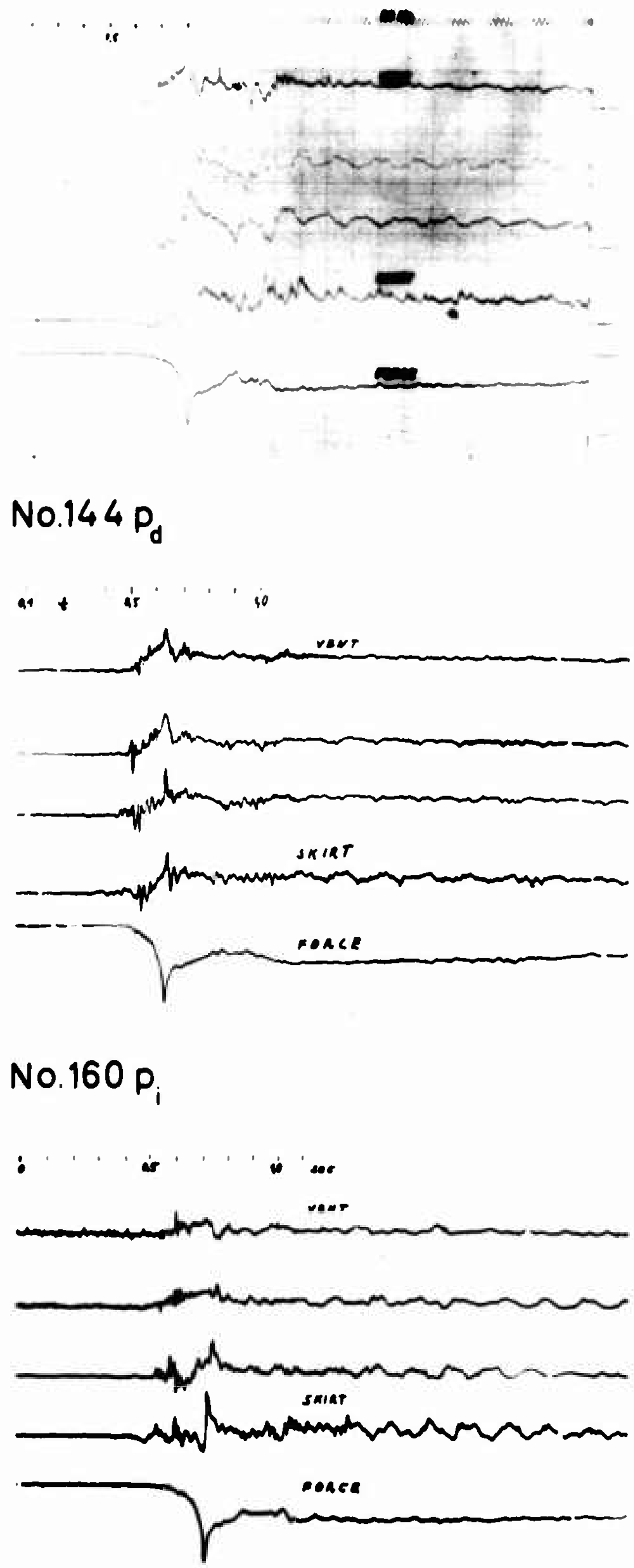

No.144 p_d

No.160 p_i

No. 226 p_e

Figure 92 c_p versus time for differential, internal and external pressure

v_0 =100 ft/sec

Type: Extended Skirt

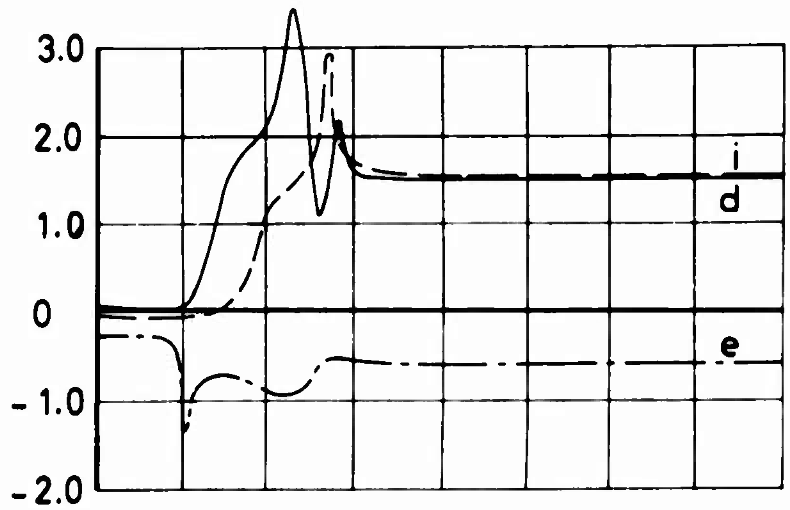

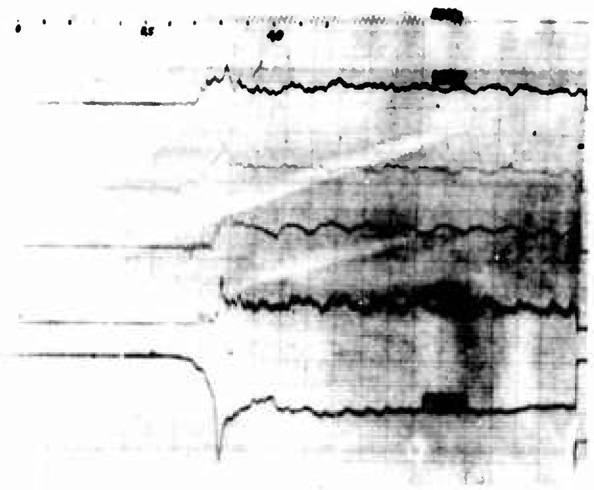

No.148 p_d

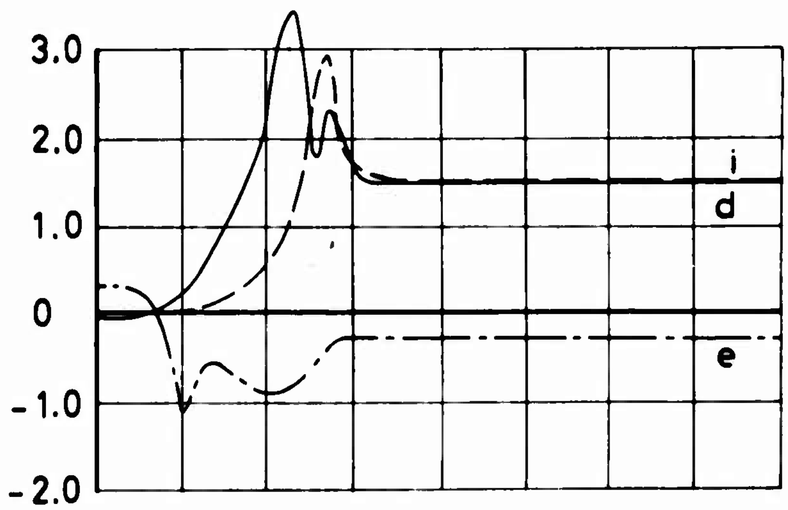

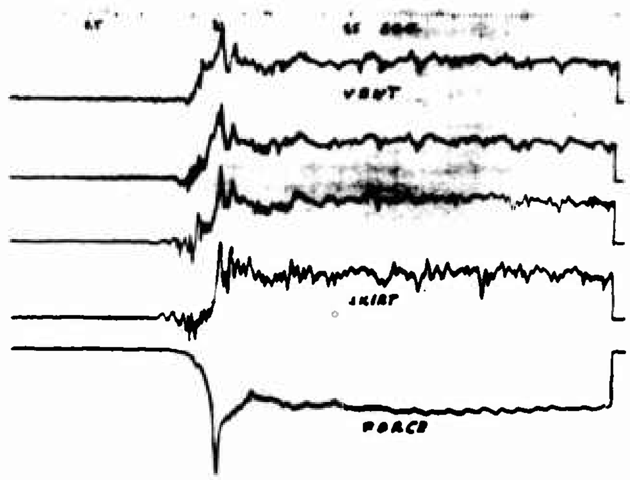

No.163 p_i

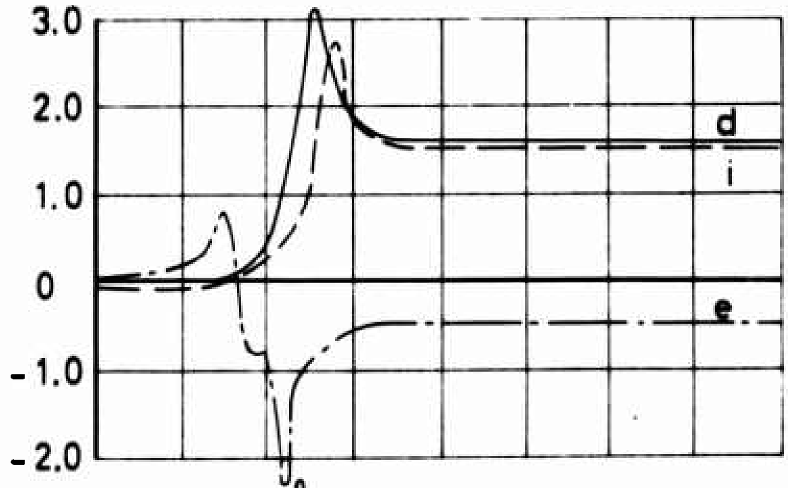

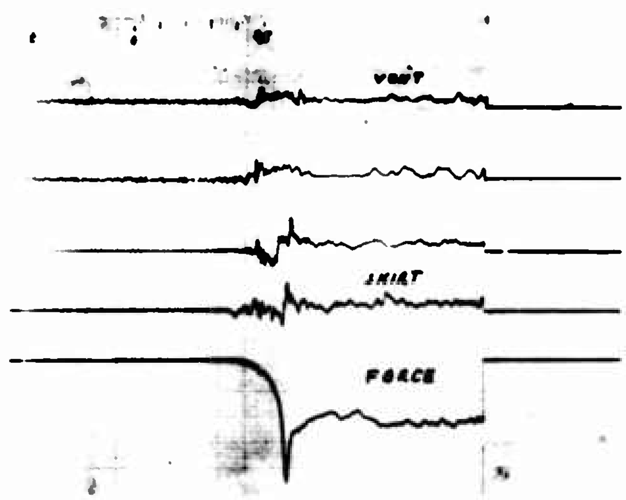

No. 231 p_e

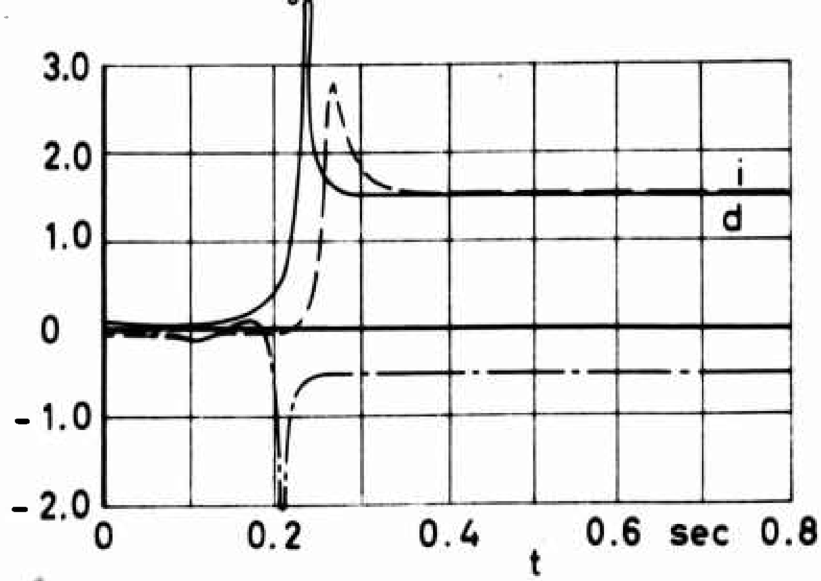

Figure 93 c_p versus time

differential, internal and

external pressure

v_0=130 ft/sec

Type: Extended Skirt

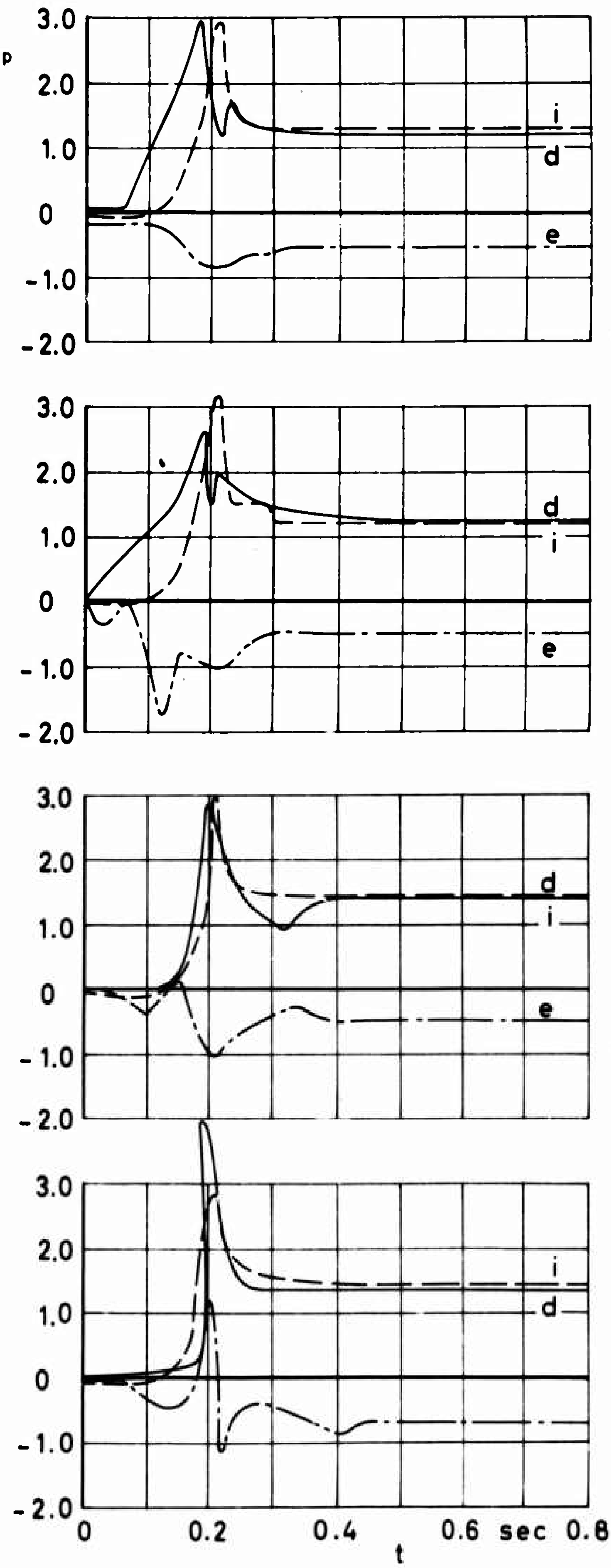

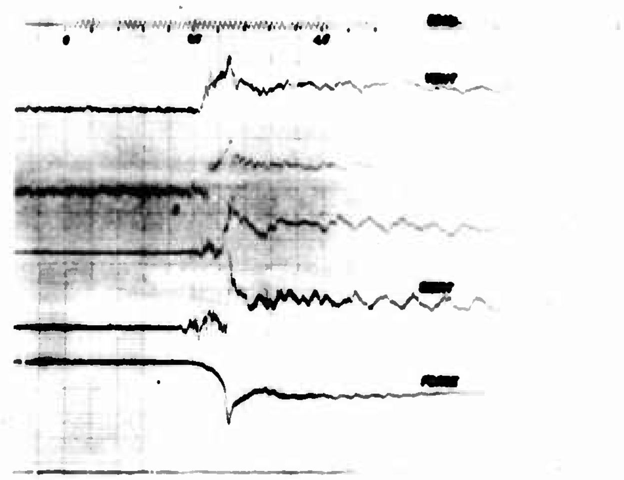

No.153 p_d

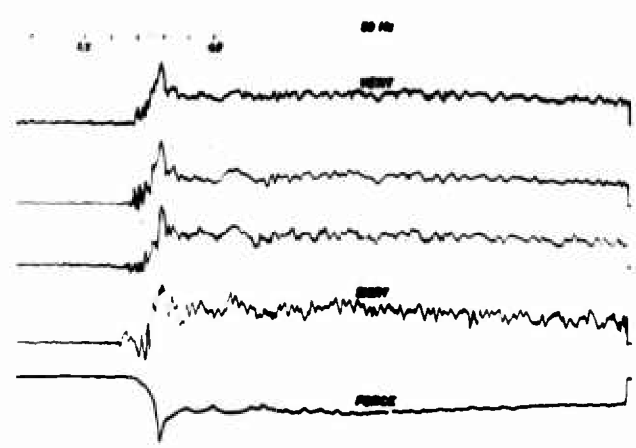

No.166 p_i

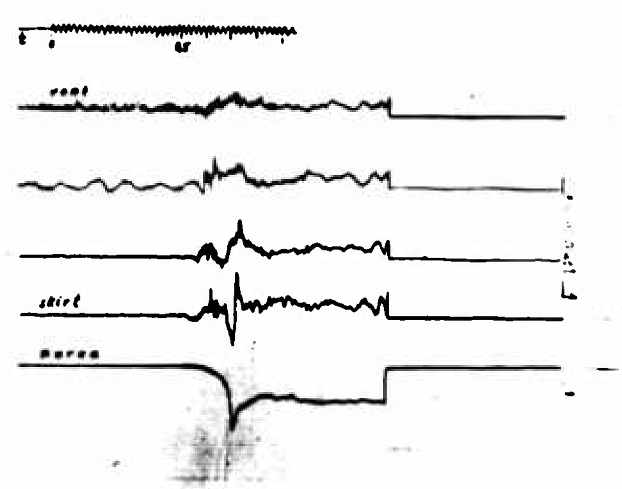

No. 235 p_e

Figure 94 c_p versus time for differential, internal and external pressure

v_0=160 ft/sec

Type: Extended Skirt

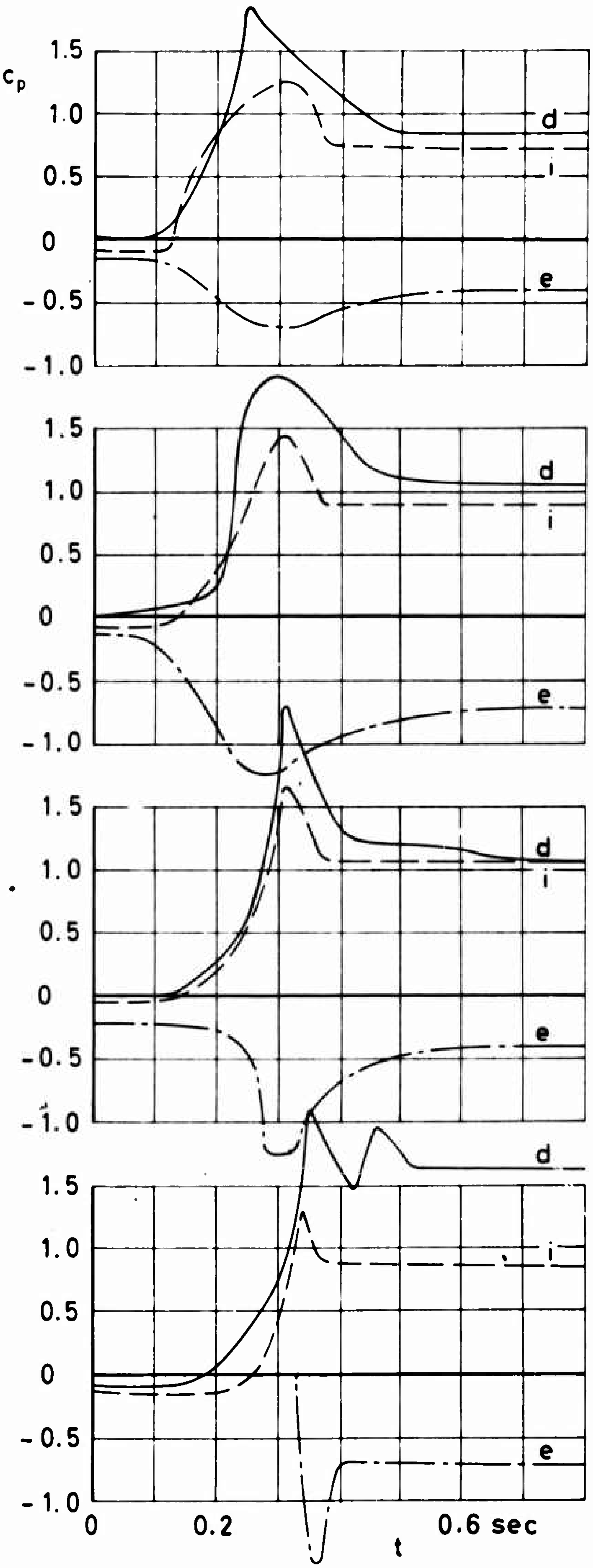

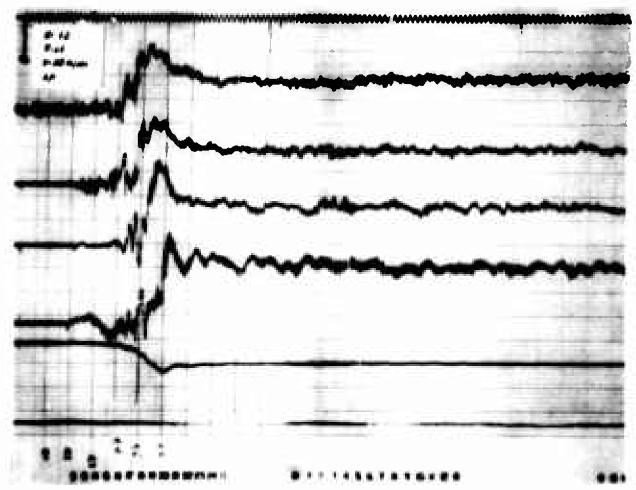

No. 72 p_d differential pressure

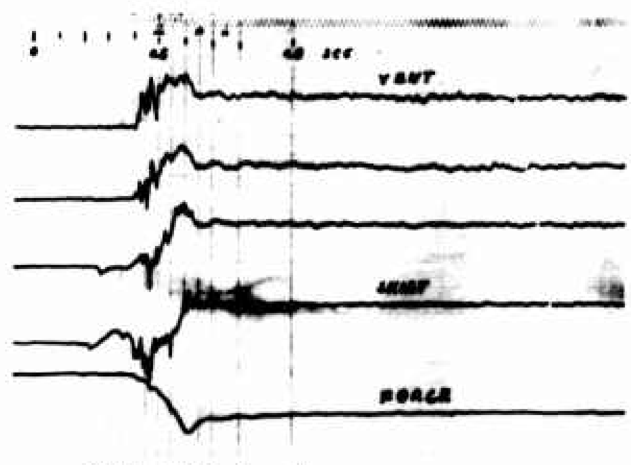

No.101 p_i internal pressure

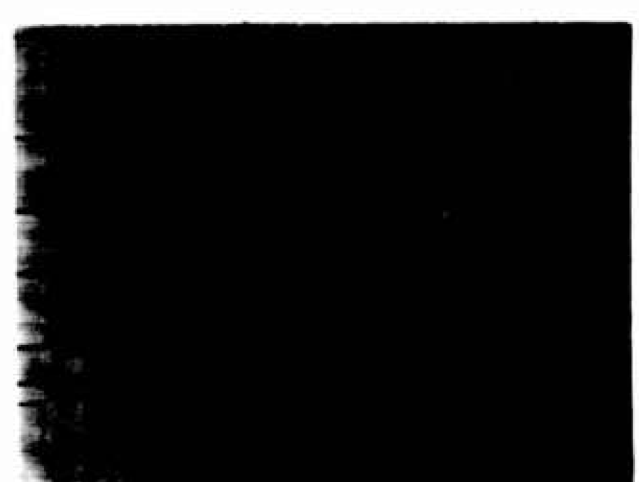

No.104 p_e external pressure

Figure 95 c_p versus time for differential, internal and external pressure

$v_0 = 70$ ft/sec

Type: Fist

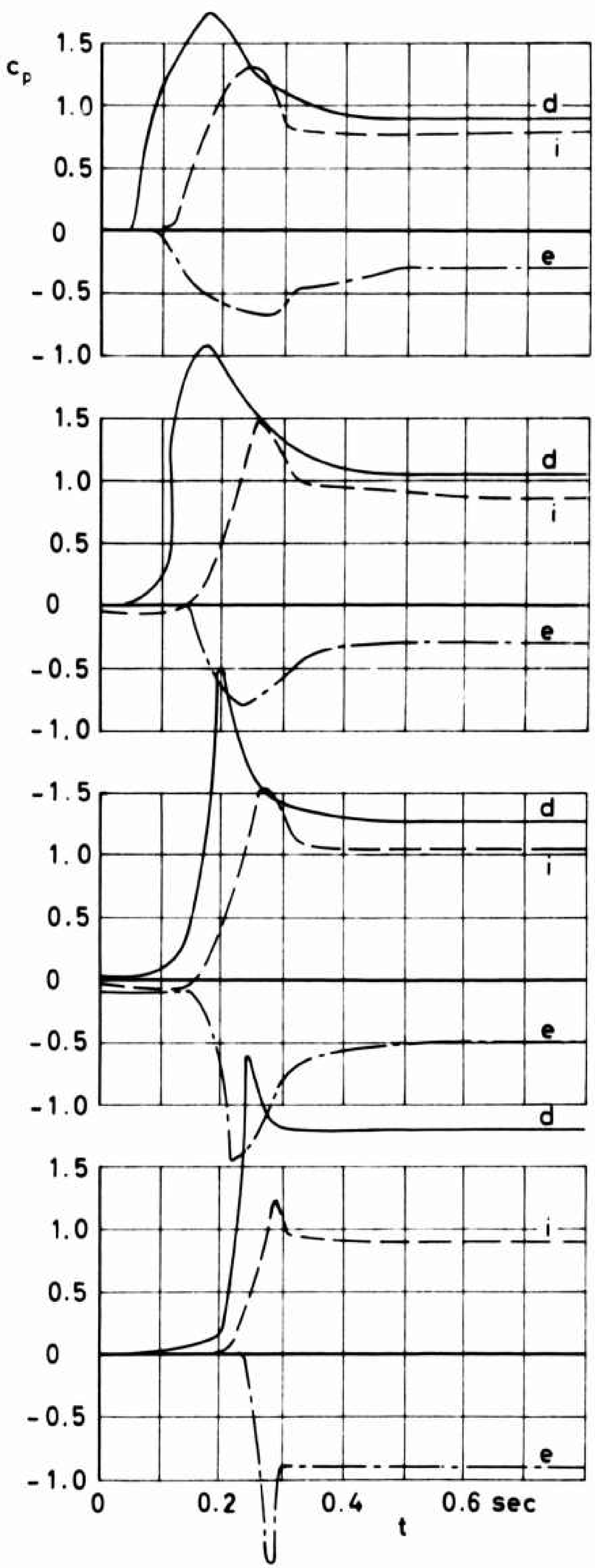

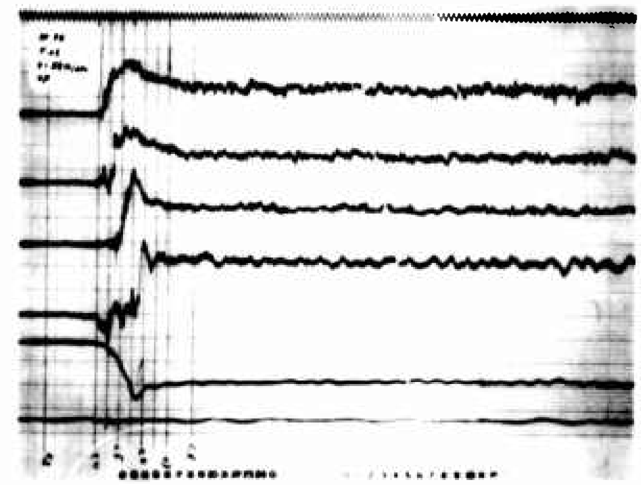

No. 76 p_d

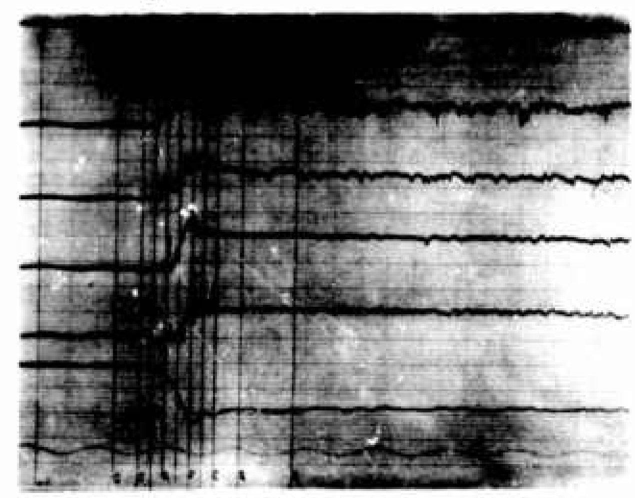

No. 97 p_i

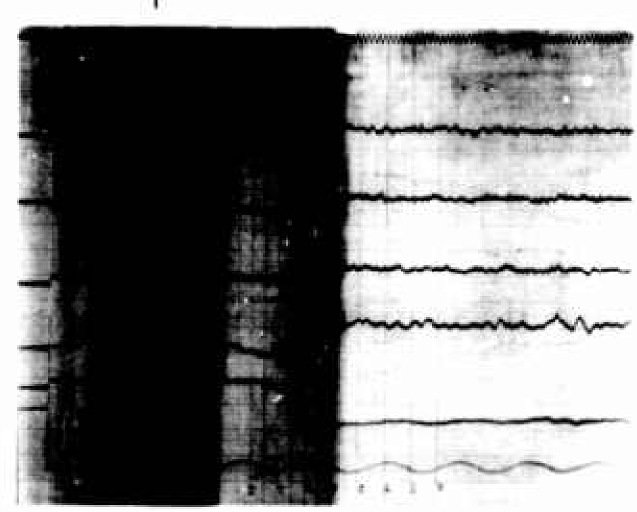

No. 110 p_e

Figure 96 c_p versus time for differential, internal and external pressure

v_0 = 100 ft/sec

Type: Fist

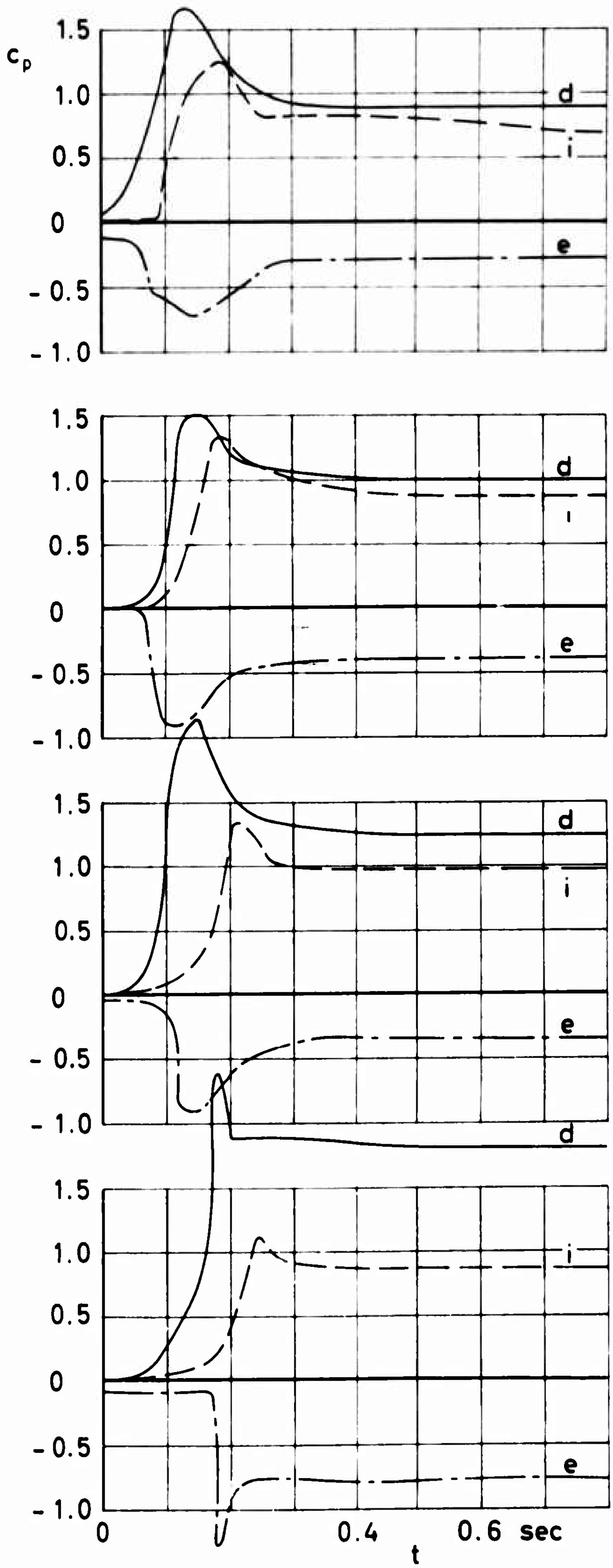

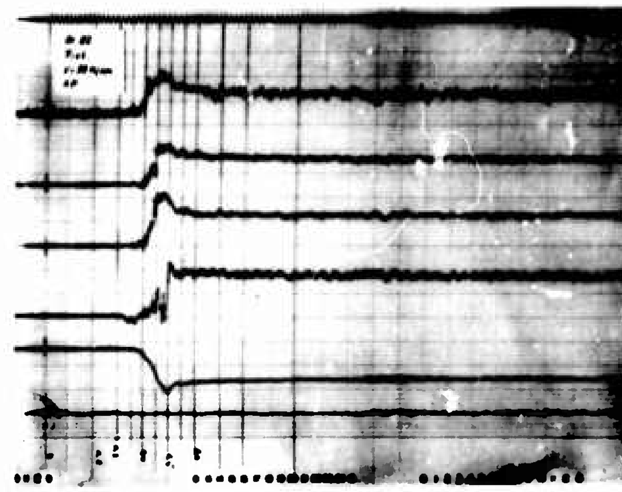

No.82 p_d

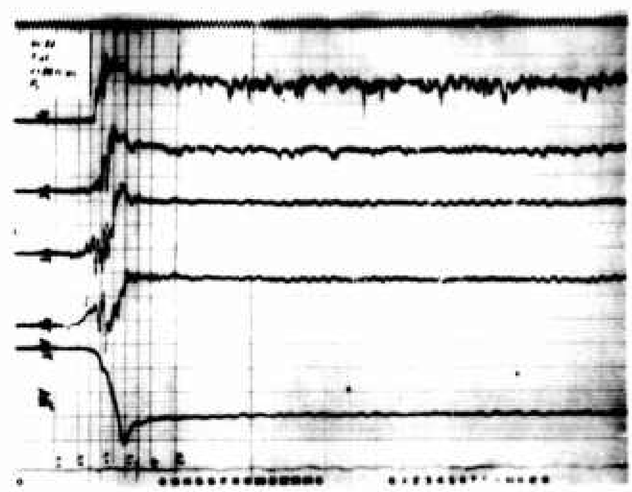

No.92 p_i

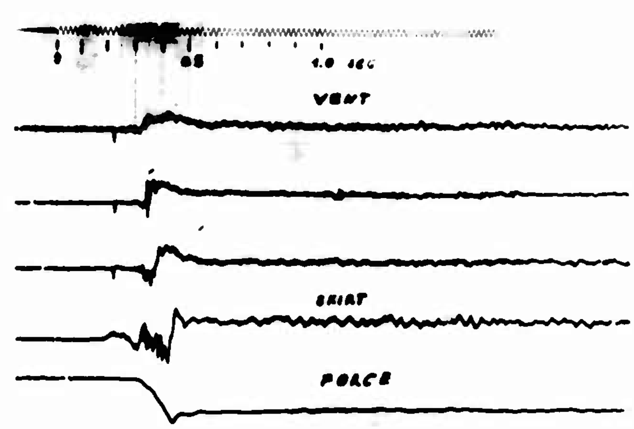

No.117 p_e

Figure 97 c_p versus time for differential, internal and external pressure

$v_0 = 130$ ft/sec

Type: Fist

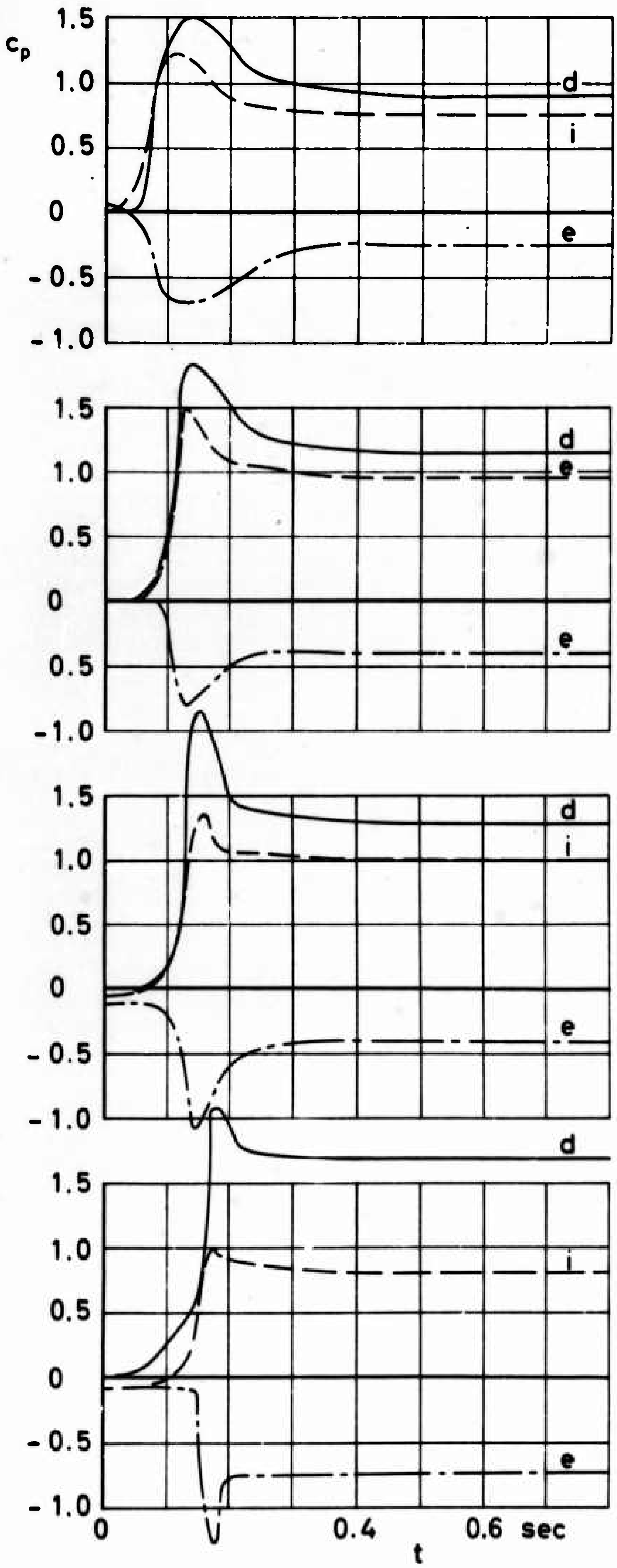

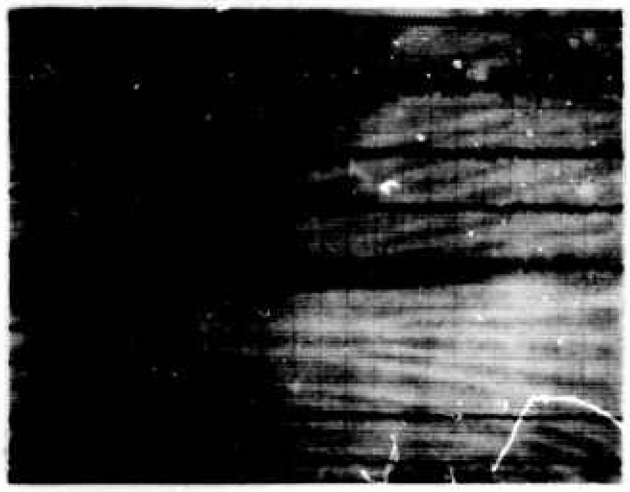

No. 86 p_d

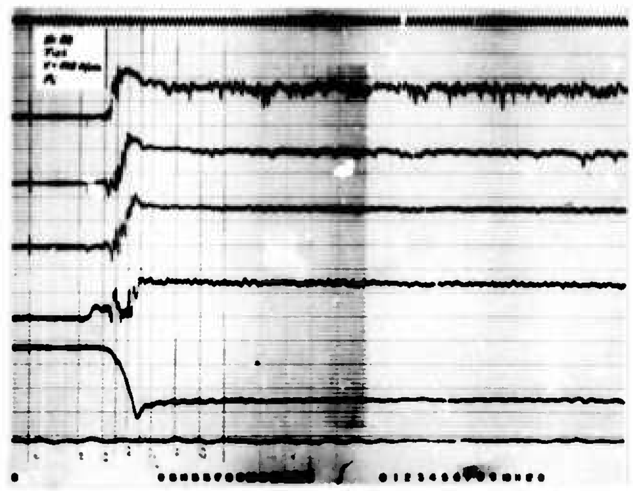

No.88 p_i

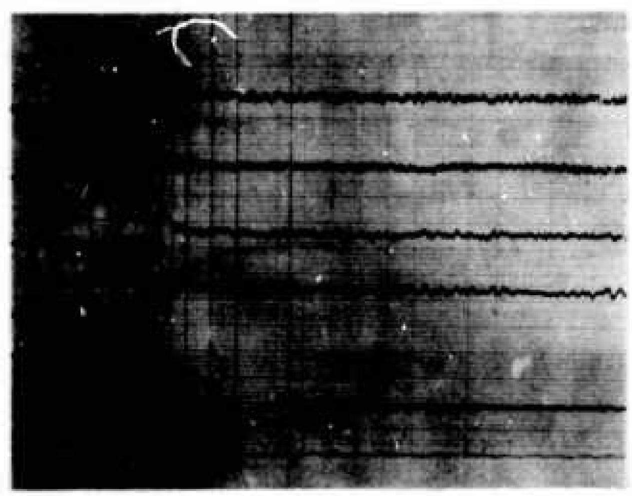

No.119 p_e

Figure 98 c_p versus time for differential, internal and external pressure

v_0 =160 ft/sec

Type: Fist

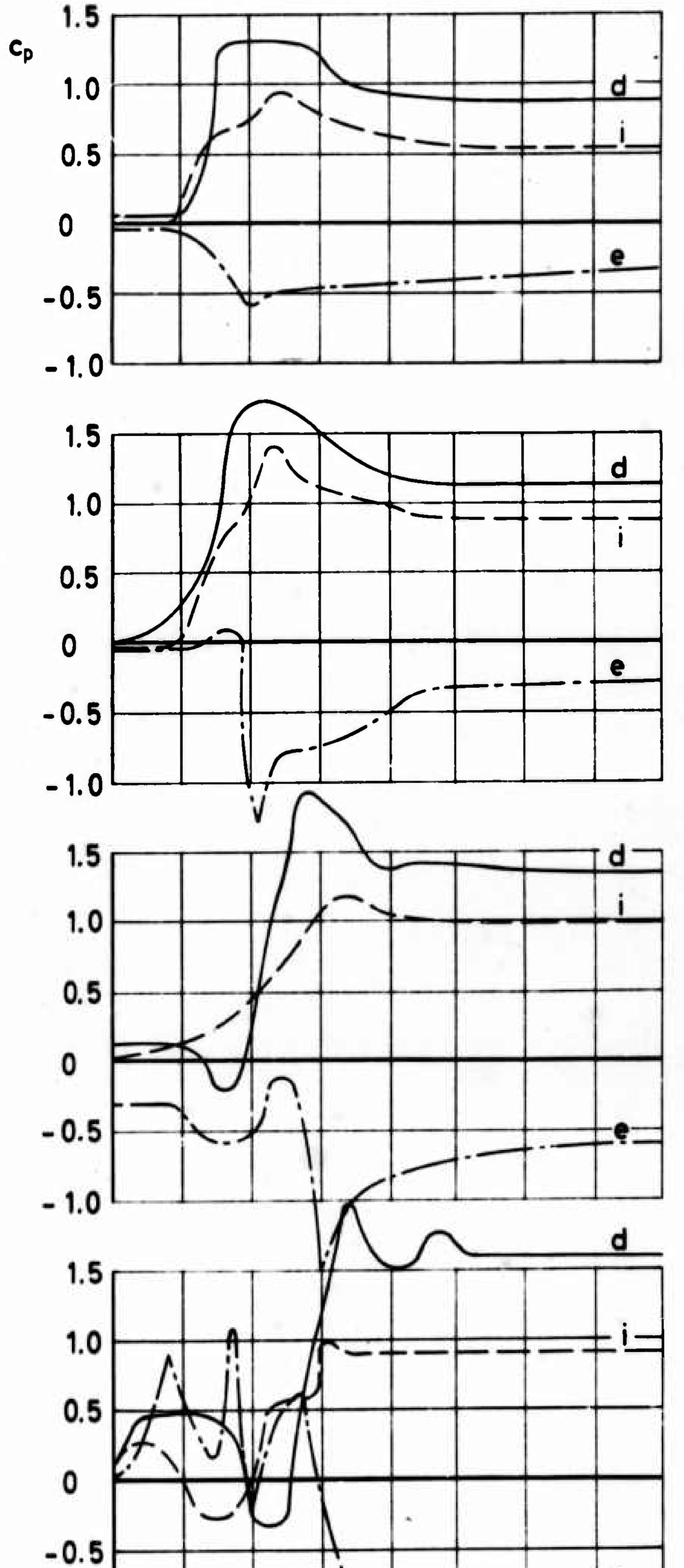

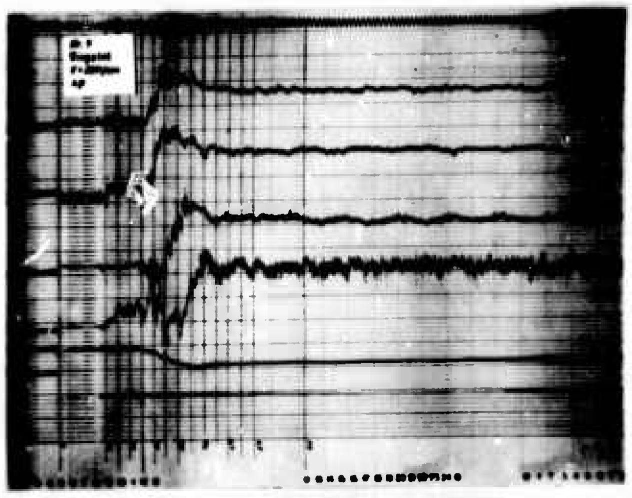

No. 7 p_d differential pressure

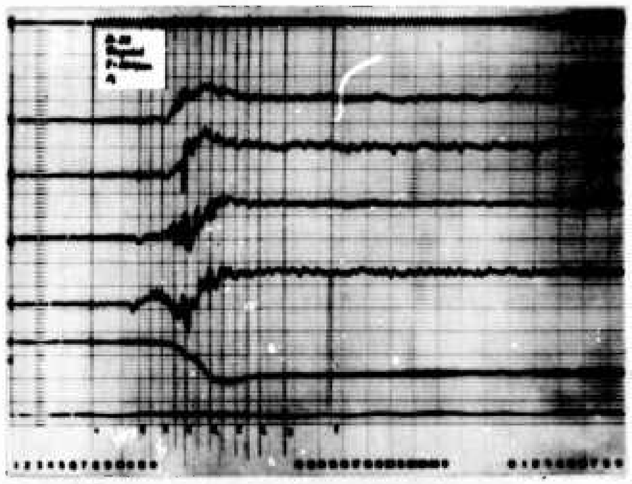

No. 22 p_i internal pressure

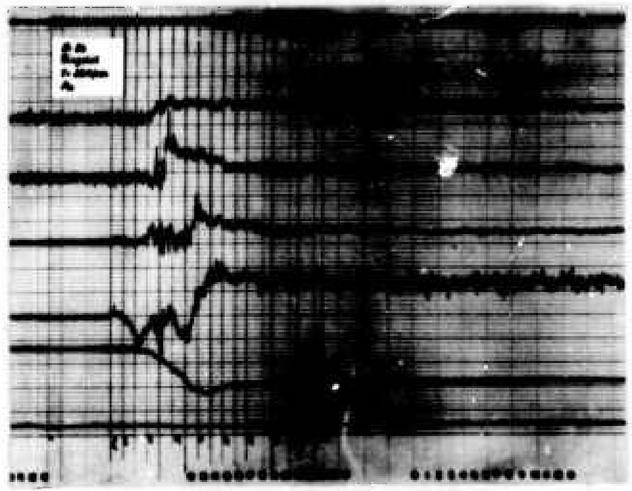

No. 34 p_e external pressure

Figure 99 c_p versus time for differential, internal and external pressure

$v_0 = 70$ ft/sec

Type: Ringslot

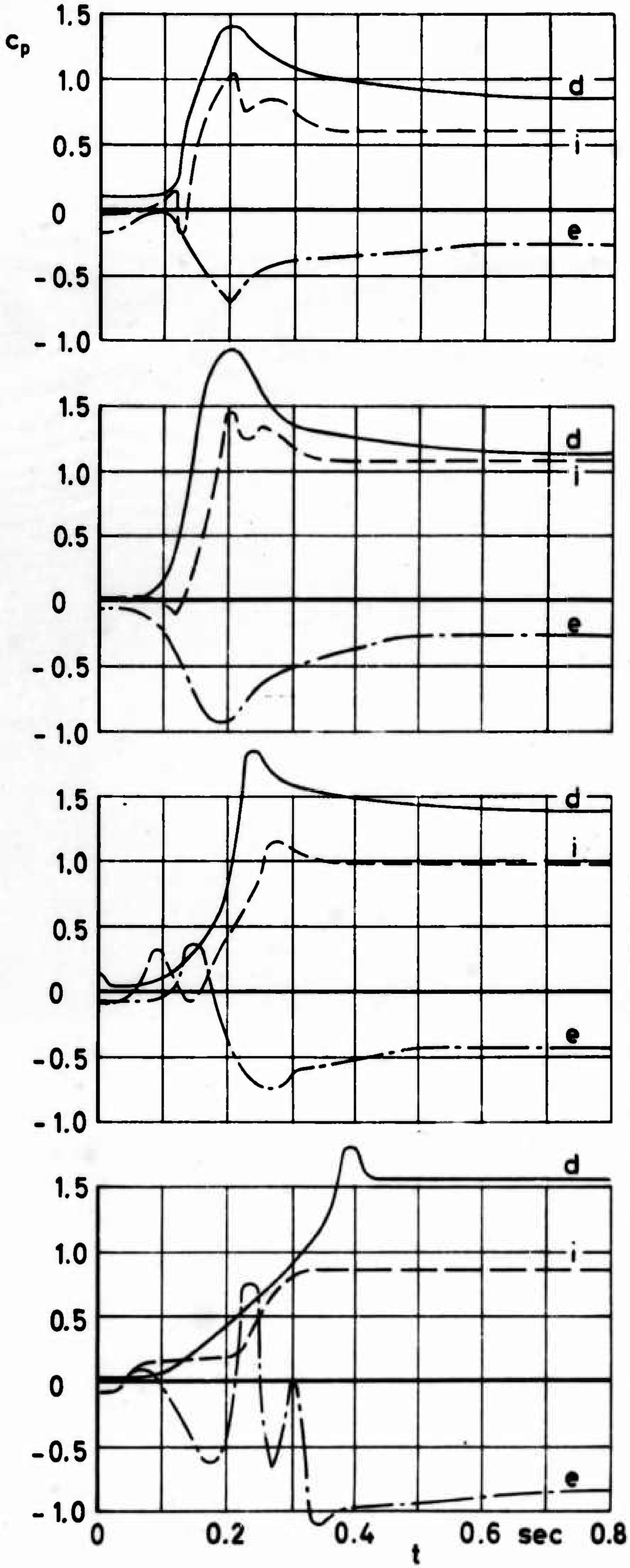

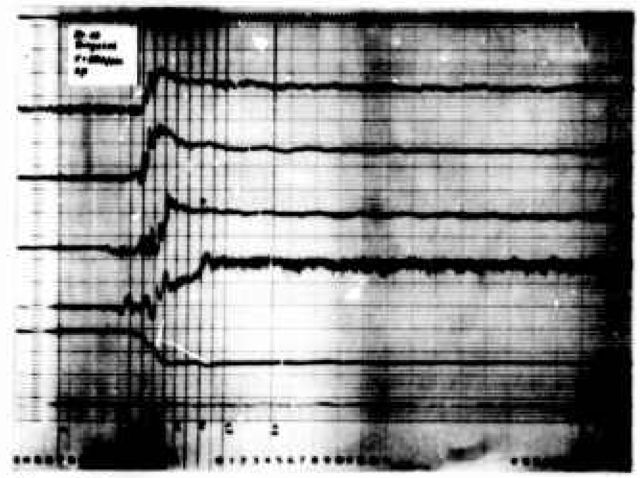

No.10 p_d

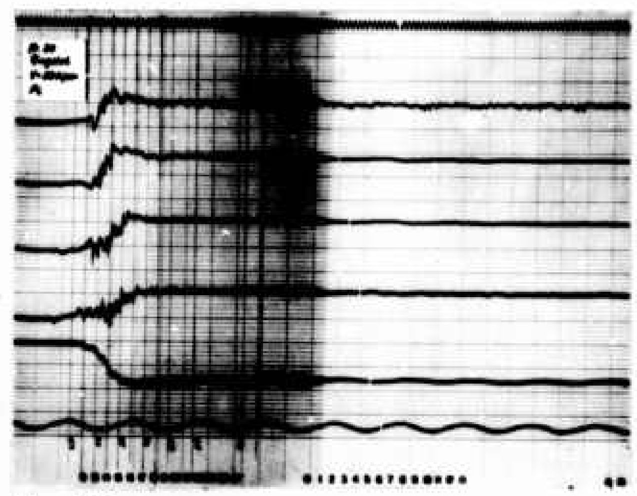

No.30 p_i

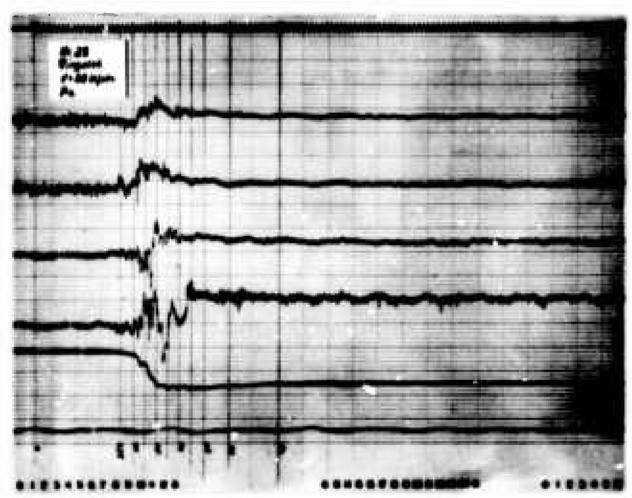

No.39 p_e

Figure 100 c_p versus time for differental, internal and external pressure

v_0 = 100 ft/sec

Type: Ringslot

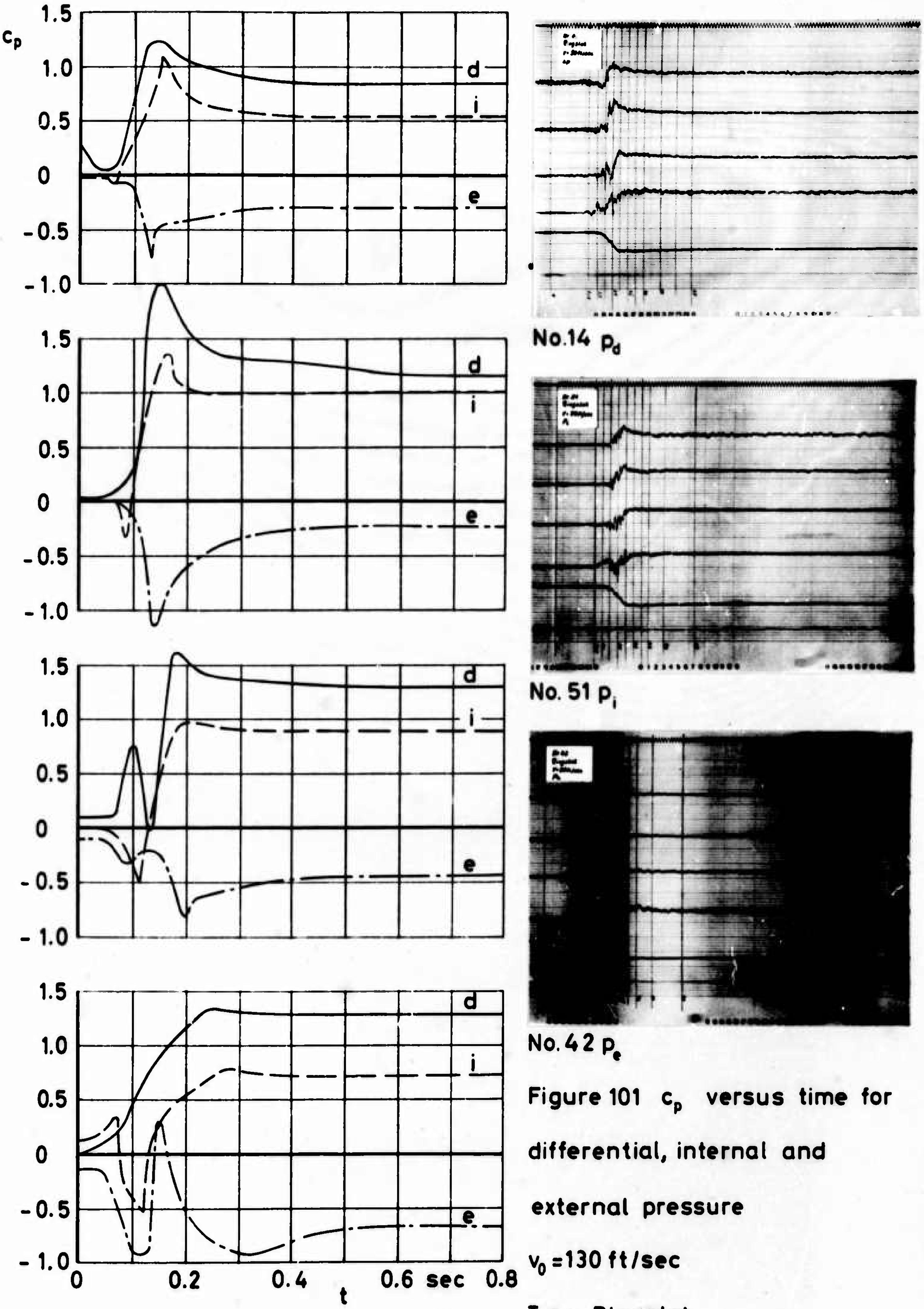

Figure 101 c_p versus time for differential, internal and external pressure

$v_0 = 130$ ft/sec

Type: Ringslot

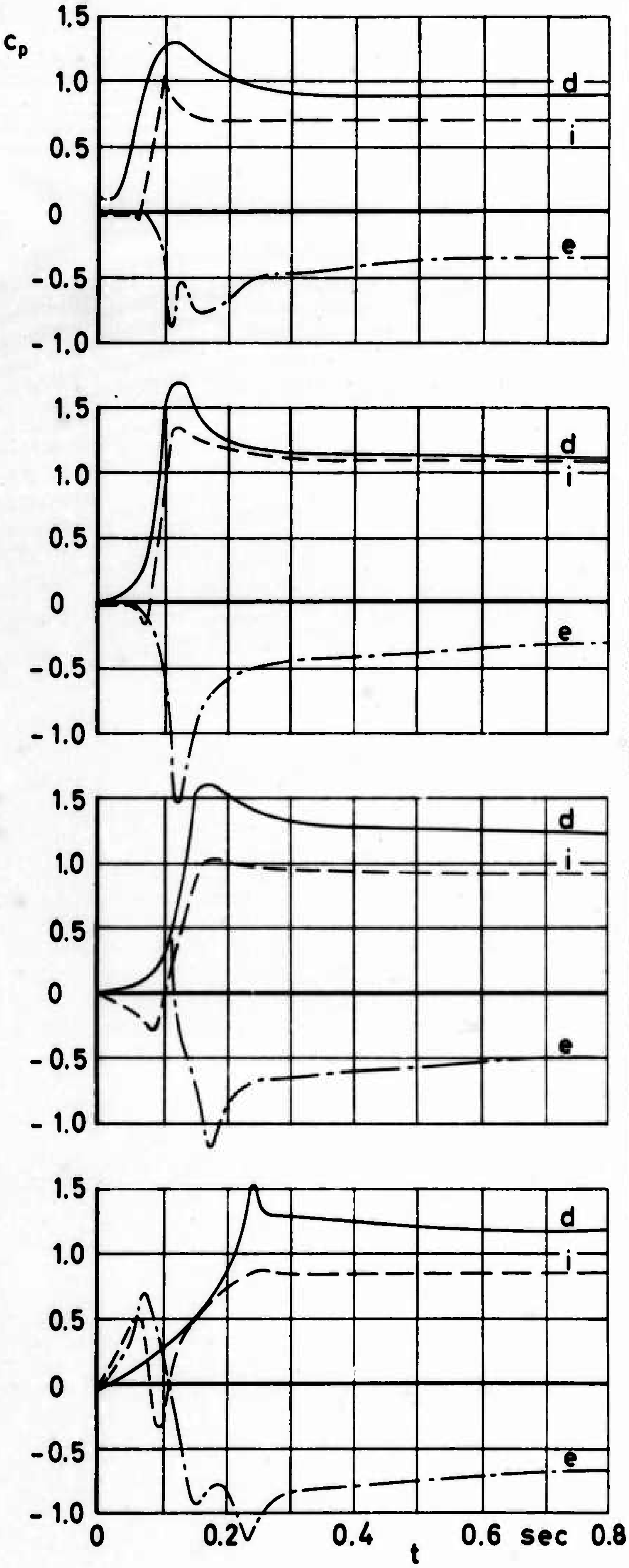

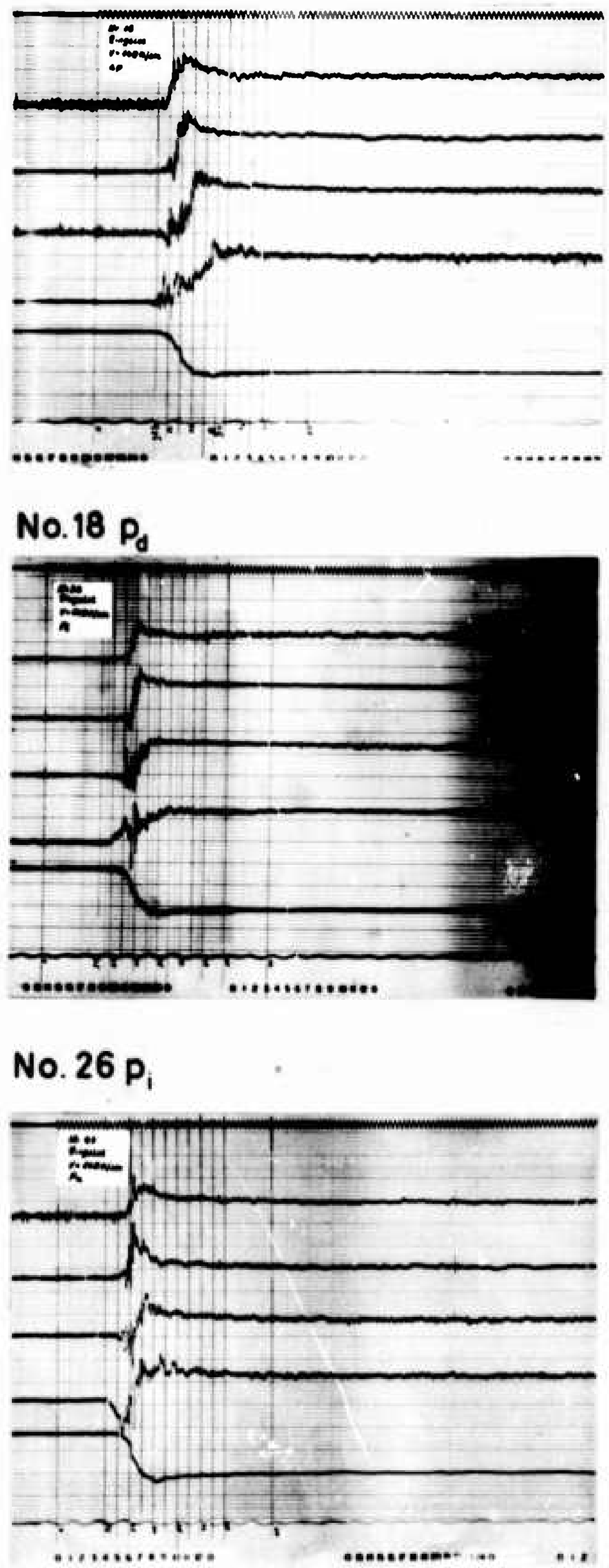

No. 18 p_d

No. 26 p_i

No. 47 p_e

Figure 102 c_p versus time for differential, internal and external pressure

$v_0 = 160$ ft/sec

Type: Ringslot

APPENDIX III

GORE CENTER LINE PRESSURE MEASUREMENTS

Additional wind tunnel tests were conducted to determine the magnitude and time relationship of local pressures at locations other than along the canopy cord centerline. During these tests, the four pressure transducers were located on the gore center line, spaced 90 degrees apart over the surface of the canopy, and arranged in a similar manner as for the previous tests.

Analyzing all data obtained, no significant difference in either the magnitude or time relationship of the pressures as compared to the measurements along the cord centerline were detected.

A typical example of the pressure data obtained during this test series is presented in Figures 103 thru 105. These graphs show the relationship between the differential pressure coefficient, c_{pd}, and time for each of the four locations on a ringslot type canopy deployed at a free stream velocity of 100 ft/sec.

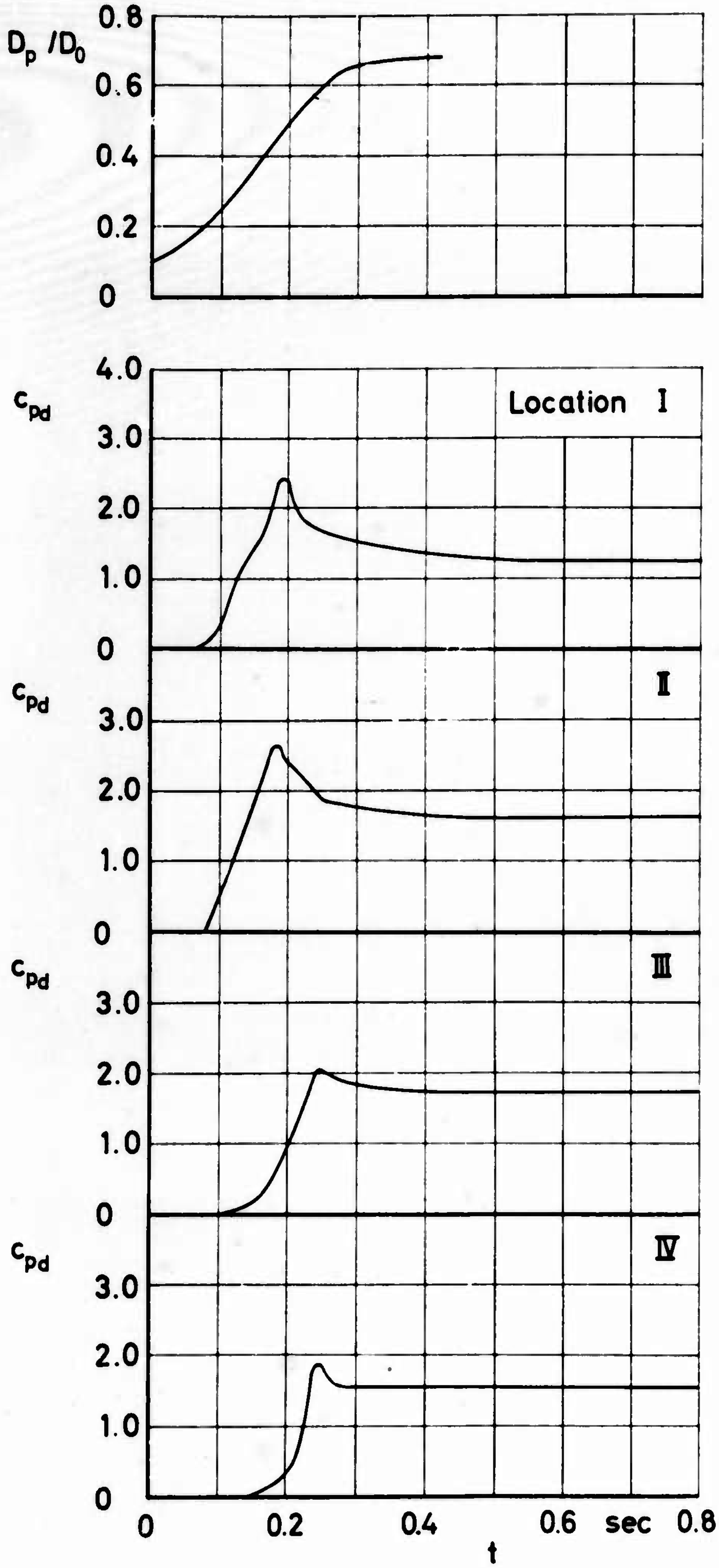

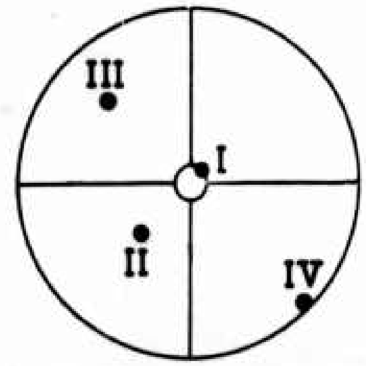

Location of pressure transducers on gore center line

Ringslot

Figure 103 c_{pd} and filling versus time

v_0 = 100 ft/sec

Run No. 173

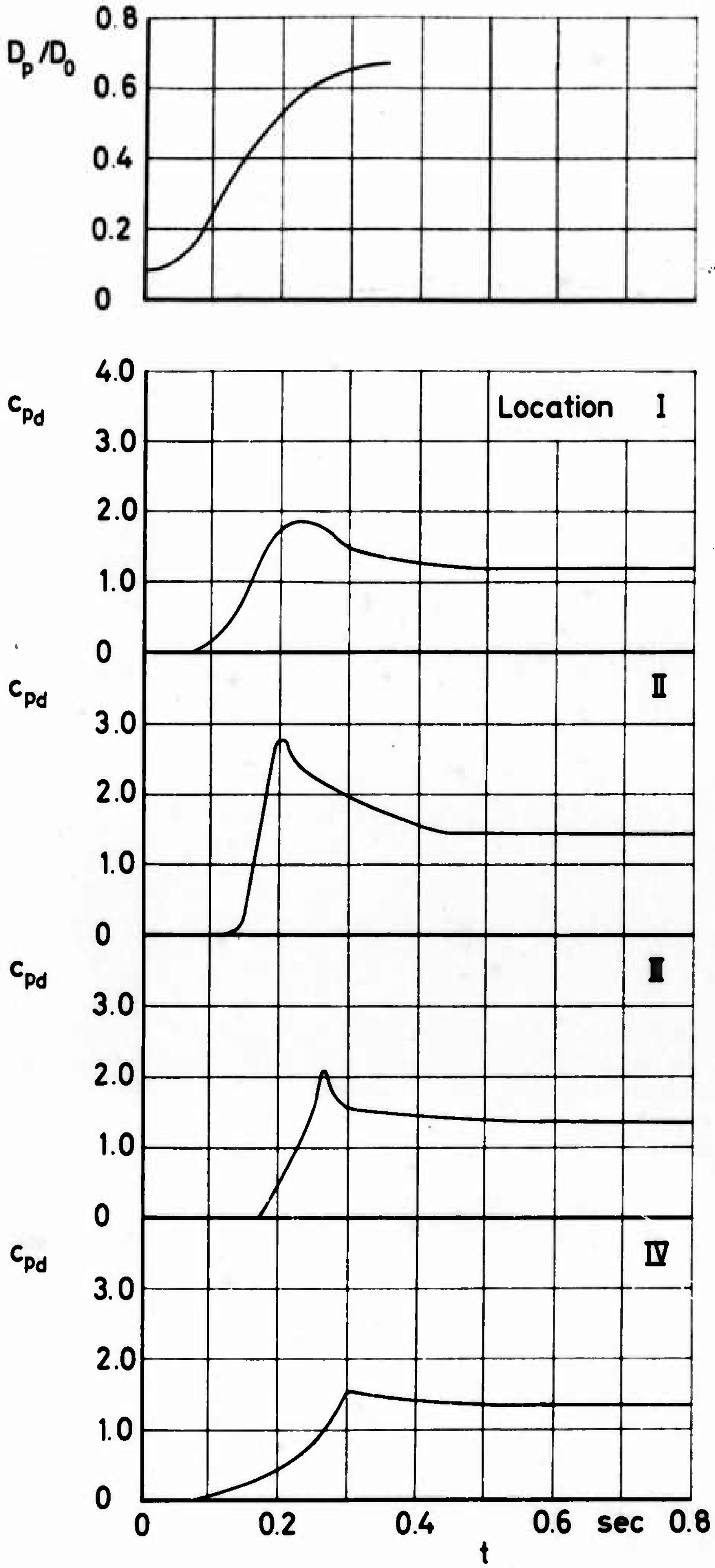

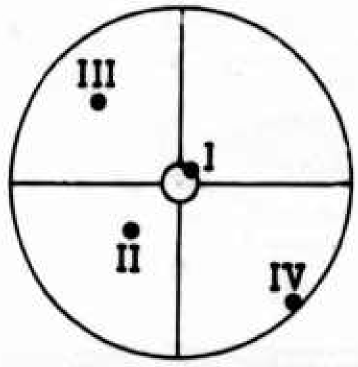

Location of pressure transducers on gore center line

Ringslot

Figure 104 c_{pd} and filling versus time

v_0 = 100 ft / sec

Run No. 174

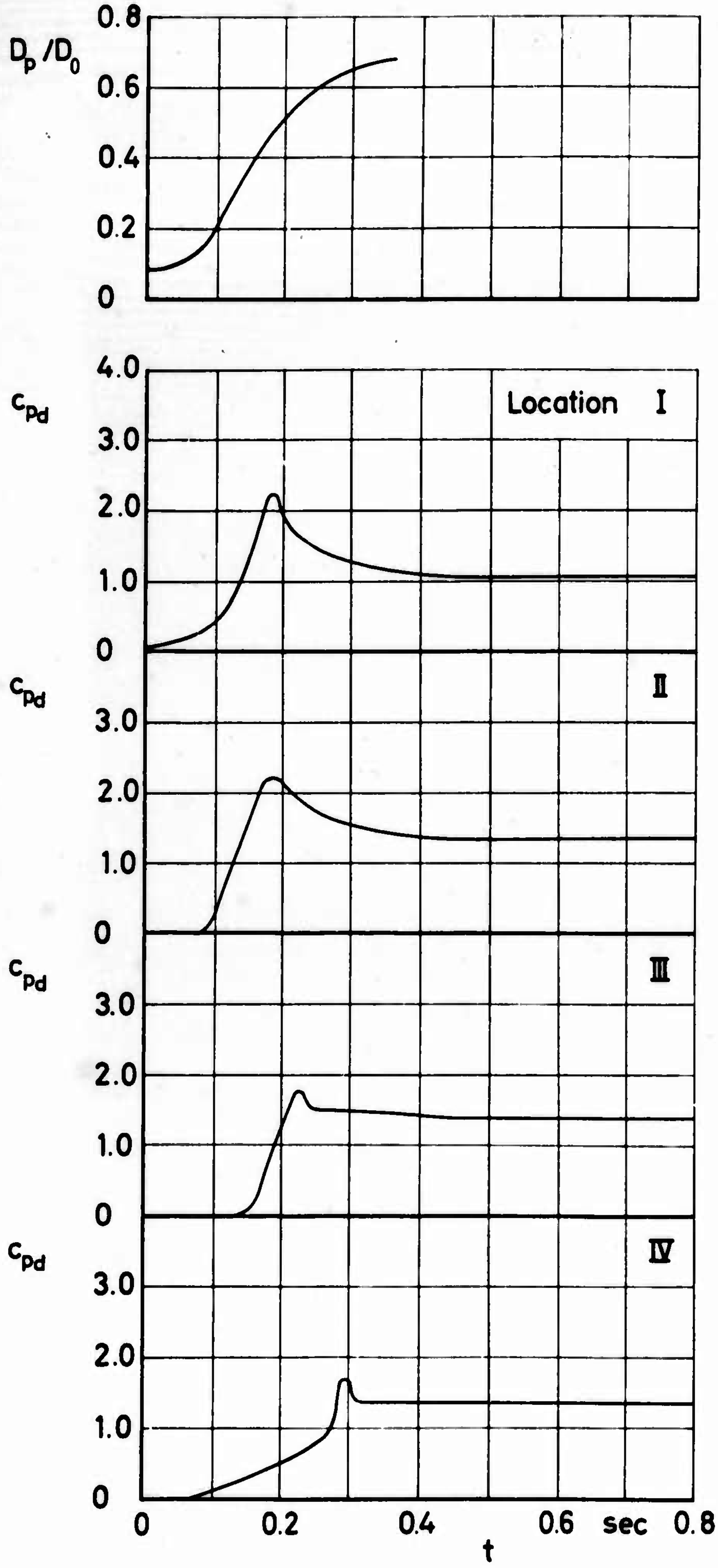

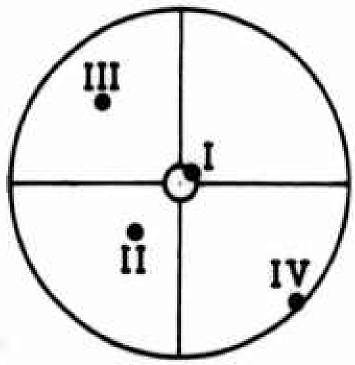

Location of pressure transducers on gore center line

Ringslot

Figure 105 c_{pd} and filling versus time

v_0 = 100 ft/sec

Run No. 175